ANISOTROPY OF EXTREMELY HIGH ENERGY COSMIC RAYS

by

Ming Huey A. Huang

A dissertation submitted to the faculty of
The University of Utah
in partial fulfillment of the requirements for the degree of

Doctor of Philosophy

Department of Physics

The University of Utah

December 1996

THE UNIVERSITY OF UTAH GRADUATE SCHOOL

SUPERVISORY COMMITTEE APPROVAL

of a dissertation submitted by

Ming Huey A. Huang

This dissertation has been read by each member of the following supervisory committee and by majority vote has been found to be satisfactory.

	Chair: Pierre Sokolsky
	Dave Kieda
	Yong Shi Wu
	Clayton Williams
	Kuonan Liou

THE UNIVERSITY OF UTAH GRADUATE SCHOOL

FINAL READING APPROVAL

To the Graduate Council of The University of Utah:

I have read the dissertation of Ming Huey A. Huang in its final form and have found that (1) its format, citations, and bibliographic style are consistent and acceptable; (2) its illustrative materials including figures, tables, and charts are in place; and (3) the final manuscript is satisfactory to the Supervisory Committee and is ready for submission to The Graduate School.

Date

Pierre Sokolsky
Chair, Supervisory Committee

Approved for the Major Department

Craig Taylor
Chair/Dean

Approved for the Graduate Council

Ann W. Hart
Dean of The Graduate School

ABSTRACT

The Fly's Eye group has studied two of the most important topics of extremely high energy cosmic ray (EHECR) physics – the spectrum and composition. The results from study of these two topics show evidence of two components in EHECRs. One is a heavy source, mainly iron nuclei, which dominates at energyies lower than $3EeV$. The other is a light source, mainly protons, which dominates at energies higher than $3EeV$. This study uses several anisotropy analyses to study the arrival directions of EHECRs.

We start with a review of cosmic ray physics and the Fly's Eye detector. The system resolutions and the difference between the real detector and the Monte-Carlo are examined. Some systematic errors and differences are found. The data structure and isotropic backgrounds are then discussed. Some improvements are made to avoid large error or to increase statistics. Two types of backgrounds, scrambled events and live time, are discussed and compared. For the first time, event rate is introduced in the live time background. The two backgrounds are consistent with each other in the large scale.

The analyses consist of the six sky lobes, the harmonic analysis, the galactic plane enhancement factor, the galactic latitude gradient, the galactic plane clustering, and the supergalactic plane clustering. A consistent trend exists in all analyses except harmonics analysis and supergalactic plane clustering; the largest anisotropy is at $0.4 - 1.0EeV$ and then decreases as energy increases. This trend can be explained by an overestimation of events near the galactic plane and an underestimation of events near the poles. This trend shows that a small degree of anisotropy exists at energies below $3.2EeV$ and might be a clue to the galactic origion of these cosmic rays. We also found a clustering of events near the supergalactic plane. Although this finding is a confirmation of other reports, the relation of this clustering and the supergalactic structure is not yet clear.

To my mom HUANG TSEN, Hao Chi and my wife LIAO, Wen Wen

CONTENTS

LIST OF TABLES

LIST OF FIGURES

ACKNOWLEDGMENTS

My special thanks to my many friends and colleagues; without their support I could not have finished this dissertation. My best thanks are owed to Dr. Pierre Sokolsky whose support and comments kept this work on track. I also thank Dr. Paul Sommers and Dr. Hongyue Dai for the valuable discussions and to Mrs Barnett for her careful work. Finally, to Baocai Zhang, David Kieda, Steve Corbato, Barta Jones, and all the colleagues of Fly's Eye group, thanks for everything.

SPECIAL HONOR

"People do not come out of cancer as the same person."

In my last year of graduate study, I was diagnosed with acute myeloid leukemia on Oct. 7, 1995. It was my darkest moment. I was going to move into a new apartment the next day, was preparing for graduation, and my first baby was due in two weeks. My wife, Wen-Wen, delivered a healthy big boy; I am glad that I could stand by my wife and touch Jason when he was born. The greatest challenge is how to cope with the saddest and the happiest moments. Wen-Wen changed from a weak, dependent person to a person stronger than I could have ever imagined. I could only said "I love you, Wen!".

My mom and my sister originally came from Taiwan to celebrate the newborn baby. Instead, they were confronted with the painful surprise of careing for a sick son and brother. My cancer still brings anxiety to my family and Wen's.

My advisor, Dr. Pierre Sokolsky, encouraged me to stay strong, be optimistic and gave me full support to help me pass through the financial difficulty. The cosmic ray group secretary and my good friend Miss Barta Jones gave me moral support and reminded me that I am still somebody. My best thanks to Pierre and Barta.

Many friends from the Fly's Eye group, the Chinese Student Association, and the Great Salt Lake Chinese School reached out their hands to help my family pass through the most disappointing and yet the most exciting moment of my life. Thank you all for your hearty support.

The wonderful treatment from Dr. Buys and tender caring from doctors, nurses, and staffs of 5 North Nursing Station at the University of Utah Hospital helped me become healthy again. Thank you, my friends.

Indeed, I am not the same person I was. I owe too much to my family and my friends. Without them, I am history. In the Chinese way, when we cannot say thanks to each individual, we say "Thanks, heaven! Thanks, earth!".

CHAPTER 1

INTRODUCTION

Cosmic rays are energetic charged particles, some of which come from outside the solar system. Their energy ranges from $10^8 eV$, normally treated as high energy particles in nuclear physics, to $10^{20} eV$. These cosmic rays are fascinating not only because of their extremely high energy but also because of where they come from, how they are accelerated, and what nuclei they are composed of. These questions constitute the main topics in cosmic ray physics. The research on cosmic rays contributes not only to the understanding their nature but also to high energy physics, cosmology, and astrophysics.

The Fly's Eye is a detector of extremely high energy cosmic rays, EHECRs, which have energy greater than $10^{17} eV$. This dissertation concentrates on the question of the arrival direction of EHECRs. The anisotropy of EHECRs may indicate where these cosmic rays come from. Together with some information about the spectrum and composition of cosmic rays, anisotropy studies will help solve theoretical problems related to the acceleration models, the cosmic ray sources, and the galactic magnetic field strength.

Although the Fly's Eye 1 detector was shut down in July 1992, some of the best observational data have just been published by the Fly's Eye group [1, 2, 3, 4, 5, 6, 7, 8]. Around $0.3 \times 10^{18} eV$ (the ankle point), the spectrum is shown to become flatter than below $10^{18} eV$, and the major composition appears to change from iron to proton. This correlated change may indicate a transition between cosmic ray sources. One possibility is that a heavy, mainly iron nucleus, galactic source terminates around the ankle point; another light, mainly proton, extragalactic source begins to dominate.

Chapter 2 starts with a short summary of cosmic ray physics below $10^{17} eV$. This summary serves as a foundation to the higher energy region. We then review some basic experimental EHECR physics topics. We start with the interactions of cosmic rays in

the atmosphere, then discuss how to use these interactions to detect the primary cosmic rays. The classical topics of the spectrum, composition, and anisotropy are discussed later. Finally, the galactic magnetic field, a major factor for anisotropy, is discussed in order to understand its influence on anisotropy from several regions of the galaxy.

A brief introduction of the Fly's Eye detector is presented in Chapter 3. The software reconstruction of extensive air shower is discussed latter. The Monte-Carlo simulation of the shower and the detector is then introduced. The final section compares the virtual and real detectors.

Chapter 4 discusses the foundation of this research. It covers the processing of observed data and techniques of predicting the isotropic distribution. The most difficult part of the anisotropy study is the prediction of what an isotropic distribution will look like. Two types of prediction, event scrambling and live time, are used in this research. The latter has never been successfully used in previous analysis; but due to some improvement in algorithms, it is successfully applied to this research and is found consistent with the scrambled event methods which were used in previous analysis.

The main topics of this dissertation are in Chapter 5 which discusses the algorithms and results of anisotropy analyses. First, we compare the event probability density and live time background in several coordinates. Then we discuss and present each anisotropy analysis, such as the six-sky-lobes, the galactic latitude gradient, the galactic plane enhancement factor, the harmonic analysis, and the galactic plane clustering.

Finally, in Chapter 6 we summarize the new improvements, the new finding in system resolution from previous chapters and the results from anisotropy analyses; we then conclude with a possible explanation of those results.

CHAPTER 2

EXTREMELY HIGH ENERGY COSMIC RAY PHYSICS

This chapter reviews cosmic ray physics. The first section gives a short summary of cosmic ray physics from GeV to EeV energies; then all other sections concentrate on extremely high energy cosmic rays.

The ultimate question of cosmic ray physics is cosmic ray origin and acceleration mechanisms. Experimentally, using various kinds of detectors, we try to detect cosmic rays and to identify their energy, composition, and arrival direction. Theoretically, we apply physical laws to learn how these particles travel through space and the atmosphere and to search for where and how they are accelerated to such high energy. By using the observed data of energy spectrum, composition, and anisotropy, we may limit some possibilities and learn about physical processes that cannot be reached within the solar system.

2.1 Introduction to Cosmic Ray Physics

2.1.1 Spectrum

Cosmic rays have been studied for more than 90 years [9]. Before particle accelerators were available, cosmic rays were the only available source for high energy particles and many fundamental particles were found from the study of them [10]. Even now, the energy of EHECR is unreachable by today's accelerators.

The most distinctive feature of cosmic ray physics is that the flux of cosmic rays follows a power law of energy

$$N(E)dE \propto E^{-\gamma}dE$$

where γ is called the spectrum index. Depending on the energy range, γ is approximately 2.5 to 3.1. Due to this large index, the flux is decreasing dramatically. Therefore, it is

customary to multiply the differential flux with some power of energy. Figure 2.1 shows the differential spectrum for the sum of all nuclei from $10^{11}eV$ to $10^{20}eV$ [7, 11].

Two spectrum breaks or changes of spectrum index can be found in Figure 2.1. The first is called the *'knee'*. The spectrum index is about 2.5 - 2.7 for the all particle spectrum for energy below $10^{15}eV$. It then steepens to about 3.1 above the knee.

The second break is called the *'ankle'* and it occurs around $3 \times 10^{18}eV$, $3EeV$. Due to extremely low flux, the statistics are very poor in the EHE region. The existence of this feature is still debated. According to recent Fly's Eye results, the spectrum index rises from 3.01 at $0.1EeV$ to 3.27 at $0.3EeV$ and then falls to 2.71 above $3EeV$ [2, 7].

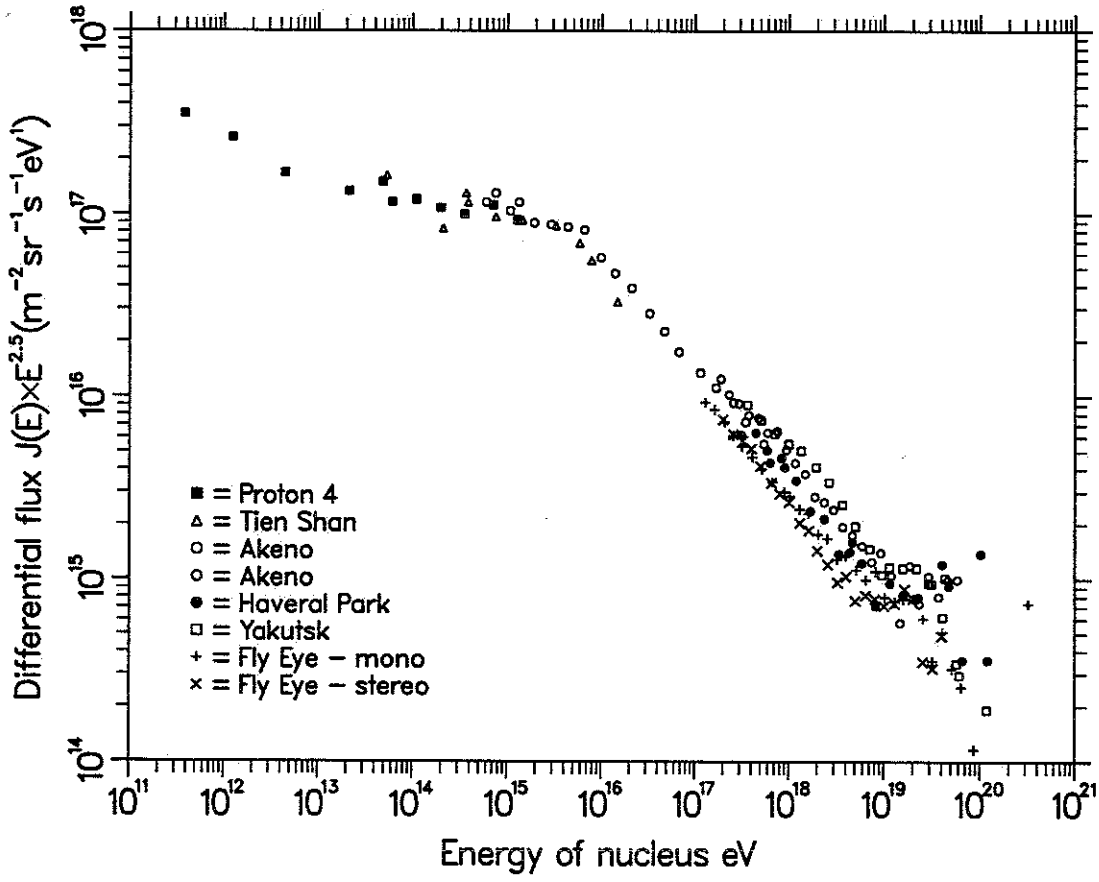

Figure 2.1. The all particle differential spectrum. The proton 4, Tien Shan, and Akeno data are from [10]. The new Akeno, Yakutsk, Haveral Park, and Fly's Eye data come from [5].

Although there is some dispute about these two points, I use them as landmarks to distinguish different methods of research and physics in the subsequent contents.

2.1.2 Detection

2.1.2.1 Below the knee. Below the knee, cosmic rays can be stopped in a small volume detector such as spark chamber, emulsion chamber, ... etc.. Therefore, both energy and chemical composition can be studied directly. Direct measurements are valid up to $10^{14}eV$ and are expected to be extended to $10^{15}eV$ in the near future. These detectors can be flown on board balloons or satellites to avoid the absorption caused by the atmosphere.

2.1.2.2 Above the knee. Due to low flux and deep penetration of the atmosphere, cosmic rays above the knee can be detected only by their interaction with the atmosphere. These detectors are discussed in detail in section 2.3.

2.1.3 Composition

2.1.3.1 Below $10^{10}eV$. Some cosmic rays below $10^{10}eV$ come from energetic solar flares and solar winds. But the flux shows an anticorrelation with sun spot activity, suggesting the existence of an extrasolar component whose transport is modified by the solar wind.

2.1.3.2 10^{10} to $10^{14}eV$. Cosmic rays above $10^{10}eV$ are less modulated by solar wind. Figure 2.2 shows the histograms of the abundance of nuclei from cosmic rays and from solar system material [12]. The composition of these cosmic rays is similar to matter in the solar system. The secondary/primary nuclei ratio such as Be/C can be used to study how much interstellar material these cosmic rays pass through. Radioactive isotopes, such as ^{10}Be, can be used to study the age of cosmic rays.

2.1.3.3 Around the knee. The reason for the formation of the knee is unknown. There are two plausible theories. One uses a rigidity dependent leakage out of the galaxy. The other assumes that the maximum energy of acceleration is limited by the acceleration mechanisms. The former predicts an increasing fall-off of the flux with energy for lighter

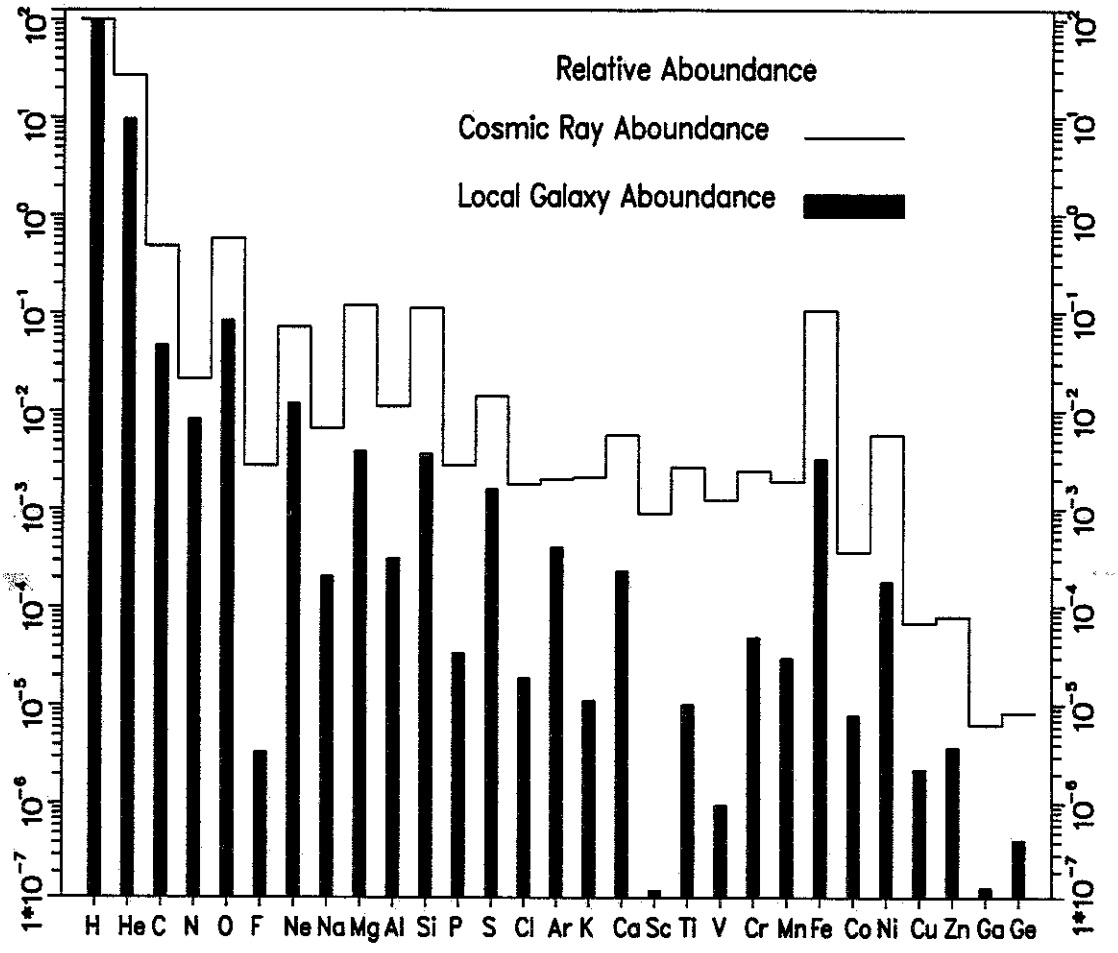

Figure 2.2. Nuclear abundances in cosmic rays and local galaxy. Data come from [12].

elements. The composition therefore will become gradually heavier [13]. Depending on the exact acceleration mechanism, the latter theory predicts that the composition as a function of energy could also be affected. Direct measurements are needed to resolve this debate.

2.1.3.4 Above the knee. Above the knee, the composition is measured indirectly and has large statistical fluctuations. The first important issue is to distinguish γ ray induced showers from charged cosmic ray showers. This distinction can be made by using the muon content of a shower. The second issue is to find the atomic weight of cosmic rays. That is difficult because only the secondary particles are recorded. Few results have

been reported. Recently the Fly's Eye group reported that the EHECRs are dominated by heavy (probably iron) nuclei from 0.1 to $0.3EeV$ and change gradually to predominantly light (protons) above $10EeV$.

2.1.4 Anisotropy

The large scale anisotropy is normally defined as

$$\delta = \frac{I_{max} - I_{min}}{I_{max} + I_{min}}$$

where I_{max} and I_{min} are the maximum and minimum flux at some coordinate. But this definition is hard to use. Instead, harmonic analysis, discussed in sec 2.6, is the most widely used technique.

2.1.5 Source and acceleration

2.1.5.1 Below the knee. The seeds of cosmic rays are believed to be generated by violent star activity such as flares and supernova explosions. These particles are then accelerated by supernova shock waves [16, 16]. Some gamma rays have been observed from supernova remnants [14]. These gamma rays come from the interaction of cosmic rays with the surrounding gas. Their direction and periodicity all show positive correlation with supernova remnant activity.

2.1.5.2 Above the knee. It is generally believed that the source of above the knee cosmic rays is galactic. But the acceleration mechanisms are still a mystery. Some shock acceleration models are modified to work in these energy regions [17, 18].

2.1.5.3 Above the ankle. Due to the limit of proposed galactic acceleration mechanisms, cosmic rays above the ankle are supposed to be extragalactic. Further investigation is needed.

2.2 Interaction in the Atmosphere

2.2.1 The extensive air shower

Cosmic rays entering the atmosphere will collide with nuclei of atoms such as nitrogen or oxygen. These interactions generate secondary particles such as nuclei and pions.

These secondary hadrons collide with atmospheric nuclei and generate further secondary particles in similar ways. The pions decay into muons and neutrinos or gamma rays, which can generate secondary electron-positron pairs and electron neutrinos. This cascade process, called an extensive air shower or EAS, continues until the mean energy of the individual particle is too low to generate new particles and the number of particles, or the shower size, reaches a maximum. This point is called the shower maximum, and the depth of shower maximum is called X_{max}. After this point, the energy loss mechanisms dominate over the particle production mechanisms. These parameters and the primary energy are related to each other.

An easy toy model can explain some important connections between these variables. Suppose the initial energy is E and each cascade generates M particles and passes through $\lambda\ gm/cm^2$ of matter. The first interaction would occur in $\lambda\ gm/cm^2$ and have M secondary particles, each having energy E/M. The second interaction happens at $2\lambda\ gm/cm^2$ and has $M * M$ particles each having energy E/M^2, ...et cetera. So the Nth interaction will take place in $N\lambda\ gm/cm^2$ and have M^N particles. If the mean energy reaches the critical energy E_c, the energy at which particles stop multiplying, then the maximum size S_{max} is M^N, the depth of shower maximum X_{max} is $N\lambda$, and E_c is E/S_{max}. So

$$\begin{aligned} N &= \frac{\ln S_{max}}{\ln M} = \frac{\ln E/E_c}{\ln M} \\ E &= E_c * S_{max} \propto S_{max} \\ X_{max} &= \lambda * (\ln S_{max}/\ln M) \propto \ln S_{max} \end{aligned}$$

where the total initial energy is proportional to shower size at maximum and the depth at maximum is proportional to the logarithm of the shower size.

Of course, the real world is not so simple. The cascade generates different secondary particles according to the high energy interaction, and the interaction lengths depend on the cross sections σ_{cr-air} which depend on the energy of incident and secondary particles.

2.2.2 High energy interaction

Ignoring heavy meson production, the first interaction can be simplified to be either

hadronic shower :	CR + N or O	$\rightarrow$ Hadron + $\pi^{\pm,0}$ or $K^{\pm}$
electromagnetic shower :	γ + N or O	$\rightarrow$ Hadron + $\pi^{\pm,0}$ or $K^{\pm}$
	γ + N or O	$\rightarrow e^+ + e^-$

There are three channels of interaction after the first interaction.

Hadronic channel:

inelastic scattering	Hadron + N or O	$\rightarrow$	Hadron + $\pi^{\pm,0} + K^{\pm,0}$

Electromagnetic channel :

pion decay	π^0	$\rightarrow$	2γ
pair production	γ	$\rightarrow$	$e^+ + e^-$
compton scattering	$e^{\pm} + \gamma$	$\rightarrow$	$e^{\pm} + \gamma$

Muonic channel :

pion/kion decay	$\pi^{\pm}$ or $K^{\pm}$	$\rightarrow$	$\mu^{\pm} + \nu_{\mu}(\overline{\nu}_{\mu})$
muon decay	$\mu^{\pm}$	$\rightarrow$	$e^{\pm} + \nu_e(\overline{\nu}_e) + \overline{\nu}_{\mu}(\nu_{\mu})$
bremsstrahlung	e	$\rightarrow$	$e + \mu^+ + \mu^-$

These reactions are well known but not in the extremely high energy region. The interaction cross sections must be extrapolated from the low energy region and therefore depend on extrapolation models. These interactions can be Monte-Carloed with some assumption and model-dependent cross sections. Chapter 3 explains the energy reconstruction and Monte-Carlo. Figure 2.3 shows a schematic of an EAS, the three channels, and three types of detectors.

2.2.3 Longitudinal development

For gamma ray induced showers, EAS simulations use two approximations. For the first approximation, only bremsstrahlung and pair production are counted for the particle generating process. Other processes are neglected and asymptotic diffusion equations are used. For the second approximation, only the ionization loss of electrons and the compton scattering of gammas are counted is for energy balance. For an electromagnetic shower, the number of electrons, N_e, can then be parametized as [19]

$$N_e = \frac{0.31}{\sqrt{y}} e^{t(1.0 - 1.5 \ln s)}$$

where s is the shower age parameter [20] which is 0 at the first interaction, 1 at maximum, and 2 at the point where the number of particles is less than 1. The variable t is the

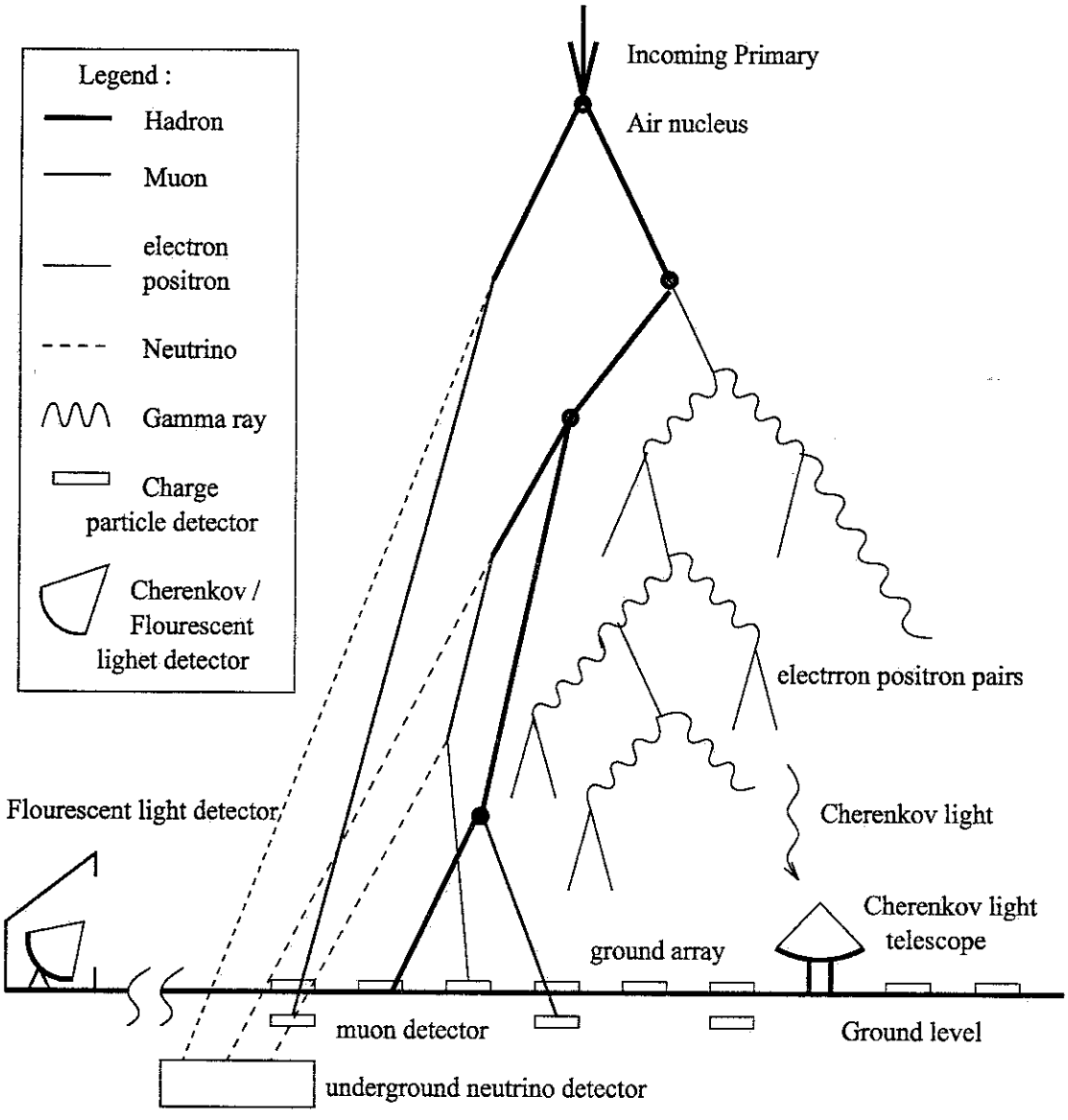

Figure 2.3. Schematic of an extensive air shower. The three channels of interaction and several types of detectors are shown in this figure.

depth into the shower in radiation lengths. The variable y is similar to interaction times N in the toy model. Here $y = ln(E_0/E_c)$. The y, t, and s are related by

$$s = \frac{3}{1 + \frac{2y}{t}}$$

For a hadronic shower, the first interaction plays an important role since it generates secondary hadrons and pions/gammas which then initiate electromagnetic showers. Therefore the hadronic shower can be treated as hadronic core plus electromagnetic subshowers. Due to this complexity, the hadronic shower lacks a well–defined shower age. After shower maximum, the hadron generation stops; therefore the rest is just a superposition of electromagnetic showers.

Gaisser *et al.* developed a model to describe the longitudinal development of nucleons and pions $\pi^{\pm}$ [21]. The π^0 is not fed into the hadronic cascade since it decays electromagnetically. The muon and neutrino are counted in the pion part.

$$\frac{dN_{E_0}(E,X)}{dx} = -\frac{N_{E_0}(E,X)}{\lambda_{N(E)}} + \int_e^{\infty} \frac{F_{NN}(E,E')}{E} \frac{N_{E_0}(E',X)}{\lambda_{N(E')}} dE'$$

$$\frac{d\Pi_{E_0}(E,X)}{dx} = -\Pi_{E_0}(E,X)\left[\frac{1}{\lambda(E)} + \frac{\epsilon_\pi}{EX_{cos\theta}}\right] + \int_E^{\infty} \frac{F_{N\pi^c}(E,E')}{E} \frac{N_{E_0}(E',X)}{\lambda_{N(E')}} dE' + \int_E^{\infty} \frac{F_{\pi^c\pi^c}(E,E')}{E} \frac{N_{E_0}(E',X)}{\lambda_{\pi(E')}} dE'$$

$N_{E_0}(E,X), \Pi_{E_0}(E,X)$: Number of nucleons and pions at energy E and depth X for primary energy E_0.

$\lambda_{N(E')}, \lambda_{\pi(E')}$: Interaction length of nucleons and pions which are determined primarily by σ^{inel}_{p-air} and $\sigma^{inel}_{\pi-air}$

$F_{ab}(E,E')$: Feynman scaling for the reaction

$$a + air \rightarrow b + anything$$

$$F_{ab}(E,E') = \frac{\pi}{\sigma^{inel}} \int \frac{d\sigma_{ab}}{d^3p} dp_\perp^2$$

To find a solution one need to make some assumptions about scaling. According to Monte-carlo calculation the result for a proton initiated shower can be parametized as

$$N(X) = N_{max} \left(\frac{X - X_o}{X_{max} - X_0}\right)^{(X_{max}-X_0)/\lambda} e^{(X_{max}-X)/\lambda} \qquad (2.1)$$

N_{max} : shower size at maximum
$N(X)$: shower size at depth X
X_0 : depth at first interaction
λ : interaction length = $70 gm/cm^2$

Although this formula is derived for a proton initiated shower, the shower generated by a heavy nucleus with atomic number Z can be treated as superposition of Z subshowers, each with energy E_0/Z. This formula is used in Fly's Eye data reconstruction and is in good agreement with observed data.

2.2.4 Lateral development

The lateral distribution of an electromagnetic shower can be viewed from the center of momentum system as electrons' multiply scattering. The particle density at a perpendicular distance r from the core is [20]

$$\rho(r) = \frac{N}{r^2} f\left(s, \frac{r}{r_1}\right) \tag{2.2}$$

N : total number of electrons
s : age of electromagnetic shower
r_1 : Moliere multiple scattering unit $\simeq$ 79 meter at sea level
f : Nishimura & Kamata formula

$$f\left(s, \frac{r}{r_1}\right) = \left(\frac{r}{r_1}\right)^{s-2} \left(1 + \frac{r}{r_1}\right)^{s-4.5} \frac{\Gamma(4.5-s)}{2\pi\Gamma(s)\Gamma(4.5-2s)}$$

For hadronic showers, we can add a hadronic core to the electromagnetic shower. Since the average shower age is approximately 1.25, equation 2.2 becomes the Nishimura-Kamata-Greisen (NKG) lateral distribution

$$\begin{aligned} \rho(r) &= \frac{N}{r^2}(\frac{r}{r_1})^{-0.75}(1+\frac{r}{r_1})^{-3.25}\frac{\Gamma(3.25)}{2\pi\Gamma(1.25)\Gamma(2)} \\ &= 0.483\frac{N}{r^2}(\frac{r}{r_1})^{-0.75}(1+\frac{r}{r_1})^{-3.25} \end{aligned}$$

The whole formula is independent of atmospheric depth to the first order. But we should bear in mind that this is an average and r_1 depends on depth. This formula is valid for depths between 600 and $1600 gm/cm^2$ and large fluctuations from average should be expected.

The muon lateral development is a little bit complicated because pions are more likely to decay when the energy of the pion is less than $30GeV$ or its height is above 5km. Therefore the higher energy muons detected at sea level reflect the earlier part of the shower. This is an important clue to distinguish electromagnetic showers from hadronic showers. The muon lateral distribution for a nearly vertical shower with energy $\geq 1GeV$ is [20]

$$\rho_\mu(r) = 18r^{-0.75}(1 + r/320)^{-2.5}(N_e/10^6)^{0.75} \text{ muons/m}^2$$

The radial dependence is flatter than the electron development. This dependence enables the muon detectors to be spaced wider apart than electron detectors.

2.3 Detection High Energy Cosmic Rays

The primary cosmic ray deposits its energy into the atmosphere through three channels. Most of the hadronic channels end up as electromagnetic channels. These charged particles lose their energy by excitation and ionization. The fast moving particles also generate Čerenkov light. These different forms of energy enable three different types of detector to detect the shower. The ground/underground array detect the charge particles, the Čerenkov telescope detect, of cause, cherenkov light, the Fluorescence light detector detect the fluorescence light from excited nitrogen.

2.3.1 Charged particle detector array

These arrays use scintillation counters or other charged particle detection devices to detect charged particles. To detect muons, the detector must be buried several feet underground to shield out the vast number of electrons. For the neutrino part, deep underground detectors, such as those used for proton decay or solar neutrino experiments, must be used.

The main problem for ground arrays is that they detect only one slice of the longitudinal distribution through widely spaced detectors. It is possible to find the total number of particles, N_e, by fitting the particle density sampled by individual counters to a certain lateral distribution. Since there is no direct information on shower age s

and initial particle composition, it is impossible to directly fit lateral distribution to the NKG distribution. One way is thst the s is left as a free parameter to be determined later. When the energy is below $10^{16}eV$, the shower size rather than the primary energy is the directly measured quantity and is usually used in interpreting array data. As the energy increases, the fluctuation becomes too large to have a good lateral fit. The other way is the $\rho(600)$ method, which uses the particle density 600 meters away from the core to estimate the total number of particles. This method had been shown to be the least dependent on shower development assumption [22]. The Haverah Park group estimated the shower energy by

$$E = 7.04 \times 10^{17} \rho_v(600)^{1.018}\, eV$$

where $\rho_v(600)$ is the corrected particle density for a vertical shower [23]

$$\rho_v(600) = \rho(600) \mathrm{e}^{(1018/\lambda)(\sec\theta - 1)}$$

2.3.2 Čerenkov light

Čerenkov telescopes are widely used for gamma ray astronomy. To generate Čerenkov light, the particle velocity v must be greater than the light velocity of that media, $c/n(H)$, where n is the index of refraction at altitude H. The minimum energy at H is

$$E_{min} = 0.511 MeV/\sqrt{2\delta}$$

$$\delta = 1 - n = 0.0029 * \mathrm{e}^{-H/H_s}$$

H_s : scale height = 7.5Km at sea level

Čerenkov light is emitted in a small angle:

$$\theta_{max} = \mathrm{Cos}^{-1}(1/n) \simeq 81\sqrt{\delta} \text{ degree}$$

The angular distribution of Čerenkov photons come from this small angle plus the angular spread of electron multiple scattering. It can be approximated by [19, 24]

$$\frac{dN_p}{d\Omega} \propto \frac{\mathrm{e}^{-\theta/\theta_0}}{\sin\theta}$$

where

$$\theta_0 = 0.83 E_{min}^{-0.67}$$

which generates an intense beam within about 6 degree of the shower axis.

The primary particle energy can be found from the total light flux of Čerenkov photons.These photons are an integral over the total shower track:

$$\Phi(E_0) = \int_0^{X_g} \Psi(X) N_e(E_0, X) dx \tag{2.3}$$

$$\Psi(X) = \int_{E_{min}}^{E_0} Q(E) G(E, X) dE$$

$$Q(E) = \frac{dN_p}{dl} = 4\pi\alpha \left(1 - \left(\frac{E_m in}{E}\right)^2\right) \int \frac{\delta}{\lambda^2} d\lambda \quad \text{photons/meter}$$

$Q(E)$	:	number of photons emitted by electron of energy E per unit length
$G(E,X)$	:	normalized electron energy spectrum of EAS at depth X
$\Psi(X)$	:	total number of electrons at depth X
$Ne(E_0,X)$	:	longitudinal development of EAS with energy E_0 at depth X.

The only unknown is $G(E,X)$ which can be found from Monte Carlo simulation of hadronic showers. Results show it varies only slightly with energy and the $\Psi(X)$ is almost independent of depth X. Therefore $\Phi(E_0)$ can be simplified as

$$\Phi(E_0) = \Psi(X_{max}) \int_0^{X_g} N_e(E_0, X) dx$$

This equation simply means that the Čerenkov flux is the integral of the shower longitudinal development above the observation altitude.

The lateral distribution of Čerenkov light has a "Čerenkov ring" around the shower core which comes from early interaction at high altitude. This angular dependence and pulse profile provide information about longitudinal development and shower maximum.

2.3.3 Nitrogen fluorescence

Ionized particles can excite nitrogen molecules, which then emit fluorescence photons, mostly from the 2P band of N_2 and 1N band of N_2^+, within about 10 to 50 nanoseconds. The wavelength of this fluorescence light is about 3100Å to 4400Å. The atmosphere is quite transparent in this wavelength range (attenuation length about 15 km for a

vertical beam). The fluorescence yield is mildly dependent on altitude and temperature. Although the fluorescence yield is quite small, the huge number of electrons and the isotropic emission of fluorescence photons from the shower make it possible to detect the fluorescence light even 25 kilometers away! This far reaching sensitivity allows this detector to cover a huge area, making it suitable for the detection of an extremely low flux of EHECR.

The world's unique fluorescence light detector operated by the University of Utah Fly's Eye group is in Dugway Utah. The details of hardware and software are covered in Chapter 3.

2.4 Spectrum

2.4.1 Fly's Eye energy spectrum

Figures 2.4 and 2.5 show the spectrum using stereo and monocular Fly's Eye data [2, 7]. The stereo spectrum can be divided into three regions and a dip is clearly seen. Using the weighted least χ^2 fit, the best fit spectral indexes are listed in Table 2.1.

The expected number of events based on the overall fit (renormalized at $10^{17.6}eV$) is 5936.3; the observed number is 5477. The significance of this deficit is 5.96σ. The expected number of events above $10^{18.5}eV$ based on the overall fit (renormalized at $10^{18.5}eV$) is 230.0; the observed number is 281. The significance of this excess is 3.4σ. If we use the best fit in $10^{17.6} - 10^{18.5}$, the expected number is 205.9 which is 5.2σ.

Table 2.1. Spectral slopes and normalization of $J(E)(m^{-2}sr^{-1}s^{-1}eV^{-1})$

Type	Energy range (eV)	Power index	$\log_{10}$(normalization)	Normalized at (eV)
stereo	$10^{17.3} - 10^{19.6}$	-3.18 ± 0.01	-29.593	10^{18}
	$10^{17.3} - 10^{17.6}$	-3.01 ± 0.06	-29.495	10^{18}
	$10^{17.6} - 10^{18.5}$	-3.27 ± 0.02	-29.605	10^{18}
	$10^{18.5} - 10^{19.6}$	-2.71 ± 0.10	-32.623	10^{19}
mono	$10^{17.3} - 10^{19.9}$	-3.07 ± 0.01	-29.55	10^{18}
	$10^{17.3} - 10^{19.0}$	-3.08 ± 0.01	-29.56	10^{18}
	$10^{19.0} - 10^{19.7}$	-2.89 ± 0.15	-29.62	10^{18}

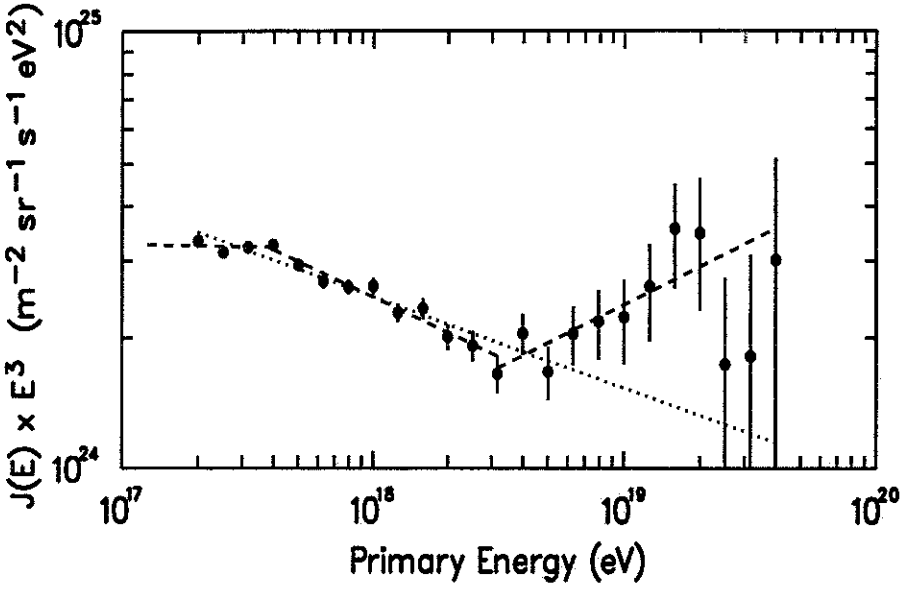

Figure 2.4. Fly's eye Stereo energy spectrum. Points : data. Dashed line : Best fit in each region. Dotted line : Best fit up to $10^{18.5}eV$.

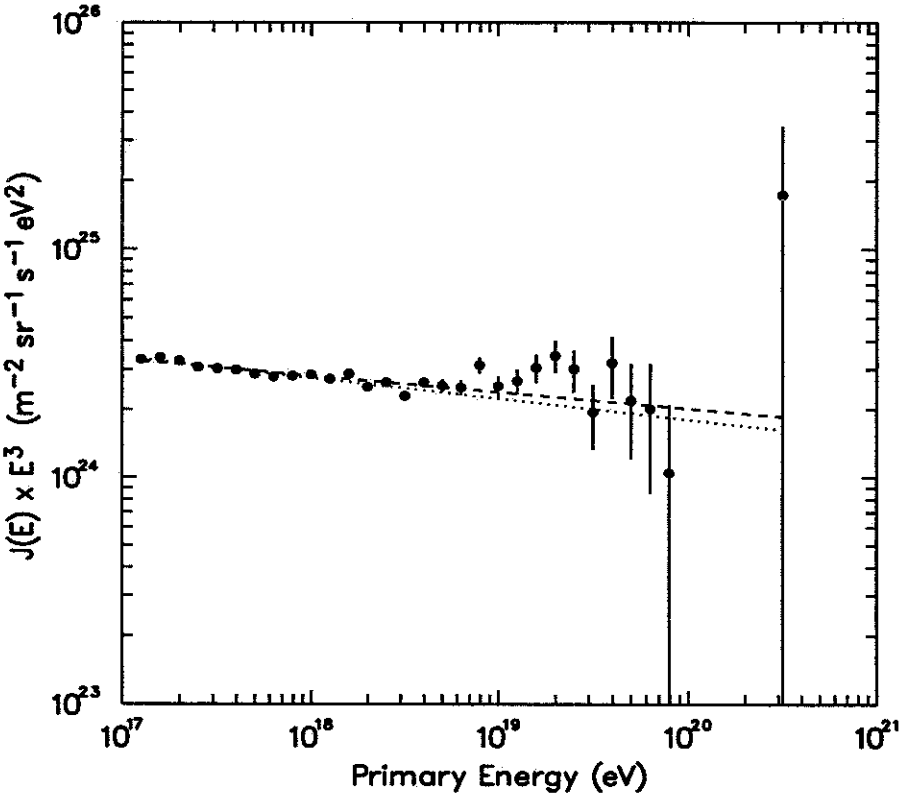

Figure 2.5. Fly's eye monocular energy spectrum. Points : data. Dashed line : Best fit of the total spectrum. Dotted line : Best fit up to $10^{18.5}eV$.

This clear ankle feature is washed out in monocular data by poorer energy resolution, but the flattening of the spectral index is still significant.

2.4.2 Highest energy event

A $320^{+35}_{-40}\ EeV$ event was recorded by Fly's Eye 1 on Oct. 15 1991 at universal time 7:34 am [25]. The depth of shower maximum, $X_{max} = 815^{+45}_{-35} g/cm^2$, is consistent with the expected depth of a proton ($X_{max} = 850 g/cm^2$). The arrival direction is 85.2 ± 0.2 degrees of right ascension and $48.0^{+3.2}_{-4.8}$ degrees of declination or 9.6 degrees of galactic latitude and 163.4 degrees of galactic longitude. This event comes from the direction near the anticenter of the galaxy. At this energy, the gyroradius is about $150 Kpc$ for a proton in the galactic magnetic field of $2.2\mu G$. The angular deflection is less than 1 degree in galactic magnetic fields [26]. Two nearby pulsars, the Crab and Geminga, are about 20 degrees away. No other known galactic energetic sources are near the arrival direction of this event. However a radio galaxy 3C134 is in the vicinity. The source of this event is probably not in the galactic disk but could come from outside our galaxy.

2.4.3 Greisen-Zatsepin-Kuzmin effect

The 2.7°K blackbody radiation photon can interact with the cosmic ray mainly through

$$\gamma_{2.7^o} + \mathrm{p} \rightarrow \Delta^{*+}(1232 MeV) \rightarrow \mathrm{p} + \pi^0 \text{ or } \mathrm{n} + \pi^+$$

This interaction was discovered by Greisen [27] and independently by Zatsepin and Kuzmin [28] shortly after the confirmation of the existence of microwave background radiation. If cosmic rays are extragalactic, the cosmic ray flux above a certain energy is attenuated by 2.7^0K microwave photons with an attenuation length of about 6 Mpc in intergalactic space. Most of the cosmic rays will be cut off above a certain energy. Hill and Schramm [29] calculate the detailed interaction and consider the red shift of the microwave background. The cut-off energy depends on the source spectrum and the distance of the source. The further away the source, the lower the cut-off energy. If the source is 18Mpc away, (the virgo supercluster is about 20Mpc away), then cosmic rays

with energy $\geq$ 100EeV are virtually unattenuated. But if the source is 144Mpc away, the cut-off energy is about 60EeV. For a 300EeV proton, it is possible to come from 20Mpc away but almost impossible to come from 100Mpc away.

M. Teshima combined Akeno, Fly's Eye, Haveral Park, and Yakutsk data and assumed that the spectrum continues and has a power index 2.6 ± 0.1 for energy above $100EeV$ [30]. He predicted that 22 ± 5 events should be observed by all four groups. The Haveral Park group had five events and both Yakutsk and Fly's Eye had one event above 100EeV. Another 220EeV event was recorded by Akeno [31]. Although there is some systematic difficulty in combining different experiments, such as energy scale and aperture, we still see some deficit in the combined result or the results of the individual experiments; therfore, the mystery of GZK cut-off still needs more statistics to be resolved.

2.5 Composition

2.5.1 Muon content

The muon content of an EAS is the ratio of the number of muons to the number of electrons/positrons, N_μ/N_e. Most of the muons come from decays of pions. Shortly after the first interaction, the air density is low and the pion energy is high. The pions are more likely to decay than to interact with atmospheric nuclei. Therefore the highest energy muons directly reflect the early stage of shower development. If both the electron/positrons and the muons are detected, then the muon content, which is sensitive to composition, can be used to distinguish a gamma ray initiated shower from a hadron initiated shower. The muon number of a gamma ray shower is only about 5% of that of a hadron shower at comparable energy.

2.5.2 X_{max} and elongation rate

The distribution of depth of shower maximum X_{max} depends on the chemical composition of cosmic rays due to different first interaction length and cross section. Therefore X_{max} provides a sensitive clue to the original composition. The first interaction depth is about $70gm/cm^2$ for proton and $15gm/cm^2$ for iron at $10^{15}eV$ region. The larger value

of this parameter makes the depth of the first proton interaction fluctuate more than iron does. The value of X_{max} is fluctuated by the first interaction. X_{max} depends on the product of the inelastic cross section σ^{inel} and inelasticity K

$$K = \frac{E_0 - E'}{E_0 + M_n}$$

where

E_0 : initial energy
E' : energy after collision
M_n : target mass

Therefore the X_{max} distribution also depends on the hadronic interaction model.

Another clue to the composition is the elongation rate, which is the change of X_{max} per decade of energy.

$$D_{el} = \frac{dX_{max}}{d\log_{10} E}$$

For a gamma ray shower, D_{el} depends on π^0 decay only; D_{el} is then the radiation length in air $\simeq 80gm/cm^2$. For hadronic showers, however, D_{el} depends on hadronic interactions (therefore depends on models). If the composition is fixed, the elongation rate should stay at the same value. If it changes, the composition must also change. The elongation rate is less dependent on hadronic models than X_{max} is.

2.5.3 Experimental result

The Fly's Eye detector can detect X_{max} for each individual shower. The stereo X_{max} resolution is about $45gm/cm^2$. Due to fluctuations of X_{max}, the individual X_{max} cannot be used to determine which nuclei produced a given shower. Statistically, however, it is possible to determine the mean X_{max} and find the mean composition based on hadronic models.

Figure 2.6 shows X_{max} versus the primary energy for the experimental data and for the Monte-Carlo prediction for proton and iron nuclei [3, 6]. The elongation rate below 0.3EeV is consistent with a constant composition of $50g/cm^2$. For 0.3EeV to 10EeV, the X_{max} distribution is inconsistent with any pure composition and the elongation rate is $78.9 \pm 3.0g/cm^2$ a rate which indicates a changing composition, a change from predominately heavy to predominately light.

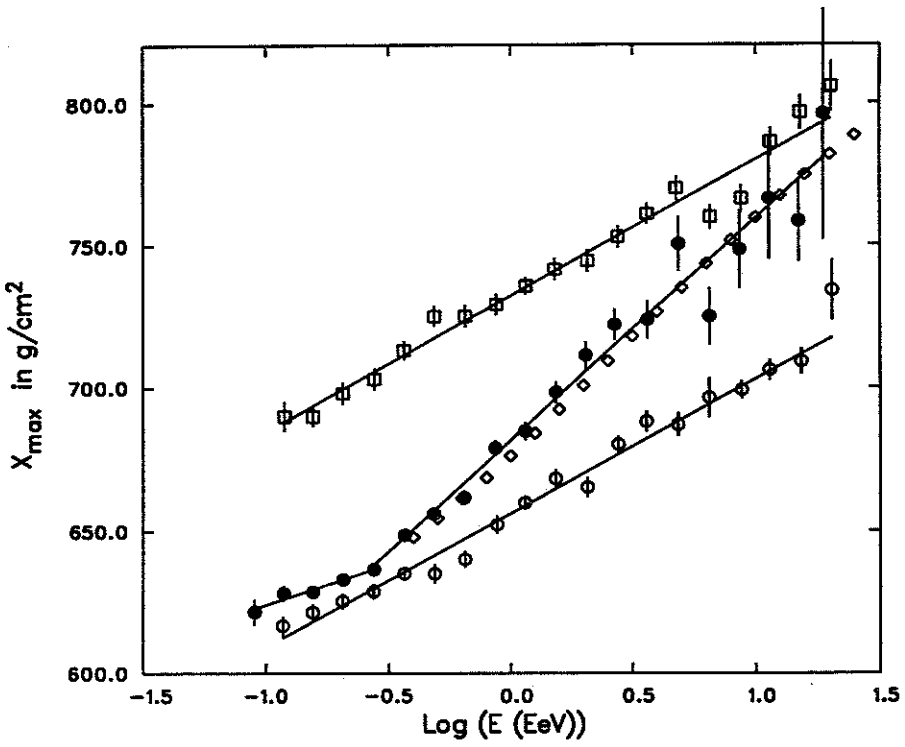

Figure 2.6. The X_{max} distribution of stereo Fly's Eye data [3,6]. The data are shown in the solid dot. The expectations of iron flux are shown as circles. The expectations for proton flux are shown in squares. The expectations from two component fit are shown in diamonds.

2.5.4 Two source fit

The dip structure of the stereo spectrum and the change of composition suggest a change of cosmic ray source. We consider a two component fit, one being a steeply falling power spectrum of predominantly iron flux, the other a flatter flux of protons. The best fit results from $10^{17.6}eV$ to $10^{19.6}eV$ are [6, 32]

$$\text{iron flux}: \quad \log[J(E)(m^2 \cdot s \cdot sr \cdot eV)^{-1}] = 33.185 - 3.496 \times \log(E)$$

$$\text{proton flux}: \quad \log[J(E)(m^2 \cdot s \cdot sr \cdot eV)^{-1}] = 16.782 - 2.610 \times \log(E)$$

The ratio of the two fluxes can be expressed as

$$\frac{\text{iron flux}}{\text{proton flux}} = 10^{-0.887 \times (\log(E) - 18.5)}$$

The prediction of composition based on this two component fit is shown in figure 2.6. It can be seen that it fits the X_{max} observation very well. The predicted elongation rate in $10^{18}eV$ to 10^{19eV} is $81g/cm^2$ which is consistent with the observed value $78.9 \pm 3g/cm^2$.

2.6 Anisotropy

A nonzero anisotropy shows that the arrival direction of cosmic rays comes from some preferred direction at either large scales or small scales. Above 1 EeV, the anisotropy should point back to a source if the cosmic rays are protons and originate inside the galactic disk. Therefore anisotropy provides a clear clue about cosmic ray sources. The energy dependence of the anisotropy also provides a consistency check on assumptions about composition.

Two coordinate systems are used in the large scale anisotropy analysis. The harmonic analysis uses celestial coordinates; other analyses use galactic coordinates.

Small scale anisotropy searches for point sources which are concentrated in a small region. This topic is important in gamma ray physics where no magnetic bending is expected.

2.6.1 Harmonic analysis

Ground arrays have nearly uniform exposure in right ascension, (RA or α); the event reconstruction does not depend strongly on RA but does depend strongly on declination, (δ). Therefore harmonic analysis is normally done in RA for a certain declination band.

For an N event data set, if the RA of each event is α_i, the Rayleigh vector components (x, y) are defined as

$$x = \frac{2}{N}\sum_{i=1}^{N}\cos(\alpha_i) \qquad\qquad y = \frac{2}{N}\sum_{i=1}^{N}\sin(\alpha_i)$$

and the Rayleigh vector magnitude is given by $r = \sqrt{x^2 + y^2}$ with a phase $\psi = \mathrm{Tan}^{-1}(x/y)$. The phase points to the direction of the Rayleigh vector in RA. The expected Rayleigh vector magnitude from N random samples of uniform phase is $r_0 = 2/\sqrt{N}$. The probability of having a Rayleigh vector $\geq r$ is $P(\geq r) = \mathrm{e}^{-\kappa}$ where $\kappa = (r/r_0)^2 = Nr^2/4$. The uncertainity of phase is $\Delta\psi = 1/\sqrt{2\kappa} = \sqrt{2/Nr^2}$.

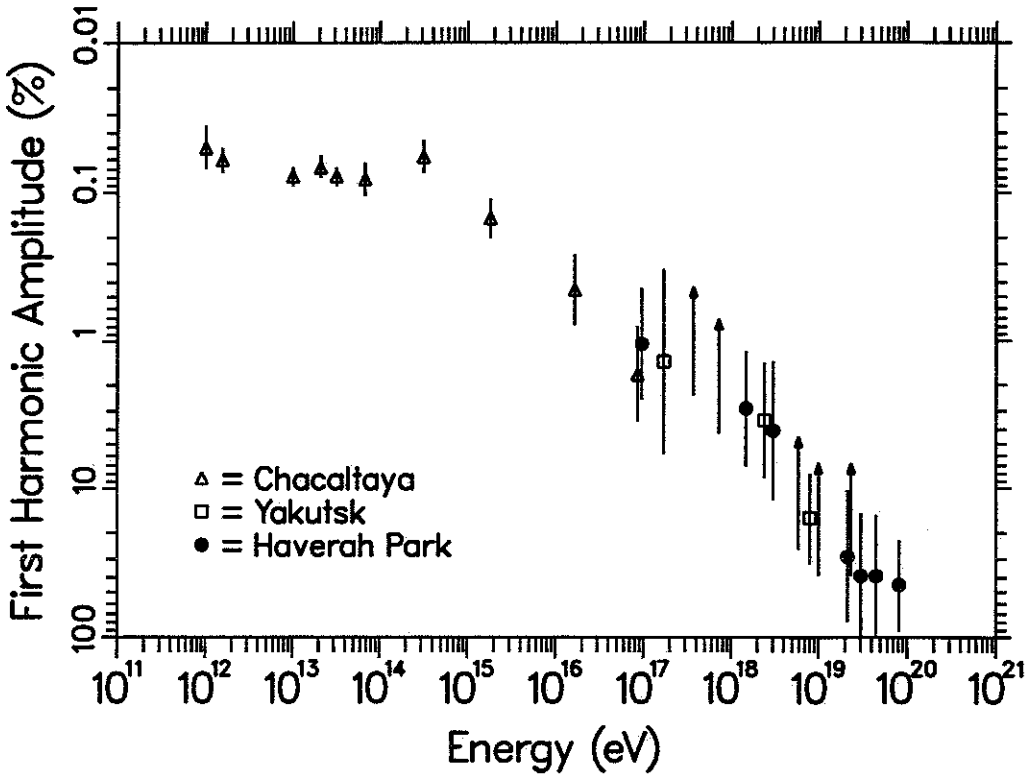

Figure 2.7. The amplitude of first harmonic as function of energy. Data come from [11].

The experimental result is normally expressed as a percentage which ranges from 0.1% at TeV to about 10% at EeV. Figure 2.7 shows the anisotropy as a function of energy [11, 33]. This anisotropy has features similar to those of the spectrum. Below the knee, the anisotropy is less than 1%; then it rises to several %s above the knee. There are large differences around the ankle, but the amplitude is about 10% to 30% with large uncertainty. The phases of first harmonics also show some dependence on energy [34].

2.6.2 Six sky lobes

Since most cosmic rays most likely come from our own galaxy, galactic coordinates should be a better choice. The nonuniform exposure of a detector in galactic coordinates is an additional complication.

The galactic coordinate consists of two components, galactic longitude (l) and galactic latitude (b). The galactic latitude is the elevation angle from the galactic plane. The

northern sky is positive; the southern sky is negative. The galactic longitude of an object is the angle from galactic center to the projection of the object on the galactic plane. The direction of motion of the spiral arm of Orion in which the solar system resides is in the direction of $l = 90°$. The galactic center is at (l=0, b=0).

Figure 2.8 shows the three major axes of galactic coordinates: Center-Anticenter, Forward-Backward, and North-South. These three axes are used to separate all the sky into 6 equal area lobes centered on each axis. The sky lobe analysis searches for excess/deficit from an isotropic prediction. Results from previous analyses [35] [36] and a recent analysis [4] all show no consistent and significant deviation from isotropic prediction for several energy ranges starting from $10^{17.5}eV$. Table 2.2 shows the result of recent analysis [4].

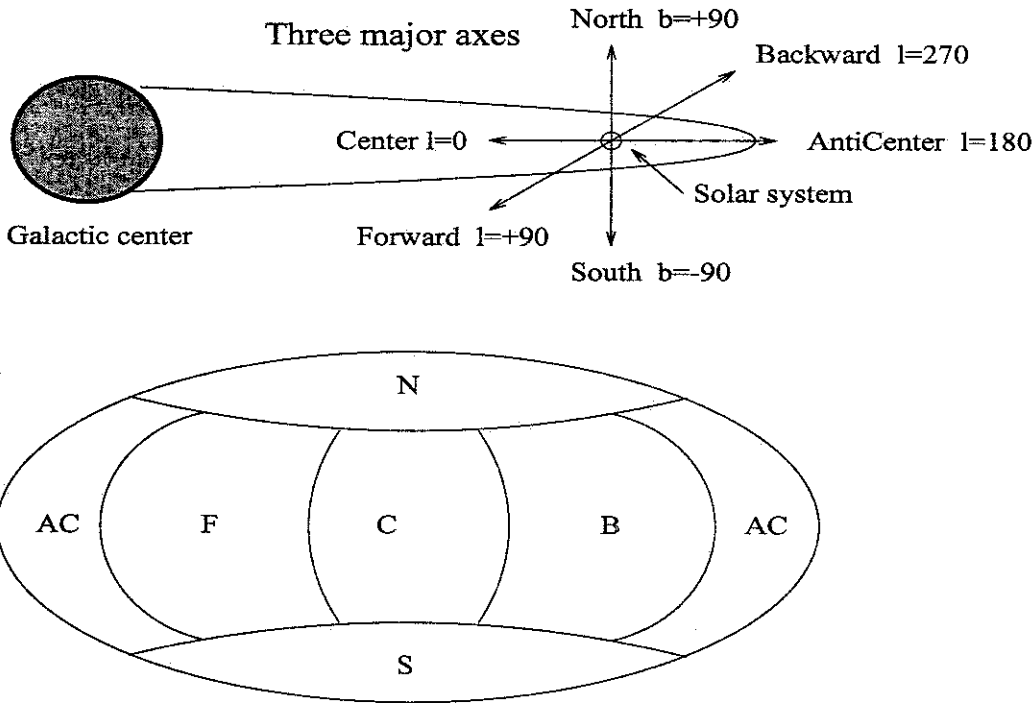

Figure 2.8. The six sky lobes and three major axes of galactic coordinate.

Table 2.2. Results from sky lobes analysis. # : Number of observed events. σ : Excess in unit of σ.

log(E) range		Sky Lobes North	South	Center	Anticenter	Forward	Backward
17.5 - 18.0	#	2855	682	481	2928	4276	84
	σ	-0.54	0.33	-0.19	-0.87	1.47	-0.72
18.0 - 18.5	#	942	362	270	1087	1404	78
	σ	-1.13	1.21	0.73	1.35	-1.48	0.64
18.5 - 19.0	#	267	90	68	251	380	39
	σ	1.20	-0.68	-1.03	-1.65	0.50	2.99
> 19.0	#	59	33	20	71	91	14
	σ	-0.84	0.83	-0.93	0.22	0.04	1.52

2.6.3 Galactic latitude dependence

If cosmic rays come from the galactic disk, the strong magnetic field of the galactic disk may confine more particles in the disk and the arrival direction of cosmic rays may have a galactic latitude (b) dependence. Wolfendale and Wdowczyk proposed a galactic disk enhancement formula [37]

$$I(b) = I_0 \left(1 - f_E + f_E \mathrm{e}^{-b^2}\right)$$

which was later modified to [38]

$$I(b) = I_0 \left(1 - f_E + 1.402 * f_E \mathrm{e}^{-b^2}\right)$$

to conserve total flux. A positive f_E indicates that the arrival directions favor the galactic disk. Figure 2.9 shows experimental results on the Wolfendale and Wdowczyk galactic disk enhancement factor.

The normalization for this formula has been recalculated again; see Appendix A. It should be 1.437 rather than 1.402. To compare our results with Wolfendale predictions, 1.402 was used for Figure 2.9. In this dissertation, I use 1.437 as the normalization constant.

Although Wolfendale *et al.* stated that an increasing f_E was observed in his compilation of world data [37, 38], most of their f_E are less than 3σ away from isotropy

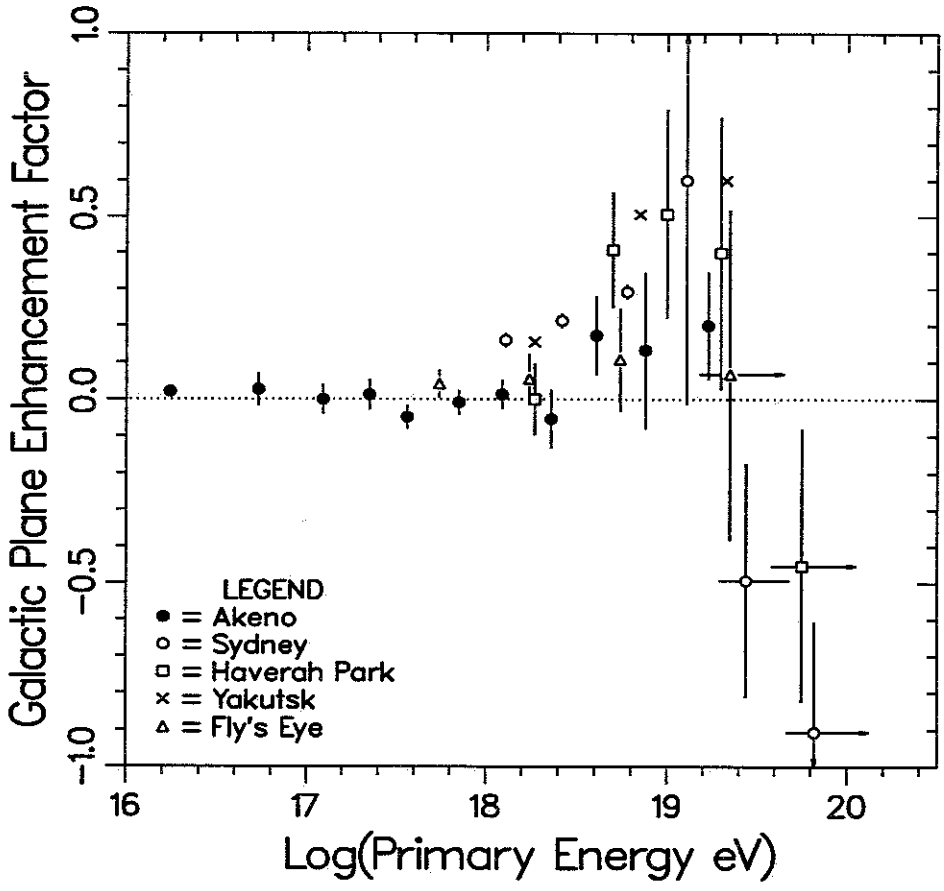

Figure 2.9. Wolfendale and Wdowczyk galactic disk enhancement factor.

predication ($f_E = 0$). There is no confirmation of galactic plane enhancement from the Fly's Eye analysis [5].

The other possible dependence is a galactic latitude gradient

$$I(b) = I_0(1 + s \times b)$$

where s is the gradient of latitude b [39, 40]. This formula searches for the extragalactic source on one side of the galactic disk. If the cosmic ray sources are in the northern galactic sky, such as the Virgo cluster, there should be more events from the northern sky and a positive s could be expected. But no results have confirmed this dependence.

Table 2.3 lists the results of the galactic plane enhancement factor and the galactic latitude gradient of the stereo Fly's Eye data in 1993 analysis [8].

Table 2.3. The results of galactic latitude dependent anisotropy, s is the galactic latitude gradient and f is the galactic plane enhancement factor. The sigma is the uncertainty from the least χ^2 fit.

Energy (EeV)	# of events	$s \pm \sigma_s$	σ	$f \pm \sigma_f$	σ
0.3 - 1.0	5971	-0.0316 ± 0.0207	-1.52σ	0.0420 ± 0.0376	1.12σ
1.0 - 3.0	1772	-0.0757 ± 0.0384	-1.97σ	0.0551 ± 0.0688	0.80σ
3.0 - 10.0	363	0.1422 ± 0.0829	1.72σ	$0.0863 \pm 0.1397^*$	0.62σ
≥ 10.0	63†	$0.1019 \pm 0.1824^*$	0.56σ	$0.0686 \pm 0.4510^*$	0.15σ

† : This bin has only 63 events, large fluctuation should be expected.

2.6.4 Point source search

Observation of some high energy gamma ray sources has been claimed. These gamma rays could come from interactions of charged cosmic rays with the surrounding gas of these sources; therefore, these gamma ray sources could also be charged cosmic ray sources. Two of these sources had also been reported as cosmic ray sources. Cygnus X-3 had been observed by the Fly's Eye group [41, 42] and the Akeno group [43]. However, there is no further indication that these sources are still producing excess flux [44]. Hercules X-1 had been identified as EHE gamma ray source by Fly's Eye group [45] and Dingus *et al.* [46], but again there is no further identification.

The small scale anisotropy search for excess flux from a certain area of sky uses techniques similar to those of large scale anisotropy but in a smaller cell. The excess of flux should be compared to a set of simulated data to determine whether it is statistical fluctuation. P. Sommers *et al.* find that no statistical significant point sources exist in Fly's Eye data [1]. Table2.4 list the result of small scale anisotropy of some candidates of point source.

2.7 Cosmic Magnetic Field

Most cosmic rays are charged particles; their trajectories are bent by the magnetic fields. It is essential to know the resolution of arrival direction under the influence of the magnetic field. This section discusses the measurement of magnetic fields in several regions of the universe and their influence on the propagation of cosmic rays.

Table 2.4. Result for candidate sources for energy $\geq 0.5EeV$

source	Expected density $(/deg^2)$	Percent excess	Chance probability	95% C.L. flux upper limit $(cm^{-2}sec^{-1})$
Cyg X-3	0.233	-7.73%	0.60	7.0×10^{-18}
Her X-1	0.188	-13.9%	0.69	6.2×10^{-18}
Crab	0.205	-4.92%	0.56	8.0×10^{-18}

2.7.1 Measurement of magnetic field

Several methods can be used for direct measurement of a magnetic field. The most exact way employs a satellite to measure the local field when the satellite flies through space. This method is valid only inside the solar system. Astronomers also measure the synchrotron radiation from gas clouds or H_{II} regions. They measure the polarization, Faraday effect, and Zeeman effect of star light to determine the magnetic field. Table 2.5 lists some magnetic fields found in the galaxy. [47]

2.7.2 Dynamics of charged particles in magnetic fields

Magnetic fields are the invisible veil of cosmic ray sources. Charged particles circle around the magnetic field lines and lose information about the direction of their source. A charged particle with charge ze, mass m and velocity $\vec{v}$ traveling through a magnetic fields $\vec{B}$ will be subject to a Lorentz force

$$\vec{F} = \frac{d}{dt}(\gamma m\vec{v}) = ze\vec{v} \times \vec{B}$$

$$\gamma m\frac{d\vec{v}}{dt} = ze\vec{v} \times \vec{B}$$

where γ is the Lorentz factor $\gamma = (1 - v^2/c^2)^{-1/2}$. If the pitch angle of the particle and the magnetic field is θ, and $v_{||}$ and $v_{\perp}$ are the projection of the particle velocity v parallel and perpendicular to the magnetic field, the centrifugal acceleration is

$$\frac{mv_{\perp}^2}{r} = \gamma m\frac{dv}{dt} = zev_{\perp}B = zevB\sin\theta$$

Table 2.5. Magnetic field in astrophysics†

Astrophysical object	Field *(Gauss)*	characteristic scale
Quarsers and radio galaxies	100	$\sim 1pc$
Intergalactic field	$< 10^{-9}$	
Galaxy - regular field (southern hemisphere)	2×10^{-6}	$\sim 4kpc$
Galaxy - regular field (northern hemisphere)	$(0.7 \pm 0.3) \times 10^{-6}$	
Galaxy - irregular field	2×10^{-6}	$\sim 100pc$
Interstellar clouds	10^{-5}	$10pc$
Dense cold clouds	$10^{-2} - 10^{-3}$	$10^{16}cm$
Sun - general poloidal field	1	0.1 - 1 $R_\odot$
Sun - sub-photospherical azimuthal field	$\geq 10^3$	
Sun - corona	10^{-5}	
Earth‡	1	$6.4 \times 10^8 cm$
Mars‡	6×10^{-4}	$3.4 \times 10^8 cm$
Interplanetary space	10^{-5}	
White dwarf	$10^6 - 10^8$	
X-ray binary near black hole	$\sim 10^9$	
Pulsars‡	10^{12}	$\sim 10^8 cm$
X-ray binary near neutron star	$\sim 10^{10} - 10^{13}$	

† Compiled from table 2.2 of *Ya.B. Zeldovich, A.A. Ruzmaikin, and D.D. Sokoloff* "Magnetic Fileds In Astrophysics", p34.
‡ The scale of magnetic field is approximated to be the size of the object.

where r is the gyroradius given by

$$r = \frac{\gamma m v \sin\theta}{zevB} = \left(\frac{pc}{ze}\right)\frac{\sin\theta}{Bc}$$

and p is the momentum of the particle. For relativistic particles, the total energy $E \simeq pc$. The variable pc/ze is called the rigidity. Particles with the same rigidity and pitch angle will have the same dynamical behavior in the same field. In most astrophysics work, the $\sin\theta$ term is ignored and gaussian units are used,(1 volt=1/300 statvolt). The gyroradius is then simplified as

$$r = \frac{E}{zecB} = \frac{E}{300zB}$$

This equation can be transformed to more convenient units

$$r = 3521\frac{E_{18}}{zB_\mu}\ (light\ year) = 1.1\frac{E_{18}}{zB_\mu}\ (kpc)$$

where E_{18} is Energy in EeV, 10^{18}eV, and B_μ in micro-gauss, 10^{-6}gauss.

The angular deflection is defined as the angular distance the particle travels,

$$\Delta\theta = \int \frac{v_\perp}{r} dt \simeq \frac{v_\perp D}{r v_\parallel}$$

where D is the distance the particle travels through. For simplicity, we assume $v_\perp \sim v_\parallel$; therefore

$$\Delta\theta \simeq D/r = (\frac{z}{E_{18}}) \frac{B_\mu D_{kpc}}{1.1}$$

The angular deflection depends on the magnitude and dimension of the magnetic field. Table 2.6 compares the strength and dimension in several regions of the universe. The angular deflections are $\Delta\theta = z\kappa/E_{18}$ where $\kappa = B_\mu D_{kpc}/1.1$ is an indicator of the strength of a specific field of B_μ and characteristic scale D_{kpc} to deflect a charged particle.

If the $\Delta\theta \geq 1$, the source direction information will be lost. But for protons, when energy $\geq$ 50EeV, the $\Delta\theta < 1$; therefore, it is possible to see clustering of cosmic rays around the source.

From the comparison in table 2.6, the local solar magnetic field has little impact on the high energy charged particles. The galactic disk and halo have the most important role regardless of whether the cosmic rays are galactic or come from extragalactic sources.

Table 2.6. Angular deflection from different regions of the galaxy

Source region	Magnetic field		Strength	$\Delta\theta$ (rad)*	
	$B(\mu G)$	Dimension	κ	$10^{15}eV$	$10^{18}eV$
Solar wind	10	$6 \times 10^9 Km$	2×10^{-6}	2×10^{-3}	2×10^{-6}
earth	10^6	$6.4 \times 10^3 Km$	2×10^{-4}	0.2	2×10^{-4}
galactic arm thickness	2	100 pc	0.2	200	0.2
galactic center to sun	2	10 kpc	20	2×10^4	20
galactic halo	0.2	50 kpc	10	10^4	10
intergalaxy space	$< 10^{-3}$	10 Mpc	10	$< 10^4$	< 10

* : The angular deflection is calculated for proton; multiply by 26 for iron.

CHAPTER 3

FLY'S EYE DETECTOR

In this chapter we discuss the Fly's Eye detector and the reconstruction of cosmic ray events. Section 3.1 discusses the physical components and operation of the detector. Section 3.2 and 3.3 describe the geometric and shower profile reconstruction. Section 3.4 discusses the virtual detectors, i.e., the Monte-Carlo that simulates the real detector. Section 3.5 discusses the basic data cuts. Section 3.6 checks the consistency between the detector and Monte-Carlo. The last section discusses the resolution of detector.

3.1 Fly's Eye Detector

The details of the Fly's Eye experiment have been presented in earlier papers [48, 49]. Some brief descriptions are given in this section. Information that has been updated or not mentioned before is also included in this section.

3.1.1 The physical components

The Fly's Eye detector, located at Dugway, Utah, is a unique cosmic ray detector which detects the fluorescent light generated by the secondary particles that cascade from the primary cosmic ray. There are two detectors, Fly's Eye 1, (FE1,) and Fly's Eye 2, (FE2,) located 3.4 km away from FE1. FE1 consists of 67 spherical mirrors; each mirror contains 12 to 14 photomultiplier tubes (PMT) 5.5 degrees in diameter. The mirrors and PMT's are arranged so that the whole night sky is imaged. FE2 consists of 36 spherical mirrors and covers half of the night sky in the direction of FE1. The physical parameters of both detectors are listed in Table 3.1.

Table 3.1. Fly's Eye 1 and 2 parameters

parameter	FE1	FE2
Longitude	112°50′9.25″	112°48′59.07″
Latitude	40°11′47.78″	40°13′18.00″
Height above sea level	1593 m	1459 m
Atmospheric depth	852 gm/cm^2	867 gm/cm^2
FE1 to FE2 vector	(1.668, 2.942, -0.134) (Km)	
Number of mirrors/PMTs	67 / 880	36 / 464
Number of mirrors	67	36
Number of PMTs	880	464
PMT type	EMI-9861B	EMI-9793B
PMT peak quantum eff.	0.17	0.26
Mirror diameter	1.575 m	
Focal length	1.520 m	
Mirror Obscuration	13%	
PMT-Winston Cone aperture	6.57×10^{-3} steradian	
Standard Winston Cone eff.	0.80	
UV filter type	Hoya U-360	
Peak filter transmission (350nm)	0.81	

3.1.2 Different stages of Fly's Eye operation

FE1 began full operation in November 1981, and FE2 in November 1986. Both detectors had many modifications, and the data are separated into several epochs. The details of these modifications are listed in Appendix B. Table 3.2 lists the date and major modifications of Fly's Eye operation.

Table 3.2. The six epochs of Fly's Eye operation.

Epoch	Start	End	Major Modification
1	11/81	05/85	FE1 start operation
2	11/85	06/87	UV filter installation; FE2 start operation
3	07/87	06/88	Mirror anodization
4	07/88	04/90	Remove channel 2 trigger
5	05/90	09/91	Hires 1 prototype start operation
6	10/91	07/92	Reinstall channel 2

3.1.3 Data acquisition and electronics

The data acquisition is illustrated in Figure 3.1. Fluorescent light travels through the atmosphere, is collected by mirrors, passes through an optical filter, and is collected by a Winston cone. The resultant light is transformed and amplified to electric pulse by the photomultiplier (PMT). The pulse is then integrated, amplified, and digitized by ommatidial boards (OMB). If the triggering conditions are satisfied, the digitized signals are stored on a computer disk. Three stages of trigger are required. The first stage is that the pulse height of the signal must be greater than a controllable threshold which keeps the signal rate constant. The second stage is a local coincidence which requires two or more tubes in a mirror triggered within the coincidence gate time, typically 8 to 50 μsec. The third stage is the master coincidence. It requires two or more mirrors triggered within a gate time. K. Green gives a detailed description of the electronics and triggering requirement in his dissertation [50].

3.1.4 System calibration

The calibration can be separated into several parts. The first part is the calibration of the geometry of the system (for example, mirror alignment). Green discusses the mirror alignment in detail in his dissertation. The second part is the calibration from fluorescent light production to signals detected by the PMTs. The fluorescent efficiency is compiled by Bunner from several articles in his dissertation [51]. There are two ways to calibrate mirror reflectivity. An optical flasher is located inside each mirror can. Flasher data are taken several times in the two week run period. Once every year, a standard tube and roving flasher are placed in each mirror to measure absolute reflectivity and the flasher intensity. Detailed descriptions of this calibration are covered in [50] and [52]. The transmission efficiency of the UV filter and reflection coefficient of the Winston cone is measured in the laboratory. The quantum efficiency of the PMT is also measured in the laboratory. The third part is the daily electronics calibration made by the operator before each night's run. Occasionally, laser shot calibrations are made. The procedure and physics are similar to the Lidar experiments which are used by atmospheric scientists.

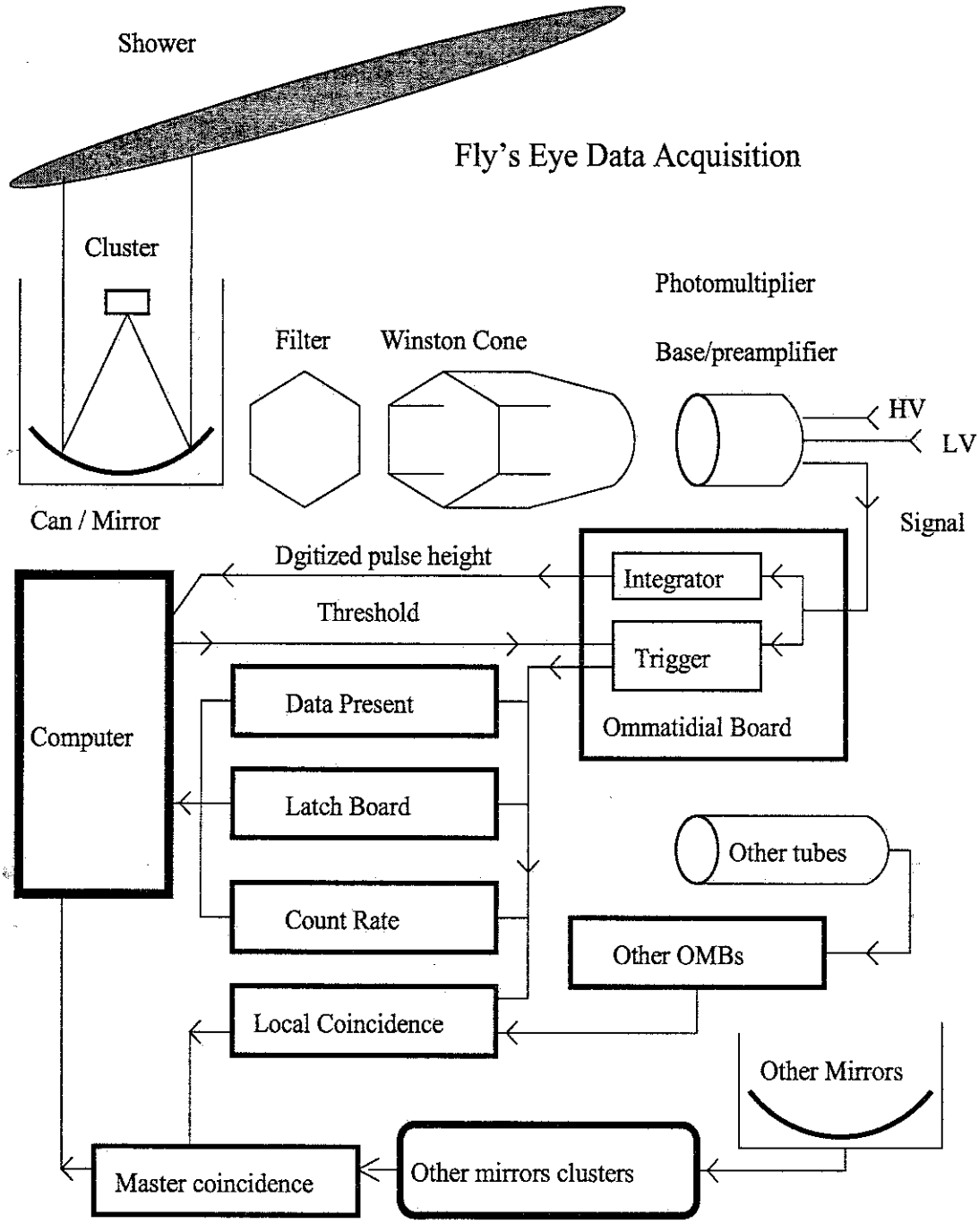

Figure 3.1. Schematic representation of Fly's Eye data acquisition system.

The known geometry and energy of the laser track provide a good check for the entire system.

3.1.5 Atmosphere and weather monitoring

The most unreliable part of the calibrations is the atmosphere. Fortunately, the Fly's Eye was sited in the United States western desert where the atmosphere is quite stable and the standard desert atmosphere model gives a reasonably good fit to the atmosphere.

To monitor the local weather, about 20 optical flashers are installed around the FE1 and flash every 30 minutes. These flashers provide a calibration of mirror reflectivity and are good tools to detect clouds and fog. The other way to monitor the sky is the weather code. The operator checks the night sky and reports a 4 digit weather code to the computer at the start of data collection and once every hour. Table 3.3 lists the definition of each digit in the code.

The weather code is somewhat subjective and is recorded only once an hour. In winter, FE2 could be buried in valley fog but FE1, which is on top of Five Mile Hills, could still have a clear night.

Table 3.3. Definition for weather code = FAOH. Horizon is defined as the part of sky with elevation angle less than 20 degrees. Above 20 degrees is overhead.

Digit	Type	Code	Definition
1 F	Frost	0	No frost on mirrors, tubes, or cones
		1	Frost on mirrors, tubes, or cones
2 A	Atmosphere Clarity	0	Negligible scattering
		1	Moderate scattering
		2	Heavy scattering (star below 30° probably affected)
		3	Totally socked in fog (should not run)
3 O	Overhead Cloud	0	No clouds visible
		1	$< 1/4$ sky cloudy
		2	$< 1/2$ sky cloudy
		3	$< 3/4$ sky cloudy
		4	$\geq 3/4$ sky cloudy
4 H	Horizon cloud	0	No cloud visible
		1	Cloud visible

3.2 Geometry Reconstruction - GEO

The raw data registered by the computer contain the trigger time, tube id, latch time, and pulse height of the triggered tubes. Operators scan the raw data to separate flashers and cosmic ray showers from noise. The resulting data are written to a file called $*.scn$. The $*$ is the month/day or month/year stamp. This information is used to reconstruct the cosmic ray event. There are three levels of software reconstruction, GEO, SIZE, and SHAPE. The data processing stream is

$$*.scn \rightarrow \boxed{\text{GEO}} \rightarrow *.geo \rightarrow \boxed{\text{SIZE}} \rightarrow *.siz \rightarrow \boxed{\text{SHAPE}} \rightarrow *.shp$$

for monocular data and

$$*.scn(FE1) \rightarrow \boxed{\text{GEO}} \rightarrow *.geo \qquad * .scn(FE2) \rightarrow \boxed{\text{GEO}} \rightarrow *.ge2$$

$$*.geo \ * .ge2 \rightarrow \boxed{\text{STEREO}} \rightarrow *.trk \rightarrow \boxed{\text{SIZE}} \rightarrow *.siz \rightarrow \boxed{\text{SHAPE}} \rightarrow *.shp$$

for stereo data.

This section concentrates on the geometry reconstruction GEO. Section 3.3 discusses the shower profile reconstruction SIZE and SHAPE. The GEO consists of these steps:

1. Use triggered tube direction to calculate the shower-detector plane.
2. Use stereo fitting or time fitting to find the shower track.
3. Calculate the azimuth angle ϕ and zenith angle θ.
4. Calculate celestial and galactic coordinates.

3.2.1 Shower-detector plane

3.2.1.1 Coordinates system. The Fly's Eye uses the east direction as the positive X axis, north as the positive Y axis, and upward as the positive Z axis. Some of the angles used in Fly's Eye data have different definitions than those normally used by astronomers. For instance, the zenith angle is used instead of the elevation angle. The azimuth angle

starts from the east and rotates counter-clockwise which is consistent with mathematics but not with astronomy.

3.2.1.2 Shower detector plane. The shower-detector plane, shown in Figure 3.2, is the plane which contains the shower track and the detector. This plane is specified by a plane normal vector $\vec{N}$ and can be found simply by the cross product of each tube direction vector. The exact algorithm used in GEO is a least χ^2 fit of the weighted sum of the dot product of the shower normal vector and tube center direction vector.

$$\text{minimize} \qquad \chi^2 = \sum_{i=1}^{N_{tubes}} \frac{\left(0 - \vec{X}_i \bullet \vec{N}\right)^2}{\sigma_i^2}$$

subject to the constraint :

$$\vec{N} \bullet \vec{N} = 1$$

Lagrange multipliers are used to solve these three linear equations. The eigenvector corresponding to the largest eigenvalue is the plane's normal vector. Detailed discussion can be found in Green's dissertation [50].

Those tubes away from the shower plane by more than 3° or nonconsecutive in time sequence are treated as noise tubes and deleted from all reconstruction. After noise tubes are removed, the same procedures are iterated again until all noise tubes are deleted.

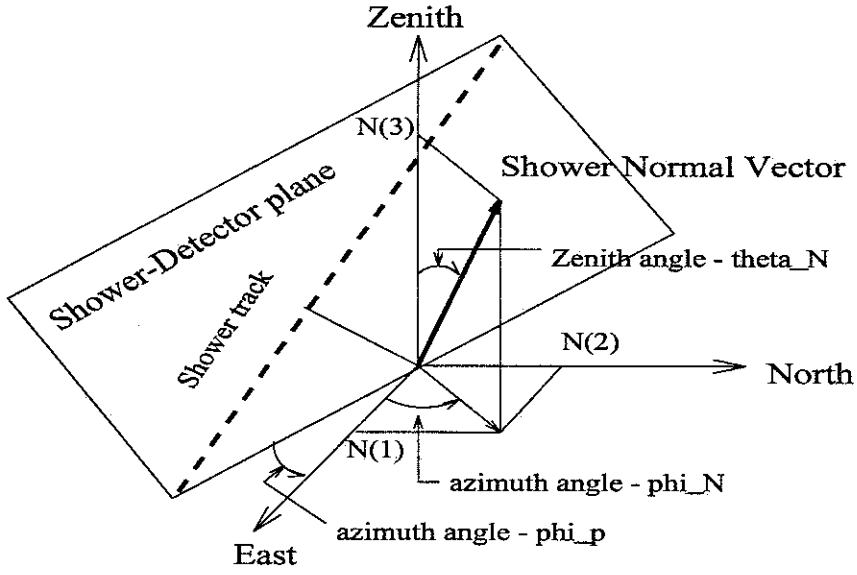

Figure 3.2. The shower-detector plane and shower normal vector.

The shower plane can be identified by two Eulerian angles, ϕ_p and θ_N. ϕ_p is the angle between the east and the intersection line of the shower plane and the horizon. The angle θ_N is the tilt angle between the zenith and the plane normal vector $\vec{N}$ or the angle between the shower plane and the horizon. These two angles can be derived from $\vec{N}$ by

$$\begin{aligned} \theta_N &= \mathrm{Cos}^{-1} N(3) \\ \phi_N &= \mathrm{Tan}^{-1}\left(\frac{N(2)}{N(1)}\right) \\ \phi_p &= \phi_N - \frac{\pi}{2} \end{aligned}$$

3.2.2 Shower track

3.2.2.1 Stereo fitting. The program STEREO reads $*.geo$ files from FE1 and FE2 and does the stereo fitting. First, STEREO decides if this is a stereo event by checking the triggering time. True coincidence events are within $1msec$ of each other. Then the shower track is found by the intersection of the shower-FE1 plane and the shower-FE2 plane. Then the STEREO program does all the same things as GEO to find all the geometrical variables. Timing information is used to determine the direction of shower, i.e., whether it is going up or down.

3.2.2.2 Time fitting. For monocular data, the latch times are used to find the track. The latch time is the relative time that a tube fires with respect to the first triggered tube. The geometry of shower track and latch time are shown in Figure 3.3. The latch time is counted by a 20MHz clock which is independent from the trigger time which comes from a WWVB clock. Let T_0 be the time when the shower front passes the closest approach point to the detector. If the impact parameter is R_p and the incident angle is ψ, the distance from shower core to the i'th tube is $r_i = R_p/\sin\theta_i$. Here θ_i is the opening angle between the track and the line of sight of the ith tube. So the propagation time is

$$t_i = \int_0^{r_i} \frac{dr}{C(h)}$$

where C(h) is the speed of light at altitude h. Although the speed of light is a function of atmospheric density, and therefore a function of altitude, this effect is negligibly small.

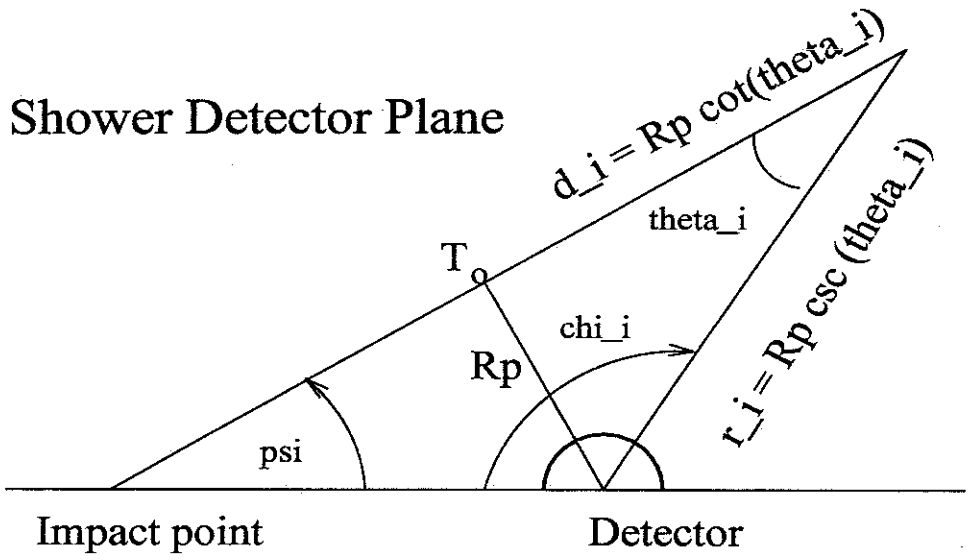

Figure 3.3. The shower track and latch time

Assume $C(h) = C$; then

$$t_i = \frac{R_p}{C \sin \theta_i} = \frac{R_p \csc \theta_i}{C}$$

The velocity of these secondary particles can be assumed as C due to their high energy. For a particle traveling from the intersection to the ith sighted point of the ith tube, the distance is $d_i = R_p \cot \theta_i$.

Thus the recorded time of the ith tube is

$$\begin{aligned} T_i &= T_0 - \tfrac{d_i}{C} + t_i \\ &= T_0 + \tfrac{R_p}{C}(-\cot\theta_i + \csc\theta_i) \\ &= T_0 + \tfrac{R_p}{C}(\tan\tfrac{\theta_i}{2}) \end{aligned}$$

The angle θ_i is related to ψ by $\theta_i = \pi - \psi - \chi_i$ where χ_i is the angle from the line of detector-impact point to the line of sight of the ith tube. The $\cos\chi_i$ is the inner product of the ith tube unit vector and $(\cos\phi_p, \sin\phi_p, 0)$. Replace the θ_i by $\pi - \psi - \chi_i$,

$$T_i = T_0 + \frac{R_p}{C} \cot \frac{\psi + \chi_i}{2}$$

Due to the width of the shower track, T_0 is not well defined. T_0 is left as a running variable. A recursive process is used to find the values of R_p and ψ that fit the latch time best.

3.2.3 Local coordinatees

To find the local coordinate zenith angle θ and azimuth angle ϕ, a unit vector along the track is used to transform back to local coordinates. Assume the original East-North-Zenith coordinates form a Cartesian x-y-z system. The first rotation is counterclockwise through an angle ϕ_p about the zenith. The second rotation is clockwise through an angle θ_N about X'. The third rotation is clockwise through an angle ψ about $\vec{N}$. The Euler angle is (ϕ_p, -θ_N, -ψ) and the transformation matrix is

$$\begin{pmatrix} \cos\psi\cos\phi_p + \cos\theta_N \sin\phi_p \sin\psi & \cos\psi\sin\phi_p - \cos\theta_N\cos\phi_p\sin\psi & \sin\theta_N\sin\psi \\ +\sin\psi\cos\phi_p - \cos\theta_N\sin\phi_p\cos\psi & \sin\psi\sin\phi_p + \cos\theta_N\cos\phi_p\cos\psi & \sin\theta_N\cos\psi \\ \sin\theta_N\sin\phi_p & \sin\theta_N\cos\phi_p & \cos\theta_N \end{pmatrix}$$

Replace ϕ_p by $\phi_N - \pi/2$. The unit shower vector is (1,0,0) in the new coordinates. So in the East-North-Zenith coordinates , the unit vector is (x, y, z)

$$(\cos\psi\sin\phi_N - \cos\theta_N\cos\phi_N\sin\psi, \quad -\cos\psi\cos\phi_N - \cos\theta_N\sin\phi_N\sin\psi, \quad \sin\psi\sin\theta_N)$$

The zenith angle θ and azimuth angle ϕ are derived from the unit vector (x, y, z) by

$$\begin{aligned} \theta = \quad & \mathrm{Cos}^{-1}z \quad && = \mathrm{Cos}^{-1}(\sin\psi\sin\theta_N) \\ \phi = \quad & \mathrm{Tan}^{-1}(y/x) && = \mathrm{Tan}^{-1}\left(\frac{\cos\psi\sin\phi_N - \cos\theta_N\cos\phi_N\sin\psi}{-\cos\psi\cos\phi_N - \cos\theta_N\sin\phi_N\sin\psi}\right) \end{aligned}$$

After θ and ϕ are found, the event trigger time is added to calculate the celestial and galactic coordinates.

3.2.4 Coordinate transformation

3.2.4.1 Celestial coordinates. To find the celestial and galactic coordinates, we first transform the event trigger time to Julian day, JD, and sidereal time, ST. These formulas all come from Jean Meeus *"Astronomical Formulas for Calculators"*. From this book, the declination δ, local hour angle H, and right ascension α are

$$\begin{aligned} \sin\delta &= \sin\phi\sin h - \cos\phi\cos h\cos A \\ \tan H &= \frac{\sin A}{\cos A\sin\phi + \tan h\cos\phi} \end{aligned}$$

$$H = \theta_{JM} - \alpha$$

where ϕ is the observer's latitude, which will be written as ξ to avoid confusion. θ_{JM}, the sidereal time, will be written as ST. A is the azimuth angle, measured from the south counting clockwise. Note that this definition is different from the Fly's Eye definition. They are, however, related by $A_{JM} = 270° - \phi_{FE}$. (The altitude angle h which is $90° - \theta$ in Fly's Eye definition.) Changing to Fly's Eye terminology,

$$\begin{aligned} \sin\delta &= \sin\xi\cos\theta + \cos\xi\sin\theta\sin\phi \\ \tan H &= \frac{-\cos\phi}{-\sin\phi\sin\xi + \cot\theta\cos\xi} \\ \alpha &= ST - H \end{aligned}$$

3.2.4.2 Precession correction. The coordinates just calculated refer to the equinox of the event date. Precession correction must be made to the equinox of 1950. According to the formula in Meeus' book, the corrections are

$$\begin{aligned} \alpha(1950) &= \alpha - T(M + N\sin\alpha\tan\delta) \\ \delta(1950) &= \delta - T(N\cos\alpha) \end{aligned}$$

where T is the difference of Julian day in units of years between event date and 1950. M, N are two constants defined by

$$\begin{aligned} M &= 3^s.07234 + 0^s.00186 * T_{century} && [seconds] \\ &= 2.2342686 * 10^{-4} + 1.3526301 * 10^{-7} * T_{year} && [radians] \\ N &= 20''.0468 - 0''.0085 * T_{century} && [seconds] \\ &= 9.7189629 * 10^{-5} + 4.1209162 * 10^{-8} * T_{year} && [radians] \end{aligned}$$

Both second terms of M and N contribute less than 1.5% of the first term and less than 0.02° even at year 2000. This error is far less than the system resolution; therefore, it is safe to ignore these terms and use only the first order of T.

3.2.4.3 Galactic coordinates. The galactic longitude l and galactic latitude b are

$$\begin{aligned} \tan x &= \frac{\sin(192°.25-\alpha)}{\cos(192°.25-\alpha)\sin 27°.4 - \tan\delta\cos 27°.4} \\ l &= 303° - x \\ \sin b &= \sin\delta\sin 27°.4 + \cos\delta\cos 27°.4\cos(192°.25-\alpha) \end{aligned}$$

3.2.5 Time-slewing effect

A tube triggers when the pulse height is greater than the threshold. Therefore, the trigger time is not the time that the track passes through the center of the tube. This time difference is called the slewing time. Green did an extensive study of the time-slewing effect; the result is shown in Appendix A of his dissertation [50]. The slewing time depends on the pulse shape, tube threshold, and Winston cone response. The tube-Winston cone response is measured in the laboratory. The absolute thresholds are recorded every 10 minutes; the relative threshold changes are recorded with each event. The pulse shape depends on the shower track geometry. A closer track will have a shorter pulse width. For the same distance track, a higher energy track will produce a larger integral. The pulse shapes are modeled as a trapezoid. The slewing time is introduced in the timing fit to produce a better geometry and is reiterated until the slewing time and geometry converge.

3.3 Shower Longitudinal Profile Reconstruction

3.3.1 SIZE - Shower size reconstruction

The detected photoelectron signals comes from four parts: Scintillation photons, direct Čerenkov photons, Rayleigh scattered Čerenkov photons, and Atmosphere (Mie) scattered Čerenkov photons.

$$P = S + C + R + A$$

The number of Cherenkov photons C is the integral of all the past history of a shower. To subtract these photons and convert to the number of electrons in the section viewed by the PMT, an iterative process must be used. The details of these calculations can be found in Green's dissertation [50]. Here I give a short summary of how the SIZE program works.

1. We combine PMT data into 6° bins. The mirror spot size, tube overlap region, and shower lateral distribution must be taken into consideration. For stereo data, the FE1 data are separated into 6° bins, and FE2 data are split into variable angular bins fixed to correspond to FE1 bins.

2. First bin : Assuming NO scattered Čerenkov contamination in the early part of the shower:

$$\begin{aligned} P_1 &= S_1 + C_1 \\ S_1 &= \alpha N e_1 \qquad (\alpha : \text{ scintillation efficiency}) \\ C_1 &= \beta N e_1 \qquad (\beta : \text{ direct Čerenkov production efficiency}) \end{aligned}$$

Thus the number of electrons is

$$Ne_1 = P_1/(\alpha + \beta)$$

and the number of Čerenkov photons is

$$B_1 = \epsilon * Ne_1 \qquad (\epsilon : \text{ Čerenkov detection efficiency})$$

3. For the ith bins ($i \geq 2$) :

$$B_i = fC_{i-1} * B_{i-1} + \epsilon(Ne_i + Ne_{i+1})/2$$

where fC_{i-1} is the ratio of Cherenkov light from $i-1$ bin to i bin,

$$P_i = (\alpha + \beta)Ne_i + (\gamma + \eta)B_i$$

where γ is the Rayleigh scattering efficiency and η is Mie scattering efficiency.

All efficiencies are functions of wavelength and elevation; sums over all wavelengths are needed and are implicit in these formulas. For data with optical filter over the tubes, 16 intervals of wavelength are necessary. It takes 40 intervals for data without filters.

3.3.2 SHAPE - Shower longitudinal profile reconstruction

After the number of electrons Ne_i is found, the shower longitudinal profile can be expressed as $Ne(X_i)$, where X_i is the atmospheric depth of the i-th bin. The total electron number and depth at shower maximum can be found by fitting the shower profile to a Gaisser–Hillas formula

$$N(X) = N_{max}\left(\frac{X - X_0}{X_{max} - X_0}\right)^{(X_{max}-X_0)/\lambda} e^{(X_{max}-X)/\lambda} \tag{3.1}$$

where X_0 is the depth of first interaction, $\lambda = 70 g/cm^2$. A simplified Gaussian form is

also used

$$N(X) = N_{max} e^{-\frac{(X_{max}-X)^2}{2X^2_{width}}} . \quad (3.2)$$

where the X_{width} is the width of Gaussian distribution. Figure 3.4 shows the longitudinal profile of the $320 EeV$ event.

3.3.3 Energy reconstruction

3.3.3.1 Electromagnetic energy. The energy of the primary cosmic rays can be found from the integral of either the Gaisser and Hillas or Gaussian formula:

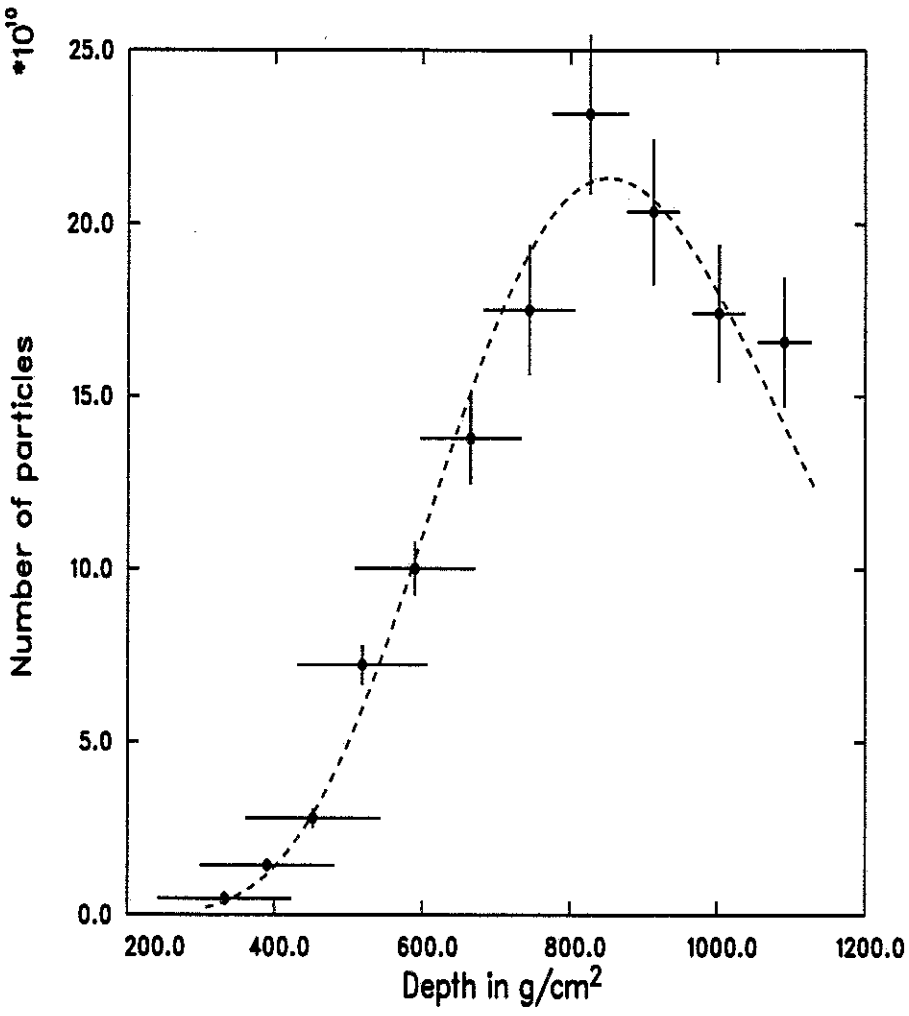

Figure 3.4. The shower profile of 320 EeV events. The crosses are the measured points.

$$E = \frac{\epsilon_0}{\chi_0} \int N(x) dx$$

where ϵ_0/χ_0 is the ratio of the critical energy of an electron to the radiation length in air and is taken as 2.18 $MeV\ g^{-1}\ cm^2$. The result of integration is

$$E_{GS} = \frac{\epsilon_0}{\chi_0}(2\pi)^{1/2} N_{max} X_{width}$$
$$E_{GH} = \frac{\epsilon_0}{\chi_0} \lambda N_{max} \alpha^{-\alpha} e^{\alpha} \Gamma(\alpha + 1)$$

and $\alpha = 0.51 \ln(E/\epsilon) - 1$.

3.3.3.2 Total energy. Some of the energy is not in the electromagnetic component. Energy in the form of muons E_μ, neutrinos E_ν, undetected hadrons and nuclear excitation E_h must be corrected for [53]. Linsley traced back the muon spectrum $N_\mu(E)$ to find the neutrino spectrum. He found $E_\nu \simeq 0.4 E_{\mu,observed}$ and $E_h \simeq 0.3 \sim 0.8 E_{\mu,observed}$. By forcing the muon spectra and electromagnetic spectra to be consistent, the missing energy can be found and corrected for [54]. The best fit parameter for Fly's Eye data is

$$E_{em} = E_{tot}(0.98995 - 0.078176 * E_{tot}^{-0.17519})$$

An iterative process is used to find the total energy. First assume the $E_{tot} = E_{em}$; then find the predicted $E_{tot(1)}$ by

$$E_{tot(1)} = \frac{E_{em}}{0.98995 - 0.078176 * E_{em}^{-0.17519}}$$

then use the new $E_{tot(1)}$ as E_{tot} to find new $E_{tot(2)}$.

$$E_{tot(2)} = \frac{E_{em}}{0.98995 - 0.078176 * E_{tot(1)}^{-0.17519}}$$

This process is iterated until E_{tot} converge.

3.3.3.3 Normalization constant. Due to an underestimate in the PMT calibration, a multiplicative fudge factor of 1.1 must be used for all the data.

Due to changes in different epochs of the Fly's Eye, the mirror reflectivity and calibration scale are different for each epoch. The timing fit and stereo fit have a systematic difference in R_p which causes a difference in energy. This systematic error can be studied

from the difference of stereo energy and monocular energy for FE1 and FE2 coincident events ([50] p149, fig. 5.15). A normalization constant is used to normalize the energy scale over all epochs. Table 3.4 lists the normalization constant (including the fudge factor 1.1) for each epoch.

3.4 Monte-Carlo Simulation

The detector performance was carefully modeled through Monte-Carlo simulation. The Monte-Carlo has two levels. The first is a shower Monte-Carlo which uses high energy interaction models to generate shower profiles. The second is the detector Monte-Carlo which simulates the detector triggering condition and response. The Monte-Carlo program writes out simulated data files. These files are processed through the same software reconstruction stream as the real data.

3.4.1 Shower Monte-Carlo simulation

There are several versions of the shower Monte-Carlo. The most recent version, which is used in this analysis, uses high energy interaction models to simulate the shower cascade.

Since there is no accelerator data in the Fly's Eye energy range, we used three models to extrapolate the accelerator data. These models are characterized by different predictions of the energy dependence of *inelasticity*, the fraction in energy that is not carried out by fragments of the primary particle. These three models are the low inelasticity statistical

Table 3.4. The normalization factor for Fly's Eye data

Data	Epoch	Date	normalization factor
stereo	2-6	11/86 - 07/92	1.1
monocular	1	11/81 - 05/85	1.320
	2	11/85 - 07/87	1.595
	3	08/87 - 06/88	1.331
	4	07/88 - 04/90	1.573
	5	05/90 - 09/91	1.826
	6	10/91 - 07/92	1.397

model, the large and increasing high inelasticity QCD Pomeron model, and the slowly increasing high inelasticity QCD minijet model [6].

The predicted mean X_{max} for these three models are listed in Table 3.5. Although different absolute values of X_{max} are predicted, the difference between proton and iron is always approximately $100 g/cm^2$. The statistical model predicts an X_{max} too deep to fit the Fly's Eye data for any composition. The QCD-pomeron and QCD-minijet models are both adequate fits and differ little from each other in prediction. The QCD-Pomeron model results in a somewhat better fit and is therefore used in this analysis.

3.4.2 Detector Monte-Carlo

The detector is simulated by using the real data and threshold, OMB amplification, mirror reflectivity, ...etc. The simulation use random numbers to generate input values of variables such as R_p, θ, ϕ ...etc. A simulated shower profile from the real data base or simulated data base is then read in. The scintillation photons, Čerenkov photons, Rayleigh scattered Čerenkov photons, and Mie scattered Čerenkov photons are calculated for each bin; then the night sky noise is added. These signals are detected by simulated PMTs, then amplified by OMBs, and must pass all the trigger requirements. Finally, a simulated data file is written in the same format as that for the real data. All the simulated data are processed in the same way as the real data.

The detector Monte-Carlo does not model the short term variation in electronics, mirror reflections, and weather. Typical values of electronic gain and mirror reflectivity are used. Thus fluctuations in real data are expected to be larger than these in Monte-Carlo data.

Table 3.5. Mean X_{max} for three models and primary nuclei at 1 EeV.

Model	H	CNO	Fe
QCD-Pomeron	750±1.9	711±0.9	653±0.8
QCD-Minijet	761±1.9	719±1.0	663±0.8
Statistical	789±2.4	744±1.1	681±0.8

3.4.3 Two component Monte-Carlo

In this dissertation, we use two component models to perform the Monte-Carlo simulation. First we separate energy into five intervals, $0.2-0.4EeV$, $0.4-1.0EeV$, $1.0-3.2EeV$, $3.2-10.0EeV$, and $\geq 10.0EeV$. The heavy component uses iron nuclei as the primary cosmic ray to generate the air showers. The light component uses protons as primary cosmic rays to generate air showers. There are 5000 simulated events in each energy interval. From the two component fit, the heavy component dominates at $E \leq 0.4EeV$; therefore, we have only iron Monte-Carlo events at the first energy interval, $0.2-0.4EeV$.

3.5 Basic Data Cuts

All the Fly's Eye data are subject to a data quality cut, listed in Table 3.6. These cuts make sure the reconstructed data are reasonable. Typical cuts for geometric variables are their range; the maximum error for these variables is half of the range. Because the detector is spread out in an ellipse with a long axis of about 100 meters, the effect of parallax and Čerenkov contamination is reduced by having a minimum impact parameter cut at one kilometer. The minimum track length is 30°; that would require at least five tubes triggered.

The lowest energy threshold of the detector is about $0.1EeV$; the energy cut is from 0.01 to 10^4EeV. The shower size cuts, $10^7 - 10^{13}$, correspond to energy cuts. The maximum X_{max} cut is $10^5 gm/cm^2$ which corresponds to a slant depth of zenith angle 89.5°, well below the typical zenith angle cutoff of 80° in the data. The relative error dRp/Rp, dX_{max}/X_{max}, and dE/E has a cut of 10 or 1000%. The first interaction depth cut is $-1000gm/cm^2$. Although it may sound unphysical to have a negative depth, it just shows that the X_0 is dominated by large statistical fluctuation. Due to the few particles in the early stage of the shower, it is very difficult to extrapolate data to the first interaction.

Although these basic cuts are very loose, only about 20% to 25% of monocular data and 45% to 50% of stereo data pass these cuts. Most cut-out events fail to pass the shower profile cuts. These numbers also show that the monocular timing fit has larger errors than the stereo fit.

Table 3.6. Basic data quality cuts for Fly's Eye data. † : Relative error is used for these variables.

Variable		Min	Max	Uncertainity	Max
Impact distance	Rp	1.00	50.0	dRp †	10.0
Zenith angle of shower	θ	0.0	90.0	$d\theta$	45.0
Azimuth angle of shower	ϕ	-180.	360.0	$d\phi$	180.0
Plane angle	γ	-180.	360.0	$d\gamma$	180.0
Incline angle	ψ	0.0	180.0	$d\psi$	45.0
Track length	$trln$	30.0	180.0		
Zenith angle of shower normal	θ_n	0.0	180.0	$d\theta_n$	45.0
Azimuth angle of shower normal	ϕ_n	0.0	360.0	$d\phi_n$	180.0
Minimum viewing angle	θ_1	0.0	180.0		
Right Ascension	α	0.0	360.0		
Declination	δ	-90.0	90.0		
Galactic longitude	l	0.0	360.0		
Galactic latitude	b	-90.0	90.0		
Julian time		0.0	10^5		
Weather code		-10.0	10^5		
Shower size	S	10^7	10^{13}	dS †	10.0
Shower depth at maximum	X_{max}	0.0	10^5	dX_{max} †	10.0
Shower width	W	10.0	10^4	dW †	10.0
Depth of first interaction	X_0	-1000.0	5×10^3	dX_0	10^4
Energy	E	0.01	10^4	dE †	10.0
Photo electron yield		0.0	10^{20}		

Will such loose cuts deteriorate our data quality? Since the Rp, X_{max}, and energy variables play a minor role in anisotropy analysis, the most important effect is angular resolution. From study of the Monte-Carlo data, a minimum track length cut at 40° cuts out about 12% of data and improves the mean theta error by 0.3°. Besides, the large error will spread the event probability density into a larger area. It is not necessary to cut out events with large geometric error. To increase statistics, I use the basic cuts only.

3.6 Resolution

The resolution can be defined in several different ways. The easiest way is to define it as the uncertainty of each variable. Another way to define it is the reconstruction error. In this section, we looks at the two definitions then examine these resolutions in detail.

3.6.1 Definition of resolution

3.6.1.1 Uncertainty. The uncertainty of a variable first comes from the fitting of a shower track. The uncertainties in Rp and ψ are defined as the difference of Rp (ψ) between the fit at χ^2_{min} and $\chi^2_{min} + 1$. The uncertainty of θ and ϕ is just the error propagated from δRp and $\delta\psi$. Normally $\delta\theta$ and $\delta\phi$ have an asymmetric distribution. The uncertainties of celestial and galactic coordinates are not calculated in program GEO.

The uncertainties of size and energy come from two sources: uncertainty propagated from geometric reconstruction and uncertainty in calculating the longitudinal profile reconstruction in the program SIZE and SHAPE. The uncertainty in SIZE and SHAPE is defined in a way similar to the geometric uncertainty, i.e. the difference of the best fit value at χ^2_{min} and the value at $\chi^2_{min} + 1$. Table 3.7 shows the mean value of uncertainty of real data and Monte-Carlo.

3.6.1.2 Reconstruction error. Before jumping into any serious analysis, we need to know how well our software reconstructs events. Since we do not know the actual information about a real cosmic ray event, we must work with Monte Carlo data. The reconstruction error is defined as the difference between the reconstructed data, which is saved in the shape file $*.shp$, and the input data, which is saved in the file $*.ful$. Due to added noise, the reconstructed data will not be identical to the input value. The reconstruction errors show the systematic error of the reconstruction programs. The standard deviation of the resolution error therefore reflects the statistical error and the system resolution.

The data chosen for this analysis are the Monte-Carlo of epoch 2, 3 and 4. To look for dependence on primary composition, two types of composition, pure proton and pure iron, are assumed. The errors of geometric variables do not depend on epoch or composition. Epochs 2 and 4 have results very similar to those of epoch 3. The mean and standard deviation of geometric variables of epoch 3 are listed in Table 3.7. The errors of X_{max} depend on composition, probably because of the difference in shower profile and X_{max} distribution. The energy error depends on shower profile fitting and therefore, depends on

Table 3.7. Resolution of some important parameters od epoch 3 real data and Monte-Carlo. The stereo data and Monte-Carlo have a zenith angle cut at 70°.

Parameter	Energy (EeV)	Monocular data			Stereo data		
		Data	Monte-Carlo		Data	Monte-Carlo	
		unce.	unce.	error	unce.	unce.	error
δRp (%)	0.2 - 0.4	8.5	7.8	-1.0± 7.9	5.9	4.9	-0.2± 6.2
	0.4 - 1.0	8.9	8.2	3.1± 9.5	10.2	7.6	0.0± 9.2
	1.0 - 3.2	10.0	8.3	4.4± 11.4	17.1	13.6	-0.7±14.7
	3.2 - 10.0	9.8	9.3	7.4± 13.5	23.6	21.5	-2.5±25.9
	≥10.0	11.0	8.6	6.6± 12.7	16.2	21.8	-3.6±30.7
$\delta\psi$ (deg)	0.2 - 0.4	10.7	12.4	-1.2± 10.0	1.9	1.7	0.04±1.70
	0.4 - 1.0	10.2	11.9	2.0± 10.8	2.8	1.9	-0.03±2.36
	1.0 - 3.2	10.8	9.6	2.2± 11.0	4.4	2.3	-0.07±2.60
	3.2 - 10.0	10.9	9.9	4.2± 11.3	7.4	3.2	0.24±3.81
	≥10.0	11.0	8.3	2.8± 10.2	9.4	4.1	0.23±4.62
$\delta\theta$ (deg)	0.2 - 0.4	7.1	8.0	1.1± 6.3	1.3	1.1	0.08±1.17
	0.4 - 1.0	6.8	7.5	-0.4± 7.0	2.1	1.3	0.12±1.45
	1.0 - 3.2	7.0	6.0	-1.1± 6.7	3.0	1.7	0.12±2.04
	3.2 - 10.0	6.8	5.9	-1.5± 6.6	4.4	4.5	-0.15±2.75
	≥10.0	6.7	4.8	-0.1± 5.2	3.4	3.4	-0.14±3.26
$\delta\phi$ (deg)	0.2 - 0.4	7.3	8.3	-0.8± 5.9	1.5	1.3	0.6±14.4
	0.4 - 1.0	7.0	8.2	1.0± 6.2	2.0	1.3	-0.1±14.1
	1.0 - 3.2	7.6	6.7	1.2± 7.0	3.3	1.5	0.4±16.7
	3.2 - 10.0	8.1	7.3	2.9± 8.0	5.8	2.3	-0.3±22.4
	≥10.0	8.5	6.4	2.0± 7.5	9.5	3.3	-0.3±24.1
GS X_{max} (%)	0.2 - 0.4	42.7	47.3	15.4± 40.5	16.4	9.4	10.1±16.6
	0.4 - 1.0	57.5	49.4	5.2± 41.3	17.9	11.4	8.5±18.0
	1.0 - 3.2	69.5	40.8	2.3± 42.7	24.6	12.3	6.7±18.2
	3.2 - 10.0	75.2	50.9	-3.9± 44.0	34.9	13.7	4.4±19.1
	≥10.0	111.3	40.5	0.4± 43.1	12.2	13.2	3.3±21.1
GH X_{max} (%)	0.2 - 0.4	30.2	40.3	11.9± 32.5	13.7	10.7	5.9±15.8
	0.4 - 1.0	30.3	43.2	2.8± 35.1	14.4	10.3	5.3±18.0
	1.0 - 3.2	33.2	37.5	-0.3± 37.8	18.1	10.8	4.1±17.5
	3.2 - 10.0	29.1	48.5	-6.2± 38.6	29.1	13.7	2.8±19.4
	≥10.0	36.5	39.4	-2.5± 36.6	14.1	13.8	2.8±21.1
GS $Energy$ (%)	0.2 - 0.4	63.5	51.9	-13.7± 75.2	24.4	15.6	-15.8±20.5
	0.4-1.0	69.7	40.4	-2.5±102.9	22.7	16.1	-15.8±23.8
	1.0 - 3.2	79.8	32.6	-2.7±120.7	26.2	14.8	-17.0±18.2
	3.2 - 10.0	88.9	39.6	-1.8±253.8	33.4	16.8	-21.7±18.9
	≥10.0	110.4	39.2	1.4±578.0	19.6	18.8	-27.3±17.8
GH $Energy$ (%)	0.2 - 0.4	68.3	71.6	-21.7± 34.5	51.3	39.4	-13.4±19.7
	0.4 - 1.0	59.0	57.5	-12.0± 40.5	48.8	35.4	-13.8±22.1
	1.0 - 3.2	53.8	40.9	-8.8± 38.1	46.1	25.1	-14.2±18.8
	3.2 - 10.0	35.7	34.1	-7.9± 43.7	55.5	20.1	-16.2±15.9
	≥10.0	40.7	27.5	-11.3± 51.4	24.6	17.5	-18.0±27.0

composition too. The energy error also depends on epoch because of different reflectivities and efficiencies. The errors of X_{max} and energy are shown in Tables 3.8 and 3.9.

3.6.2 Systematic error in stereo fitting

Although stereo fitting is generally more precise than time fitting. The stereo fitting has large error at some position. If a shower coming at an azimuth angle near 60° and 240°, the direction of FE1 to FE2 vector, the stereo angle will be very small. The smaller the stereo angle, the worse the stereo fitting. This azimuth dependence affects both data and Monte-Carlo.

The other case, if the shower is near horizon, zenith angle $\theta \geq 70°$, two shower-detector planes will almost coincide with each other. In this case, the stereo fitting has difficulty determining the shower track and has large error in Rp and ψ. Few real events have zenith angle $\theta \geq 70°$, but some Monte-Carlo events do. To compare data in a realistic

Table 3.8. The reconstruction error in X_{max} and energy of the stereo Monte-Carlo. All numbers are in percentage %. In the second column, P means proton shower, Fe means iron shower.

parameter		epoch	0.2 - 0.4	0.4 - 1.0	1.0 - 3.2	3.2 -10.0	≥10.0
X_{max}	P			6.3	5.4	4.2	3.2
GS fit	Fe		10.2	8.7	6.7	4.9	3.3
X_{max}	P			3.6	3.5	2.9	2.9
GH fit	Fe		6.0	5.2	4.0	2.9	2.4
	P	2		-12.9	-11.3	-18.0	-24.0
	P	3		-14.0	-15.7	-20.7	-27.3
Energy	P	4		-13.3	-14.4	-20.4	-26.4
GS fit	Fe	2	-14.4	-16.2	-15.3	-19.8	-24.2
	Fe	3	-15.8	-16.1	-17.4	-22.5	-27.4
	Fe	4	-15.9	-15.2	-15.4	-22.1	-26.6
	P	2		-8.3	-9.6	-13.2	-16.2
	P	3		-10.6	-11.4	-14.5	-18.1
Energy	P	4		-9.9	-10.5	-13.9	-17.2
GH fit	Fe	2	-9.8	-13.8	-13.7	-15.9	-17.7
	Fe	3	-13.4	-14.2	-15.1	-17.7	-17.7
	Fe	4	-12.5	-13.2	-13.1	-17.3	-19.5

Table 3.9. The reconstruction error in X_{max} and energy of the monocular Monte-Carlo files. All numbers are in percentage %. In the second column, P means proton shower, Fe means iron shower.

parameter		epoch	0.2 - 0.4	0.4 - 1.0	1.0 - 3.2	3.2 -10.0	≥10.0
X_{max}	P			3.9	3.4	-1.6	2.1
GS fit	Fe		14.1	7.6	3.8	1.3	1.2
X_{max}	P			0.6	0.1	-2.8	-0.7
GH fit	Fe		12.6	4.8	0.6	-2.4	-2.3
	P	2		5.6	12.6	17.5	3.8
	P	3		6.8	4.9	-0.4	-1.6
Energy	P	4		40.7	12.2	1.4	0.3
GS fit	Fe	2	-8.4	0.5	9.8	5.1	25.8
	Fe	3	-7.7	6.3	4.0	3.6	15.1
	Fe	4	10.9	29.2	18.5	-2.6	-10.3
	P	2		-2.8	3.5	9.0	1.6
	P	3		-1.1	-1.5	-2.7	-10.7
Energy	P	4		11.1	2.1	-2.1	-13.1
GH fit	Fe	2	-14.4	-12.2	-0.3	1.6	-1.6
	Fe	3	-17.6	-6.9	-6.3	-7.9	-11.8
	Fe	4	-1.3	7.0	8.7	-5.5	-11.9

situation, we apply a zenith angle cut at $\theta = 70°$ for stereo data. No zenith angle cut is used in mono data.

3.6.3 Geometric variables

3.6.3.1 Track length. The reconstruction error of the track length is not listed in Table 3.7. It is less than 0.1° for stereo data and less than 0.5° for mono data.

3.6.3.2 Impact parameter *Rp*. There is a systematic error in the impact parameter *Rp*. As the energy increases, the error ΔRp increases in the mono data. The time-fitting tends to push events farther away from their real position. The stereo fitting has a negligible dependence on energy. This systematic shift also affects the error of angle ψ, but the tendency is less significant than for ΔRp. Figure 3.5 shows the relative error of Rp as a function of energy. The effect of increasing *Rp* is to overestimate the energy.

The other effect is that the uncertainty δRp and standard deviation of error, ΔRp_{RMS}, of stereo data are greater than those of mono data at energies above $1EeV$. This effect reflects the decreasing stereo angle with increasing *Rp*.

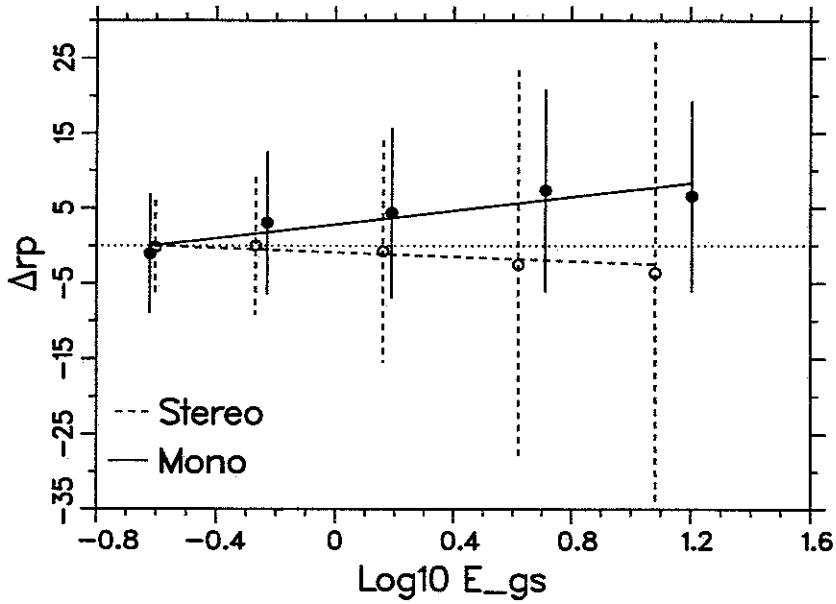

Figure 3.5. The relative error of Rp as function of energy. The error bar is the RMS width of distribution.

3.6.3.3 Angular variables. For stereo data, the reconstruction errors of angular variables have no significant correlation with any other variable or variables. The mean error of all angular parameters is less than 0.6°, far less than the PMT size of 5.5°. Therefore it is reasonable to say that the stereo reconstruction is statistically faithful to the real value. For mono data, the mean error $\Delta\theta$ is still less than 2° and the mean error $\sin\theta\Delta\phi$ is less than 3°. We may still consider time-fitting a reasonable fit.

The standard deviation of the error is approximately equal to the uncertainty for both stereo and mono data. This equivalence confirms that the error comes from random fluctuation of the signal.

3.6.4 Angular resolution

Angular resolution is defined as the mean angular separation between the reconstructed arrival direction $\vec{V}_{shp}$ and the input arrival direction $\vec{V}_{mc}$ of Monte-Carlo data:

$$\Delta\Re = \mathrm{Cos}^{-1}\left[\vec{V}_{shp} \bullet \vec{V}_{mc}\right]$$

$$\Delta\Re = \mathrm{Cos}^{-1}[\cos(\phi_{shp} - \phi_{mc}) * \sin\theta_{shp} * \sin\theta_{mc} + \cos\theta_{shp} * \cos\theta_{mc}]$$

We may substitute reconstruction error by angular uncertainty:

$$d\Re = \sqrt{d\theta^2 + \sin^2\theta d\phi^2}$$

For the real data, $d\Re$ is the only available information to estimate the error of arrival direction.

Table 3.10 lists the angular resolution as function of energy and track length of monocular Monte-Carlo data. Figure 3.6 shows the resolution $\Delta\Re$ and $\delta\Re$ in five energy bins.

From Table 3.10, it seems that the angular resolution $\Delta\Re$ and $\delta\Re$ is sensitive to track length and energy. An event with longer track length has more degrees of freedom to

Table 3.10. The angular resolution for Monte-Carlo epoch 3 files.

Composition	Energy	Track Length (deg)		$\delta\Re$ (deg)		$\Delta\Re$ (deg)	
	(EeV)	mean	RMS	mean	RMS	mean	RMS
mono Iron	0.28	61.3	19.7	12.51	10.22	7.61	7.13
	0.59	62.2	21.5	12.08	10.24	8.06	8.10
	1.53	63.9	22.2	9.92	8.08	8.10	8.27
	4.94	62.7	21.6	10.50	8.34	8.54	8.92
	14.89	66.9	23.3	8.94	8.40	7.35	8.26
mono Proton	0.63	62.7	22.2	11.54	9.66	8.23	8.37
	1.71	63.8	22.6	9.76	8.12	8.12	8.08
	5.26	64.4	22.3	9.92	8.22	8.36	8.82
	15.85	67.9	23.4	8.38	7.83	7.05	7.94
stereo Iron	0.30	63.6	20.4	1.83	1.48	1.27	1.25
	0.62	69.1	22.9	2.00	1.75	1.37	1.45
	1.57	77.0	22.3	2.46	2.15	1.76	1.86
	4.94	80.0	21.0	3.44	2.57	2.52	2.89
	14.52	83.7	22.0	4.29	3.22	2.99	3.55
stereo Proton	0.64	70.1	23.8	2.05	2.10	1.39	1.38
	1.73	77.5	22.3	2.48	2.15	1.77	2.23
	5.20	81.2	21.1	3.43	2.64	2.43	2.93
	15.95	85.1	21.7	4.28	3.26	3.11	2.54

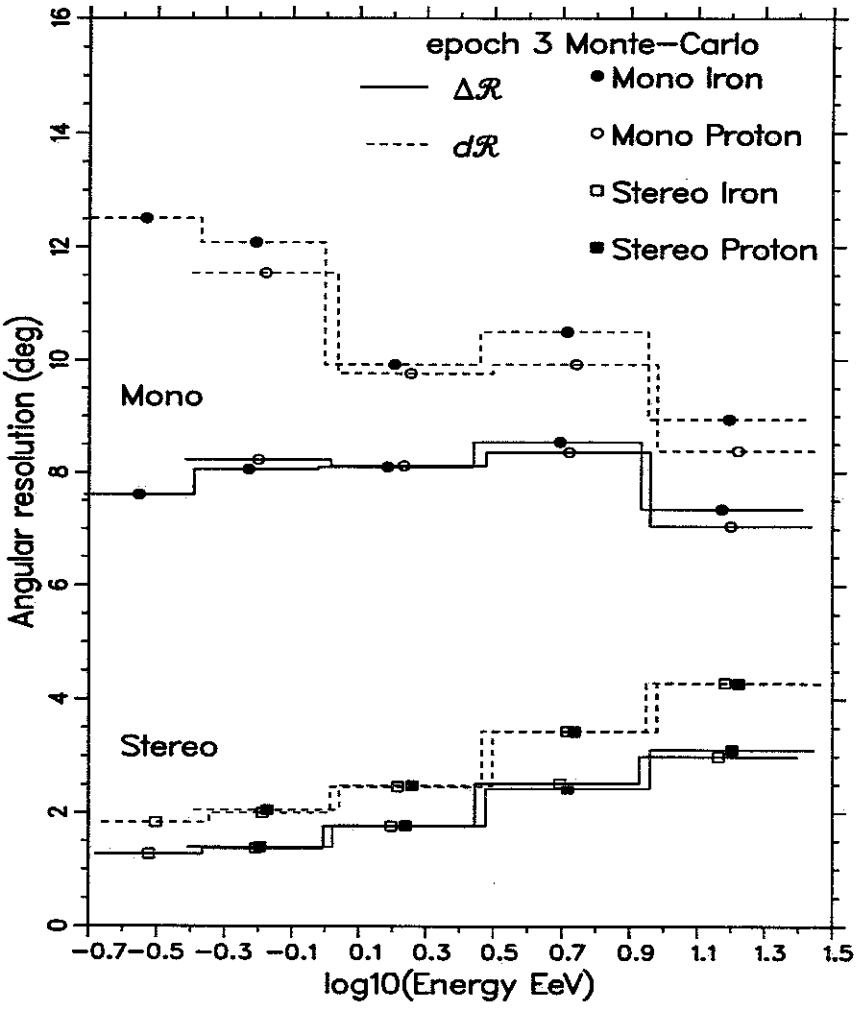

Figure 3.6. The angular resolution of Monte-Carlo epoch 3 data.

determine arrival direction; therefore, it has better angular resolution. For the same track length and Rp, the higher the energy, the higher the luminosity. However the Rp also increases and the detected signals are inversely proportional to the square of distance whereas the luminosity increases linearly with energy. Therefore the signal to noise ratio does not improve too much. The angular resolution has only a weak dependence on energy due to the longer track length at higher energy. We may use a two variable linear fit to look for the dependence of reconstruction error $\Delta\Re$ on track length and energy. For the monocular data, the result is

$$\Delta\Re = 0.811 * log10(Energy) - 0.354 * track + 30.29$$

For typical values, $track = 60°$ and $Energy = 1.0EeV$; the contribution from the energy term is only 2.3% of the contribution from the track length term. Using the same fit as that of $\Delta\Re$, the dependence of $\delta\Re$ on energy and track length is

$$\delta\Re = -0.993 * log10(Energy) - 0.341 * track + 32.55$$

The contribution from energy is less than 5% of the contribution from track length. Both of the two fits prove that the reconstruction error depends mainly on track length.

Table 3.11 lists the reconstruction error $\Delta\Re$ and angular uncertainty $\delta\Re$ as function of track length of Monte-Carlo epoch 3 data. These results are also shown in Figure 3.7. It seems that the variable $\delta\Re$ overestimates $\Delta\Re$ at shorter track length ($< 80°$) and underestimates $\Delta\Re$ at longer track length ($> 120°$). The stereo data have better angular resolution than mono data because stereo reconstruction is more precise than time fitting.

We may use the reconstruction error to predict overall resolution. The mean angular resolution is about 8.24° for mono data and 1.45° for stereo data. Due to the shorter track length in real data than in MC data, the real resolution could increase to approximately 8.8° for mono data and 1.6° for stereo data.

3.6.5 X_{max} and energy resolution

3.6.5.1 Systematic error in energy. The systematic uncertainty in energy comes from uncertainty in the fluorescent efficiency, the atmospheric scattering and transmission of light, Cherenkov subtraction, and uncertainty in geometric reconstruction. The systematic errors for the first three are $\sim$ 20%, $\sim$ 10%, and $\leq$ 4% respectively. For the stereo data, the systematic uncertainty in energy due to geometric reconstruction is $\leq$ 5%. The monocular data have an extra 20% offset in energy when compared to the stereo data; this deficit has been corrected in our analysis. In conclusion, we estimate that the maximum systematic uncertainty in energy is about 40% in the worst case. The random error is about 20% to 24% for stereo data [2, 3, 7, 55].

Table 3.11. The reconstruction error as function of track length of mono Monte-Carlo epoch 3 data. All quantities are in degrees except $\Delta\Re/\delta\Re$.

Track Length	$\Delta\Re$		$\delta\Re$		$\Delta\Re/\delta\Re$
	Mean	RMS	Mean	RMS	
30 – 40	16.09	12.15	24.93	10.43	0.646
40 – 50	11.82	9.18	16.20	7.23	0.730
50 – 60	8.46	6.44	10.34	4.18	0.818
60 – 70	5.89	4.50	6.74	2.47	0.874
70 – 80	4.40	3.42	4.81	1.71	0.915
80 – 90	3.34	2.60	3.43	1.03	0.973
90 – 100	2.66	1.99	2.71	0.97	0.982
100 – 110	2.13	1.64	2.12	0.54	1.003
110 – 120	1.93	1.25	1.65	0.35	1.169
120 – 130	1.78	1.10	1.27	0.28	1.407
130 – 140	1.72	0.94	0.98	0.17	1.759
140 – 150	1.98	0.90	0.74	0.17	2.687

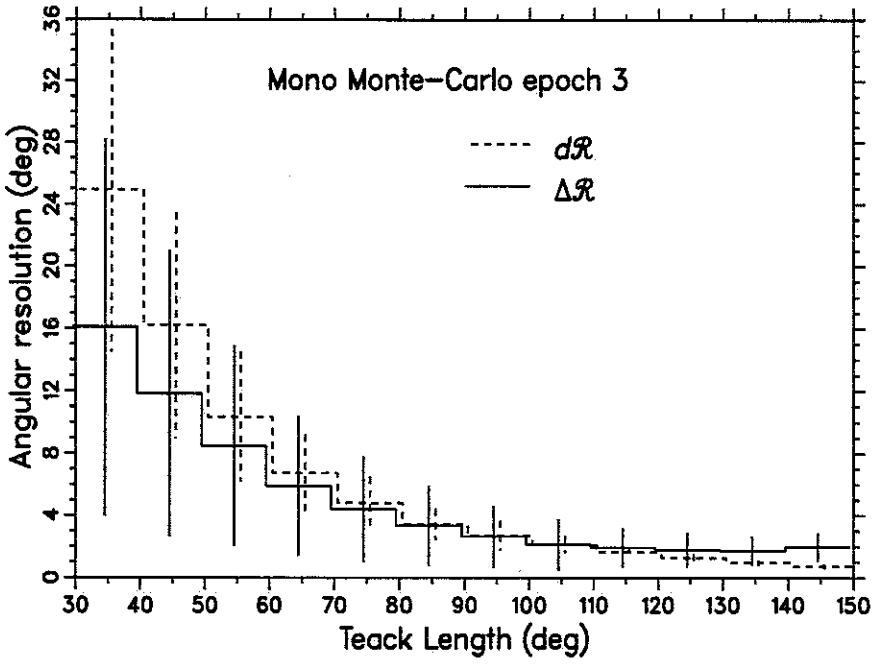

Figure 3.7. The angular resolution of mono Monte-Carlo epoch 3 data. The error bar is the RMS width of distribution.

3.6.5.2 Systematic error in X_{max}. The X_{max} resolution for stereo data is about $45g/cm^2$ on an event by event basis [3]. The systematic error of the absolute value of X_{max} is $20g/cm^2$. The systematic error of hadronic shower Monte-Carlo X_{max} prediction is $10g/cm^2$, due to approximations in the Monte-Carlo [3].

3.6.5.3 Reconstruction error. For the shower profile variables, the relative error of X_{max} and energy have a linear correlation with X_{max} and the logarithm of energy. These relations are

$$\frac{X_{max_{shp}} - X_{max_{mc}}}{X_{max_{mc}}} = A + B * X_{max_{mc}}$$

$$\frac{E_{shp} - E_{mc}}{E_{mc}} = A + B * \log(E_{mc})$$

The relations depend on the composition and longitudinal profile fitting. Table 3.12 lists the correction constants A and B. Figures 3.8 and 3.9 show the relative error vs actual value of energy and X_{max}. These errors are within systematic errors; we do not use these correction in this dissertation.

The energy had an overall normalization constant in the shape reconstruction. From this analysis, a linear function to $\log(Energy)$ would be a better normalization. Unfortunately, these are Monte-Carlo data where we know the actual composition, X_{max}, and energy. For the real data, these three factors are tangled together. The X_{max} and energy are calculated from the shower profile fitting. Although we could use X_{max} to separate events into proton flux and iron flux, the resolution is not good enough to distinguish proton from iron event by event.

Table 3.12. The energy calibration of stereo Monte-Carlo data. $(E_{shp} - E_{mc})/E_{mc} = A + B * \log(E_{mc})$

Composition	Fit model	$A \pm \sigma_A$	$B \pm \sigma_B$	$LCA\dagger$
Proton	Gauss	-0.156 ± 0.037	-0.087 ± 0.049	-0.960
	G-H	-0.118 ± 0.036	-0.043 ± 0.034	-0.928
Iron	Gauss	-0.187 ± 0.027	-0.063 ± 0.034	-0.932
	G-H	-0.153 ± 0.026	-0.024 ± 0.035	-0.851

$\dagger LCA$: Linear correlation amplitude.

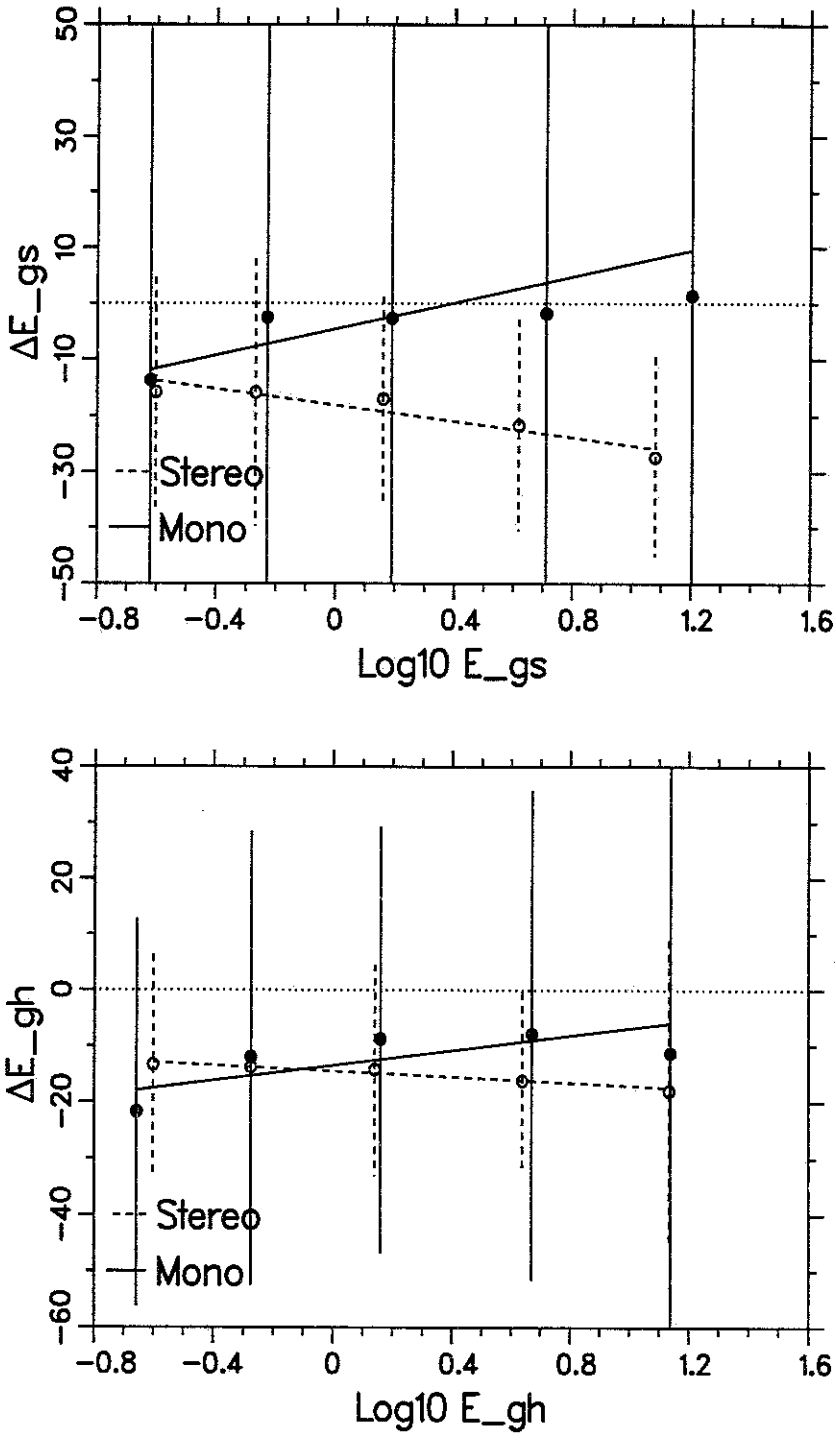

Figure 3.8. The mean error of Gaussian fit (top figure) and Gaisser-Hillas fit (bottom figure) energy of epoch 3 Monte-Carlo. The error bar is the standard deviation of distribution.

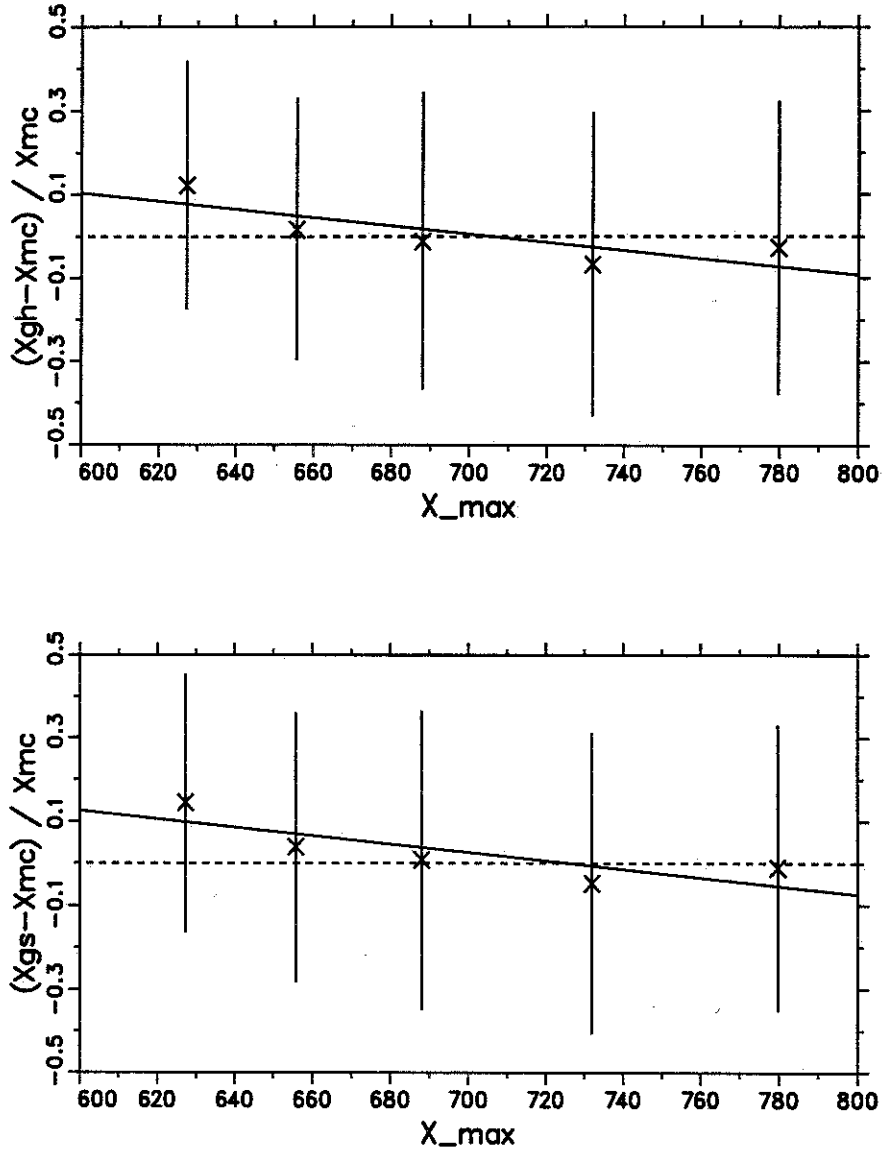

Figure 3.9. The mean value error of X_{max} of mono Monte-Carlo epoch 3 data. The error bar is the standard deviation of distribution.

Instead of untying this mysterious knot, an empirical formula could be used to correct the overall energy scale statistically. We assume an ensemble of events which consist of a given ratio of proton and iron showers and then find the linear correlation of input energy and output energy. To exclude events with large errors, a tighter cut was used in the selection of events.

3.7 Comparison of the Virtual and Real Detector

3.7.1 Gaussian fit vs Gaisser-Hillas fit

We have two ways to determine the energy and X_{max}: the Gaussian fit or the Gaisser-Hillas fit. Table 3.13 lists the typical number of events for those two fits for epoch 3 data. These data are also plotted in Figure 3.10. Comparing the number of events which pass the data cuts, the Gaussian fit gives more events than the Gaisser-Hillas fit for monocular data, but the Gaisser-Hillas fit yields more events for stereo data.

For monocular data, the Gaussian fit has lower mean χ^2 but higher mean $\Delta E/E$ than Gaisser-Hillas fit. For stereo data, when the energy $\leq 3.2 EeV$, the Gaisser-Hillas fit has lower mean χ^2 but higher mean $\Delta E/E$ than Gaussian fit. But at higher energy, this

Table 3.13. Comparison of Gaussian and Gaisser-Hillas fits of epoch 3 data. Data must pass the basic data cuts. GS : Gaussian fit, GH : Gaisser-Hillas fit.

			Energy (EeV)				
	Data	Fit	0.2 - 0.4	0.4 - 1.0	1.0 - 3.2	3.2 -10.0	$\geq$10.0
number of events	mono	GS	2922	1932	799	200	47
		GH	1483	1525	655	143	36
	stereo	GS	1434	1146	534	91	18
		GH	1458	1164	502	101	19
$< \chi^2 >$	mono	GS	0.948	1.134	1.445	1.943	2.071
		GH	1.017	1.311	1.805	2.499	2.824
	stereo	GS	1.440	1.593	2.517	3.962	7.764
		GH	1.121	1.438	2.441	4.254	8.427
$< \Delta E/E >$	mono	GS	0.661	0.806	0.831	0.830	1.218
		GH	0.686	0.604	0.519	0.295	0.487
	stereo	GS	0.209	0.277	0.417	0.406	0.671
		GH	0.466	0.433	0.472	0.402	0.266

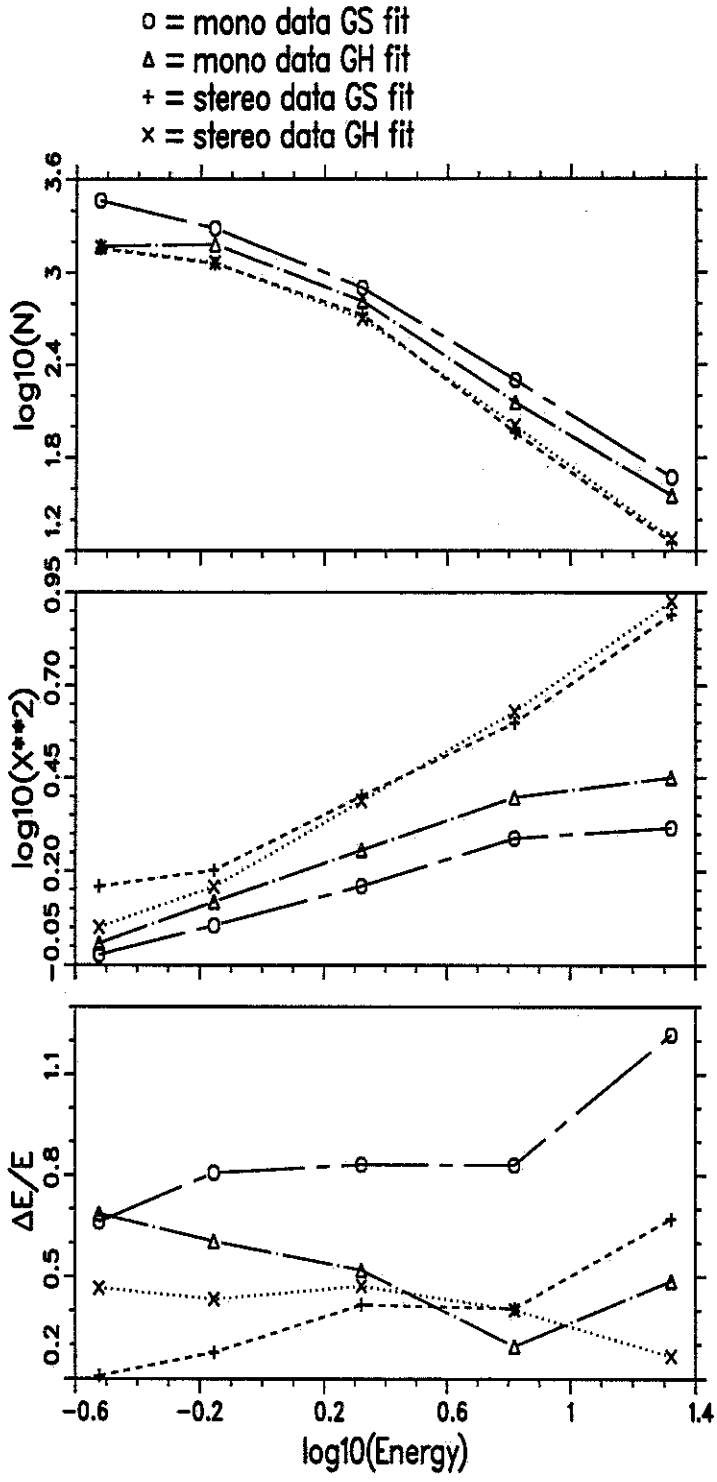

Figure 3.10. Comparison of Gaussian and Gaisser-Hillas fits of epoch 3 data. GS : Gaussian fit, GH : Gaisser-Hillas fit.

tendency reverses. It is interesting that χ^2 and ΔE have a reverse trend, but in an event by event study, this anticorrelation is not seen.

It is hard to say which fit is better. Based on these comparisons, the Gaussian fit is better for monocular data because of the larger event number and smaller χ^2 even though there is a slightly larger energy uncertainity. For stereo data, the Gaisser-Hillas fit is slightly better because it yields more events. For energy $\geq 3.2 EeV$ the Gaisser-Hillas fit has higher χ^2 but lower $\Delta E/E$.

Although the Gaussian fit is not a good a priori physical model for shower development, it is a slightly better fit than the Gaisser-Hillas function for monocular data because of poorer detector resolution. In this dissertation, I will use the Gaussian fit for monocular data and the Gaisser-Hillas fit for stereo data to provide more events for better statistics.

3.7.2 Consistency check of data and Monte-Carlo

The most important test of the Monte-Carlo is whether it is a good representation of the real detector. Because there is no intrinsic connection between Monte-Carlo and real data, we cannot compare them on an event by event basis as we did in the previous section. We compare the distribution of Monte-Carlo and real data in various variables. Both data sets are successfully reconstructed by all the software and pass through the same cuts. We use the same program to generate histograms. Several significant differences are found from this study. The mean value and standard deviation of MC and data of these variables are listed in Table 3.14.

3.7.2.1 Track length. The mean track length of real data is shorter than that of MC at higher energy. Figure 3.11 shows the track length as a function of energy for real data and for MC. Because longer track length means more degrees of freedom to determine shower geometry, we expect that the real data will have worse resolution than MC.

3.7.2.2 Impact parameter *Rp*. The mean impact parameter of MC data is less than that of real data. This difference indicates that the MC triggers on more nearby events than the real detector does. Figure 3.12 show the mean Rp as a function of energy. We fit the Rp as a function of $\log_{10} Energy$, the fitted line of real data and that

Table 3.14. Comparison of real data and Monte-Carlo of epoch 3 data. The number shown in data and Monte-Carlo are mean ± RMS width.

Stereo Data			
parameter	Energy (EeV)	Data	Monte-Carlo
Rp (km)	0.2 - 0.4	2.35 ± 0.76	2.05 ± 0.68
	0.4 - 1.0	3.15 ± 1.18	2.58 ± 1.08
	1.0 - 3.2	4.46 ± 1.68	3.66 ± 1.68
	3.2 - 10.0	6.15 ± 2.13	5.39 ± 2.51
	≥ 10.0	7.24 ± 2.40	6.83 ± 2.92
Psi (deg)	0.2 - 0.4	76.5 ± 22.4	81.3 ± 23.5
	0.4 - 1.0	71.9 ± 25.3	73.2 ± 25.1
	1.0 - 3.2	64.9 ± 25.5	59.5 ± 24.8
	3.2 - 10.0	66.5 ± 26.8	49.7 ± 25.0
	≥ 10.0	75.3 ± 23.1	45.1 ± 24.4
Theta (deg)	0.2 - 0.4	32.4 ± 12.8	33.4 ± 13.1
	0.4 - 1.0	36.3 ± 14.3	37.1 ± 14.3
	1.0 - 3.2	40.1 ± 15.7	43.5 ± 15.9
	3.2 - 10.0	41.3 ± 17.1	50.6 ± 17.3
	≥ 10.0	43.7 ± 13.1	54.7 ± 17.1
Track length (deg)	0.2 - 0.4	63.8 ± 19.7	63.8 ± 20.5
	0.4 - 1.0	65.0 ± 20.4	69.5 ± 23.1
	1.0 - 3.2	66.8 ± 20.8	77.3 ± 22.5
	3.2 - 10.0	64.7 ± 23.0	80.8 ± 21.2
	≥ 10.0	64.8 ± 24.8	84.9 ± 21.9
Mono Data			
Rp (km)	0.2 - 0.4	2.41 ± 0.72	2.17 ± 0.67
	0.4 - 1.0	3.29 ± 1.19	3.09 ± 1.25
	1.0 - 3.2	4.91 ± 2.09	4.73 ± 2.15
	3.2 - 10.0	7.28 ± 3.23	7.56 ± 3.51
	≥ 10.0	11.21 ± 5.48	9.54 ± 4.11
Psi (deg)	0.2 - 0.4	72.9 ± 23.6	78.6 ± 26.3
	0.4 - 1.0	68.9 ± 25.0	75.6 ± 27.2
	1.0 - 3.2	65.9 ± 28.3	65.6 ± 27.1
	3.2 - 10.0	68.1 ± 32.0	57.9 ± 29.4
	≥ 10.0	66.2 ± 34.5	52.4 ± 30.8
Theta (deg)	0.2 - 0.4	33.1 ± 14.9	35.0 ± 14.3
	0.4 - 1.0	36.9 ± 16.2	37.8 ± 15.0
	1.0 - 3.2	42.0 ± 16.8	43.1 ± 15.9
	3.2 - 10.0	46.0 ± 16.4	50.5 ± 16.7
	≥ 10.0	50.1 ± 17.8	56.4 ± 16.8
Track length (deg)	0.2 - 0.4	61.8 ± 18.4	61.8 ± 19.9
	0.4 - 1.0	60.4 ± 18.6	62.8 ± 21.8
	1.0 - 3.2	58.4 ± 20.0	64.4 ± 22.4
	3.2 - 10.0	55.6 ± 21.1	64.0 ± 22.2
	≥ 10.0	50.3 ± 18.8	68.1 ± 23.5

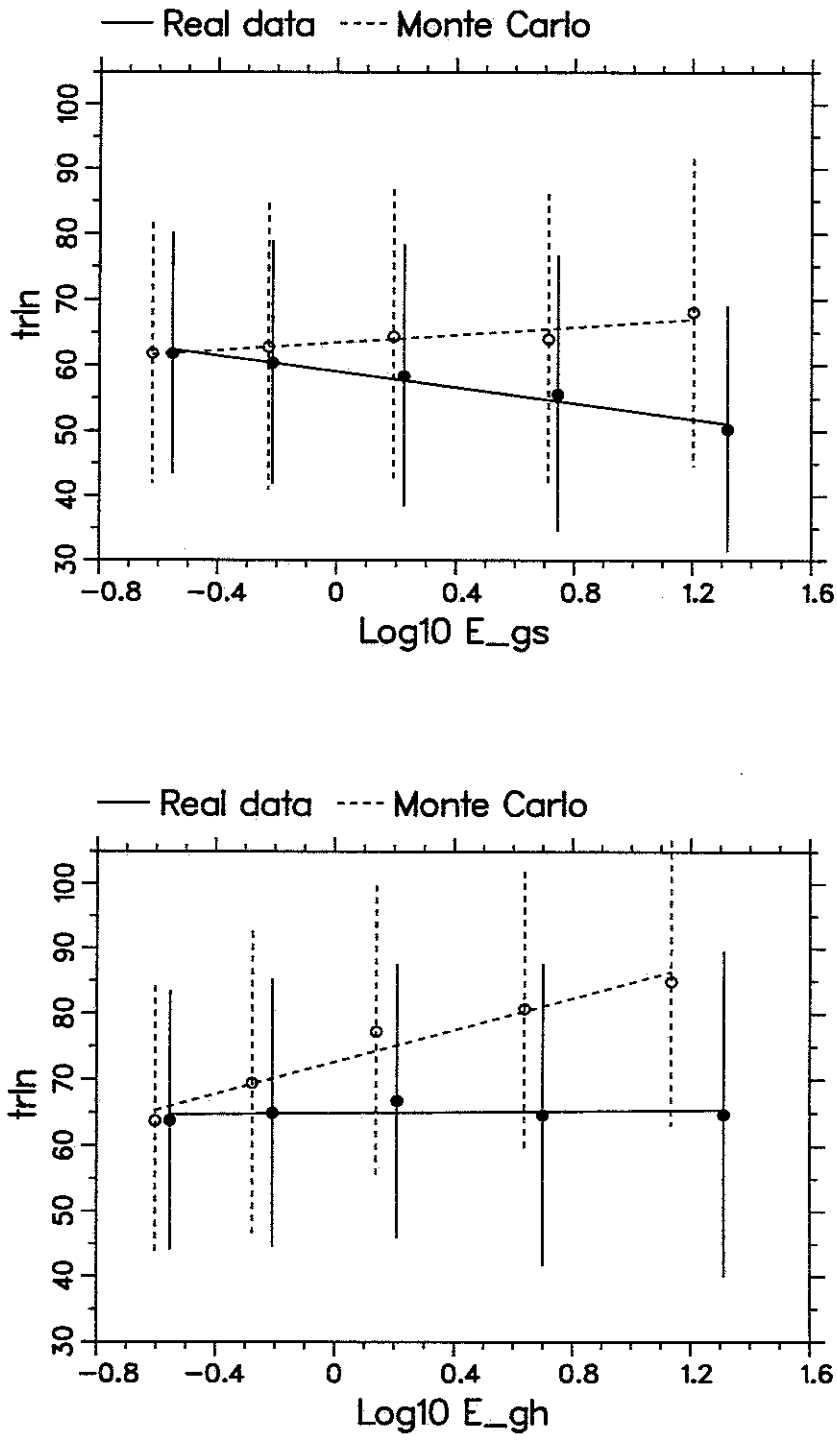

Figure 3.11. The mean track length as function of energy. The top figure is mono data. The bottom figure is stereo data.

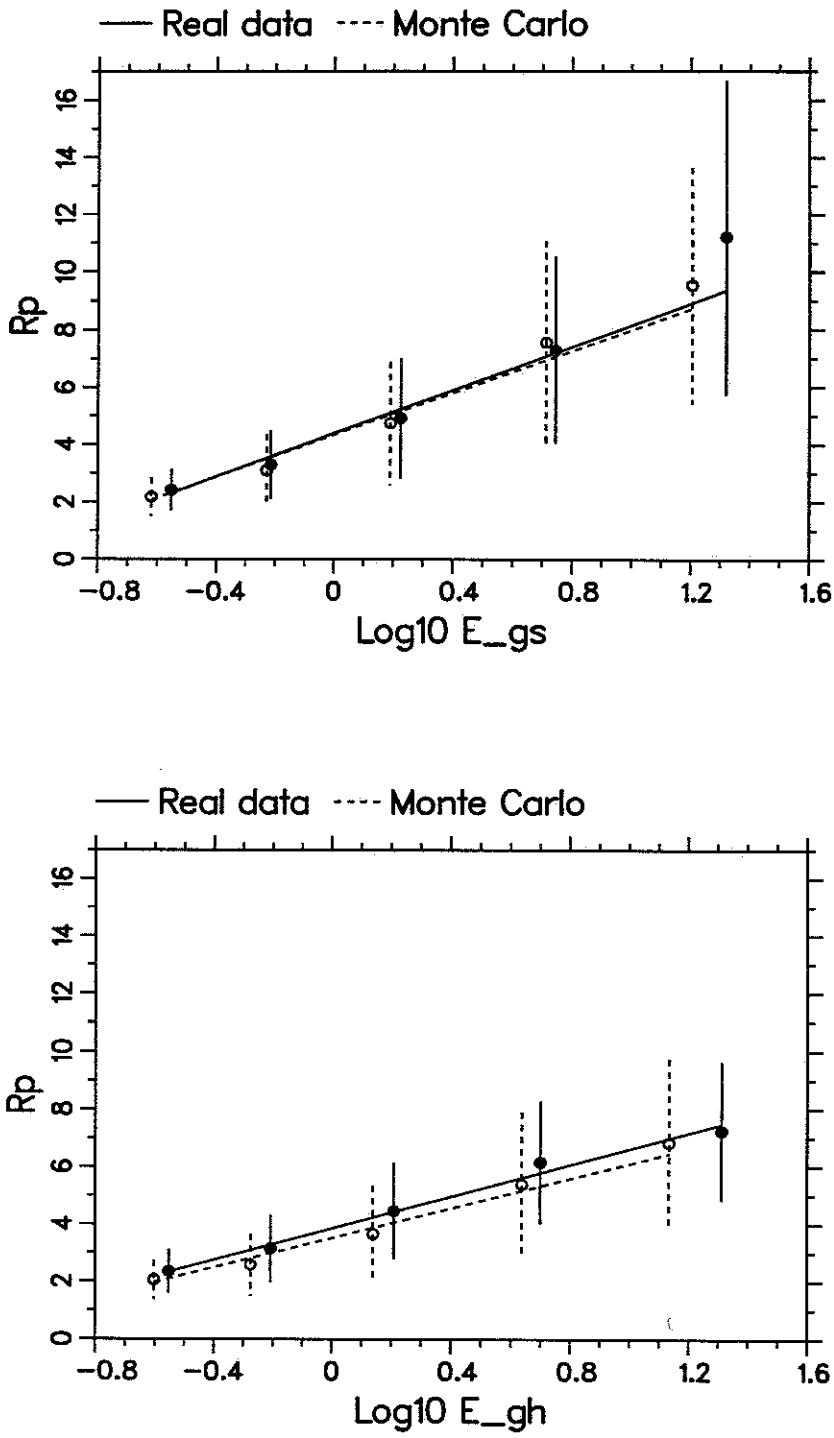

Figure 3.12. The mean Rp as function of energy. The top figure is mono data. The bottom figure is stereo data.

of Monte-Carlo are almost identical to each other. Those two lines may suggest that there is no difference in triggering between the real detector and Monte-Carlo. The problem is that the mean energy of Monte-Carlo is less than the mean energy of real data. This systematic difference could be caused by a steeper spectra index in the Monte-Carlo than in the real data.

3.7.2.3 Azimuth angle ψ and zenith angle θ. The mean ψ distribution for the real detector is quite flat. But the mean ψ of MC decreases as the energy increases. Figure 3.13 shows this tendency. As a consequence, the mean zenith angle θ increases as the energy increases. Figure 3.14 show the mean θ as a function of energy. This systematic difference suggests that the MC triggers more than real data on events from lower elevation.

3.7.3 Conclusion

In the previous section and this section, we discuss some systematic errors in event reconstruction and in the detector Monte-Carlo. Here is a short summary.

1. The relative error of Rp of mono data increases as energy increases.
2. The relative error of X_{max} and energy have linear relations with X_{max} or $\log_{10} Energy$. These relations may depend on composition and epoch.
3. The mean track length of real data is shorter than the Monte-Carlo prediction.
4. The mean Rp of real data is larger than the Monte-Carlo prediction.
5. The mean ψ of real data does not change much with energy. But the mean ψ of Monte-Carlo decreases as the energy increases.
6. The mean θ of real data is smaller than the Monte-Carlo predictation.

The combined effect of 1 and 4 is to underestimate the number of distant events. If this underestimation is corrected, the aperture should increase. However the effect of 6 on θ could compensate for this increase [62]. Therefore, the overall effect does not change

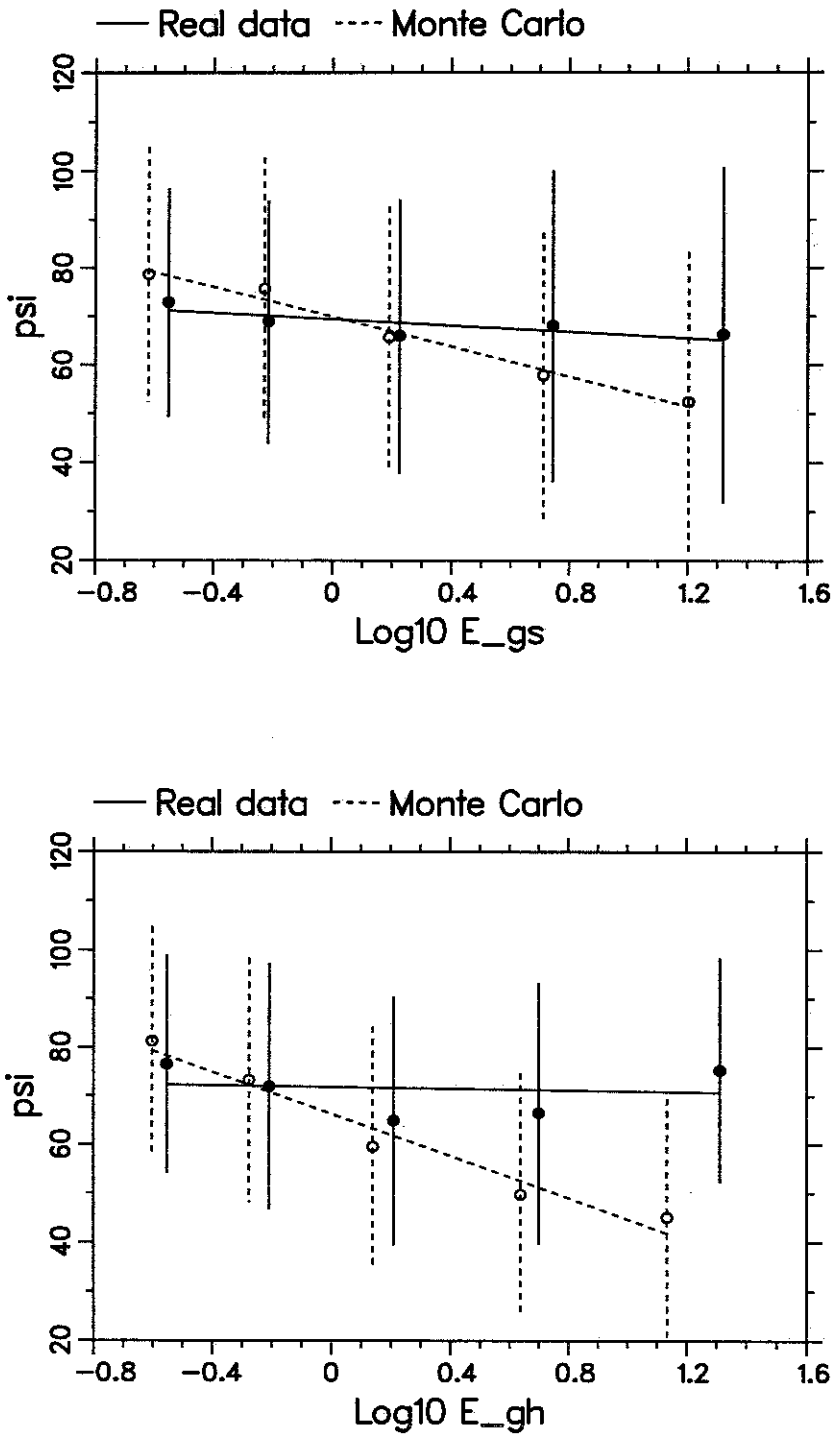

Figure 3.13. The mean incline angle ψ as function of energy. The top figure is mono data. The bottom figure is stereo data.

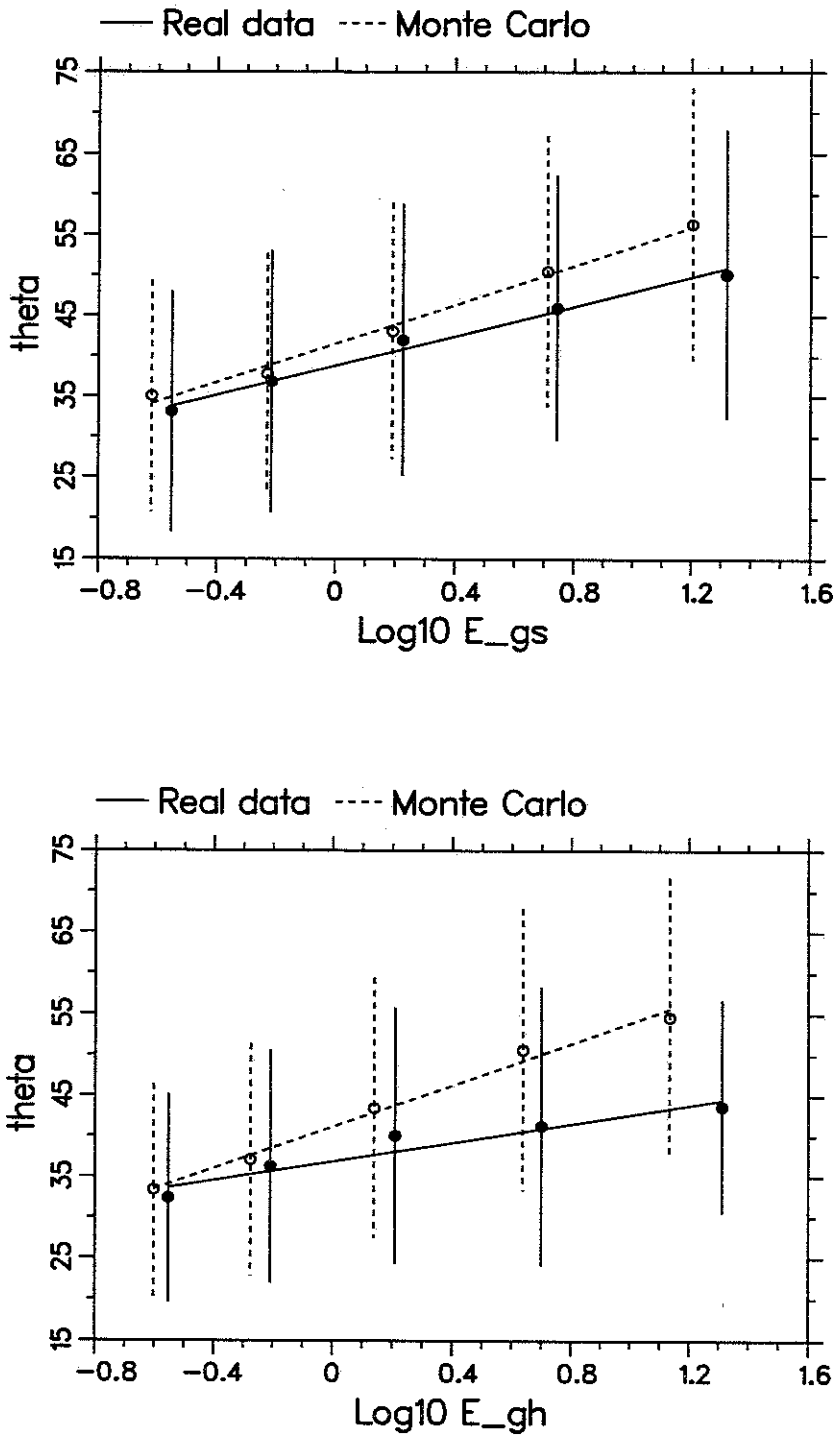

Figure 3.14. The mean zenith angle θ as function of energy. The top figure is mono data. The bottom figure is stereo data.

the aperture much. The energy calibration (as mentioned in the previous section) boosts individual energies up approximately 5% to 20%, and therefore increases statistics at higher energy. Those two effects will certainly change the spectrum and composition.

The best way to reduce these errors would be to find out where the energy deficit and trigger bias are coming from, correct them, and then rerun the spectrum analysis and rerun the Monte-Carlo simulation according to the new spectrum index and composition model. This process is out of reach of my research. Furthermore the energy plays only a minor part in the anisotropy analysis since we separate the data into five energy intervals. In order to simplify the calculation, the energy calibration is treated as a second order effect which does not change the spectrum index.

In this dissertation, I compare data with all previous analyses on composition and spectrum. In these analyses, a constant energy normalization was used. I will use the same normalization as these analyses and **DO NOT** introduce an energy dependent correction.

The systematic difference 3 (track length) will make angular resolution of real data worse than that of Monte-Carlo prediction. The systematic difference of ψ andθ will also affect the background prediction when we do the anisotropy analysis. As we saw, the Monte-Carlo has a different θ distribution than the real data and the difference is greater than angular resolution at energy $E > 32.EeV$ where we need Monte-Carlo data to calculate acceptance (detector efficiency as a function of zenith angle θ). Therefore the **Monte-Carlo data is used in the analyses.** Section 4.2 discusses a special treatment to overcome the real data errors.

CHAPTER 4

ISOTROPIC BACKGROUND PREDICTION AND DATA PROCESSING

This chapter discusses data structure first; then two types of background prediction techniques are discussed. This dissertation tries to use a single set of data files and different analysis programs to perform all the anisotropy analyses.

4.1 Data Processing

The data processing stream is shown in Figure 4.1. The raw data (**.scn, *.sim*) are processed through GEO, SIZE, and SHAPE. The filter program ANIFLTR reads these shape files (**.shp*) and stores data in several files (**evn.dat, *dir.dat, and *tim.dat*). The program EVN2GAL transforms the event into an event probability and stores it in galactic coordinates. The program MCEPD reads event arrival direction from **dir.dat* and randomly chooses a run time from **tim.dat* to make a fake event and then does the same things as EVN2GAL. The program CALACC reads the arrival direction from **dir.dat* and calculates the acceptance. The program LIVETIM reads the acceptance and **tim.dat*, then calculates the acceptance weighted live time. These programs are covered in later sections.

4.1.1 Energy intervals

Anisotropy may change with energy, so we need to separate data into several energy intervals. Based on the study of spectrum and composition, five intervals are chosen. The minimum energy of our data is about $0.2EeV$. The elongation rate becomes steeper at $0.4EeV$. At about $3EeV$ the spectrum flattens and the iron flux is almost equal to the proton flux. Instead of 3, I chose 3.2 because it is one half of an interval in log scale. The five intervals are $0.2-0.4EeV$, $0.4-1.0EeV$, $1.0-3.2EeV$, $3.2-10.EeV$, and $\geq 10EeV$.

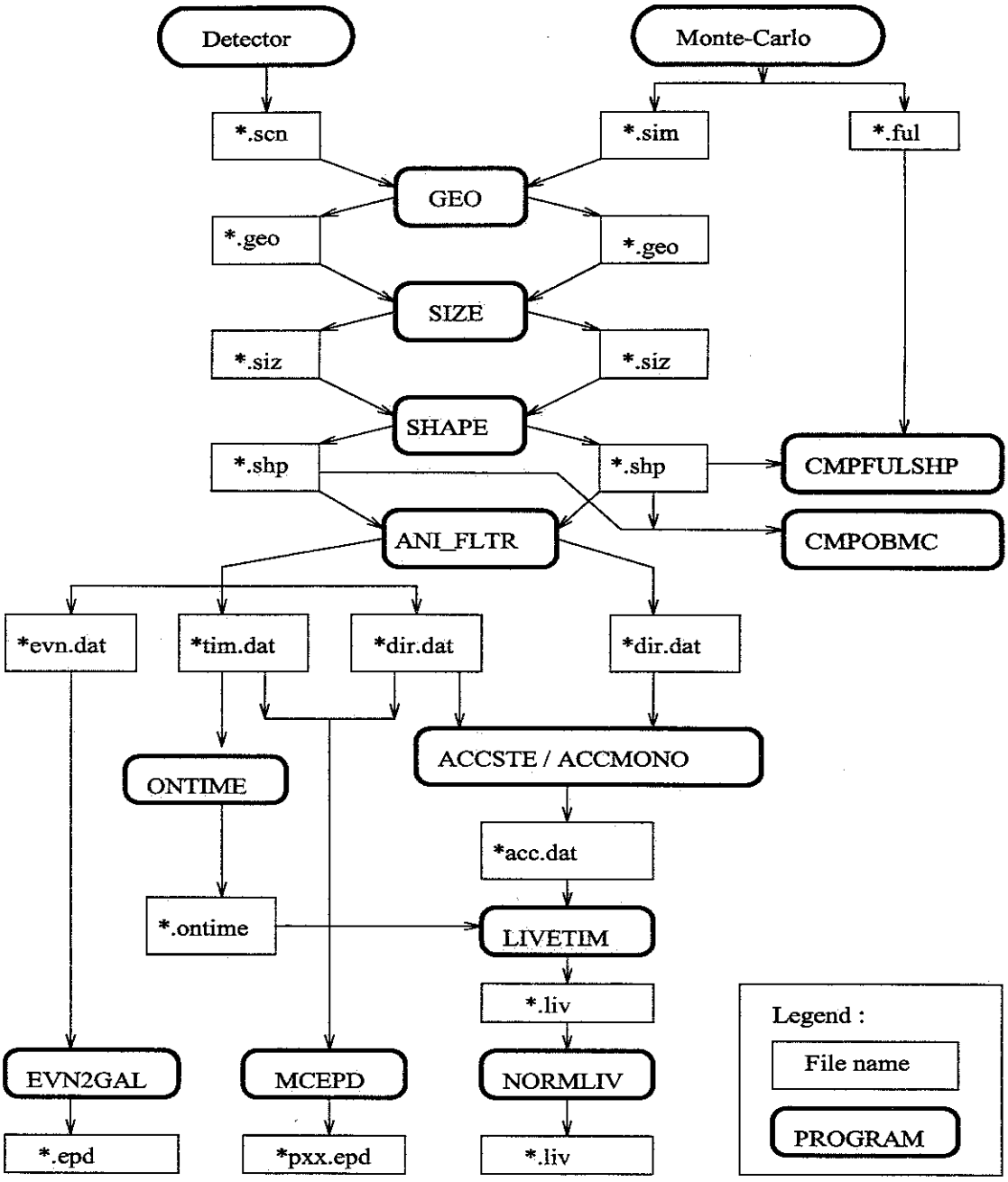

Figure 4.1. Flow chart of data processing and analysis. The data file names are enclosed in rectangles. The command or program is enclosed in the rounded rectangles and capitalized. The final data files used in anisotropy studies are at the bottom, $*.pxx.epd$, $*.epd$, and $*.liv$.

4.1.2 Pixel size

In the previous analysis, an equal area bin of 10° of galactic longitude and 0.174 of sin(*galactic latitude*) which is about 10° near the galactic plane is used. This method has the disadvantage that the bin shape is distorted at higher latitudes. In addition this bin is too large to perform small scale anisotropy. In this work, a fine resolution, $1^\circ \times 1^\circ$ grid is used to store data for all small scale and large scale analyses.

4.1.3 Event number vs event probability

Event numbers per bin were used for most oprevious analysis. But some events have a large error in arrival direction, causing large fluctuation in the number of events for each pixel. There are two methods to smooth out the large fluctuation. One is using a larger pixel size, but at the same time, good resolution is sacrificed. The other is using a tight cut to cut out events with large errors, but this method will reduce the number of events.

Instead of event number count, an event probability density is used. Section 4.2 discusses the point spread function which explains how the event probability is spread out over an area. The point spread function of each event is carefully calculated; the probability density is then transformed from local coordinates to galactic coordinates. The details are covered in the next section. This method preserves the original information. An event with a large error will spread out over a large area. It is unnecessary to apply tight cuts and therefore increase the statistics.

4.1.4 Selection of events

The main concern of this analysis is the study of arrival direction. The more events we have, the smaller the fluctuation will be. In the next section, we show the techniques used to estimate the error distribution; therefore, we do not worry about the large uncertainities of arrival direction. We use only the basic data cut. As mentioned above, we use the Gaussian fit energy for monocular data and Gaisser-Hillas fit energy for stereo data. The number of events for all epochs are listed in Table 4.1.

4.1.5 Isotropic background prediction

A background based on an isotropic distribution is necessary for comparison to the data. How to predict the isotropic background is the most difficult part of the anisotropy analysis. A different prediction could lead to totally different results. Two methods are used in this analysis to insure we have a self consistent background prediction. The scrambled event method uses real events with randomly chosen event arrival direction (θ , ϕ) and arrival times T to simulate a fake event. Section 4.3 discusses this method. The live time method uses the detection efficiency and live time of the detector to calculate the effective detection aperture. Section 4.4 discusses the detection efficiency, called the acceptance in this dissertation. Section 4.5 discusses the live time of the detector. The consistency of these two methods is discussed in the first section of Chapter 5.

4.2 Point Spread Function

The point spread function, PSF, is the spread of probability around the detected direction. In the previous analysis, the PSF was assumed to be a Gaussian probability distribution. However, do our data really obey a normal distribution? This analysis

Table 4.1. The total number of events of all epochs

epoch	Date	Energy (EeV)					
	month/Year	0.2 - 0.4	0.4 - 1.0	1.0 - 3.2	3.2 -10.0	$\geq$10.0	All
				Monocular Data			
1	11/81 - 05/85	1208	1331	787	228	85	3639
2	11/85 - 07/87	2170	1696	829	227	51	4973
3	08/87 - 06/88	2895	1966	842	198	55	5956
4	07/88 - 04/90	2300	2156	1146	262	70	5934
5	05/90 - 09/91	1094	1095	595	136	52	2972
6	10/91 - 07/92	1245	979	438	95	28	2785
	Total	**10912**	**9223**	**4637**	**1146**	**341**	**26259**
				Stereo Data			
2	11/86 - 06/87	456	382	215	32	6	1091
3	07/87 - 06/88	1489	1127	476	90	15	3197
4	07/88 - 04/90	1725	1470	659	113	23	3990
5	05/90 - 09/91	841	721	350	66	15	1993
6	10/91 - 07/92	657	491	209	42	4	1403
	Total	**5168**	**4191**	**1909**	**343**	**63**	**11674**

intends to understand more about the intrinsic nature of Fly's Eye data rather than assuming some known probability function to study the unknown in nature.

How well can the Fly's Eye reconstruct the arrival direction of a cosmic ray event? We can use the Monte-Carlo data to study this question, because we know the real direction which are stored in **.ful* files. The reconstruction errors are defined as

$$\Delta\theta = \theta_{shp} - \theta_{ful} \qquad \Delta\phi = \phi_{shp} - \phi_{ful}$$

If we plot the $\Delta\theta$ distribution, it is certainly not a good normal distribution. It is biased because of the different uncertainties $d\theta$ of different events. A standardized variable must be used to look for a point spread function.

$$Z_\theta = \Delta\theta/d\theta \qquad Z_\phi = \Delta\phi/d\phi$$

Figure 4.2 and 4.3, show the Z_θ and Z_ϕ distribution. The mean value and standard deviation of these distributions are also listed in these figures. If the point spread function is a perfect normal distribution, the mean should be 0 and the SD should be 1. From these figures, we see clearly that they are not perfect normal distributions. For the stereo data, the mean value is approximated 0 but the SD is quite large. It is a leptokurtic normal distribution, which means it has a thin central peak and a long tail. A special algorithm is developed to perform the fitting. A normal distribution fits the central peak, another normal distribution fits the long tail, and we let the width and ratio of those two distributions be varied to find a minimum χ^2. We sample all the Monte-carlo data, more than 5000 events, to find the best fit dual width normal distribution. The total probability is

$$P(Z) = rG(Z,0,w_1) + (1-r)G(Z,0,w_2)$$

$$G(z,a,w) = \frac{1}{\sqrt{2\pi}} \mathrm{e}^{-\frac{(z-a)^2}{w^2}}$$

where $G(Z,0,w)$ is the Gaussian probability of mean value 0, width w, and variable Z. Table 4.2 lists the results of the dual width normal distribution fit.

For the real data, since we do not know the actual value, we can only scientifically guess. The probability of the expected error distribution should be similar to that of

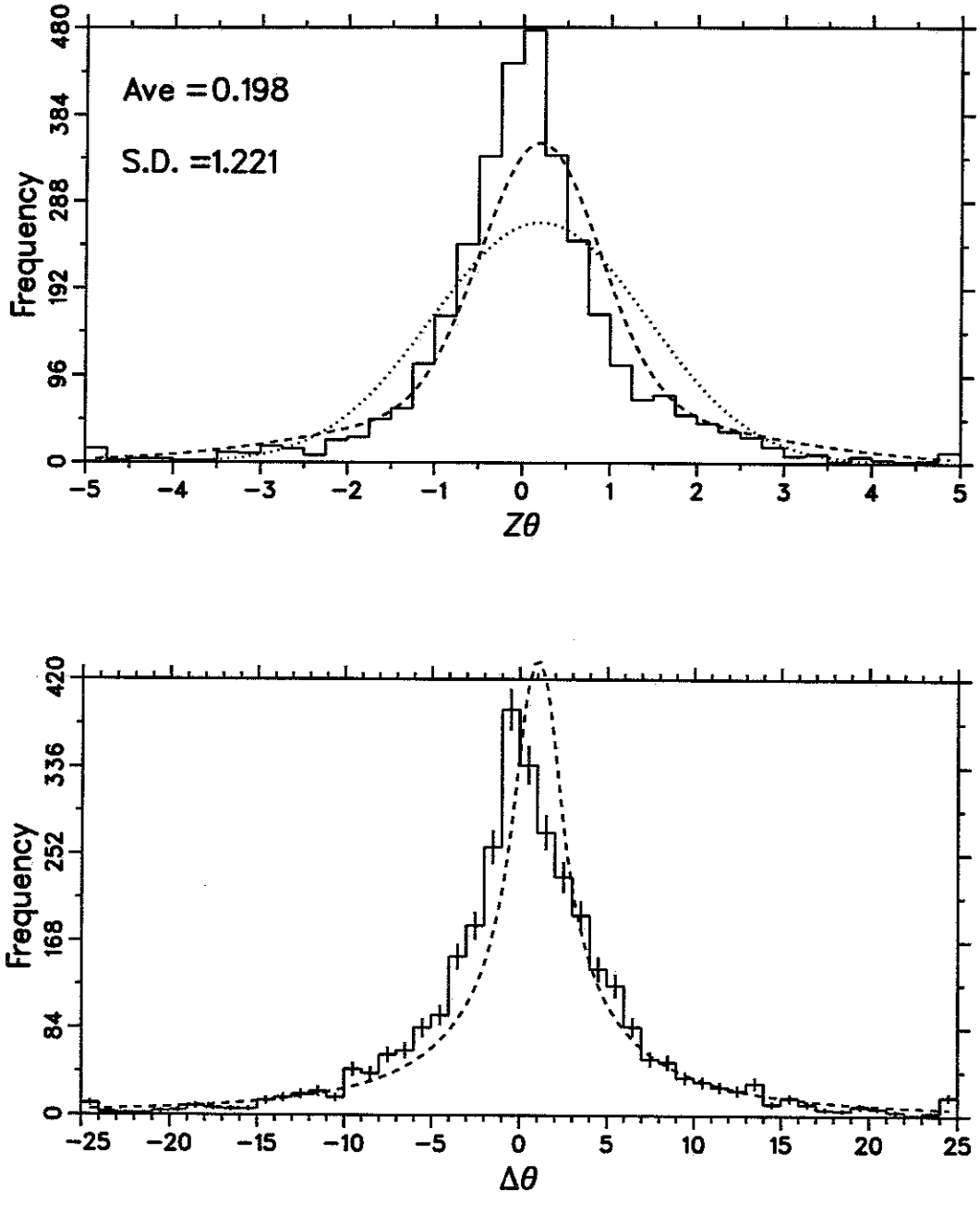

Figure 4.2. The standarized variable Z_θ and error $\Delta\theta$ distribution of monocular data epoch 3 at energy $0.2-0.4EeV$. The step function is the data distribution. The dash line is the prediction by dual width Gaussian fit. The dot line is simple Gaussian distribution based on average and standard deviation, written in upper left corner, of data distribution.

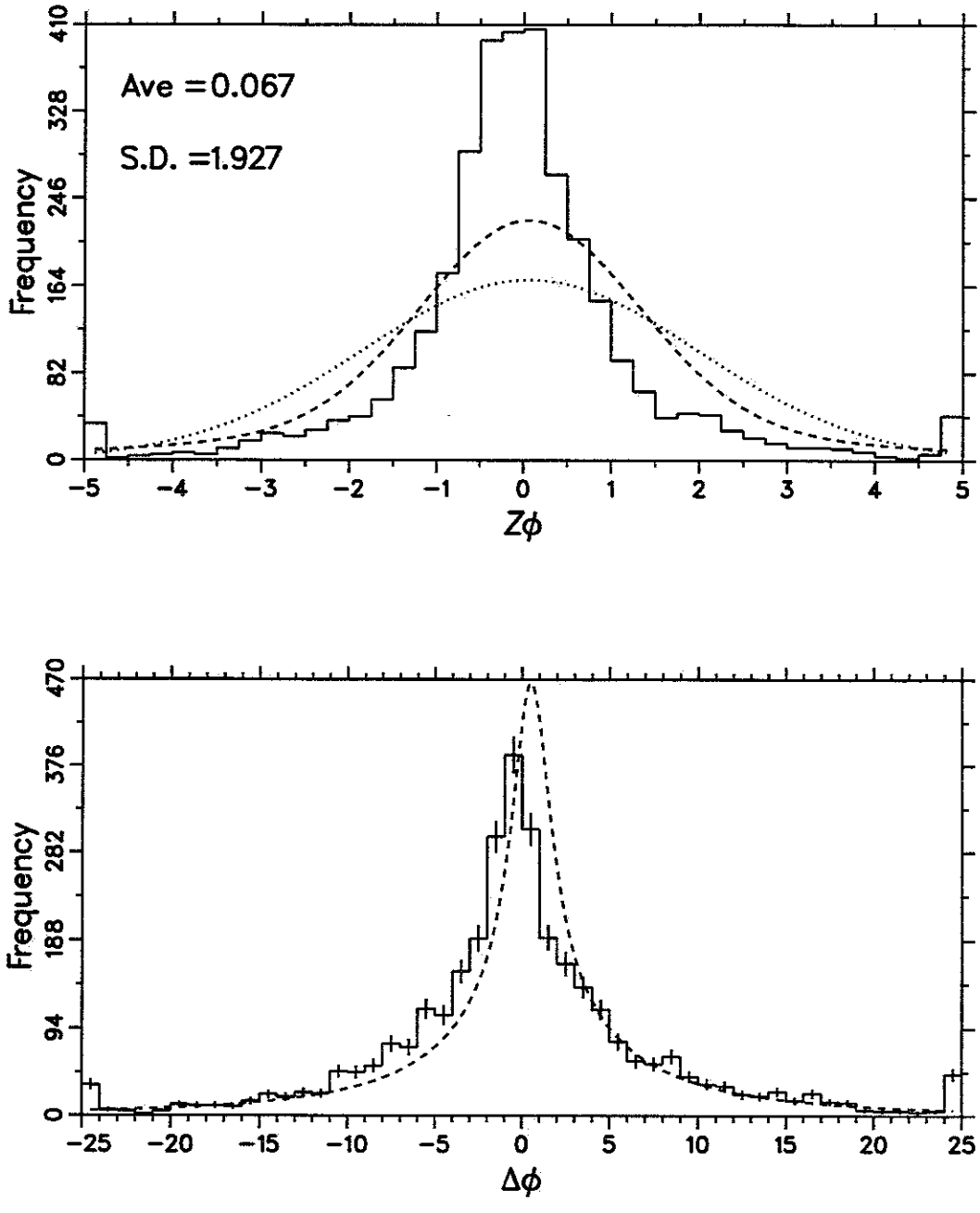

Figure 4.3. The standarized variable Z_ϕ and error $\Delta\phi$ distribution of monocular data epoch 3 at energy $0.2-0.4EeV$. The step function is the data distribution. The dash line is the prediction by dual width Gaussian fit. The dot line is simple Gaussian distribution based on average and standard deviation, written in upper left corner, of data distribution.

Monte-Carlo. Using this method, we can predict the error in the theta distribution. Figures 4.2, and 4.3 show the real error distribution and the prediction using the dual width fit. In section 3.6, we found that the angular resolution of real data is slightly greater than that of Monte-Carlo data. Because the standardized variables take care of all the differences between Monte-Carlo and real data; we do not have to modify the error distribution.

This method not only models the error distribution; it also helps to increase the statistics. In the previous analysis, because we did not quite understand the point spread function, we had to cut events that had poor resolution. Much of the monocular data were thrown away due to their poor resolution. Using this model, we can use standard cuts and almost all the data are available for analysis.

An event with arrival direction $(\theta \pm d\theta\ ,\ \phi \pm d\phi)$ in local coordinates, could come from nearby pixels, each with a certain probability. The probability of this event comes from $(\theta'\ ,\ \phi')$ is $P(\theta', \phi')$ which can be calculated by

$$\begin{aligned} Z_\theta &= (\theta' - \theta)/d\theta \\ P_\theta(Z_\theta) &= r_\theta G(Z_\theta, 0, w_{\theta,1}) + (1 - r_\theta) G(Z_\theta, 0, w_{\theta,2}) \\ Z_\phi &= (\phi' - \phi)/d\phi \end{aligned}$$

Table 4.2. Result of dual width normal distribution fit

			Energy (EeV)				
			0.2 - 0.4	0.4 - 1.0	1.0 - 3.2	3.2 -10.0	$\geq$ 10.0
monocular data	θ	r	0.6565	0.6815	0.6525	0.6225	0.5585
		w1	0.5559	0.6797	0.7069	0.6917	0.6994
		w2	1.6121	1.7281	1.7261	1.6789	1.6009
	ϕ	r	0.7364	0.7255	0.7495	0.8225	0.8185
		w1	0.6444	0.7582	0.8061	0.8769	0.9379
		w2	1.8416	1.8876	1.9543	2.1884	2.1742
stereo data	θ	r	0.7476	0.7641	0.8000	0.7900	0.8218
		w1	0.7755	0.7874	0.8379	0.8509	0.8786
		w2	2.9909	3.1590	2.9713	3.2302	4.7654
	ϕ	r	0.8127	0.8244	0.9133	0.8900	0.9052
		w1	0.6980	0.6800	0.7146	0.6696	0.6832
		w2	2.4718	2.3148	4.0630	4.3917	7.0975

$$P_\phi(Z_\phi) = r_\phi G(Z_\phi, 0, w_{\phi,1}) + (1 - r_\phi) G(Z_\phi, 0, w_{\phi,2})$$
$$P(\theta', \phi') = P_\theta(Z_\theta) P_\phi(Z_\phi)$$

Although this point spread function comes from Monte-Carlo data, we believe the nature of the non-Gaussian distribution comes from the nature of the software reconstruction. Because the Monte-Carlo and real data use the same programs in processing data, this point spread function should be valid for real data too. In the next two sections, we use the point spread function to convert event number to event probability.

4.3 Event Probability Density

The event probability density, EPD, is the probability that an event can exist in a certain pixel. In the previous analysis, the EPD is assumed to be a Gaussian probability distribution. As the last section showed, the point spread function of Fly's Eye data is not a normal distribution. Each event spreads out the probability into some nearby pixels. If we integrate over all pixels, the total probability should be equal to the total number of events. Therefore this probability is called the event probability density.

In this analysis, galactic coordinates are used. But the point spread function cannot be applied to galactic coordinates directly because of the nonlinear transformation and time dependence. So a coordinate transformation from (θ', ϕ', T), where T is the event arrival time, to (l', b') is required.

4.3.1 Event probability density of data

The shower direction of an event with arrival direction $(\theta \pm d\theta\ ,\ \phi \pm d\phi)$ at a time T can be calculated by the dual width normal distribution as discussed in the previous section. Then we can transform the $P(\theta', \phi', T)$ to galactic coordinates $P(l', b')$. The program EVN2GAL performs this calculation and transformation. This is a very time consuming job, because for every event approximately 30 to 50 nearby pixels must be calculated and then transformed to galactic coordinates. This event probability density is stored in data file **.epd*.

4.3.2 Scrambled event background prediction

It is much simpler for ground arrays to predict the isotropic background because of their almost continuous on time and symmetry in the azimuthal distribution. This means that the right ascension distribution is isotropic. The background of any source can be chosen as the mean of some other points at the same declination by sweeping the right ascension. This method is widely used by gamma ray physicists and cosmic rays physicists. Fly's Eye operates intermittently and the stereo data are not azimuthal symmetric! So this method must be modified. In order to preserve the original arrival direction, the values of θ and ϕ are stored in a data bank which contains the geometric information. The arrival time is stored in another data bank which contains the run time and trigger rate information. Then a pseudo event is generated by randomly choosing a set of (θ, ϕ) and arrival time from each data bank. In this way, we preserve all detector biases without knowing the details of the detector. Because there is no direct link between arrival time and (θ, ϕ), this randomization destroys any relation (anisotropy, if it exists) in the original events.

In this dissertation, for each epoch, we simulate 100 scrambled event background files, then sum over all epochs. This result is transformed by using the same point-spread function and is stored in the same format as $*.epd$ files. Each file has the same number of events as real data $*.epd$. The mean value of these simulated files represents the expected isotropic background, and the fluctuation of these simulated files reflects the fluctuation of real data.

Figures 4.4 to 4.13 show the contour map of the scrambled event background. The number shown in these figures is event probability density in $5^\circ \times 5^\circ$ pixel.

How well this method works depends on the statistics. At higher energies, due to the repeated use of a few events, the scrambled events probability density is faithful to the real isotropic background only up to a certain zenith angle. From Figure 4.13, some ring structure can be seen. These rings are the results of repeated use of a few zenith angle and randomized azimuth angles and universal time. The other method previously discussed uses Monte-Carlo data to form the (θ, ϕ) data bank; thus it will eliminate the problem of

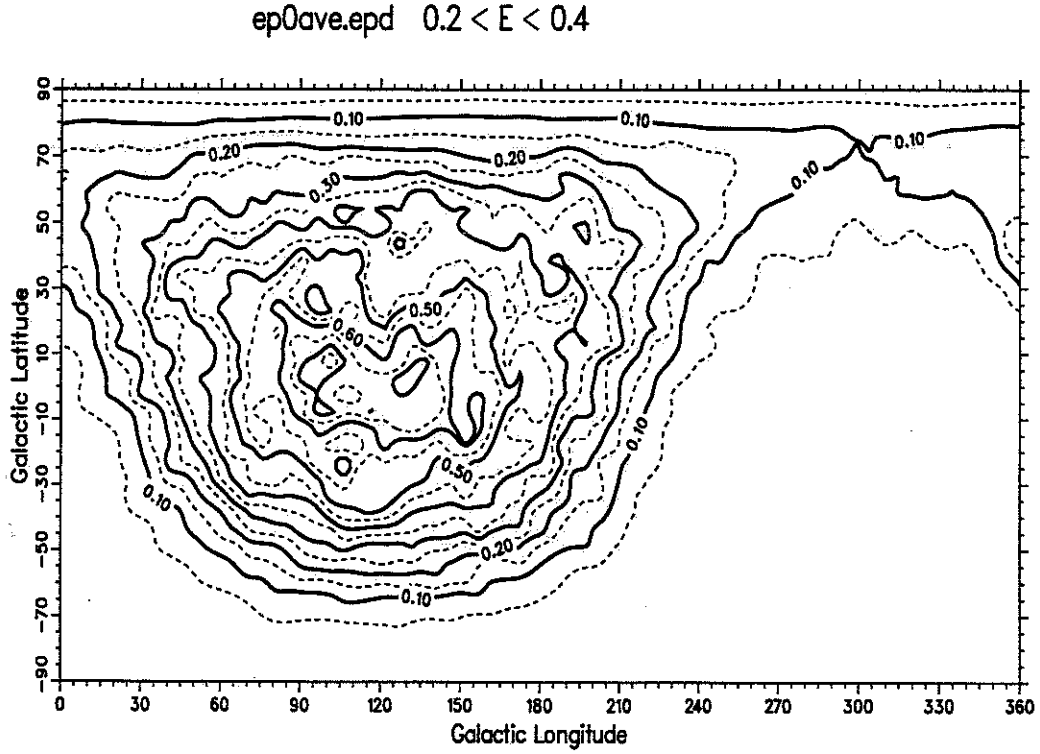

Figure 4.4. Scrambled events background of monocular data for $0.2 \leq E < 0.4 EeV$

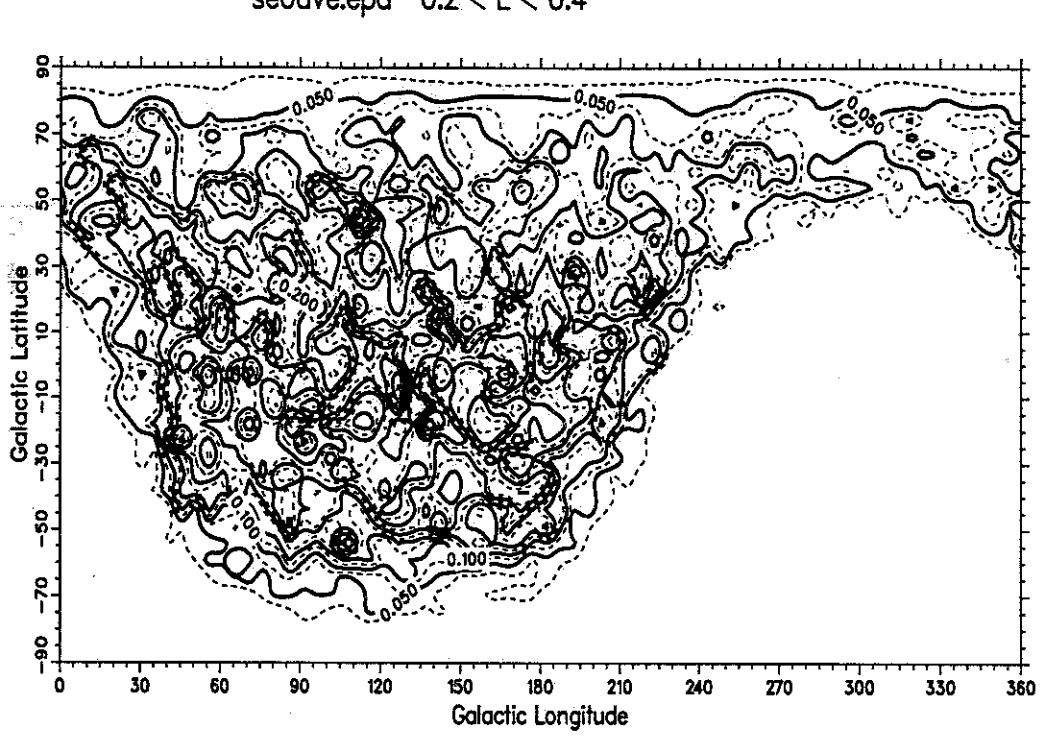

Figure 4.5. Scrambled events background of stereo data for $0.2 \leq E < 0.4 EeV$

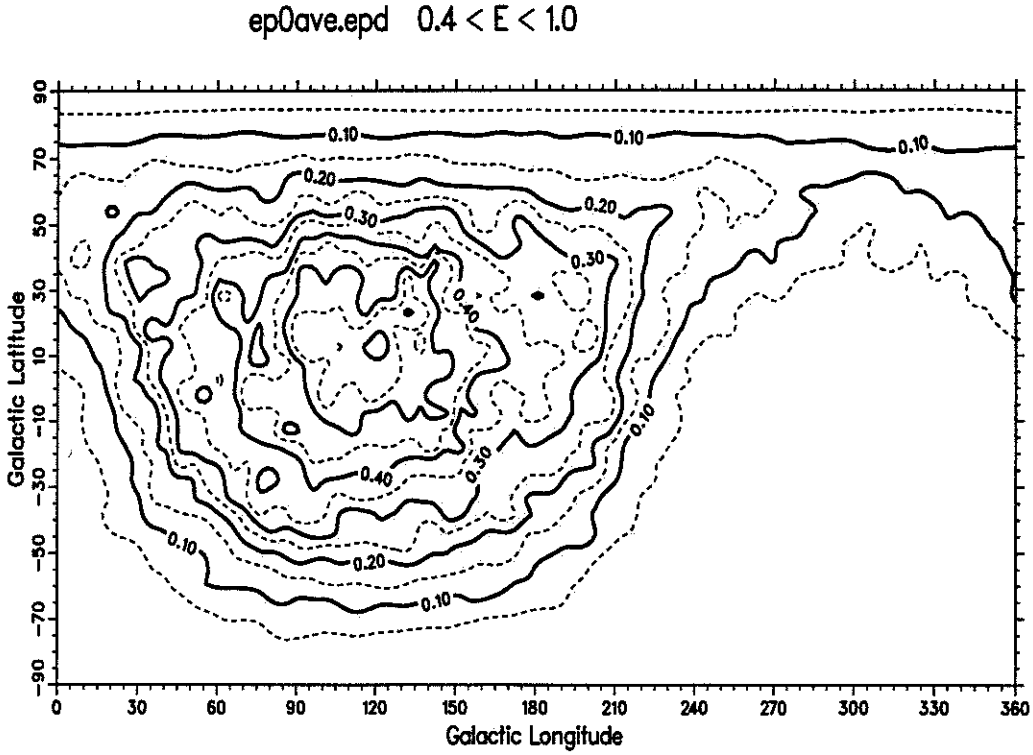

Figure 4.6. Scrambled events background of monocular data for $0.4 \leq E < 1.0 EeV$

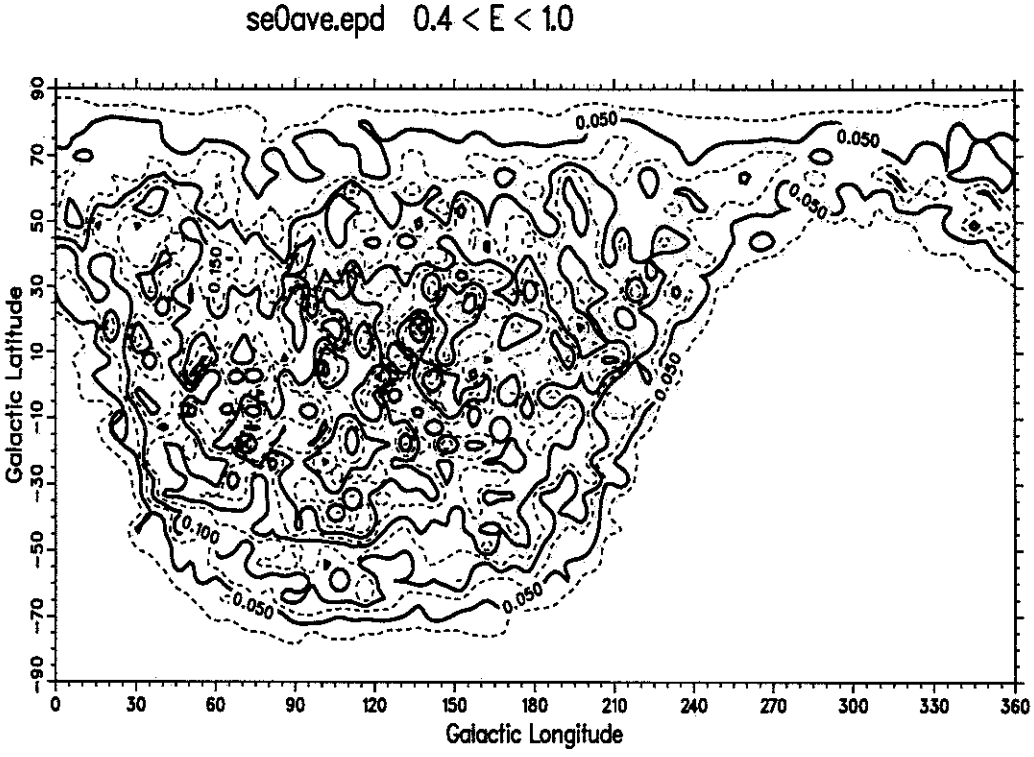

Figure 4.7. Scrambled events background of stereo data for $0.4 \leq E < 1.0 EeV$

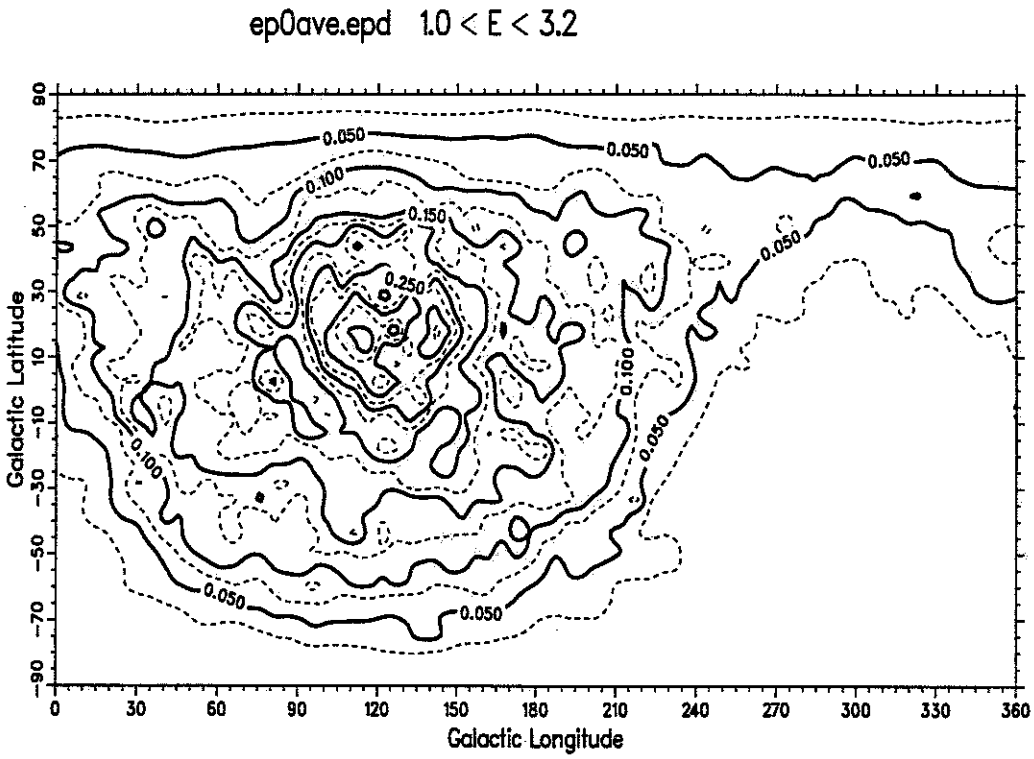

Figure 4.8. Scrambled events background of monocular data for $1.0 \leq E < 3.2 EeV$

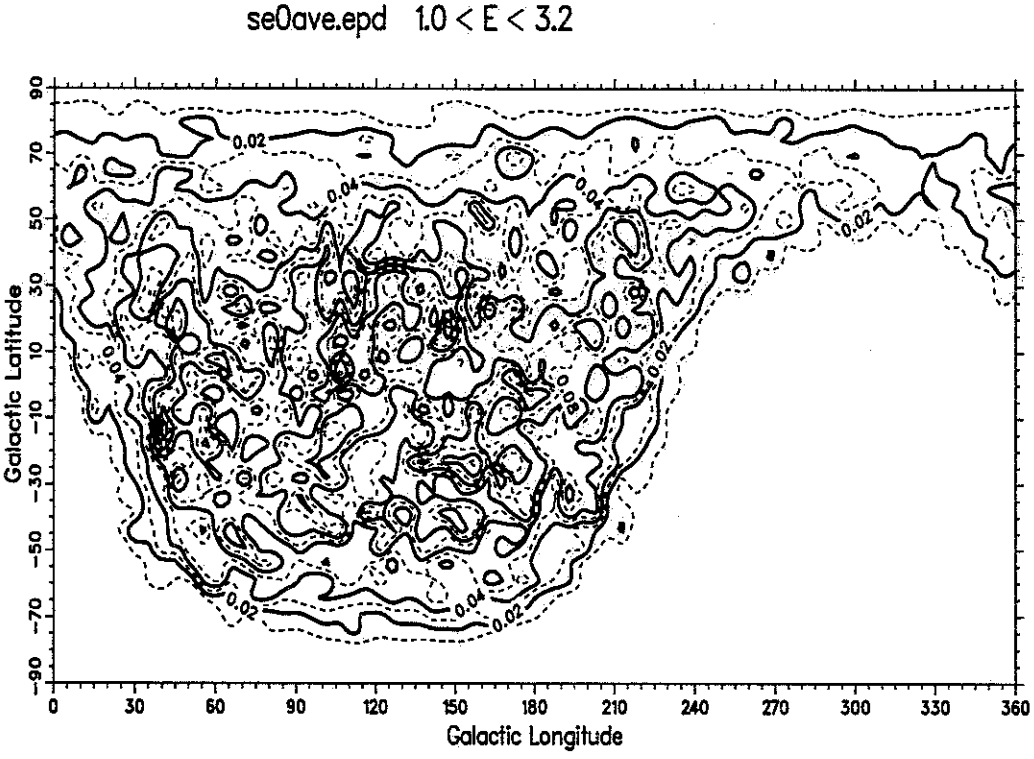

Figure 4.9. Scrambled events background of stereo data for $1.0 \leq E < 3.2 EeV$

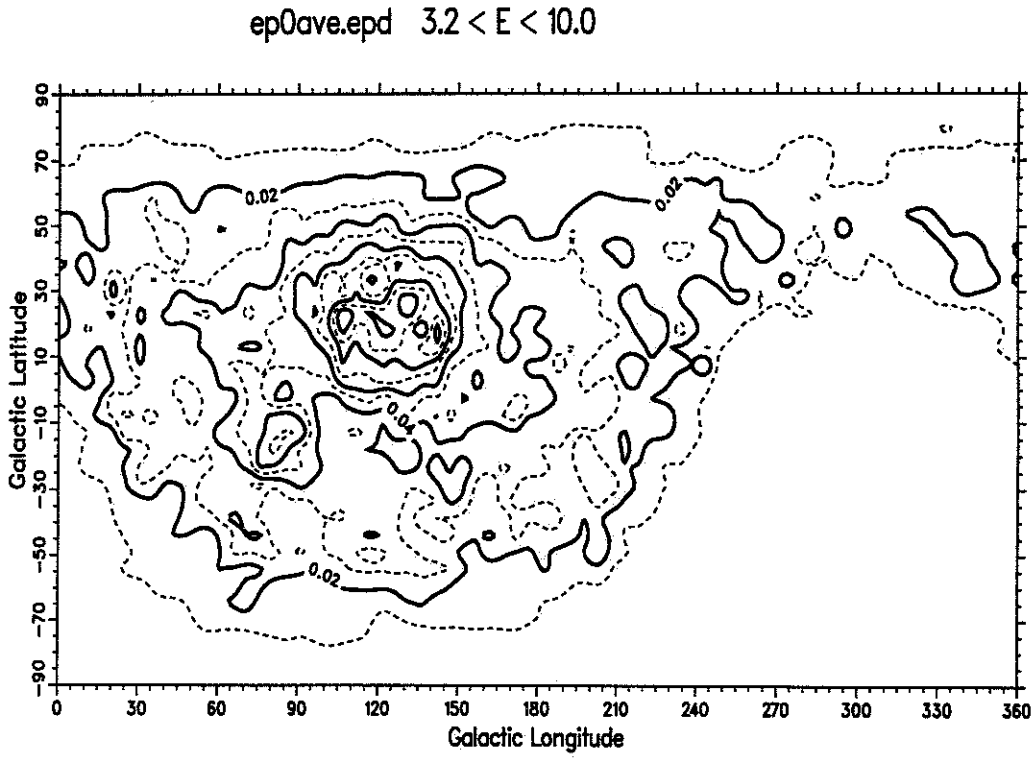

Figure 4.10. Scrambled events background of monocular data for $3.2 \leq E < 10.0 EeV$

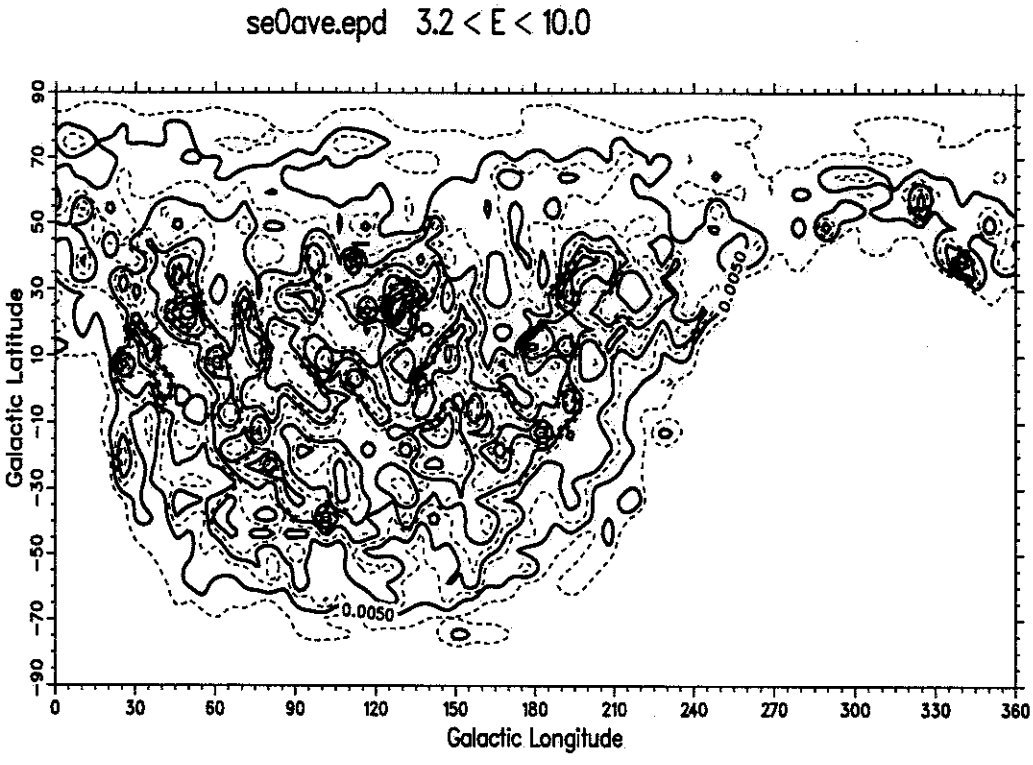

Figure 4.11. Scrambled events background of stereo data for $3.2 \leq E < 10.0 EeV$

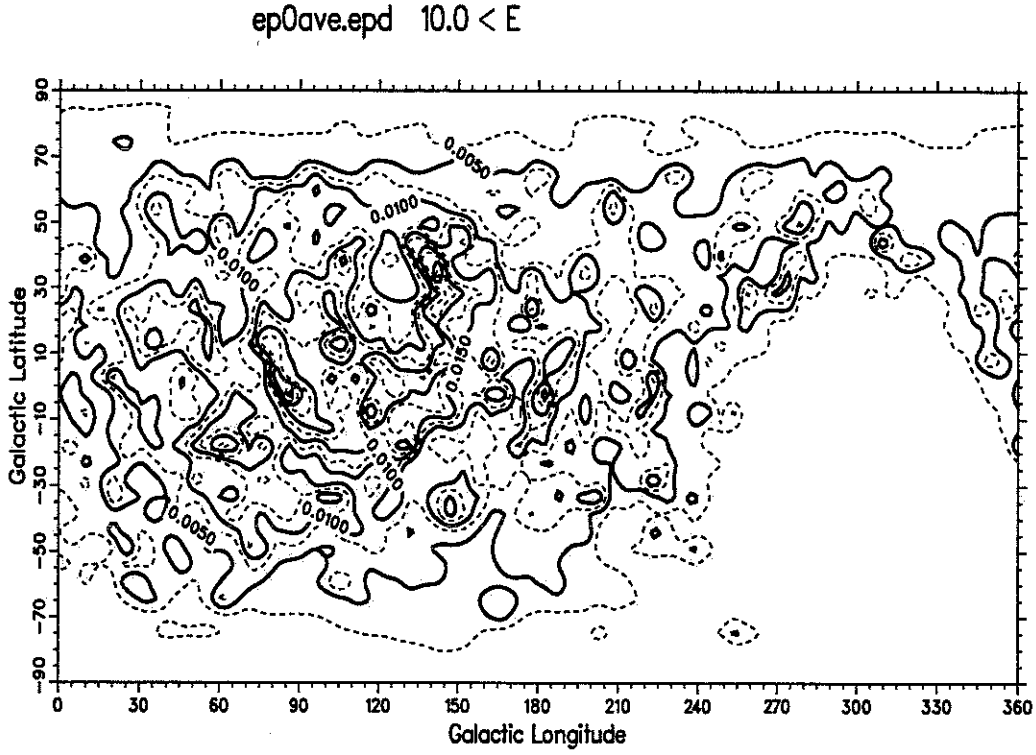

Figure 4.12. Scrambled events background of monocular data for $E \geq 10.0 EeV$

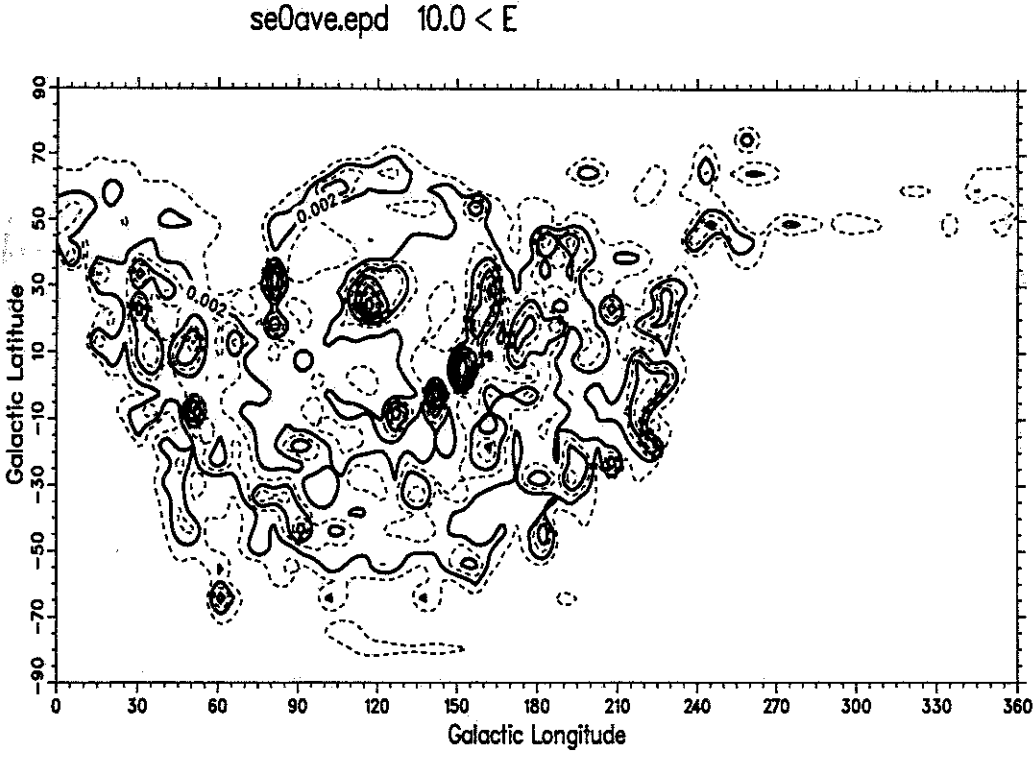

Figure 4.13. Scrambled events background of stereo data for $E \geq 10.0 EeV$

limited statistics. The problem, however, is shifted to knowing that the Monte-Carlo is a good representation of the real detector when there are few events to compare with!? There is no good answer for this question. Since we see some systematic inconsistency between the Monte-Carlo and the real detector, we will use the first method, using real data, to obtain the background.

4.4 Acceptance

Due to the geometric configuration of the detector and position of the shower, the detector has a different efficiency to detect events from different regions of the sky. This efficiency is called the acceptance in this dissertation.

$$A(\theta,\phi,E) = \frac{\text{Event probability density at } (\theta,\phi) \text{ of energy E}}{\text{Total number of events of energy E}} = \frac{P(\theta,\phi,E)}{\sum_{\theta,\phi} P(\theta,\phi,E)}$$

The acceptance is the normalized event probability density in terms of local coordinates (θ,ϕ). Acceptance is sensitive to the data acquisition system. We need enough statistics to reduce random fluctuation; therefore, it is better to collect all data from one epoch to form a data bank and then calculate acceptance. Some of the epochs have similar distributions, for example, epoch 4 and 5, because neither of them has channel 2, the fastest channel which triggers on nearby events. As the shower energy increases, the mean R_p also increases. So for the lower energy events, differences in the detector system play an important role in the θ distribution. We must separate the acceptance for different epochs. Some of the major differences are listed in Table 4.3. For higher energy events, these events are further away from the detector and the differences of the detector system become unimportant. We can sum all epochs to calculate the acceptance at high energy.

4.4.1 Monocular acceptance

Fly's Eye 1 covers the whole range in the azimuth angle; therefore, monocular FE1 data is azimuthally symmetric. We can ignore the dependence on azimuth angle ϕ. The mean value and RMS width of θ and ϕ are listed in Table 4.4. Figure 4.14 plots the θ

Table 4.3. Major differences between epochs. *Yes* means the feature exists in that epoch, *NA* means that the feature is not available.

	Epoch					
Features	1	2	3	4	5	6
UV filter	NA	Yes	Yes	Yes	Yes	Yes
Mirror Anodization	NA	NA	Yes	Yes	Yes	Yes
Channel 2	Yes	Yes	Yes	NA	NA	Yes

and ϕ distribution of monocular data. From the figure and table, the average ϕ is about 181° which is consistent with a symmetric azimuthal distribution.

Because the monocular acceptance depends on the zenith angle θ only, the number of degrees of freedom is 90 ($0^\circ \sim 90^\circ$). To have good quality data, we impose a minimum number of events per number of degree of freedom requirement. This cut is 9 events. In this case, the poisson width is $\sqrt{9} = 3$ and the significance is $9/3 = 3\sigma$. This cut sets the confidence level at 99.7%. The minimum total number of events is $9 \times 90 = 810$.

From Table 4.4, we look for small deviations between epochs in order to find some epochs to form a data bank to calculate acceptance. Table 4.5 lists the groups we used to calculate acceptance. The only group that fails the minimum events number cut of 810

Table 4.4. The mean value and RMS width of azimuth angle ϕ and zenith angle θ of monocular data.

		Energy (EeV)				
	epoch	$0.2-0.4$	$0.4-1.0$	$1.0-3.2$	$3.2-10$	≥ 10
	1	28.1 ± 13.7	31.9 ± 14.2	38.3 ± 15.8	45.0 ± 17.3	48.1 ± 20.1
	2	30.9 ± 13.7	35.2 ± 15.3	40.3 ± 16.6	45.5 ± 17.7	47.1 ± 16.0
$\theta \pm d\theta$	3	32.6 ± 14.2	36.9 ± 15.8	42.2 ± 16.7	47.8 ± 17.4	49.6 ± 17.7
	4	31.6 ± 14.3	37.4 ± 15.7	43.8 ± 16.7	48.7 ± 18.0	50.8 ± 19.1
	5	32.0 ± 13.9	36.9 ± 14.9	43.7 ± 16.6	46.9 ± 19.0	52.0 ± 16.1
	6	33.0 ± 15.4	38.6 ± 17.0	43.5 ± 17.7	44.9 ± 18.4	44.8 ± 17.6
	1	177 ± 101	181 ± 105	184 ± 104	172 ± 103	163 ± 103
	2	177 ± 103	179 ± 105	187 ± 105	178 ± 104	178 ± 98
$\phi \pm d\phi$	3	181 ± 106	181 ± 102	178 ± 102	184 ± 99	194 ± 108
	4	181 ± 103	184 ± 103	181 ± 103	181 ± 105	184 ± 98
	5	185 ± 101	180 ± 103	185 ± 106	176 ± 111	191 ± 110
	6	182 ± 102	183 ± 104	176 ± 103	182 ± 101	194 ± 104

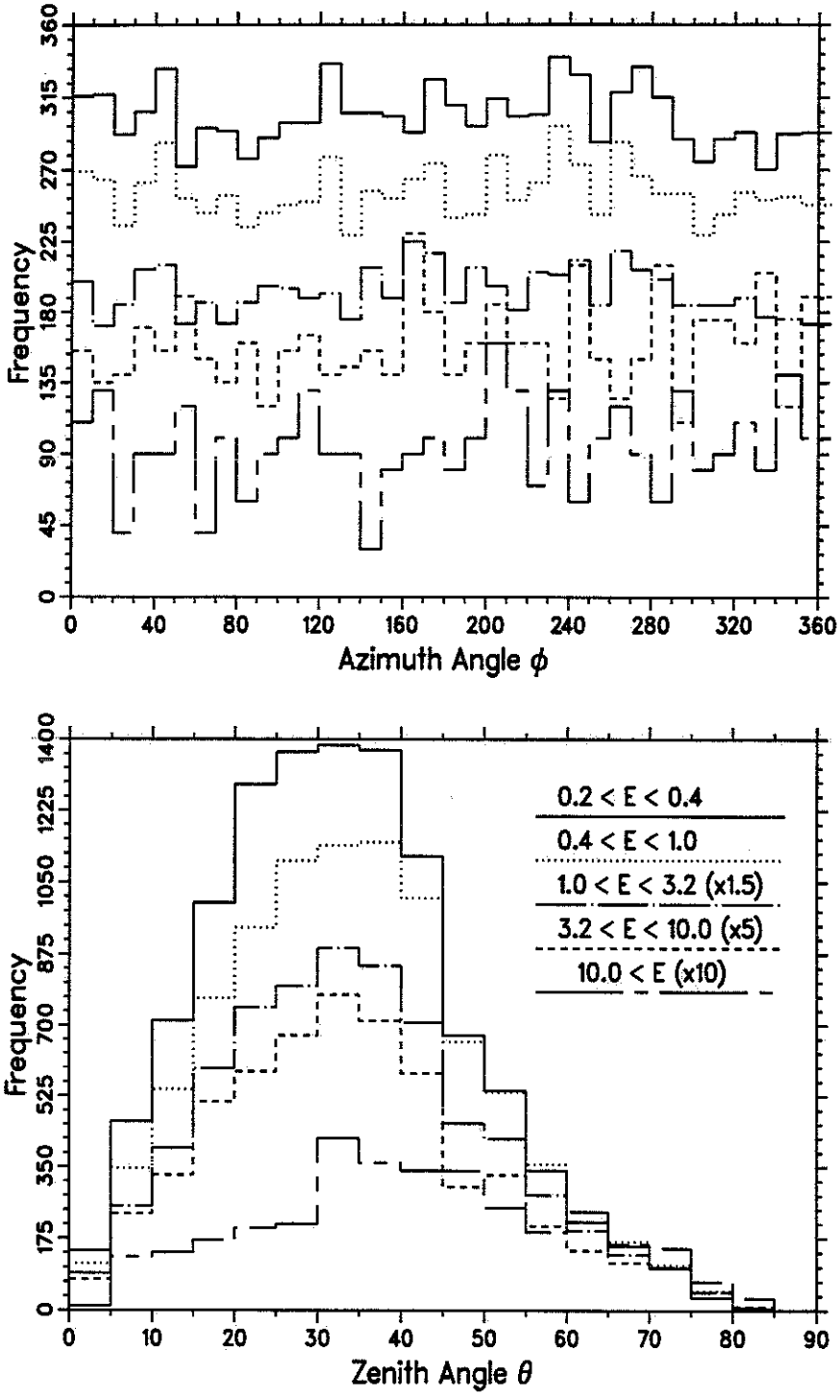

Figure 4.14. The θ and ϕ distribution of monocular data. Notice that the distributions of energy bin $1.0 < E < 3.2EeV$, $3.2 < E < 10EeV$, and $E > 10EeV$ are multiplied by 1.5, 5., and 10. respectively.

is the highest energy interval. It has only 341 events. In this case, the confidence level is $\sqrt{341} = 1.95\sigma$, or 94.9%. It is still good enough.

Figure 4.15 shows the monocular acceptance of epoch 3. As the energy increases, the system has higher efficiency at high zenith angle.

4.4.2 Stereo acceptance

Because FE2 covers only part of the sky facing FE1, the stereo data is not azimuthally symmetric. The mean value and RMS width of θ and ϕ are listed in Table 4.6. Figure 4.16 shows the θ and ϕ distribution of the stereo data. Because of the FE1 - FE2 configuration, the collecting area is an ellipse with a major axis 150° off the east. But as the energy

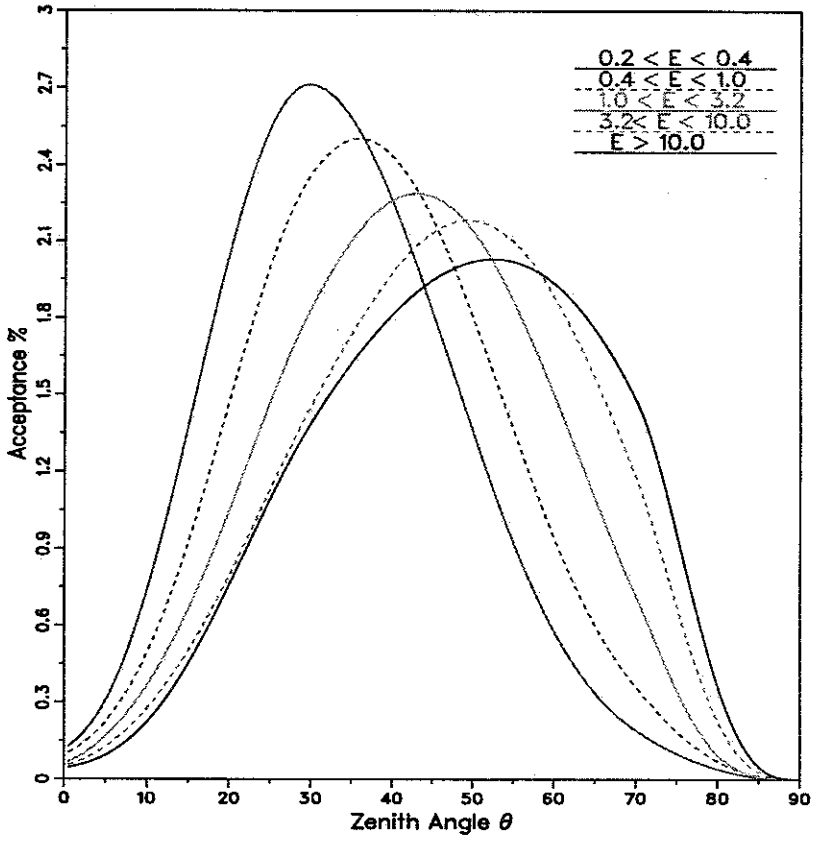

Figure 4.15. Monocular acceptance of epoch 3. Those five lines represent five energy intervals and the are under the curves are normalized to 100%.

Table 4.5. Groups of epochs for monocular acceptance.

Energy	Group of epochs			
0.2 - 0.4	1	2	(3,6)	(4,5)
0.4 - 1.0	1	2	(3,4,5)	6
1.0 - 3.2	1	2	3	(4,5,6)
3.2 - 10.0	(1-6)			
$\geq$ 10.0	(1-6)†			

† : number of events below 810

increases, the collecting area extends outward and the difference between the major and minor axes decreases; therefore, the difference between maximum and minimum acceptance decreases. When the shower coming from near $\phi = 60°$, parallel to the line of FE1 and FE2, the Čerenkov contamination is severe and most of these events will be cut out.

Because the stereo acceptance depends on the zenith angle θ and azimuth angle ϕ, the degree of freedom is $2\pi/\delta A = 2\pi/(1° \times 1°) = 20627$. But the total number of stereo events is only 11674! Using the PMT size, the δA can be replaced by effective area, $\delta A = \pi \times 5.5^2/4 = 23.8$, so the degree of freedom is about $20626.5/23.8 \simeq 868$. Because of this high degree of freedom, we will not enforce the cut on the minimum number of events. Originally, we wanted to use Monte-Carlo to find the acceptance, but

Table 4.6. The mean value and RMS width of azimuth angle ϕ and zenith angle θ of stereo data.

		Energy (EeV)				
	epoch	$0.2 - 0.4$	$0.4 - 1.0$	$1.0 - 3.2$	$3.2 - 10$	≥ 10
$\theta \pm d\theta$	2	29.8 ± 11.9	34.0 ± 12.5	37.7 ± 14.3	39.3 ± 14.4	35.9 ± 9.8
	3	32.1 ± 12.7	34.9 ± 13.7	36.9 ± 14.4	36.4 ± 15.3	41.1 ± 13.2
	4	30.7 ± 12.5	34.7 ± 13.7	37.3 ± 14.7	36.2 ± 15.6	40.4 ± 15.5
	5	30.5 ± 12.7	34.4 ± 13.5	36.4 ± 14.2	37.4 ± 15.2	39.8 ± 16.2
	6	31.9 ± 12.9	36.0 ± 13.7	37.5 ± 14.6	38.3 ± 15.7	38.0 ± 21.9
$\phi \pm d\phi$	2	197 ± 97	189 ± 103	196 ± 108	190 ± 100	227 ± 110
	3	202 ± 94	196 ± 97	197 ± 97	178 ± 89	161 ± 127
	4	194 ± 97	195 ± 98	189 ± 98	200 ± 101	189 ± 85
	5	198 ± 100	195 ± 96	196 ± 99	193 ± 104	209 ± 92
	6	192 ± 95	195 ± 96	195 ± 99	199 ± 92	279 ± 74

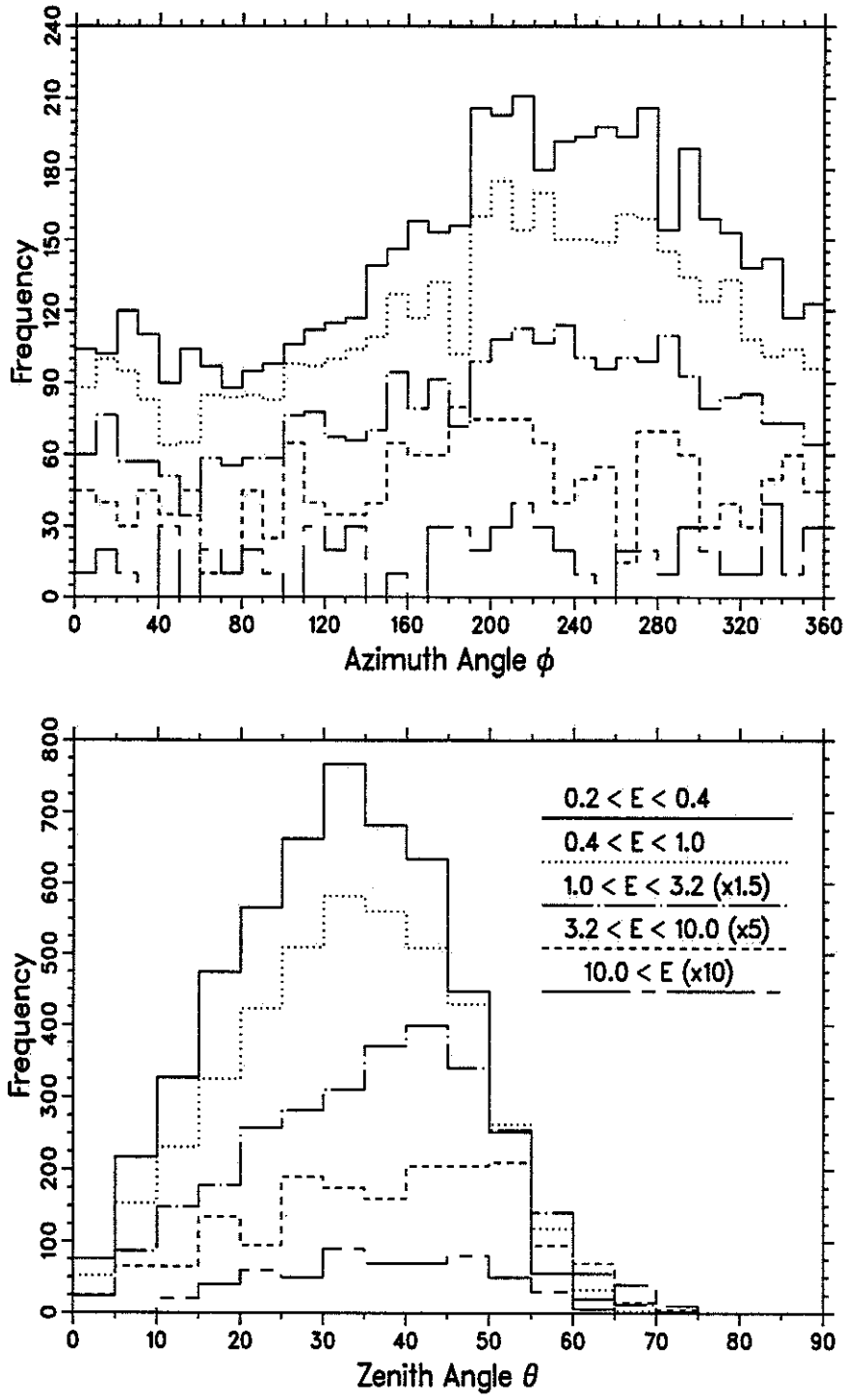

Figure 4.16. The θ and ϕ distribution of epoch 3 stereo data. Notice that the distributions of energy bin $1.0 < E < 3.2EeV$, $3.2 < E < 10EeV$, and $E > 10EeV$ are multiplied by 1.5, 5., and 10. respectively.

due to some systematic differences between the data and Monte-Carlo, we prefer using something faithful to the data. As a result, the stereo acceptance is valid only in large scale and some systematic errors are inevitable due to low statistics.

From Table 4.6, we look for small deviations between epochs in order to find some epochs to form a data bank to calculate acceptance. Table 4.7 lists the groups we used to calculate acceptance. Figures 4.17 to 4.21 show the contour plots of the stereo acceptance (in $5^\circ \times 5^\circ$ pixel) of epoch 3 data.

4.5 Live Time

4.5.1 System run time

The data acquisition system starts to record data from the time the system is permitted and stops taking data when the system is inhibited. The live time of the detector is recorded in the raw data file *mMMdDDpPP.scn*. However it is not available in the final shape files. During the operation of Fly's Eye, a weather code is input to the computer when the data acquisition starts and is then entered each hour on the hour by the operator. This process is illustrated in Figure 4.22. In the previous analysis, we used the weather code to cut out bad weather data and live time. We also used the time of the first weather code as the system permit time and the time of the last weather code as system inhibit time. The time of the first weather code could be before or after system permit (normally before the permit), and the time of the last weather code could be ahead of the system inhibit for up to almost one hour. Using the weather code, accidentally we gain a couple minutes at the beginning of the run and lose about 1/2 hour at the end. Sometimes the

Table 4.7. Groups of epochs for Stereo acceptance.

Energy	Group of epochs			
0.2 - 0.4	2†	3	(4,5)	6†
0.4 - 1.0	2†	(3,4,5)	6†	
1.0 - 3.2	(2-6)			
3.2 - 10.0	(2-6)†			
$\geq$ 10.0	(2-6)†			

† : number of events below 868

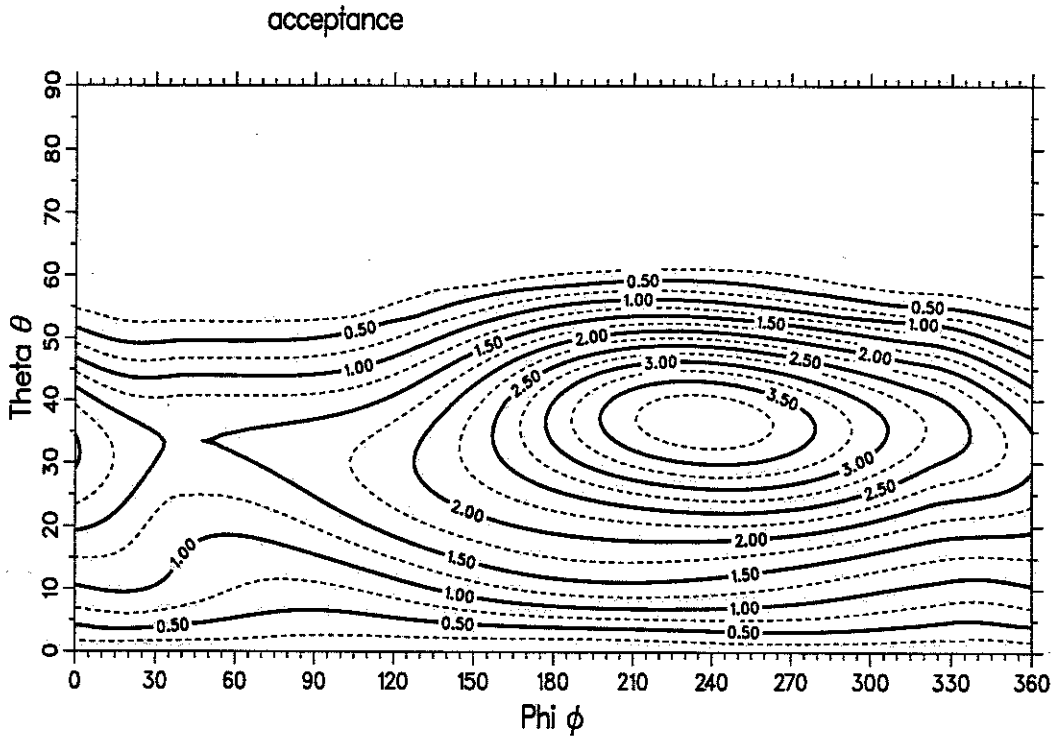

Figure 4.17. Stereo acceptance of epoch 3 at energy $0.2 - 0.4 EeV$

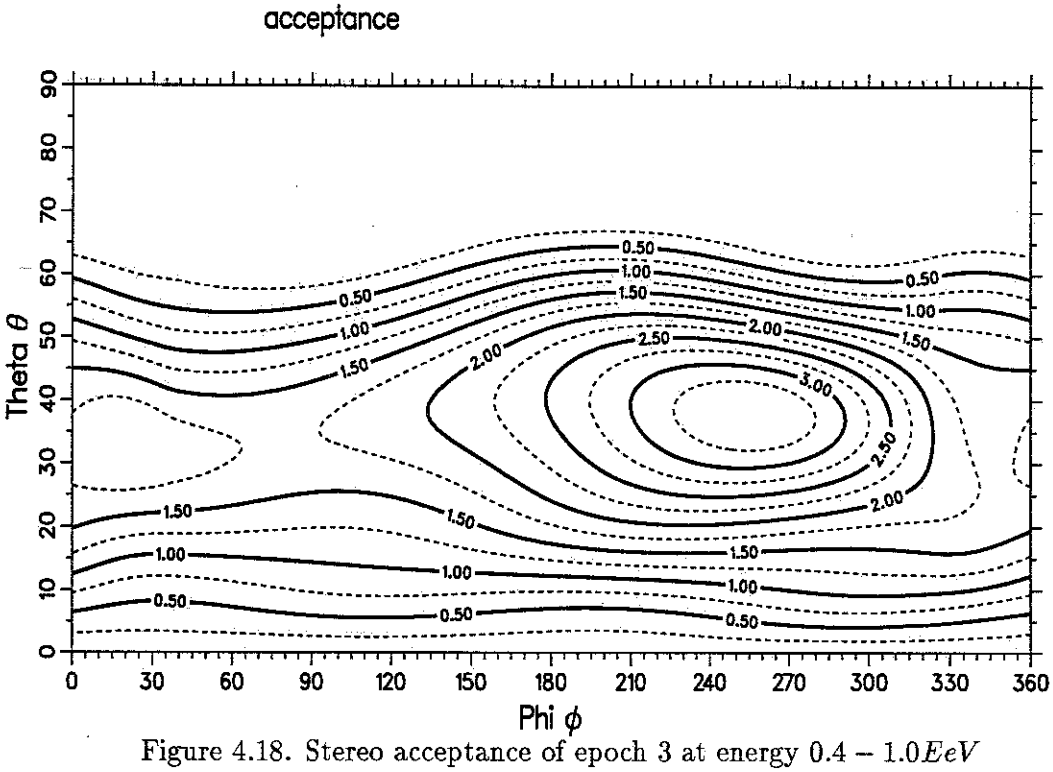

Figure 4.18. Stereo acceptance of epoch 3 at energy $0.4 - 1.0 EeV$

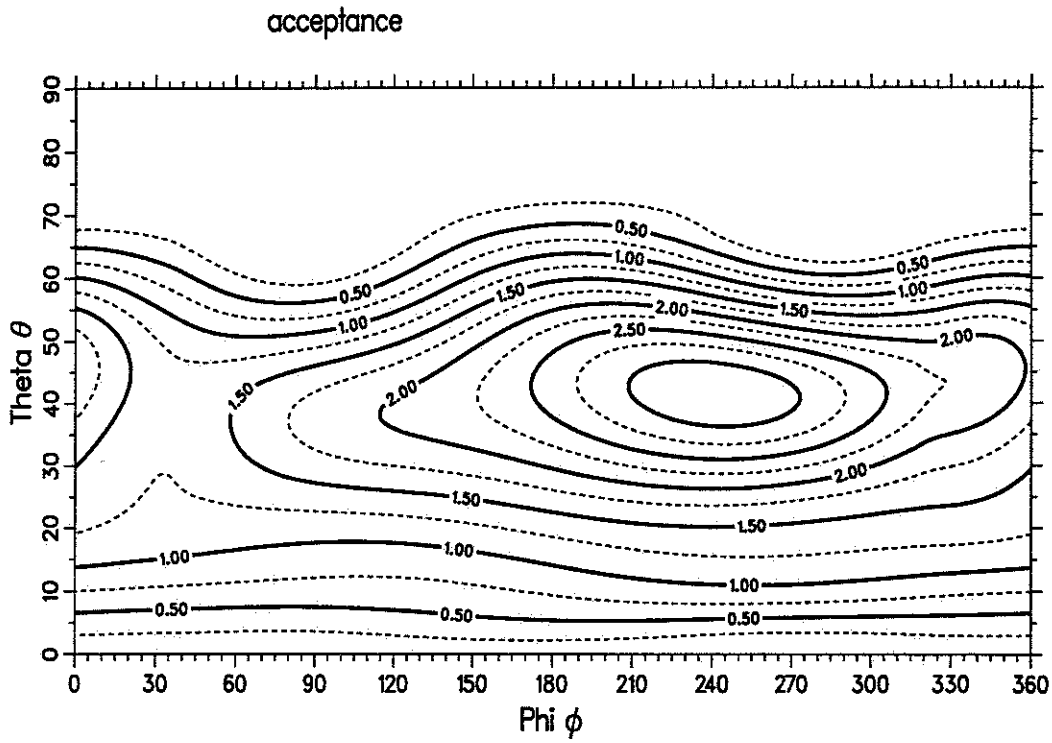

Figure 4.19. Stereo acceptance of all epochs at energy $1.0 - 3.2 EeV$

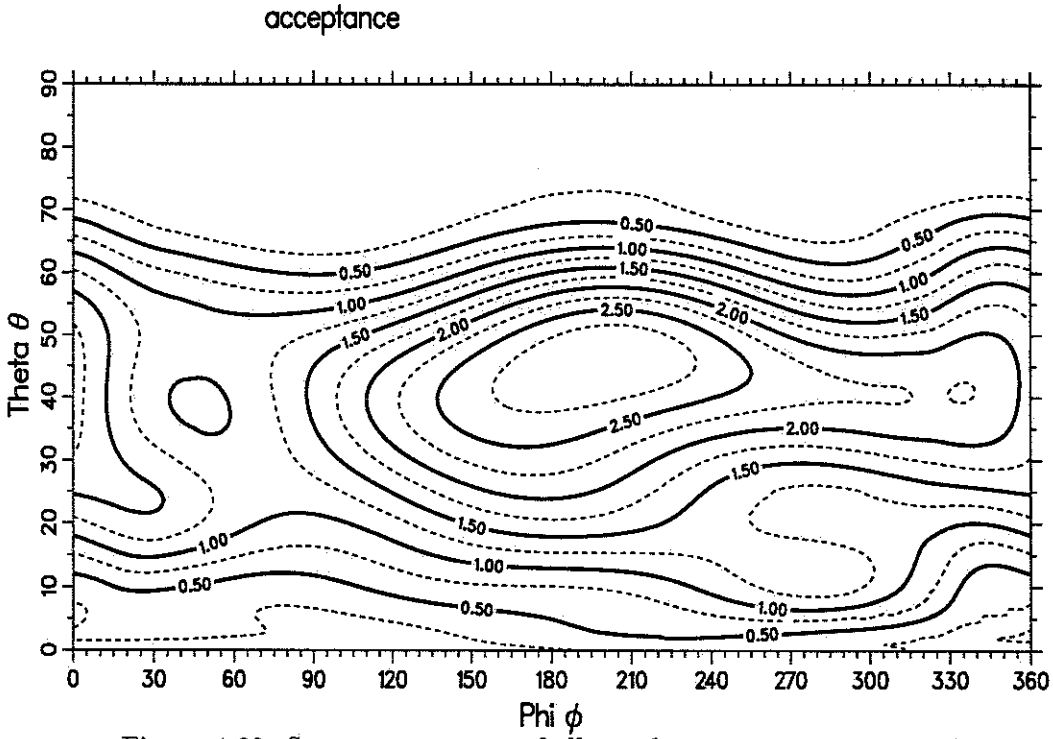

Figure 4.20. Stereo acceptance of all epochs at energy $3.2 - 10.0 EeV$

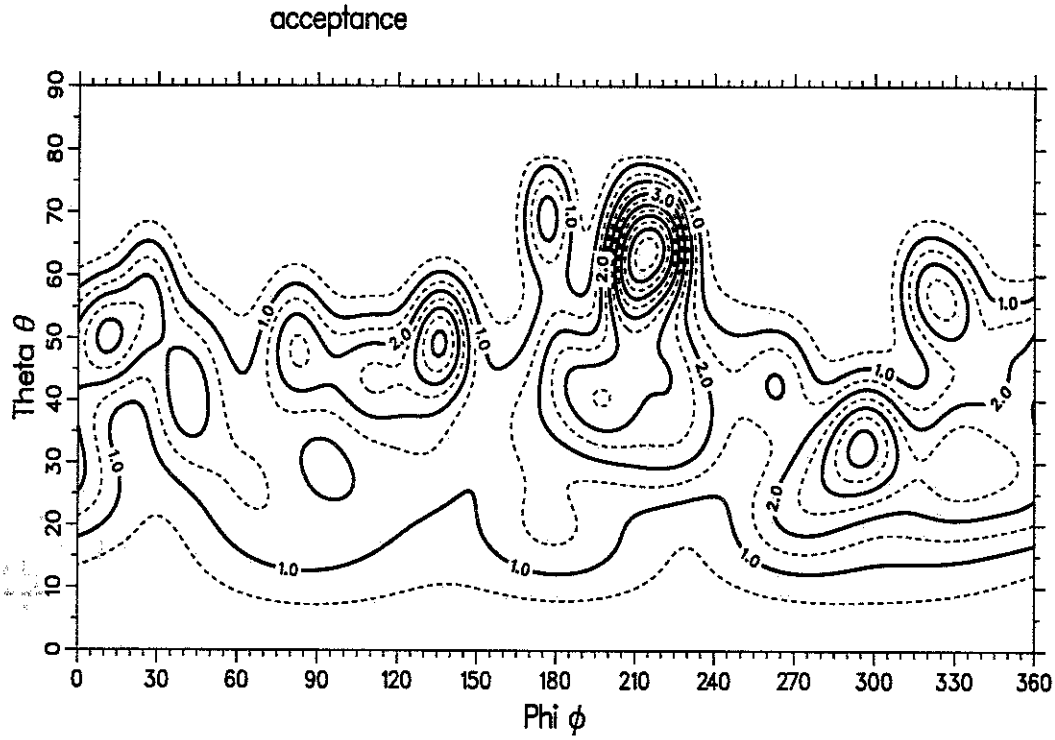

Figure 4.21. Stereo acceptance of all epochs at energy $\geq 10.0 EeV$

data are separated into several parts which could have no weather code before the system permits. This is not a good algorithm!

Instead of using the weather code time, I tried to recover the permit/inhibit time from the trigger frequency. The Fly's Eye triggers at a constant rate, so the inverse of the trigger rate is the mean separation time, ΔT, between events. Theoretically, the first trigger happens at approximately ΔT after the system is permitted, and the system is inhibited at approximately ΔT after the last trigger. However, the shape files keep only successfully reconstructed events, not the raw triggers. Even the trigger rate is not a good indicator because sometimes the sky or system is noisy and the electronic thresholds change over time. Therefore we must use the successfully reconstructed event rate instead of the trigger rate. This method could predict the permit/inhibit time with an error of less than ten minutes. Besides, the weather could cause the good event rate drop quite large but noise would still keep the system running at constant rate. The detection efficiency will certainly decrease significantly in this case and it would not be reflected in the old

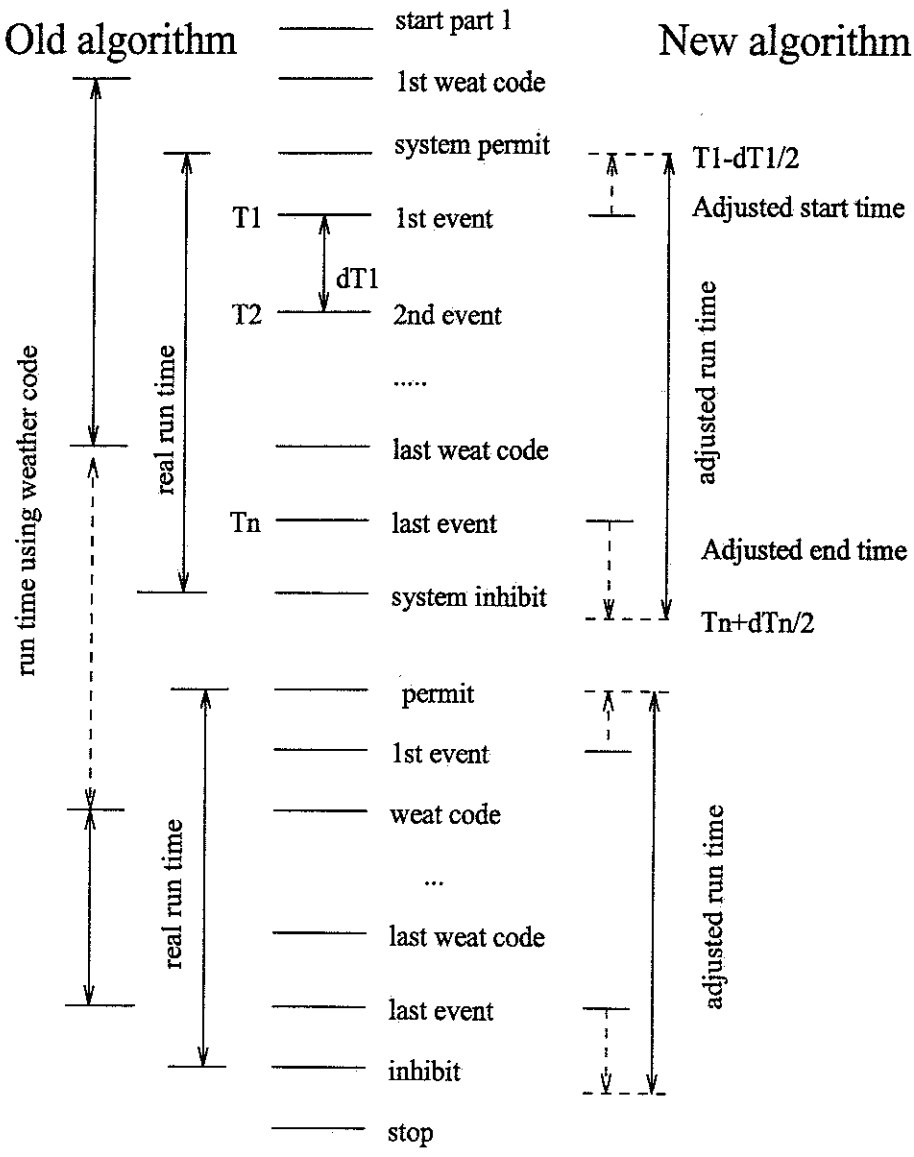

Figure 4.22. Algorithm of system run time determination.

algorithm or by using the trigger rate. The successfully reconstructed event rate could be a good indicator of the overall condition of the weather and the system.

The prediction of permit/inhibit time and event rate are calculated by program *ontime.f*. It first identifies different parts by the separation time between events, i.e., if this time is greater than 1.5 hours, it separates the events into different parts. The mean event rates (within $\pm$15minutes) are calculated. The separation time is checked; if it is longer than expected time from mean event rate, the events are separated into

different parts again. This procedure helps to reduce some parts separated less than 1.5 hours. Some mistakes will be introduced here, such as having only one event within one hour; however, this extrreme case will not affect our background prediction too much because the event rate is so low that we can safely ignore the time between events and count it only as several minutes around that event. Statistically, it would be very similar to exposure for a long time with low rate or to exposure for a short time with proper rate.

After events are separated into parts, the permit/inhibit time is calculated from the mean event rate. Both time and rate are written into a file **.ontime* to be used in live time background prediction. Figure 4.23 shows the event rate and reconstructed on/off time of the November 1988 stereo data. Table 4.8 lists the system on time of both monocular and stereo data based on the new algorithm.

Table 4.8. The total run time of all epochs. The unit is Julian day.

	Monocular Data		**Stereo Data**	
epoch	Date	run time	Date	run time
1	11/81 - 05/85	74.59157		
2	11/85 - 07/87	50.72216	11/86 - 06/87	17.50593
3	08/87 - 06/88	35.31582	07/87 - 06/88	32.82493
4	07/88 - 04/90	55.27137	07/88 - 04/90	50.58574
5	05/90 - 09/91	30.29416	05/90 - 09/91	25.97057
6	10/91 - 07/92	19.42440	10/91 - 07/92	15.92968
	Total	**265.61948**		**142.81686**

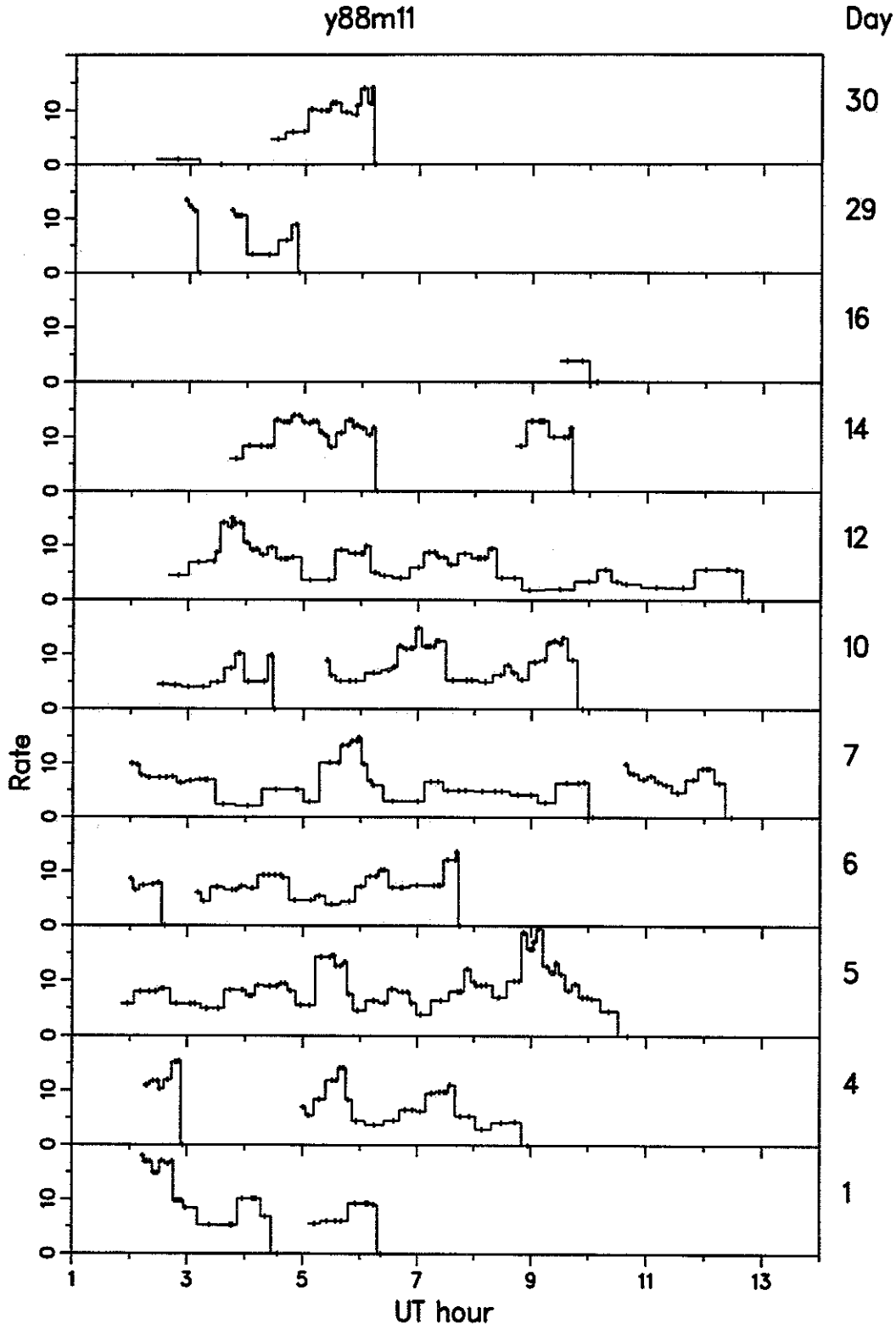

Figure 4.23. The event rate as function of universal time of November 1988 stereo data.

4.5.2 Live time background

The live time background is defined by acceptance and event rate weighted live time

$$liv(l,b,E) = \int_{T_{on}}^{T_{off}} R(T)\, A(\theta,\phi,E)\, \Omega(l,b,\theta,\phi,T)\, dT$$

where *liv* is acceptance weighted live time of longitude l and latitude b at energy E, $R(T)$ is the successfully reconstructed event rate at time T. $A(\theta,\phi)$ is acceptance, the geometric efficiency which is the relative ability to detect events from a certain θ and ϕ. Ω is a coordinate transformation which finds the θ and ϕ for (l,b) at time T.

The program *livtime.f* calculates the live time background and writes to file **.liv*. In order to have a pixel size of 1°, the step size of time dT is chosen as 4 minutes. It is a massive task to calculate 360 × 180 pixels for every 4 minutes of run time. The price is worth it since it produces a smooth background and is faithful to the limit of the visible sky.

$R(T)$ is introduced in this background calculation for the first time. It not only makes the formula dimensionally correct but also reflects the dynamic variation of the data acquisition system and the weather conditions.

After the *livetime*, the live time of each pixel should be proportional to the event probability density. A normalization to the total number of events is necessary so that the value of each pixel represents the same meaning as the event probability density. For each epoch, we sum up all monthly **.liv* and then normalize to the total number of events. Because the monthly number of events fluctuates more than the number of events of each epoch, it is better to normalize to the whole epoch rather than to individual months. This method introduces some differences between monthly event probability density *mMMdDD.epd* and live time *mMMdDD.liv*. The normalized data are overwritten to the same file. Figures 4.24 to 4.33 show the contour map of live time backgrounds.

The advantage of live time background is the smooth transition. The disadvantage is the lack of knowledge of fluctuation. Although Poisson distribution can be used to predict the fluctuation, it is not faithful to the real world when the event probability is very small. We still need scrambled event backgrounds in order to understand the fluctuation of background.

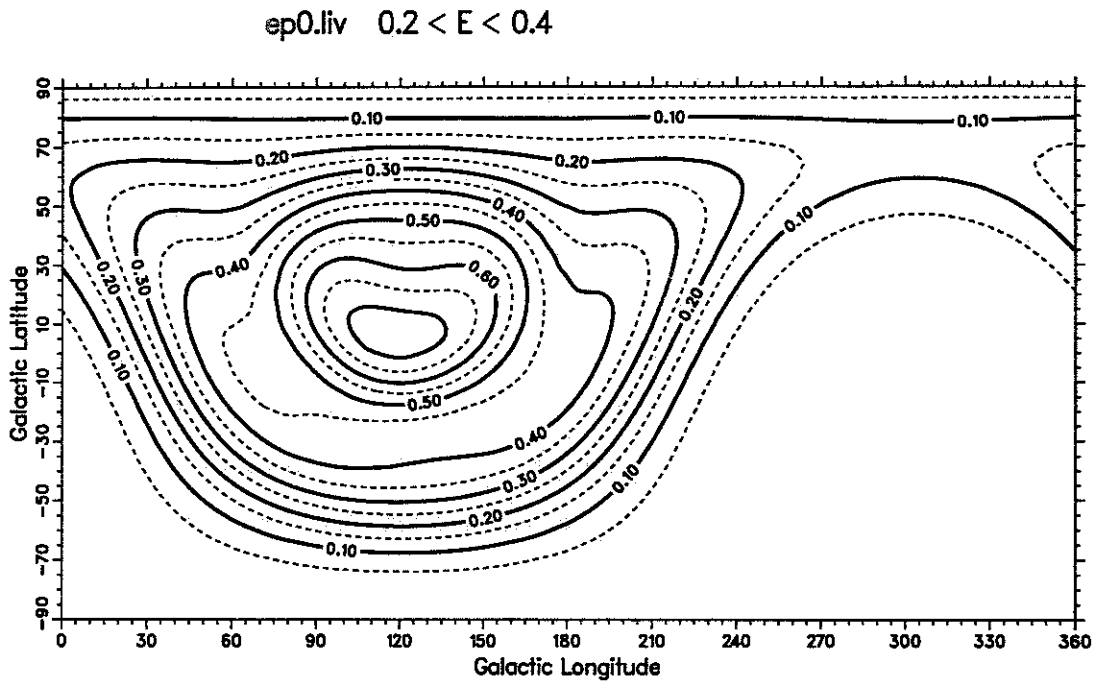

Figure 4.24. Live time background of monocular data for $0.2 \leq E < 0.4 EeV$

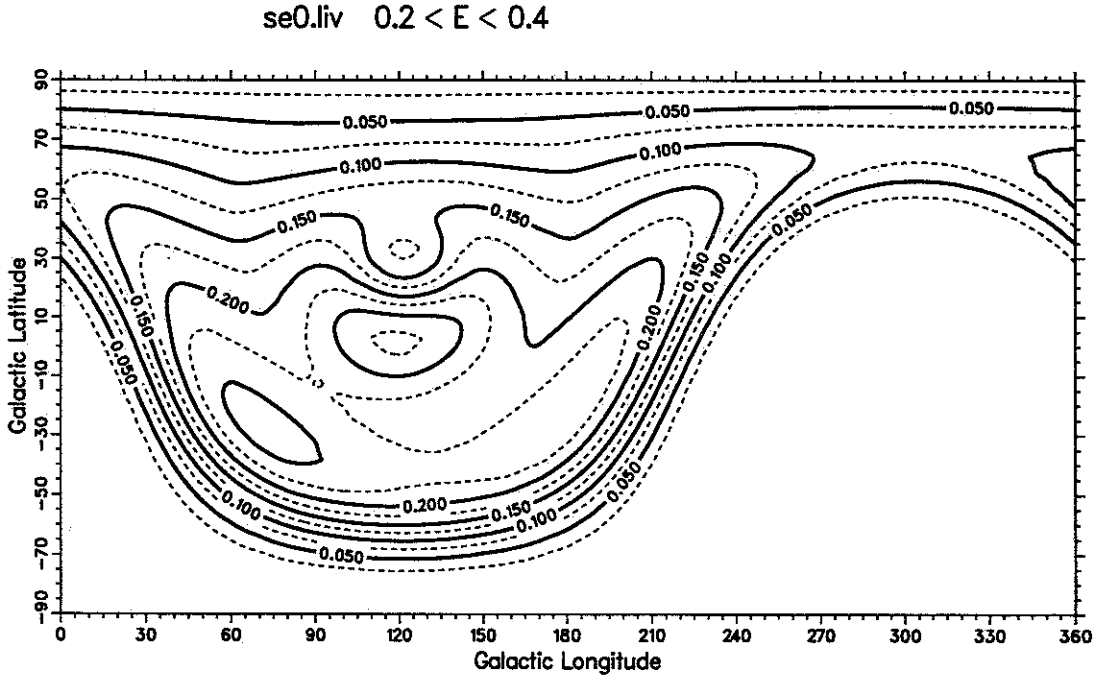

Figure 4.25. Live time background of stereo data for $0.2 \leq E < 0.4 EeV$

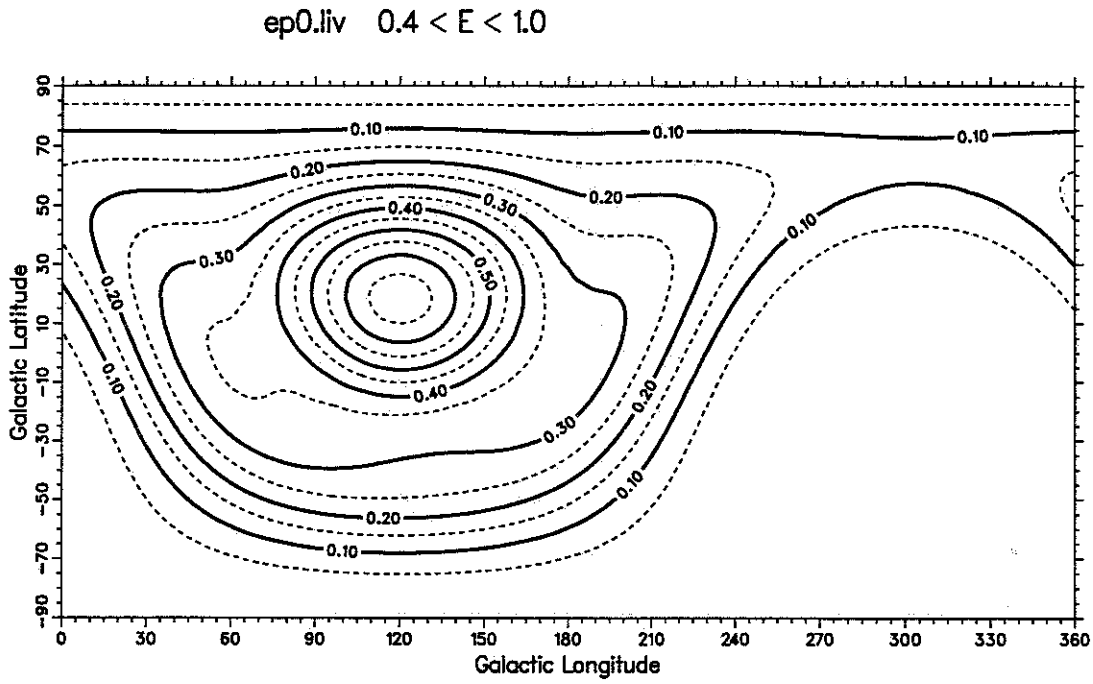

Figure 4.26. Live time background of monocular data for $0.4 \leq E < 1.0 EeV$

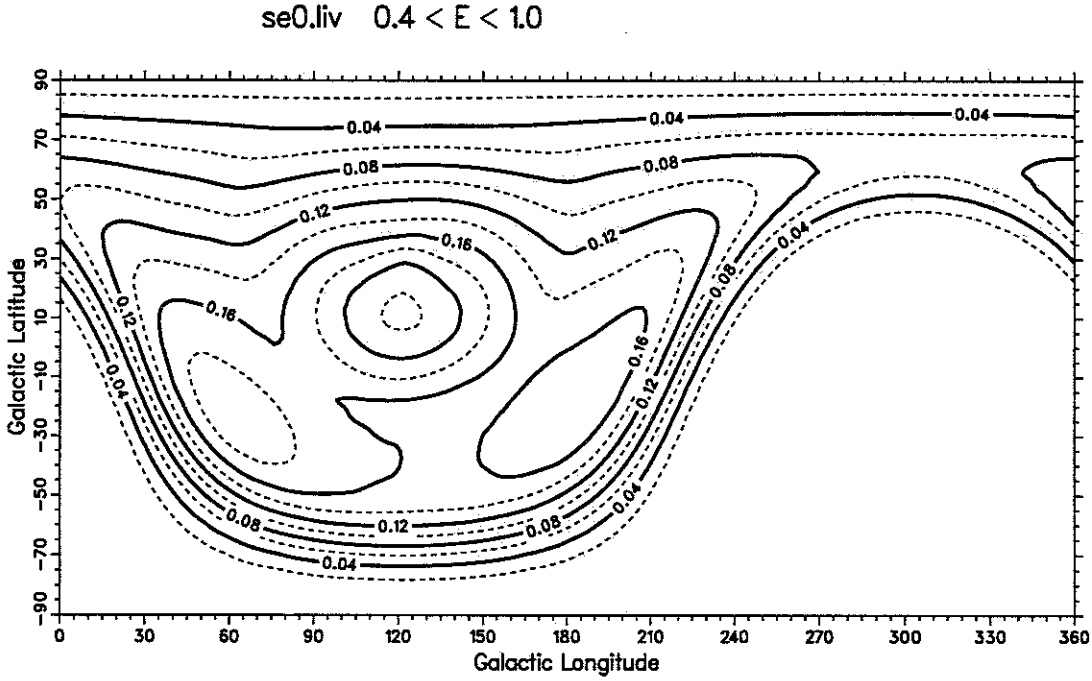

Figure 4.27. Live time background of stereo data for $0.4 \leq E < 1.0 EeV$

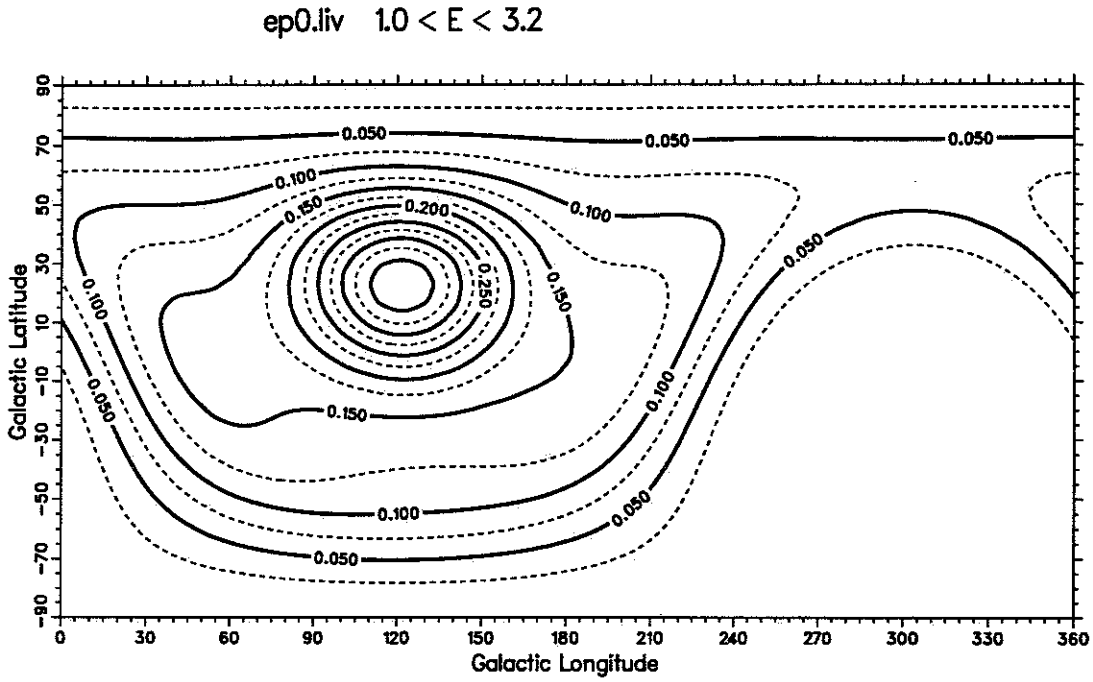

Figure 4.28. Live time background of monocular data for $1.0 \leq E < 3.2 EeV$

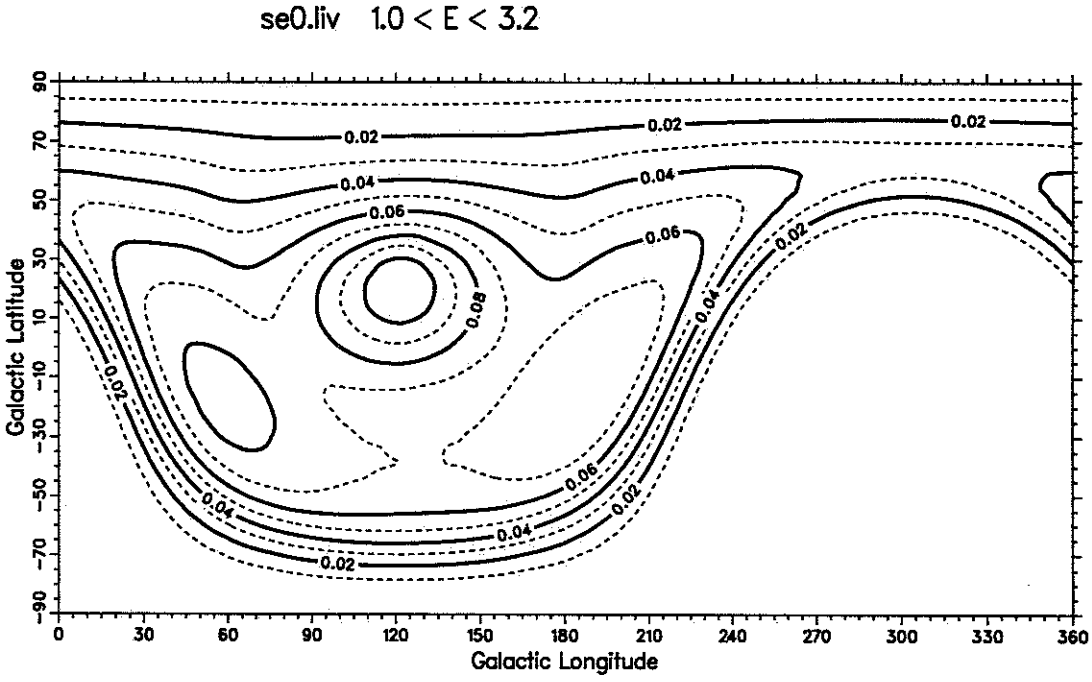

Figure 4.29. Live time background of stereo data for $1.0 \leq E < 3.2 EeV$

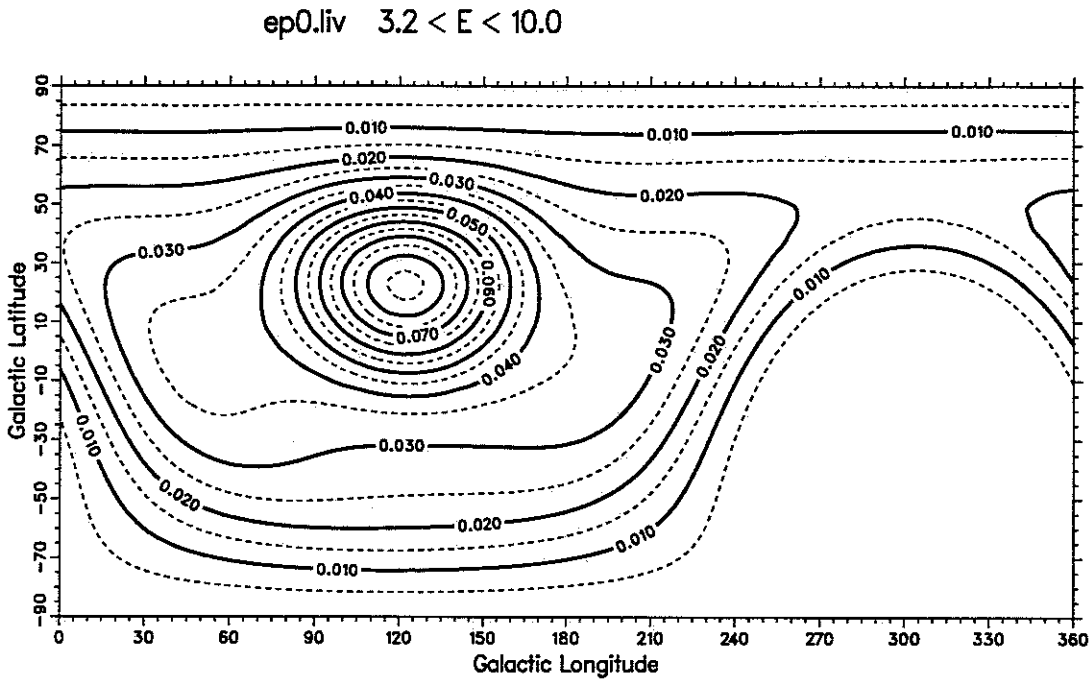

Figure 4.30. Live time background of monocular data for $3.2 \leq E < 10.0 EeV$

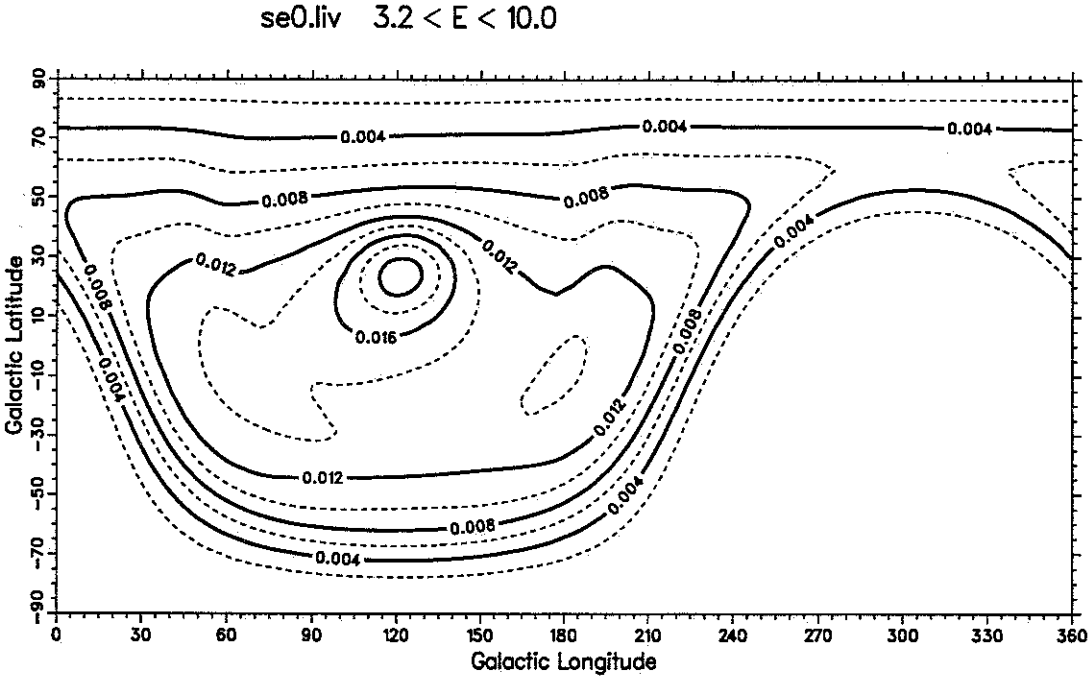

Figure 4.31. Live time background of stereo data for $3.2 \leq E < 10.0 EeV$

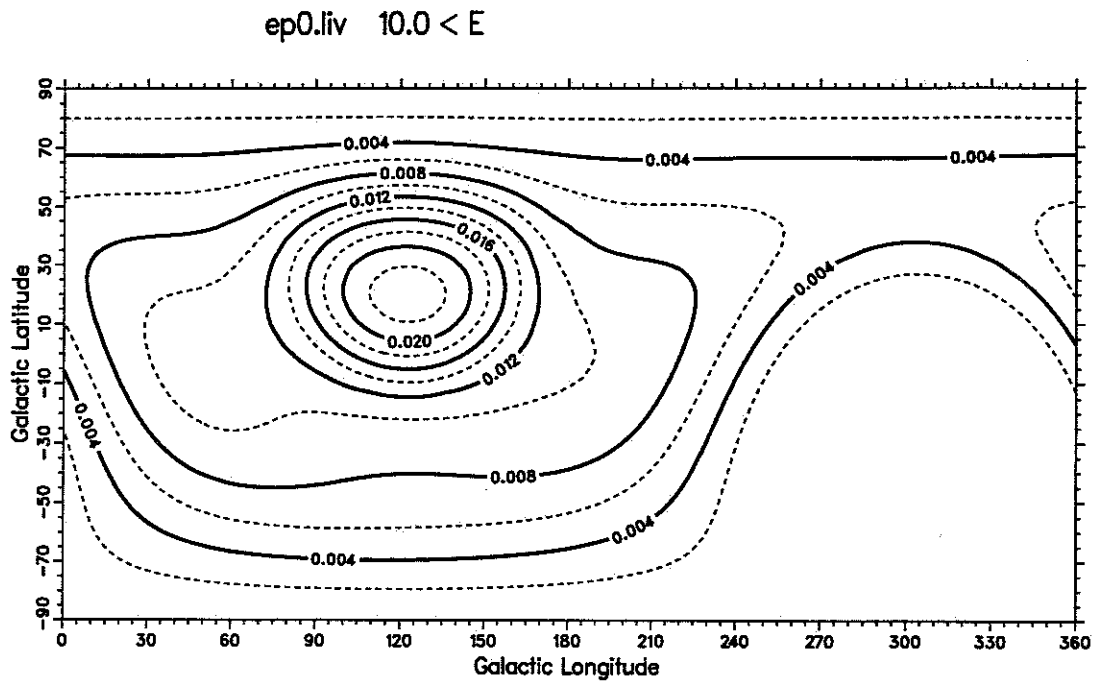

Figure 4.32. Live time background of monocular data for $E \geq 10.0 EeV$

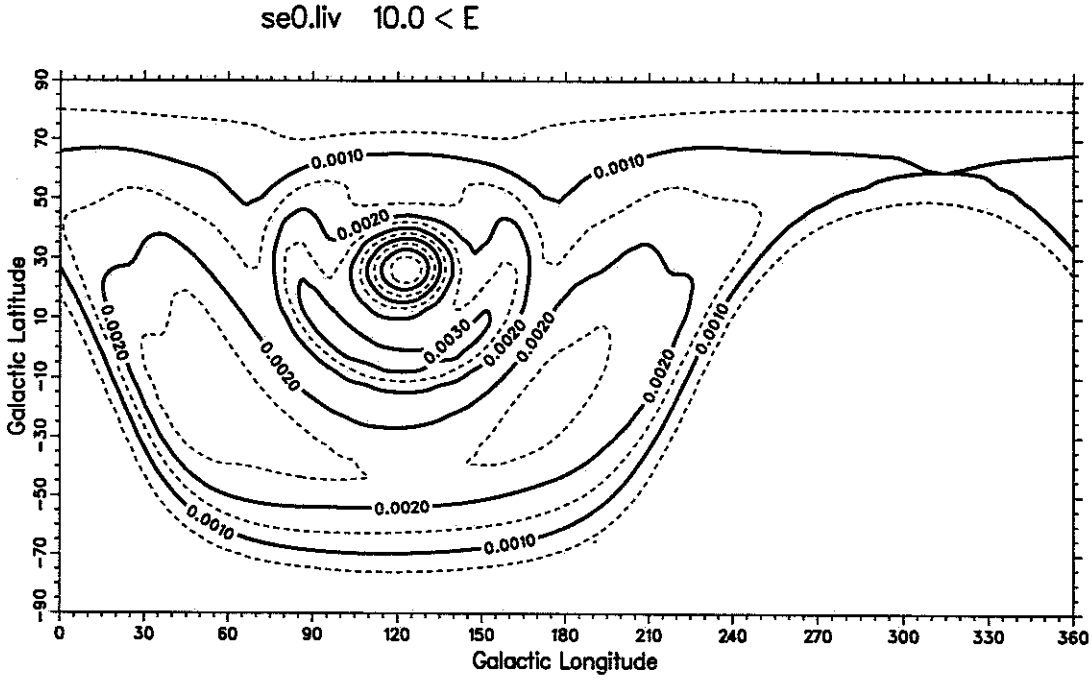

Figure 4.33. Live time background of stereo data for $E \geq 10.0 EeV$

CHAPTER 5

ANISOTROPY ANALYSIS

This chapter presents results of the anisotropy analysis. First, in section 5.1, we compare two types of background. Then several coordinates are used to search for dependence of anisotropy on these coordinates. The galactic coordinates are separated into six lobes to search for large scale excesses; the six lobe anisotropy is described in section 5.2. Section 5.3 discusses the dependence of anisotropy on galactic latitude. Section 5.4 discusses the classical topic, harmonic analysis of anisotropy. Section 5.5 discusses the most recent search for a supergalactic plane excess.

5.1 Comparison of Background

We have two types of background calculation. One is based on acceptance and live time, as mentioned in section 4.5.2. This background will be called *liv*. The other type uses scrambled event arrival direction and trigger times to calculate the event probability density as mentioned in section 4.3.2. We simulate 100 sets of scrambled events and use the average of those 100 data sets as the background; this background will be called *ave*.

This section discusses those two types of background and studies the difference between them. First we study the difference in large scale by comparing the mean value of both backgrounds in 10° bins. Then we compare the difference in $1^\circ \times 1^\circ$ pixels.

5.1.1 Difference in large scale

We group both backgrounds into 10° bins according to different coordinates, such as right ascension (α), declination (δ), galactic longitude (l), and galactic latitude (b). Then the difference of the mean value of the two backgrounds can be found by

$$\Delta(x,E) = \frac{\langle liv(x,E)\rangle - \langle ave(x,E)\rangle}{\langle liv(x,E)\rangle}$$

where x is a certain coordinate and E is energy. The results are listed in appendix C. Except for some bins which contain most of the lower declination and thus have higher

errors, most of $\Delta(\alpha, E)$, $\Delta(l, E)$ and $\Delta(b, E)$ are within $\pm 25\%$ for mono background and within $\pm 45\%$ for stereo background.

The overall means and standard deviations for the four coordinates are listed in Table 5.1. The overall mean values of all four coordinates are less than 3% for mono background and less than 5% for stereo background. We may conclude that the projections of those two backgrounds, *liv* and *ave*, are quite consistent with each other. For the right ascension band, the means and standard deviations are small for the mono background and slightly larger for the stereo background. This deviation suggests that the azimuth angle dependence of stereo acceptance needs some small adjustment. For declination, although the overall mean is still small (0.3% for mono background and 3% for stereo background), the fluctuation are greater than 10%. We may need to modify the zenith angle dependence of both the mono and stereo acceptance. For galactic longitude and latitude bands, most of the large errors come from lower declination pixels.

5.1.2 Difference in small scale

As we found, the declination bands have some systematic difference between two backgrounds. We need to understand the difference in detail. Here we use small scale, $1^\circ \times 1^\circ$ pixels, to study the relative difference between the two backgrounds. The relative difference is defined as

$$\Delta(l, b, E) = \frac{liv(l, b, E) - ave(l, b, E)}{liv(l, b, E)}$$

Table 5.1. The overall mean value and standard deviation of difference on large scale comparison. All numbers are in percentage %.

		Mono		Stereo	
		mean	SD	mean	SD
Right Ascension	α	0.219	4.981	0.562	9.629
Declination	δ	0.302	12.363	2.966	17.617
Galactic Longitude	l	2.178	7.641	5.081	13.809
Galactic Latitude	b	0.288	7.308	0.662	8.366

where l is galactic longitude, b is galactic latitude, and E is energy. In this definition, we have two extreme cases such as,

$$liv(l,b,E) \ll ave(l,b,E) \Longrightarrow \Delta(l,b,E) \ll -1$$

$$liv(l,b,E) \gg ave(l,b,E) \Longrightarrow \Delta(l,b,E) \simeq 1$$

The first case happens at the rim of visible sky where the *liv* background has very small coverage but the *ave* background could have an event come from that region and thus produce a large probability density. The second case could happen at a position where the *ave* background has no events due to limited simulation data sets. This case happens more frequently at higher energy and at the rim of visible sky because there are fewer events.

In order to avoid the first case, we apply a declination cut at $-40°$. Thatwould roughly correspond to the zenith angle θ cut at $80°$ which is quite reasonable. We do not have events which come from $\theta \geq 80°$; but due to the point spread function, some probability density is spread over these region. The only way to avoid the second case is by increasing the number of simulations. However, this increase will cost a lot of computer time and memory space. After the declination cut, both *liv* and *ave* are normalized to the number of events at each energy interval.

In order to study the systematic difference, we group $\Delta(l,b,E)$ into $10°$ bins and study the Δ as a function of declination. The declination has a closer relation to local coordinate zenith angle θ. In calculating mean and standard deviation, the first extreme case $\Delta \leq -100\%$ is excluded to avoid bias caused by these points. Tables 5.2 and 5.3 list the mean and standard deviation of Δ as a function of declination for mono and stereo background. These results are also plotted in Figures 5.1 and 5.2.

Generally, the relative difference of the mono backgrounds is less than the difference of the stereo backgrounds. This difference is reasonable because of the larger number of events and smaller degree of freedom required in mono background calculation than in stereo. However, there is still some systematic difference between *liv* and *ave*. For mono background, at declination $\delta<-20°$ and $30°<\delta<50°$ the *liv* background is less than the

Table 5.2. The mean and standard deviation of relative difference on small scale between live time background *liv* and scrambled events background *ave* for mono data.

δ	$0.2 \leq E < 0.4$		$0.4 \leq E < 1.0$		$1.0 \leq E < 3.2$		$3.2 \leq E < 10$		$10.0 \leq E$	
	mean	SD	mean	SD	mean	SD	mean	SD	mean	SD
-30	1.53	31.54	-12.28	25.63	-16.20	36.62	12.10	40.17	39.41	50.54
-20	-4.74	26.35	-14.95	29.07	-0.24	31.23	14.60	33.76	35.56	43.23
-10	10.79	14.92	10.18	20.54	10.21	20.37	11.07	31.51	26.03	33.09
0	14.86	14.49	12.78	12.96	6.66	17.36	11.97	25.75	11.32	29.91
10	12.51	9.38	9.18	12.58	8.96	15.21	4.10	26.01	4.94	29.82
20	4.81	9.10	-0.92	11.19	2.23	14.89	-0.17	22.96	7.30	30.38
30	2.47	20.68	2.03	20.81	-4.15	22.42	-2.63	32.31	-13.01	43.59
40	-18.12	12.66	-13.62	11.40	-16.33	16.55	-7.28	24.96	5.99	29.35
50	-15.50	10.25	-11.76	11.48	-10.05	18.93	1.62	21.69	-9.11	35.20
60	-2.99	10.33	0.47	10.68	-1.16	16.31	8.59	16.27	-5.59	27.75
70	6.98	8.78	5.30	9.11	0.83	11.69	-1.04	17.40	4.75	21.73
80	15.69	8.70	11.16	6.66	10.44	12.60	-6.92	16.21	19.76	31.00
90	25.28	6.73	17.97	7.49	19.62	10.31	-3.59	21.18	51.61	11.18
ave	2.59	14.15	1.20	14.58	0.83	18.81	3.26	25.40	13.77	32.06

Table 5.3. The mean and standard deviation of relative difference on small scale between live time background *liv* and scrambled events background *ave* for stereo data.

δ	$0.2 \leq E < 0.4$		$0.4 \leq E < 1.0$		$1.0 \leq E < 3.2$		$3.2 \leq E < 10$		$10.0 \leq E$	
	mean	SD	mean	SD	mean	SD	mean	SD	mean	SD
-30	86.40	28.85	83.80	30.30	68.72	31.20	17.78	54.06	94.26	10.77
-20	85.91	26.14	76.77	32.89	63.24	32.42	60.53	31.53	60.65	47.67
-10	55.17	49.03	27.09	43.25	23.35	40.24	17.04	43.51	49.01	45.75
0	28.95	42.90	13.09	33.07	12.44	33.30	26.31	35.85	52.81	40.13
10	16.79	36.19	16.76	30.71	14.56	26.85	22.54	35.98	36.01	46.52
20	7.16	34.68	7.03	29.66	5.53	29.29	16.22	35.71	13.54	42.23
30	16.32	43.62	-3.65	41.20	10.51	39.00	-2.09	42.15	30.29	42.57
40	-15.38	35.19	-15.85	32.72	-8.61	31.86	-6.53	36.16	22.39	48.45
50	-17.67	37.23	-13.06	34.95	-12.55	32.09	-3.85	38.78	30.99	41.49
60	0.10	37.09	0.06	34.56	-1.66	28.16	15.18	34.90	8.65	49.59
70	8.46	37.69	5.42	33.59	-8.98	29.61	13.22	40.11	22.82	39.48
80	13.56	37.56	2.94	33.70	13.48	27.85	28.51	32.56	27.07	33.26
90	17.10	41.51	13.74	29.07	10.07	28.05	1.26	30.57	-4.74	36.10
ave	23.30	34.85	16.47	33.82	14.62	31.53	15.86	37.84	34.13	40.31

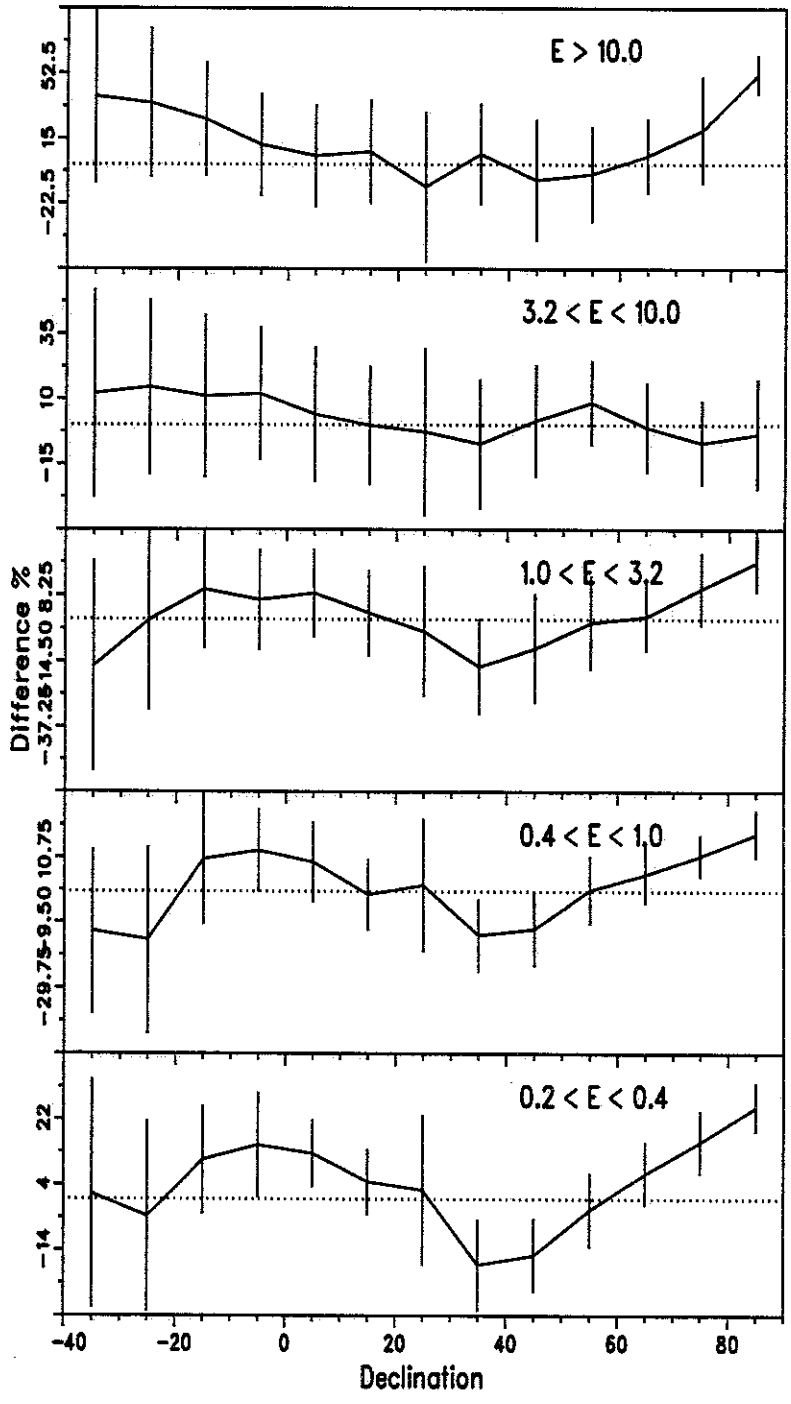

Figure 5.1. The mean and standard deviation of relative difference on small scale of *liv* and *ave* of mono background. The error bar is ± one standard deviation. The dotted line is relative difference 0%.

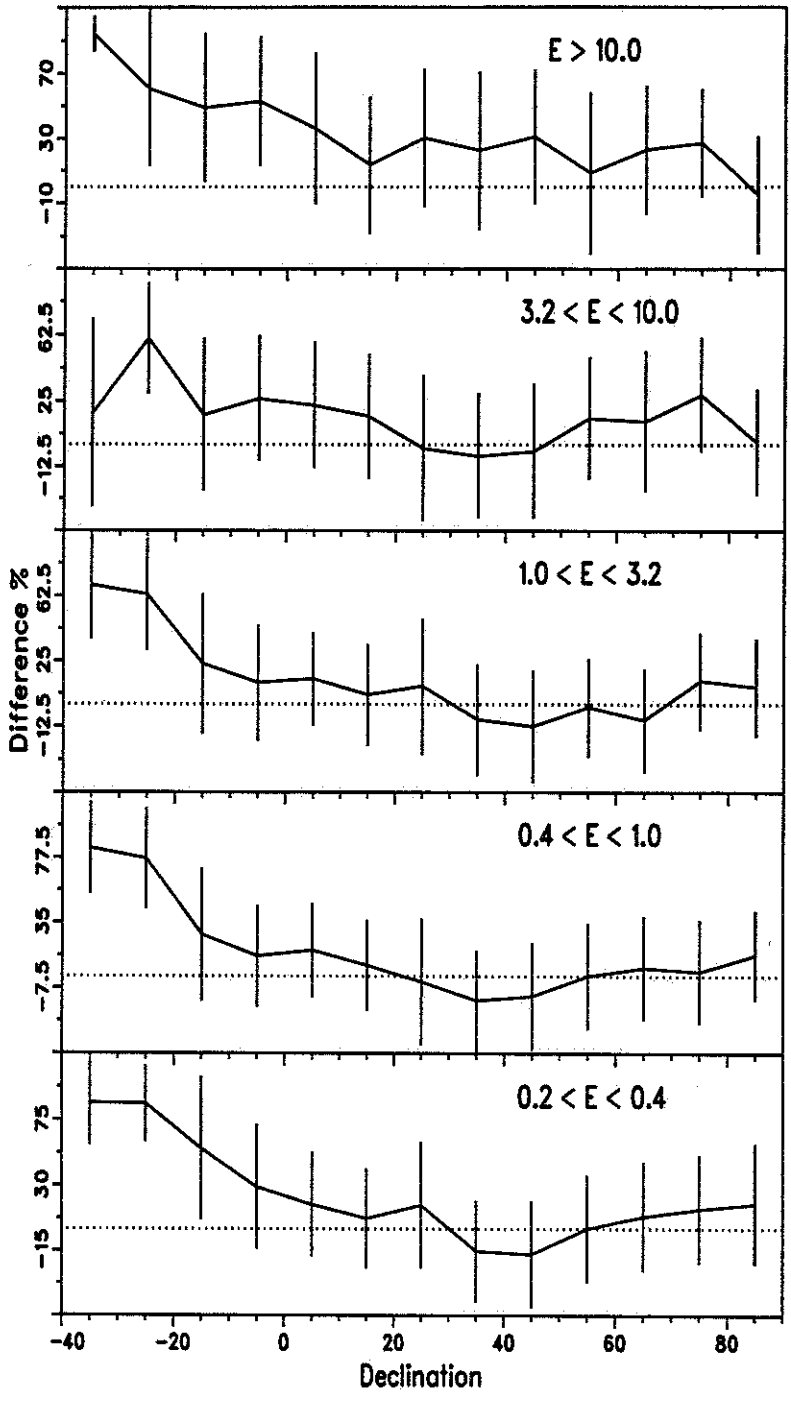

Figure 5.2. The mean and standard deviation of relative difference on small scale of *liv* and *ave* of stereo background. The error bar is ± one standard deviation. The dotted line is relative difference 0%.

ave background at $E<3.2EeV$ and larger at higher energy. At higher declination $\delta<50°$, the *liv* background is larger than the *ave* background for all energy intervals except $3.2<E<10EeV$. This difference suggests that the acceptance needs a small adjustment.

5.1.3 Conclusion

In the comparison of background in the large scale, the mean difference is less than $3 \pm 13\%$ for mono background and less than $6 \pm 18\%$ for stereo background. We may conclude that the live time background *liv* is quite consistent with the scrambled events background *ave* in the large scale, except for a small dependence on declination. We can modify the acceptance to make those two backgrounds more consistent with each other.

For comparison in the small scale, the relative difference increases significantly due to the statistical nature of the scrambled event background. For the mono background, the mean relative error is approximately 4.3% and the mean fluctuation is about 21%. For the stereo background, the mean relative error is approximately 21% and mean fluctuation is approximately 36%. For such high fluctuation, these backgrounds are not suitable for small scale anisotropy analyses.

For all further analyses, we will use the 100 sets of scrambled event background to perform the same analysis as we do on the real data. From now on, whenever we say **background**, we mean **scrambled event background**. Using scrambled event backgrounds, we will generate statistical fluctuation of the anisotropy. The anisotropy from the data should be compared with the mean and the standard deviation of results from the scrambled event backgrounds.

5.2 Coarse Lobes Analysis

5.2.1 The six sky lobes

The whole sky can be separated into six equal area lobes. Each lobe is centered at one of the three coordinates axes. These axes, shown in Figure 2.8, are center-of-galaxy to anticenter-of-galaxy, from the forward direction of the solar system in the galactic arm to the backward direction, and south to north. In this analysis, the criteria that separate the whole sky into six lobes are:

- North : if $b \geq 42°$ (b is galactic latitude)
- South : if $b \leq -42°$
- Center : if $-42° < b < 42°$ and $-45° \leq l < 45°$ (l is galactic longitude)
- Forward : if $-42° < b < 42°$ and $45° \leq l < 135°$
- Anticenter : if $-42° < b < 42°$ and $135° \leq l < 225°$
- Backward : if $-42° < b < 42°$ and $225° \leq l < 315°$

Although these criteria produce a slightly smaller area at north and south lobes, the result is not changed because both the data and the background use the same criteria.

5.2.2 Analysis and result

We compare the integrated event probability density of each lobe with the background of scrambled events. The RMS width of the scrambled event will be used as the width of distribution to find the significance of deviation from the isotropic background.

$$
\begin{aligned}
D(i) &= \textstyle\sum_{(l,b)\ of\ lobe\ i} \rho(l,b) && \text{observed event probability density} \\
B(i,j) &= \textstyle\sum_{(l,b)\ of\ lobe\ i} \rho(l,b,j) && \text{expected event probability density} \\
M(i) &= \textstyle\sum B(i,j) / \sum j && \text{mean value of isotropic background} \\
W(i) &= \sqrt{\frac{\sum_j (B(i,j)-M(i))^2}{\sum j}} && \text{width of isotropic background} \\
S(i) &= (D(i) - M(i))/W(i) && \text{significance of data deviated from background}
\end{aligned}
$$

The results of this analysis are listed in Tables 5.4 and 5.5 for monocular and stereo data, respectively.

Figure 5.3 shows the significance of mono and stereo data. From monocular data, some lobes have deviation of more than $\pm 3\sigma$ from the isotropic background; the stereo data does not show significant deviation from the isotropic background but has the same trend. From Figure 5.3 we found some common trends between mono and stereo data. The backward lobe has no common trend between mono and stereo data.

Table 5.4. The result of six lobes anisotropy analysis of monocular data.

Lobes		Energy (EeV)				
		0.2 - 0.4	0.4 - 1.0	1.0 - 3.2	3.2 - 10.0	$\geq$ 10.0
North	D	2864.2	2203.2	1030.8	262.1	76.8
	M	2869.4	2239.0	1061.7	241.3	77.8
	W	36.1	35.0	26.5	13.0	6.7
	S	**-0.15**	**-1.03**	**-1.17**	**1.59**	**-0.15**
South	D	609.8	620.1	427.8	103.3	40.0
	M	672.0	675.5	435.3	112.2	30.0
	W	20.7	21.2	16.7	9.4	5.0
	S	**-3.00**	**-2.62**	**-0.45**	**-0.94**	**1.99**
Center	D	438.7	506.3	324.7	77.0	19.0
	M	539.0	560.4	361.6	95.4	28.2
	W	18.8	19.6	15.7	6.9	4.3
	S	**-5.35**	**-2.76**	**-2.35**	**-2.69**	**-2.14**
Forward	D	3907.9	3258.7	1494.3	356.3	100.0
	M	3750.5	3155.7	1465.4	358.1	103.6
	W	36.7	38.7	31.1	14.9	9.4
	S	**4.29**	**2.66**	**0.93**	**-0.12**	**-0.39**
Anitcenter	D	2938.1	2405.2	1191.8	283.4	77.8
	M	2855.7	2315.8	1120.4	275.6	77.7
	W	29.9	32.2	26.4	11.2	6.8
	S	**2.75**	**2.78**	**2.70**	**0.69**	**0.02**
Backward	D	125.1	182.9	123.9	46.8	19.4
	M	170.0	201.7	128.2	42.8	13.8
	W	9.4	11.5	7.3	6.8	2.9
	S	**-4.80**	**-1.64**	**-0.58**	**0.59**	**1.93**

- Negative significance for north lobes at $E < 1.0EeV$ and south lobes at $E < 0.4EeV$.
- Negative significant at center lobes except a 0.15σ of stereo data at $1.0 < E < 3.2EeV$.
- Positive significance at anticenter lobe except for $E > 10.0EeV$.
- Positive significance at forward lobe for $E < 3.2EeV$.

These common trends could be explained by systematic error in background prediction and/or anisotropy. Fly's Eye has more exposure and better efficiency at north, forward, and anticenter lobes. At energy $< 3.2EeV$, we see overestimation of background at the

Table 5.5. The result of six lobes anisotropy analysis of stereo data

Lobes		Energy (EeV)				
		0.2 - 0.4	0.4 - 1.0	1.0 - 3.2	3.2 - 10.0	$\geq$ 10.0
North	D	1302.1	914.0	410.8	78.6	17.5
	M	1322.8	1018.6	449.7	77.1	11.9
	W	25.6	28.2	14.2	6.0	2.7
	S	**-0.81**	**-3.71**	**-2.74**	**0.25**	**2.03**
South	D	408.3	397.8	199.9	30.5	5.2
	M	426.1	408.0	198.2	31.5	6.2
	W	19.0	14.7	13.9	4.8	2.2
	S	**-0.94**	**-0.70**	**0.12**	**-0.21**	**-0.48**
Center	D	220.2	247.5	123.2	14.5	4.5
	M	248.7	249.2	121.1	25.0	4.8
	W	13.2	12.1	14.3	3.8	1.6
	S	**-2.16**	**-0.14**	**0.15**	**-2.82**	**-0.16**
Forward	D	1722.3	1412.1	613.8	112.5	24.8
	M	1697.7	1357.7	590.7	111.1	17.8
	W	21.4	28.9	20.2	8.6	3.4
	S	**1.15**	**1.88**	**1.15**	**0.16**	**2.07**
Anitcenter	D	1448.4	1149.1	530.6	99.5	9.8
	M	1407.8	1089.7	516.5	89.3	20.7
	W	23.0	25.5	19.5	6.2	3.3
	S	**1.77**	**2.34**	**0.72**	**1.64**	**-3.30**
Backward	D	66.8	70.2	30.6	7.3	1.1
	M	64.8	67.8	32.7	8.9	1.6
	W	6.3	5.1	5.4	2.0	1.0
	S	**0.32**	**0.48**	**-0.40**	**-0.79**	**-0.48**

north lobes and underestimation at anticenter and forward lobes. This situation may suggest that these systematic trends cannot be completely explained by systematic error in the isotropic background.

We also compare this analysis with P. Sommer's analysis, listed in Table 2.2, at common energy intervals, $E > 1.EeV$; most of the differences in significance are between -2.5σ and 1.5σ. The two analyses have quite similar results. However, if we look only at energy $E > 1EeV$, those common trends become unclear at energy $E > 1.0EeV$. Whether anisotropy exists or not needs further study.

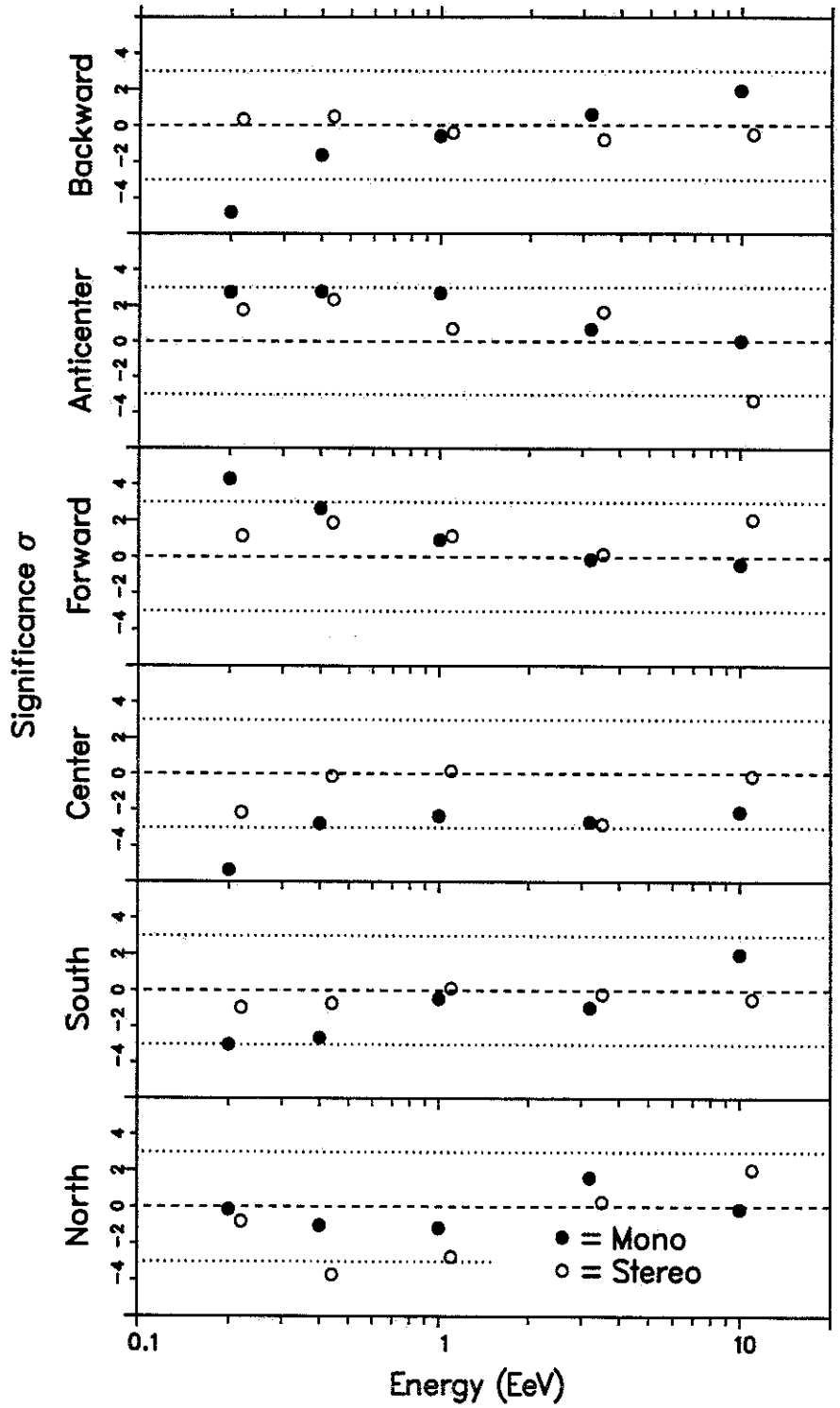

Figure 5.3. The significance of 6 lobes analysis of mono and stereo data.

5.3 Harmonic Analysis

For ground arrays, harmonic analysis is the easiest way to study anisotropy because of their uniform coverage of right ascension (RA). Therefore anything which produces a nonuniform distribution in RA must be related to anisotropy. Although this method can be applied to Fly's Eye, some differences must be noticed. Because of the intermittent operation and anisotropic coverage of stereo data, the right ascension is not uniformly covered in Fly's Eye data. Therefore the expected Rayleigh vector must be calculated from the isotropic background. The magnitude of the Rayleigh vector cannot be taken as the magnitude of anisotropy; it reflects mainly the nonuniform exposure of the detector. Only the difference between data and isotropic background has a physical meaning.

In this analysis, the declination is separated into nine approximately equal area bands. These are $-26°$, $-15°$, $-5°$, $5°$, $15°$, $26°$, $38°$, $53°$, and up to $90°$. For each band, the Rayleigh vectors of first and second harmonics are calculated by

$$\begin{aligned} x_1 &= \frac{2}{N}\sum_{\delta_1}^{\delta_2}\rho(l,b)\cos(\alpha) & x_2 &= \frac{2}{N}\sum_{\delta_1}^{\delta_2}\rho(l,b)\cos(2\alpha) \\ y_1 &= \frac{2}{N}\sum_{\delta_1}^{\delta_2}\rho(l,b)\sin(\alpha) & y_2 &= \frac{2}{N}\sum_{\delta_1}^{\delta_2}\rho(l,b)\sin(2\alpha) \\ R_1 &= \sqrt{x_1^2+y_1^2} & R_2 &= \sqrt{x_2^2+y_2^2} \\ \phi_1 &= \mathrm{Tan}^{-1}(\frac{x_1}{y_1}) & \phi_2 &= \frac{1}{2}\mathrm{Tan}^{-1}(\frac{x_2}{y_2}) \end{aligned}$$

where ρ could be the event probability density of data or scrambled events and N is the total event probability density in that declination band. α and δ are the right ascension and declination of each point (l,b) where l is galactic longitude and b is galactic latitude. The Rayleigh vector distribution of scrambled events gives the mean and width of the isotropic background. The significance is defined as

$$\text{significance} = \frac{\text{data} - \text{mean}}{\text{width}}$$

The complete result of this analysis is listed in Appendix B. The results of all sky band ($-26° \leq \delta \leq +90°$) is listed in Table 5.6 and plotted in Figure 5.4.

Table 5.6. The results of harmonics analysis of all sky band, declination from −26 degree to +90 degree.

Energy (EeV)	magnitude Data	Mean	width	sigma	phase Data	Mean	width	sigma
	Mono Data —— First Harmonic							
0.2 – 0.4	0.4746	0.4660	0.0111	**0.78**	123.41	127.11	1.52	**-2.43**
0.4 – 1.0	0.5304	0.5289	0.0150	**0.10**	124.78	128.95	1.64	**-2.54**
1.0 – 3.2	0.5395	0.5394	0.0220	**0.00**	122.86	127.47	2.47	**-1.87**
3.2 – 10.0	0.5292	0.5530	0.0396	**-0.60**	131.30	125.96	4.05	**1.32**
≥ 10.0	0.5586	0.6100	0.0774	**-0.66**	129.83	131.81	6.67	**-0.30**
	Mono Data —— Second Harmonic							
0.2 – 0.4	0.1585	0.1545	0.0114	**0.36**	9.11	10.20	2.36	**-0.42**
0.4 – 1.0	0.1059	0.0859	0.0114	**1.75**	6.40	9.25	4.36	**-0.65**
1.0 – 3.2	0.1003	0.1017	0.0221	**-0.06**	0.99	9.94	6.95	**-1.29**
3.2 – 10.0	0.1134	0.0684	0.0332	**1.36**	6.64	-12.00	28.64	**0.65**
≥ 10.0	0.1371	0.0953	0.0437	**0.96**	11.99	8.04	52.74	**0.07**
	Stereo Data —— First Harmonic							
0.2 – 0.4	0.6141	0.5897	0.0155	**1.57**	115.73	116.81	1.90	**-0.57**
0.4 – 1.0	0.6671	0.6202	0.0186	**2.52**	115.90	117.94	2.44	**-0.84**
1.0 – 3.2	0.6497	0.6286	0.0312	**0.67**	119.22	116.29	3.44	**0.85**
3.2 – 10.0	0.5723	0.6295	0.0628	**-0.91**	117.66	123.11	7.60	**-0.72**
≥ 10.0	0.9857	0.5539	0.1307	**3.31**	126.10	110.88	19.30	**0.79**
	Stereo Data —— Second Harmonic							
0.2 – 0.4	0.1705	0.1968	0.0197	**-1.33**	16.82	19.36	2.69	**-0.94**
0.4 – 1.0	0.1464	0.1507	0.0202	**-0.21**	20.18	27.32	4.69	**-1.52**
1.0 – 3.2	0.1146	0.1551	0.0409	**-0.99**	18.04	16.13	9.10	**0.21**
3.2 – 10.0	0.1288	0.1913	0.0788	**-0.79**	36.92	0.68	13.84	**2.62**
≥ 10.0	0.1234	0.2496	0.1361	**-0.93**	11.39	-12.22	38.69	**0.61**

Figures 5.5 and 5.6 plot the magnitude of first harmonics as functions of declination of monocular and stereo data. The first harmonics of data are very similar to the background prediction. Although the first harmonics magnitude is greater than 1 at declination below +15°, the isotropic background also generate a similar number and the difference between data and background are not significant, less than 2.5σ for mono data and less than 3.8σ for stereo data. Figures 5.7 and 5.8 show the histograms of significance from all declination bands of mono and stereo data. These distributions follow the normal distribution. The declination dependence of harmonics is the result of uneven exposure of sky. No significant first harmonic or second harmonic is found in this analysis.

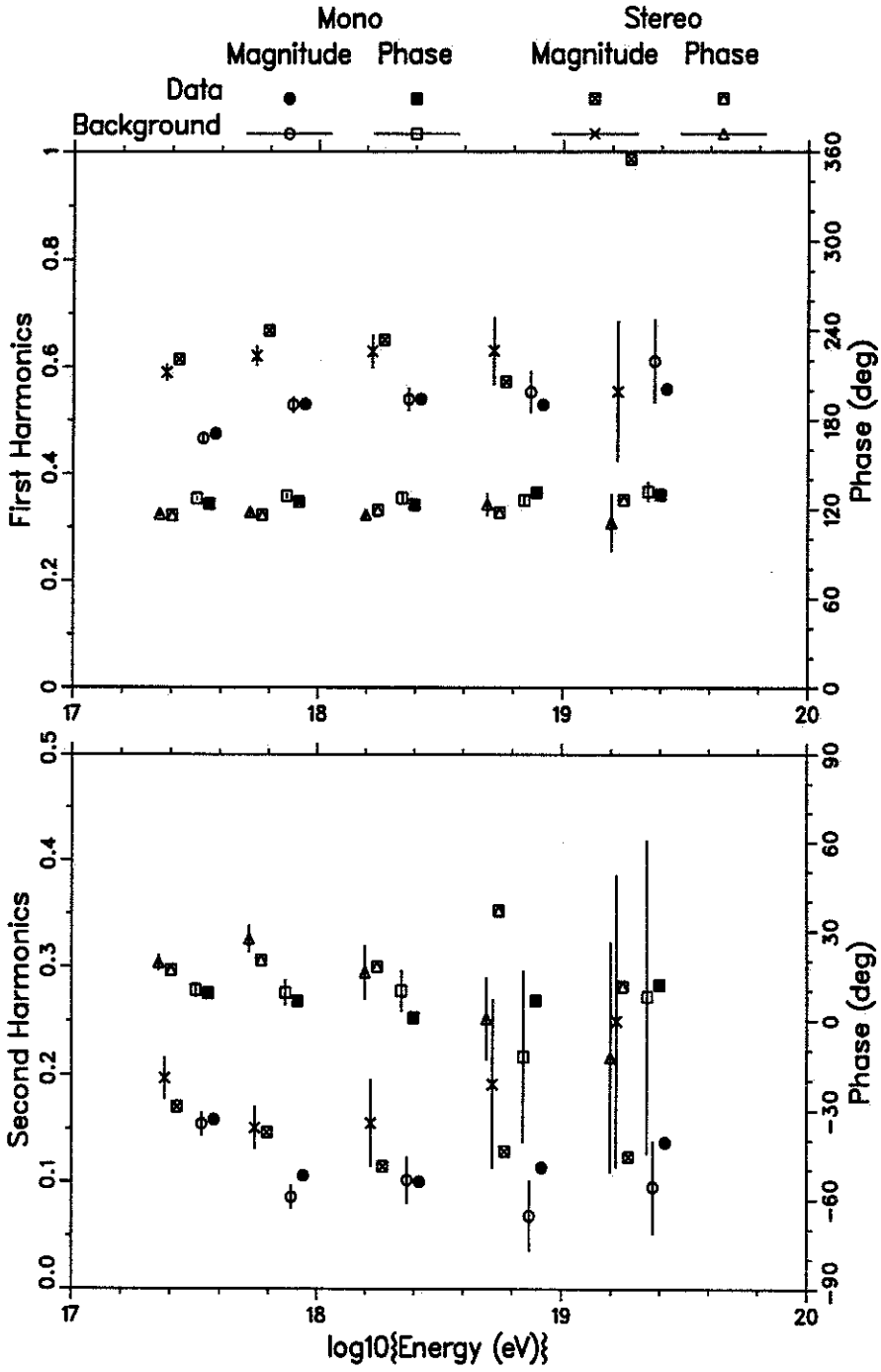

Figure 5.4. The first and second harmonics of all sky. The magnitude of Rayleigh vectors are shown in the left axes; the phases are shown in the right axes.

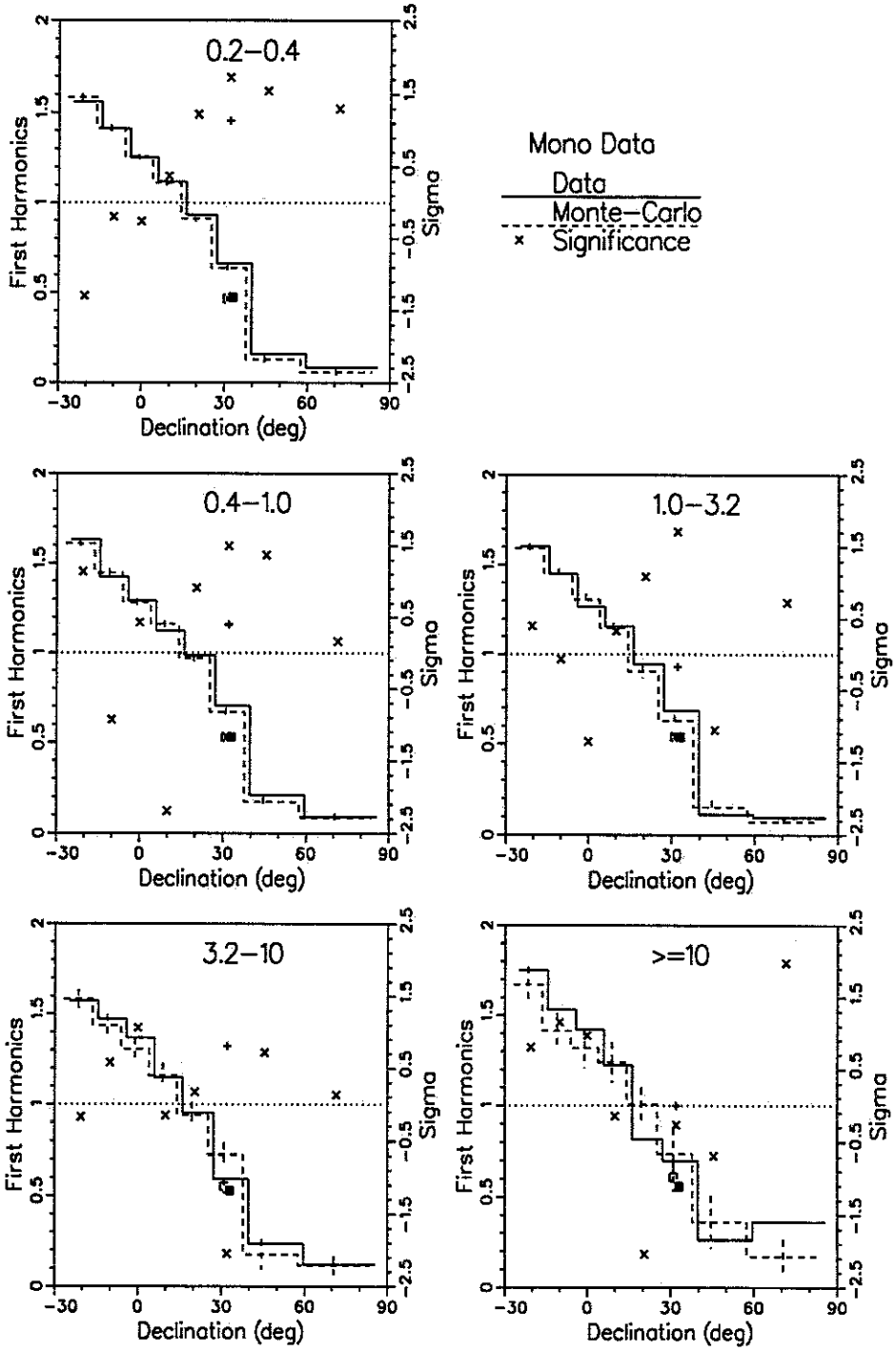

Figure 5.5. The magnitude of first harmonics as function of declination of monocular data. The data are plotted in solid line, the background are plotted in dash line. The square is the first harmonics of all declination bands $(-26° - 90°)$. The error bars are the standard deviation of backgrounds. All first harmonics use the left side axi. The significances, use the right side axi, of data are plotted in cross for individual bands and plus sign for all declination bands.

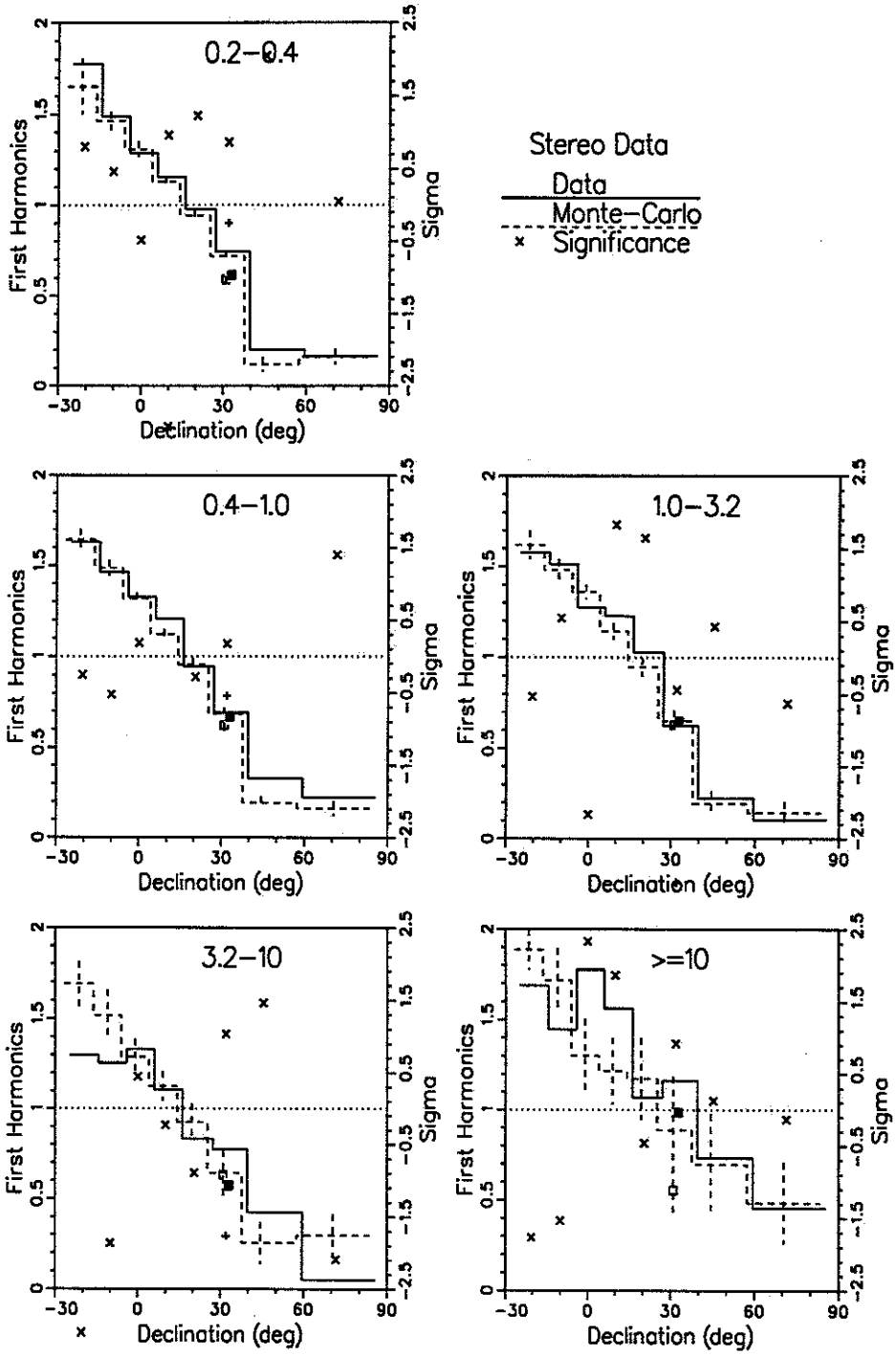

Figure 5.6. The magnitude of first harmonics as function of declination of stereo data. The data are ploted in solid line, the background are plotted in dash line. The square is the first harmonics of all declination bands ($-26°-90°$). The error bars are the standard deviation of backgrounds. All first harmonics use the left side axi. The significances, use the right side axi, of data are plotted in cross for individual bands and plus sign for all declination bands.

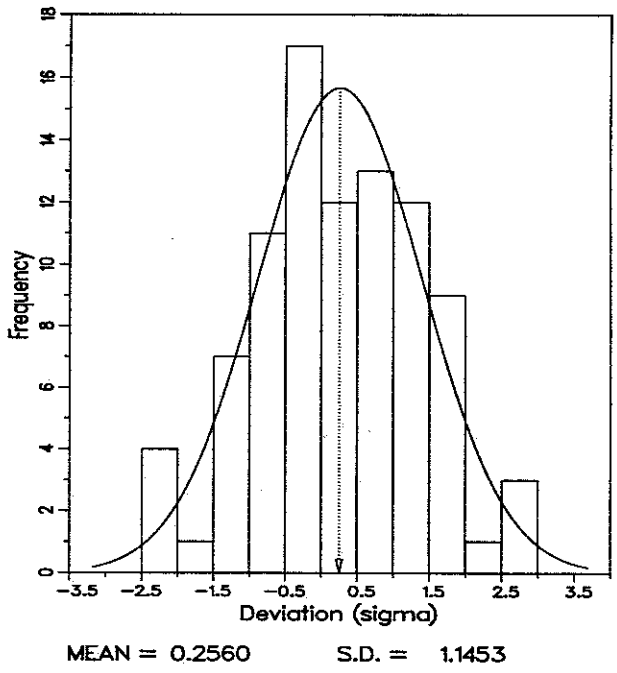

Figure 5.7. The distribution of deviation of harmonics analysis from all declination bands of mono data.

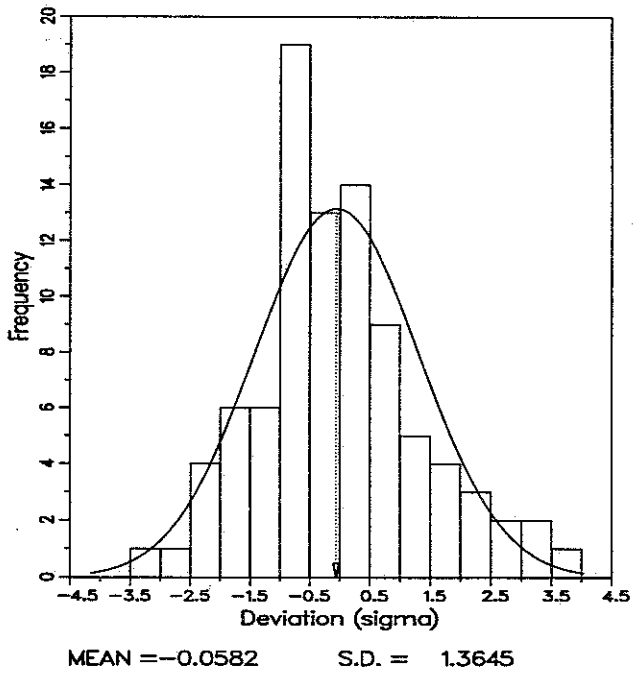

Figure 5.8. The distribution of deviation of harmonics analysis from all declination bands of stereo data.

5.4 Galactic Latitude Dependence

Two types of galactic latitude dependence are analyzed here. One is the galactic plane enhancement factor; the other is the galactic latitude gradient. Because of different magnetic field orientation, the anisotropy might be different for different regions of the sky. To look for this dependence, several regions were chosen. The simplest choice is the whole sky which covers the entire range of galactic longitude. The other choice is the four direction of major axes as mentioned in section 5.1: center, forward, anticenter, and backward. For the forward region, the regular magnetic field lines are almost facing the solar system; for the backward region, these field lines leave the solar system.

This analysis integrates over galactic longitude to find the total event probability as function of the galactic latitude, $D(b) = \sum_l \rho(l,b)_{data}$. The same process applies to the real data, the scrambled event data and the live time background, $T(b) = \sum_l \rho(l,b)_{liv}$. Then the event ratio $r(b) = D(b)/T(b)$ is used to find the latitude dependence.

In the 1993 analysis [5], we used only one scrambled event background; it was sampled 100 times then renormalized to the same number of events as real data. The galactic plane enhancement factor f_E and galactic latitude gradient s fitting only gives a number and error of this number. It is impossible to know the systematic error of this scrambled event background. We can only assume that the expected f_E/s of isotropic background is 0.; then the significance is fitted value divided by error of fitted value.

In this new analysis, in order to know how the background fluctuates, we use 100 sets of scrambled events backgrounds each has the same number of events as real data. For each set, we run through the same analysis as we did for real data. So we have 100 sets of f_E and s. The mean value and SD of these 100 data sets are the mean and SD of background. Therefore, the mean of background should be the expectation of the isotropic background and the SD is the fluctuation of the isotropic background. The mean value of background also shows the systematic error of the scrambled events background. The significance is defined as

$$\text{significance}(\sigma) = \frac{\text{data} - \text{mean of background}}{\sqrt{(\text{error of data})^2 + (\text{error of background})^2}}$$

5.4.1 Galactic plane enhancement factor

Since most stars and gas are concentrated on the galactic plane, it is natural to ask whether the arrival direction of cosmic rays is concentrated on the galactic plane. If the origin of these cosmic rays is inside the galactic plane, an enhancement near this plane could be expected. Wdowczyk and Wolfendal have developed a galactic plane enhancement formula to look for this kind of anisotropy [37].

$$I(b) = I_0(1 - f_E + c \times f_E \times e^{-b^2})$$

where c is a normalization constant and f_E is the energy dependent galactic plane enhancement factor. They use 1.402 [38]; but according to my calculation, (see appendix A), c should be 1.437. In a previous analysis, I use c=1.402 in order to compare our with their f_E [5]. However, in this dissertation, I will use 1.437. This will reduce f_E by approximately 2.5%.

If the cosmic rays are isotropic, the flux $I(b)$ should be equal to I_0. If the cosmic rays are anisotropic, the ratio of flux to the background could be a function of e^{-b^2}.

$$r(b) = \frac{D(b)}{T(b)} = \frac{I(b)}{I_0} = 1 - f_E + c \times f_E \times e^{-b^2} = 1 - f_E(1 - c \times e^{-b^2})$$

A weighted least χ^2 linear fit is used to find the enhancement factor f_E. The results are listed in Tables 5.7 and 5.8 and shown in Figures 5.9 and 5.10.

Consider the all sky data first. The most prominent effect is at energy $0.4 - 1.0 EeV$. There is a 2.24σ excess for monocular data and a 1.76σ for stereo data. The trend, the significance rises to maximum at $0.4 - 1.0 EeV$ then drops to negative above $10 EeV$, is similar for both monocular and stereo data.

For all four general directions, we do not see a consistent trend between monocular and stereo data. Only two bins have significance higher than $\pm 2\sigma$. Those two are consistent with random fluctuation. The overall results of the four general directions show that the enhancement factor f_E is quite consistent with the isotropic background for both stereo and monocular data at all energy intervals.

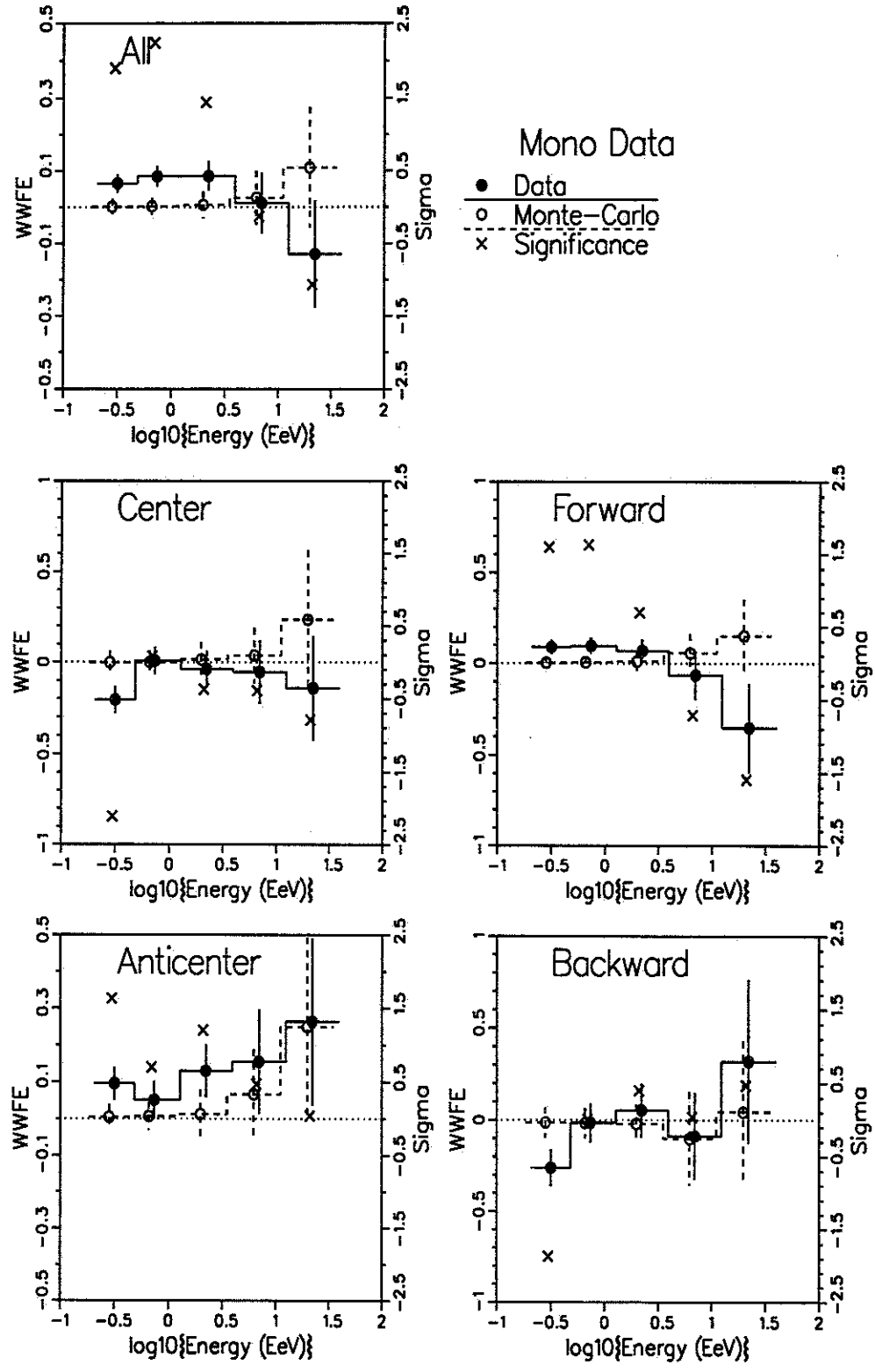

Figure 5.9. The galactic plane enhancement as function of energy of mono data.

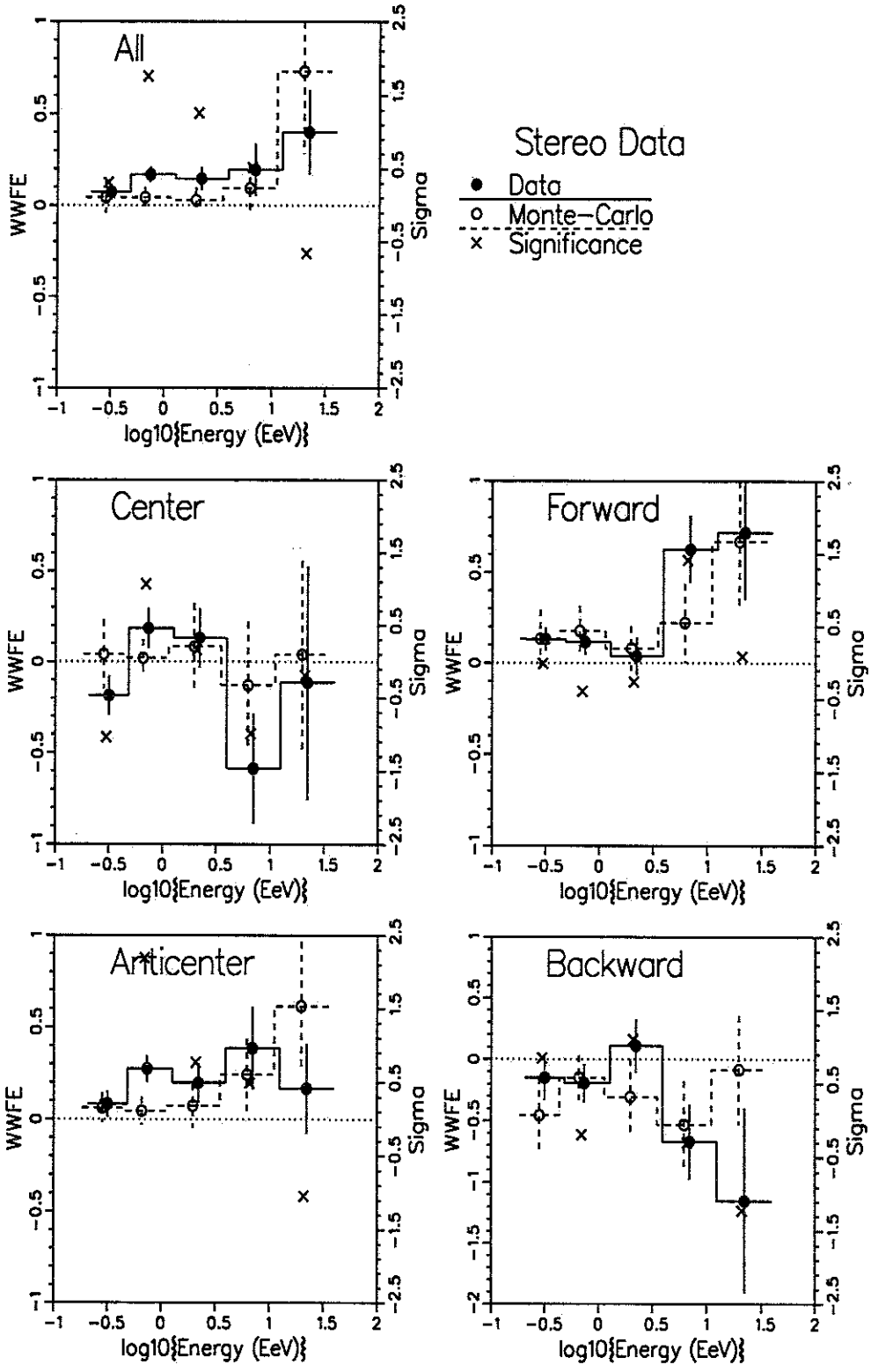

Figure 5.10. The galactic plane enhancement as function of energy of stereo data.

Table 5.7. The galactic plane enhancement factor of monocular data

Longitude (degree)	Energy (EeV)	Data Mean		SD	background Mean		SD	**Sigma** (σ)
All 1 – 360	0.2 - 0.4	0.0657	±	0.0262	0.0011	±	0.0215	**1.90**
	0.4 - 1.0	0.0852	±	0.0288	0.0024	±	0.0233	**2.24**
	1.0 - 3.2	0.0860	±	0.0412	0.0058	±	0.0376	**1.44**
	3.2 -10.0	0.0107	±	0.0833	0.0256	±	0.0746	**-0.13**
	$\geq$ 10.0	-0.1292	±	0.1478	0.1089	±	0.1663	**-1.07**
Center -45 – +44	0.2 - 0.4	-0.2055	±	0.0729	-0.0018	±	0.0635	**-2.11**
	0.4 - 1.0	0.0075	±	0.0765	-0.0008	±	0.0633	**0.08**
	1.0 - 3.2	-0.0373	±	0.1015	0.0145	±	0.0958	**-0.37**
	3.2 -10.0	-0.0537	±	0.1743	0.0362	±	0.1539	**-0.39**
	$\geq$ 10.0	-0.1423	±	0.2858	0.2351	±	0.3823	**-0.79**
Forward 45 – 134	0.2 - 0.4	0.0888	±	0.0414	0.0026	±	0.0345	**1.60**
	0.4 - 1.0	0.0956	±	0.0454	0.0055	±	0.0312	**1.63**
	1.0 - 3.2	0.0682	±	0.0642	0.0105	±	0.0512	**0.70**
	3.2 -10.0	-0.0648	±	0.1333	0.0558	±	0.1062	**-0.71**
	$\geq$ 10.0	-0.3527	±	0.2424	0.1499	±	0.2037	**-1.59**
Anticenter 135 – 224	0.2 - 0.4	0.0956	±	0.0444	0.0042	±	0.0343	**1.63**
	0.4 - 1.0	0.0510	±	0.0512	0.0064	±	0.0373	**0.70**
	1.0 - 3.2	0.1298	±	0.0719	0.0122	±	0.0661	**1.20**
	3.2 -10.0	0.1551	±	0.1421	0.0666	±	0.1213	**0.47**
	$\geq$ 10.0	0.2637	±	0.2265	0.2494	±	0.2440	**0.04**
Backward 225 – 314	0.2 - 0.4	-0.2603	±	0.1015	-0.0137	±	0.0842	**-1.87**
	0.4 - 1.0	-0.0151	±	0.1056	-0.0164	±	0.0824	**0.01**
	1.0 - 3.2	0.0529	±	0.1468	-0.0204	±	0.1066	**0.40**
	3.2 -10.0	-0.0872	±	0.2365	-0.1014	±	0.2548	**0.04**
	$\geq$ 10.0	0.3183	±	0.4444	0.0434	±	0.3865	**0.47**

5.4.2 Galactic latitude gradient

If the cosmic rays source is extragalactic and comes from one side of the galactic plane, the particle flux could be higher on one side of the galactic plane than on the other. This situation could lead to a galactic latitude gradient [39, 40].

$$I(b) = I_0(1 - s \times b)$$

where s is the galactic latitude gradient. The ratio of event probability density can be fitted to find the gradient.

$$r(b) = \frac{D(b)}{T(b)} = \frac{I(b)}{I_0} = 1 - s \times b$$

Table 5.8. The galactic plane enhancement factor of stereo data

Longitude (degree)	Energy (EeV)	Data Mean		SD	background Mean		SD	**Sigma** (σ)
All 1 – 360	0.2 - 0.4	0.0725	±	0.0406	0.0426	±	0.0856	**0.31**
	0.4 - 1.0	0.1687	±	0.0434	0.0429	±	0.0567	**1.76**
	1.0 - 3.2	0.1457	±	0.0638	0.0282	±	0.0683	**1.26**
	3.2 –10.0	0.1949	±	0.143	0.0939	±	0.1326	**0.52**
	$\geq$ 10.0	0.4002	±	0.2302	0.7290	±	0.4441	**-0.66**
Center -45 – +44	0.2 - 0.4	-0.1866	±	0.1089	0.0404	±	0.1892	**-1.04**
	0.4 - 1.0	0.1835	±	0.1130	0.0190	±	0.1038	**1.07**
	1.0 - 3.2	0.1297	±	0.1627	0.0837	±	0.2366	**0.16**
	3.2 -10.0	-0.5850	±	0.2988	-0.1303	±	0.3490	**-0.99**
	$\geq$ 10.0	-0.1149	±	0.6403	0.0388	±	0.5178	**-0.19**
Forward 45 – 134	0.2 - 0.4	0.1295	±	0.0627	0.1318	±	0.1617	**-0.01**
	0.4 - 1.0	0.1147	±	0.0698	0.1755	±	0.1382	**-0.39**
	1.0 - 3.2	0.0372	±	0.1048	0.0797	±	0.1230	**-0.26**
	3.2 -10.0	0.6275	±	0.1854	0.2211	±	0.2170	**1.42**
	$\geq$ 10.0	0.7189	±	0.3688	0.6709	±	0.3549	**0.09**
Anticenter 135 – 224	0.2 - 0.4	0.0825	±	0.0701	0.0621	±	0.0809	**0.19**
	0.4 - 1.0	0.2733	±	0.0718	0.0447	±	0.0758	**2.19**
	1.0 - 3.2	0.1973	±	0.1065	0.0731	±	0.1203	**0.77**
	3.2 -10.0	0.3856	±	0.2243	0.2418	±	0.1937	**0.49**
	$\geq$ 10.0	0.1663	±	0.2447	0.6128	±	0.3542	**-1.04**
Backward 225 – 314	0.2 - 0.4	-0.1494	±	0.1812	-0.4554	±	0.3102	**0.85**
	0.4 - 1.0	-0.1946	±	0.1570	-0.1493	±	0.1807	**-0.19**
	1.0 - 3.2	0.1098	±	0.2179	-0.3070	±	0.3084	**1.10**
	3.2 -10.0	-0.6700	±	0.3067	-0.5303	±	0.3575	**-0.30**
	$\geq$ 10.0	-1.1532	±	0.7564	-0.0845	±	0.4423	**-1.22**

The results for both monocular and stereo data are listed in Tables 5.9 and 5.10. Figures 5.11 and 5.12 show the overall results

Only two bins have high significance. Both are monocular data at energy $0.2-0.4EeV$. One is 2.53σ at the center direction. The other is 2.05σ at the backward direction. The results show that the galactic latitude gradient s is quite consistent with the isotropic background for both stereo and monocular data at all energy intervals. No significant difference is found between the four general directions.

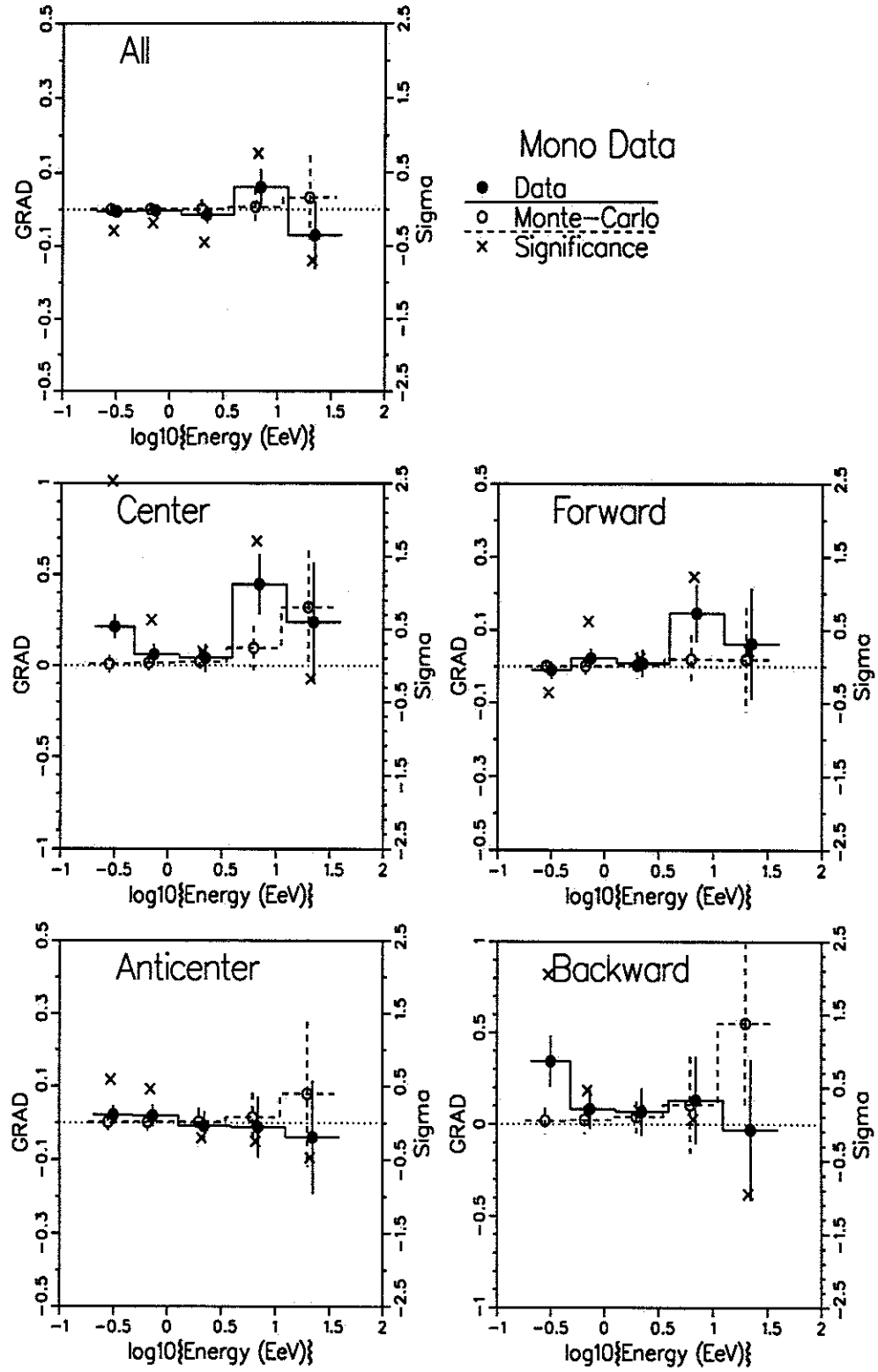

Figure 5.11. The galactic latitude gradient as function of energy of mono data.

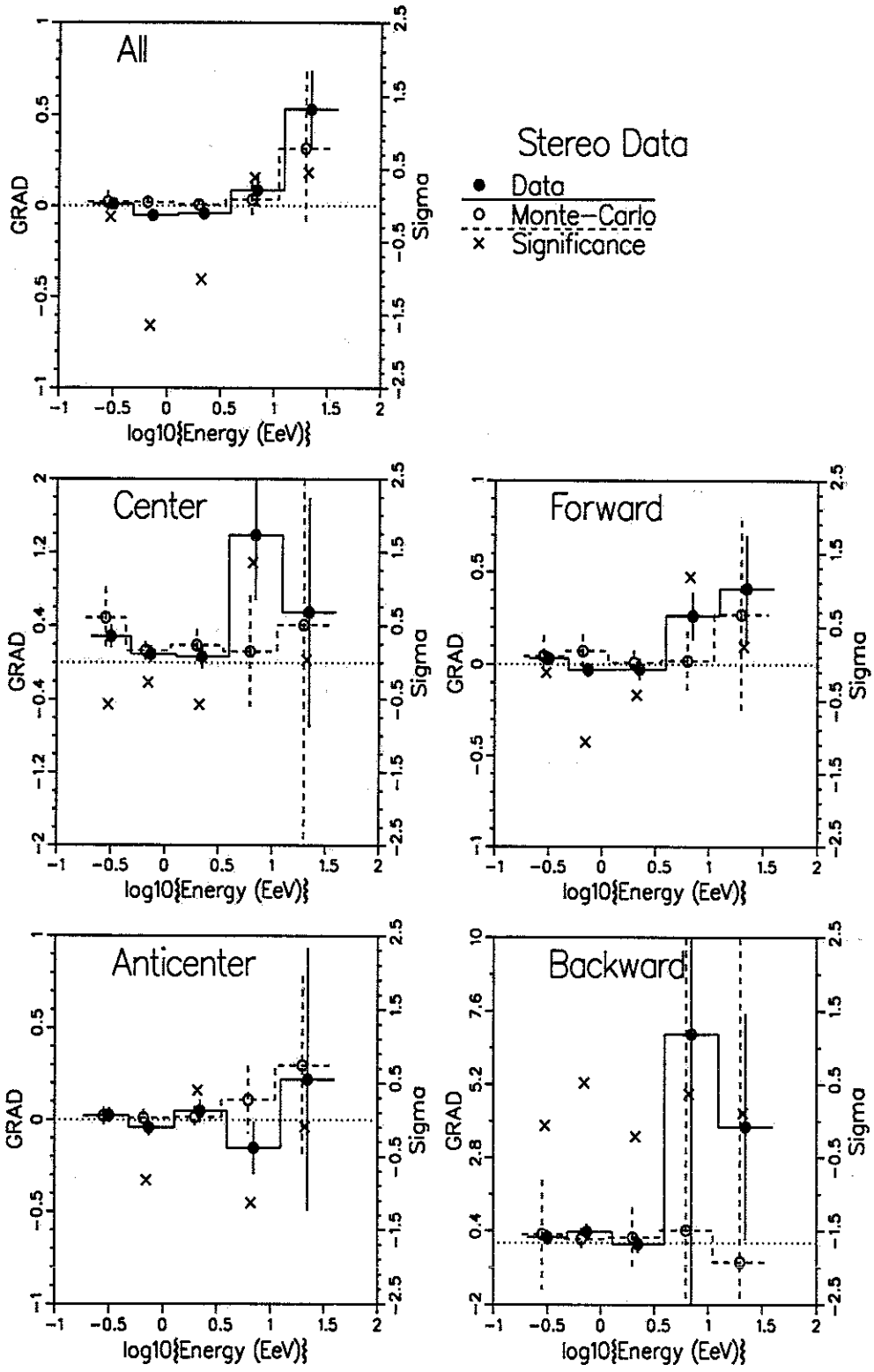

Figure 5.12. The galactic latitude gradient as function of energy of stereo data.

Table 5.9. The galactic latitude gradient of monocular data

Longitude (degree)	Energy (EeV)	Data Mean		SD	background Mean		SD	Sigma (σ)
All 1 – 360	0.2 - 0.4	-0.0052	±	0.0155	0.0005	±	0.0126	**-0.29**
	0.4 - 1.0	-0.0029	±	0.0169	0.0011	±	0.0145	**-0.18**
	1.0 - 3.2	-0.0143	±	0.0233	0.0013	±	0.0255	**-0.45**
	3.2 -10.0	0.0605	±	0.0486	0.0069	±	0.0511	**0.76**
	$\geq$ 10.0	-0.0710	±	0.0928	0.0321	±	0.1138	**-0.70**
Center -45 – +44	0.2 - 0.4	0.2142	±	0.0659	0.0084	±	0.0480	**2.53**
	0.4 - 1.0	0.0604	±	0.0582	0.0147	±	0.0439	**0.63**
	1.0 - 3.2	0.0406	±	0.0752	0.0213	±	0.0669	**0.19**
	3.2 -10.0	0.4467	±	0.1656	0.0963	±	0.1214	**1.71**
	$\geq$ 10.0	0.2398	±	0.3278	0.3224	±	0.3070	**-0.18**
Forward 45 – 134	0.2 - 0.4	-0.0097	±	0.0231	0.0005	±	0.0167	**-0.36**
	0.4 - 1.0	0.0224	±	0.0254	0.0011	±	0.0232	**0.62**
	1.0 - 3.2	0.0086	±	0.0359	0.0029	±	0.0359	**0.11**
	3.2 -10.0	0.1466	±	0.0786	0.0198	±	0.0667	**1.23**
	$\geq$ 10.0	0.0617	±	0.1525	0.0181	±	0.1431	**0.21**
Anticenter 135 – 224	0.2 - 0.4	0.0217	±	0.0258	0.0020	±	0.0216	**0.59**
	0.4 - 1.0	0.0197	±	0.0292	0.0024	±	0.0237	**0.46**
	1.0 - 3.2	-0.0080	±	0.0387	0.0025	±	0.0372	**-0.20**
	3.2 -10.0	-0.0114	±	0.0819	0.0147	±	0.0667	**-0.25**
	$\geq$ 10.0	-0.0385	±	0.1532	0.0795	±	0.1975	**-0.47**
Backward 225 – 314	0.2 - 0.4	0.3422	±	0.1401	0.0183	±	0.0725	**2.05**
	0.4 - 1.0	0.0823	±	0.1054	0.0231	±	0.0749	**0.46**
	1.0 - 3.2	0.0683	±	0.1277	0.0397	±	0.0850	**0.19**
	3.2 -10.0	0.1307	±	0.2378	0.1062	±	0.2638	**0.07**
	$\geq$ 10.0	-0.0294	±	0.3827	0.5520	±	0.4787	**-0.95**

5.4.3 Compare with previous result

Table 5.11 lists the f_E and s of the current analysis and the 1993 analysis. For the galactic plane enhancement factor f_E, three data sets all give a consistent trend. Maximum deviation from the isotropic background happens at around $0.4 - 1.0 EeV$; then the significance drops at higher energy. For the galactic latitude gradient, although the 1993 analysis had some positive gradient, this analysis shows no signs of galactic latitude gradient.

Table 5.10. The galactic latitude gradient of stereo data.

Longitude (degree)	Energy (EeV)	Data Mean		SD	background Mean		SD	**Sigma** (σ)
	0.2 - 0.4	0.0108	±	0.0233	0.0210	±	0.0623	**-0.15**
All	0.4 - 1.0	-0.0511	±	0.0246	0.0203	±	0.0358	**-1.64**
1 – 360	1.0 - 3.2	-0.0408	±	0.0361	0.0078	±	0.0320	**-1.01**
	3.2 -10.0	0.0850	±	0.0866	0.0354	±	0.0953	**0.39**
	$\geq$ 10.0	0.5301	±	0.2089	0.3164	±	0.4179	**0.46**
	0.2 - 0.4	0.2823	±	0.1226	0.4837	±	0.3322	**-0.57**
Center	0.4 - 1.0	0.0931	±	0.0897	0.1300	±	0.1001	**-0.27**
-45 – +44	1.0 - 3.2	0.0678	±	0.1293	0.1904	±	0.1726	**-0.57**
	3.2 -10.0	1.3849	±	0.7065	0.1232	±	0.6026	**1.36**
	$\geq$ 10.0	0.5454	±	1.2478	0.4090	±	2.8237	**0.04**
	0.2 - 0.4	0.0314	±	0.0361	0.0445	±	0.1119	**-0.11**
Forward	0.4 - 1.0	-0.0298	±	0.0394	0.0718	±	0.0869	**-1.06**
45 – 134	1.0 - 3.2	-0.0274	±	0.0584	0.0089	±	0.0650	**-0.42**
	3.2 -10.0	0.2610	±	0.1274	0.0190	±	0.1619	**1.18**
	$\geq$ 10.0	0.4077	±	0.2916	0.2671	±	0.5167	**0.24**
	0.2 - 0.4	0.0257	±	0.0403	0.0221	±	0.0474	**0.06**
Anticenter	0.4 - 1.0	-0.0411	±	0.0416	0.0116	±	0.0486	**-0.82**
135 – 224	1.0 - 3.2	0.0498	±	0.0614	0.0156	±	0.0607	**0.40**
	3.2 -10.0	-0.1512	±	0.1415	0.1101	±	0.1840	**-1.13**
	$\geq$ 10.0	0.2198	±	0.7138	0.2968	±	0.4856	**-0.09**
	0.2 - 0.4	0.1861	±	0.2445	0.2868	±	1.7938	**-0.06**
Backward	0.4 - 1.0	0.3645	±	0.2708	0.1294	±	0.3612	**0.52**
225 – 314	1.0 - 3.2	-0.0352	±	0.2915	0.1807	±	0.9899	**-0.21**
	3.2 -10.0	6.8436	±	14.4536	0.4156	±	10.0039	**0.37**
	$\geq$ 10.0	3.8126	±	3.7058	-0.6275	±	38.5181	**0.11**

Table 5.11. Summary of galactic latitude dependent analyses in sigma. Stereo 93 means results in 1993 analysis using stereo data. The lowest energy bin of stereo 93 is $0.3 - 1.0 EeV$.

	f_E			S		
Energy (EeV)	mono	stereo	stereo 93	mono	stereo	stereo 93
0.2 – 0.4	1.90	0.31		-0.29	-0.15	
0.4 – 1.0	2.24	1.76	1.12	-0.18	-1.64	-1.53
1.0 – 3.2	1.44	1.26	0.80	-0.45	-1.01	1.97
3.2 – 10.	-0.13	0.52	0.77	0.76	0.39	1.72
> 10.	-1.07	-0.66	0.15	-0.70	0.46	0.55

5.5 Super Galactic Plane

The supergalactic plane is a plane in the sky which runs through the Virgo cluster and most of the nearby galaxies. Shaver and Pierre extend this to radio galaxies with an approximate distance cutoff of red shift $z = 0.03$ [56, 57, 58]. This plane intersects the galactic plane at a longitude about $l = 137°$ and $317°$ at an angle of about $82°$.

5.5.1 Clustering along super galactic plane

The cosmic rays may come from some sources related to the distribution of stars. The majority of stars lie in the galactic disk. Cosmic rays above the EeV energy range have a gyroradius longer than the thickness of the galactic disk. Therefore the arrival direction of EeV cosmic rays may follow the mass distribution of the local galaxy or clusters of galaxies, depending on where the sources are. It might be interesting to look for clustering of cosmic rays along the galactic or the supergalactic plane [59, 60, 61]. The absolute and root-mean-square values of both the galactic latitude and the supergalactic latitude are calculated and compared to background data.

$$\langle |b(E)| \rangle = \frac{\sum_i |b_i|}{N(E)} \qquad \langle |sgl(E)| \rangle = \frac{\sum_i |sgl_i|}{N(E)}$$

$$RMS_b(E) = \sqrt{\frac{\sum_i \times b_i^2}{N(E)}} \qquad RMS_{sgl}(E) = \sqrt{\frac{\sum_i sgl_i^2}{N(E)}}$$

where b and sgl are the galactic/supergalactic latitude, and E is the energy bin. If cosmic rays are clustering around the galactic plane, they should produce smaller $\langle |b(E)| \rangle$ and $RMS_b(E)$ than an isotropic background does. By counting how many background files produce smaller values than data, we have a probability that represents the chance of an isotropic background producing a better clustering than the data do.

$$P(\langle |b(E)| \rangle) = \frac{Number\ of\ background\ files\ that\ \langle |b(E)| \rangle_{background} < \langle |b(E)| \rangle_{data}}{Total\ number\ of\ background\ files}$$

Stanev *et al.* claim that EHECRs are clustering around the supergalactic plane [61]. The effect is most prominent at energy greater than $40EeV$. Here we use a similar analysis and use monocular FE1 data to search for this effect.

There is a small difference between the work of Stanev *et al.* and this work. They use ground array data, (including Haverah Park, part of AGASA data, Volcano Ranch, and Yakutsk); they need to use a zenith angle cut at 45°. Since Fly's Eye is more sensitive to showers near zenith angle 45° when the energy is greater than $10EeV$, it is not necessary to use such a cut.

We use a filter program to read out events with energy (from Gaussian fit) greater than $10EeV$ and write them to a file. Because the number of events is low, data quality becomes important. To make sure we have good events, we add several strict cuts:

- The angular error $d\theta$ and $\sin\theta d\phi$ must be less than 15°.
- The shower maximum must be between two boundaries $X_{max-low}$ and $X_{max-high}$.

$$X_{max-low} = 300 + 80\log_{10}(E)$$

$$X_{max-high} = 1100 + 80\log_{10}(E)$$

  where E is energy in EeV.

- The relative error of shower maximum dX_{max}/X_{max} must be less than 1.
- The shower width must be between $140gm/cm^2$ and $400gm/cm^2$.
- If the Gaisser-Hillas fit is available, the first interaction depth must be less than $400gm/cm^2$.

After these strict cuts, we are left with 195 events with energy greater than $10EeV$, compared with 341 events using standard cuts. Then 10,000 background files are simulated by using the zenith angle of real events, the randomly assigned azimuth angle, and the scrambled real run time.

Figure 5.13 plots the position of all events used in this analysis. Table 5.12 lists the number of events in each energy interval for Fly's Eye and Stanev *et al.*.

Results from Stanev *et al.* and our analysis are listed in Table 5.13. Some systematic difference can be found. Due to the zenith angle cut, the results from Stanev *et al.* are

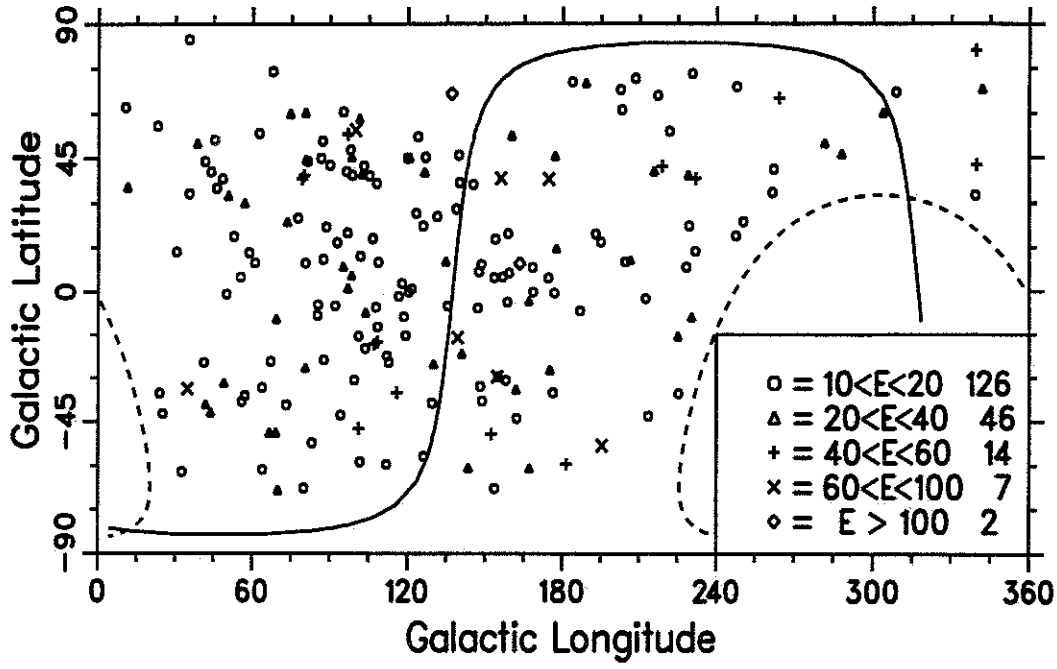

Figure 5.13. The position of events used in supergalactic plane clustering. The solid line is the supergalactic equator. The dash line is the declination –30 degree, approximately the lower limit of the visible sky of Fly's Eye.

Table 5.12. The result of supergalactic plane clustering. The world data set includes data from Haverah Park, part of AGASA data, Volcano Ranch, and Yakutsk only!

Energy (EeV)	Haveraph Park	World data set	Fly's Eye
$\geq 10.$			195
$\geq 20.$	73	143	69
$\geq 40.$	27	42	23
$\geq 60.$	12	16	9
$\geq 100.$		8	2

smaller than our results both in data and background. From Table 5.13, we see some results similar to those of Stanev *et al.* The probabilities of both analyses are shown in Figure 5.14. The probability reaches a minimum at energy greater than $40EeV$. We have a probability 0.0662 of $\langle|sgl|\rangle$ and 0.0173 of RMS_{sgl}. That would correspond to 1.34σ and 2.13σ effect. Figure 5.15 shows the distribution of the supergalactic latitude at energy $E \geq 40EeV$. Due to the low number of events, the probability rises at energy

Table 5.13. The result of supergalactic plane clustering

	Energy	Fly's Eye			Stanev *et al.*		
	(EeV)	Data	background	**Prob.**	Data	background	**Prob.**
$\langle\|b\|\rangle$	≥ 10	33.58	32.63	0.7397			
	≥ 20	38.21	32.68	0.9853	31.2	30.2	0.880
	≥ 40	42.00	32.68	0.9814	38.3	30.0	0.998
	≥ 60	37.71	32.64	0.7608	41.0	31.3	0.978
	≥ 100	38.12	32.78	0.6529	35.5	31.4	0.690
RMS_b	≥ 10	39.50	38.84	0.6731			
	≥ 20	42.93	38.98	0.9453	37.9	36.7	0.890
	≥ 40	46.35	39.42	0.9437	45.6	36.8	0.998
	≥ 60	44.02	40.57	0.6688	48.1	38.4	0.976
	≥ 100	67.33	52.37	0.7784	47.9	40.2	0.820
$\langle\|sgl\|\rangle$	≥ 10	31.83	31.76	0.5174			
	≥ 20	30.71	31.80	0.3453	25.5	27.3	0.310
	≥ 40	24.94	31.70	0.0662	20.3	27.4	0.012
	≥ 60	21.94	31.50	0.0890	19.7	29.5	0.027
	≥ 100	15.17	31.60	0.1566	18.8	30.4	0.058
RMS_{sgl}	≥ 10	37.53	38.45	0.2760			
	≥ 20	36.17	38.61	0.1794	31.9	33.5	0.340
	≥ 40	28.86	38.90	0.0173	26.2	33.8	0.012
	≥ 60	27.37	39.64	0.0584	26.4	36.6	0.038
	≥ 100	25.09	49.19	0.1701	26.2	38.3	0.072

greater than $60EeV$. Our results seems to reproduce the low probabilities of $\langle|sgl|\rangle$ and RMS_{sgl} as observed by Stanev *et al.* However if the standard cuts instead of strict cuts were used, the low probabilities disappear. This disappearance might be caused by those poorly reconstructed events which have large error and wash out the effect of clustering.

5.5.2 Clustering along galactic plane

To see whether lower energy cosmic rays cluster along the galactic plane, we extend the previous analysis to lower energy. Two data sets are used in this analysis. The first set uses the same strict data cuts and a program similar to those used in previous analysis. This strict data set contains events that have good geometric and energy resolution. Six energy intervals are used, from $0.2EeV$ to above $32EeV$. The background files are generated in the same way they are generated in previous analysis but only 2500 data sets are generated. The results are shown in Table 5.14.

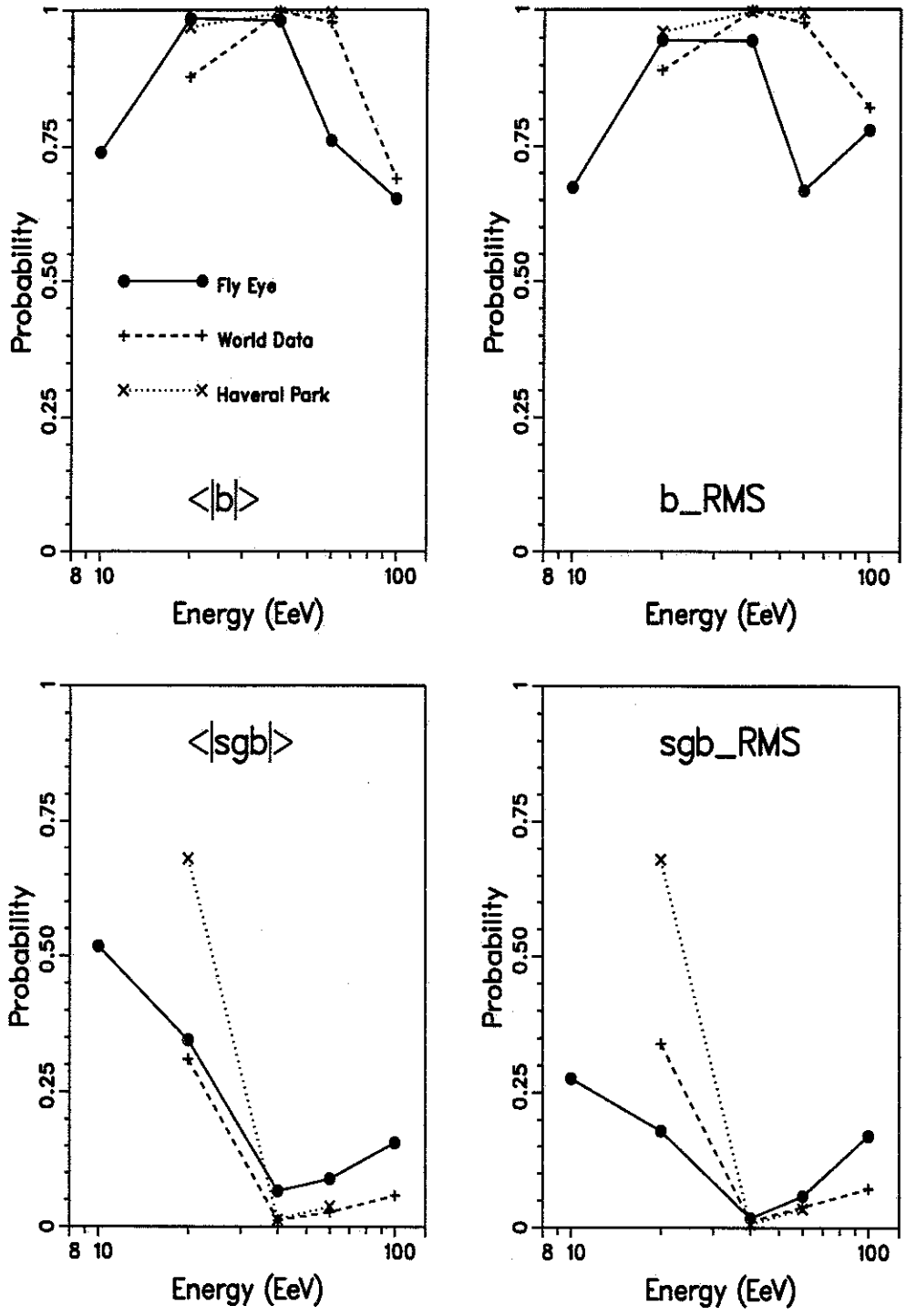

Figure 5.14. The probability of clustering along galactic plane and supergalactic plane that come from isotropic background.

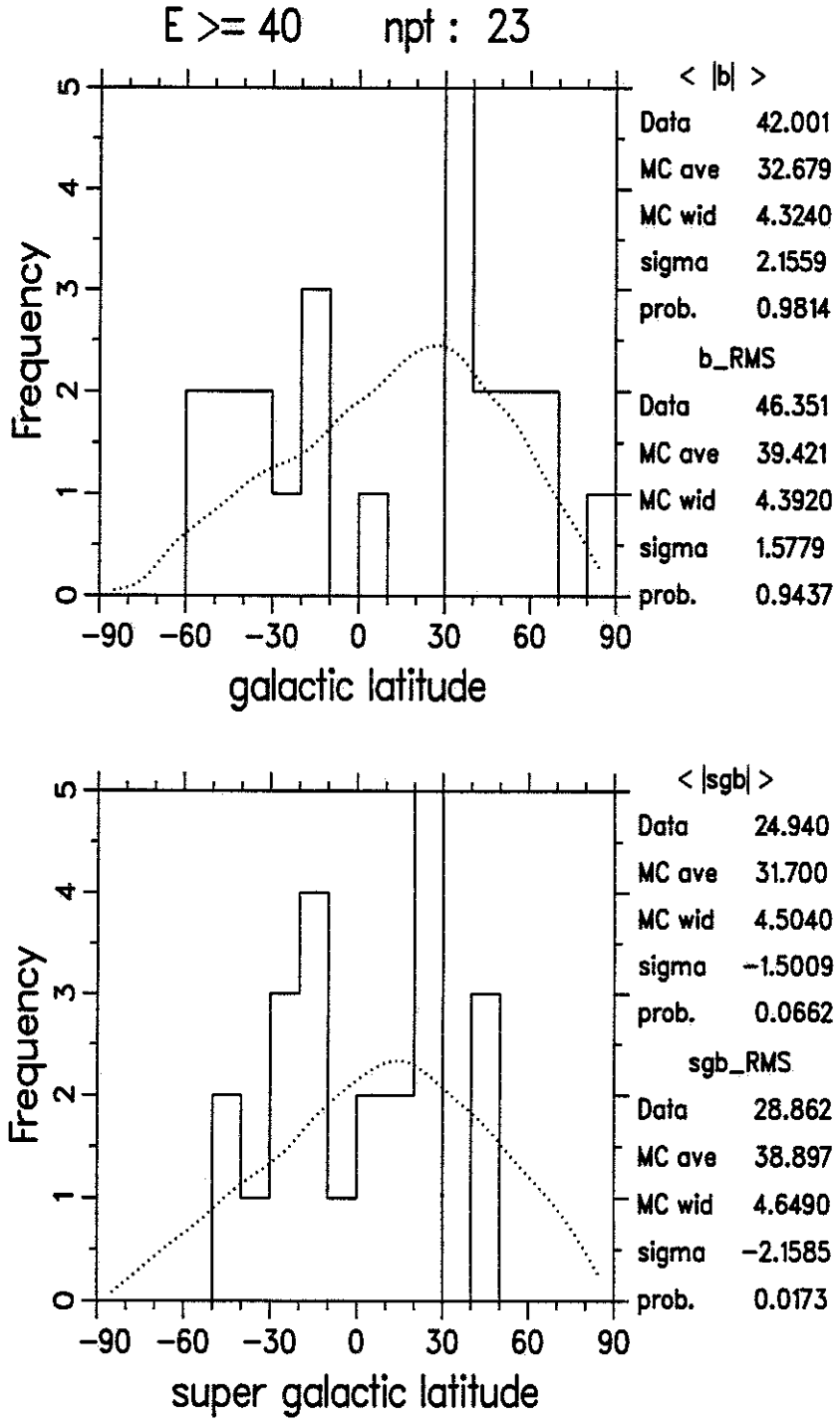

Figure 5.15. The galactic latitude and supergalactic latitude distribution at energy $E \geq 40EeV$. The solid line is the distribution of mono Fly's Eye data. The dash line is the prediction from isotropic background.

Table 5.14. The result of clustering analysis of strict data set.

	Energy (EeV)	Data	Mean	width	sigma	Probability
$\langle\|b\|\rangle$	0.2 – 0.4	32.50	32.17	0.31	1.068	0.852
	0.4 – 1.0	31.74	32.33	0.31	-1.856	0.026
	1.0 – 3.2	31.95	32.49	0.40	-1.342	0.098
	3.2 – 10.0	31.56	32.56	0.78	-1.281	0.100
	10.0 – 32.0	32.00	32.62	1.59	-0.389	0.350
	$\geq$ 32.0	42.67	32.71	3.95	2.526	0.991
RMS_b	0.2 – 0.4	39.37	38.97	0.31	1.298	0.896
	0.4 – 1.0	38.36	38.86	0.31	-1.585	0.054
	1.0 – 3.2	38.23	38.78	0.40	-1.415	0.085
	3.2 – 10.0	37.67	38.77	0.77	-1.415	0.081
	10.0 – 32.0	38.15	38.85	1.58	-0.806	0.324
	$\geq$ 32.0	47.54	39.42	3.98	2.039	0.977
$\langle\|sgl\|\rangle$	0.2 – 0.4	30.05	30.28	0.29	-0.817	0.208
	0.4 – 1.0	31.44	30.68	0.30	2.487	0.993
	1.0 – 3.2	31.91	31.20	0.40	1.765	0.964
	3.2 – 10.0	31.74	31.54	0.79	0.251	0.608
	10.0 – 32.0	33.05	31.85	1.70	0.705	0.757
	$\geq$ 32.0	23.63	31.71	4.04	-2.000	0.019
RMS_{sgl}	0.2 – 0.4	36.32	36.61	0.30	-0.993	0.164
	0.4 – 1.0	37.85	37.13	0.31	2.35	0.991
	1.0 – 3.2	38.53	37.74	0.41	1.946	0.975
	3.2 – 10.0	37.97	38.15	0.79	-0.221	0.425
	10.0 – 32.0	38.96	38.54	1.710	0.243	0.591
	$\geq$ 32.0	27.67	38.77	4.14	-2.68	0.005

For the second data set w use the event probability density we used in other analyses. This data set contains some events with large error but has a built-in point spread function. The analysis program is similar to the program used for the strict data set. The definition is somewhat different: the absolute and root-mean-square value of both galactic latitude and super galactic latitude are weighted by the event probability density.

$$\langle|b(E)|\rangle = \frac{\sum_{l,b}\rho(l,b,E)\times|b|}{\sum_{l,b}\rho(l,b,E)} \qquad \langle|sgl(E)|\rangle = \frac{\sum_{l,b}\rho(l,b,E)\times|sgl|}{\sum_{l,b}\rho(l,b,E)}$$

$$RMS_b(E) = \sqrt{\frac{\sum_{l,b}\rho(l,b,E)\times b^2}{\sum_{l,b}\rho(l,b,E)}} \qquad RMS_{sgl}(E) = \sqrt{\frac{\sum_{l,b}\rho(l,b,E)\times sgl^2}{\sum_{l,b}\rho(l,b,E)}}$$

where $\rho(l, b, E)$ is the event probability density of data or scrambled events. The results are shown in Tables 5.15 and 5.16. Figure 5.16 show the probability of clustering along the galactic plane and the supergalactic plane.

For the galactic plane clustering, both monocular and stereo data show a rising probability as the energy increases and the maximum deviation that happens at energy interval $0.4 - 1.0EeV$. This effect is washed out at energy above $3.2EeV$. Figure 5.17 shows the distribution of the galactic latitude of the mono data and the background at $0.4 - 1.0EeV$. The excess of events come from a small bump near the galactic plane. There are about 925 events in $-10° \leq b \leq 10°$ but only 862.3 events are expected. This excess is approximately 2σ, similar to the result integrated from $-90°$ to $+90°$.

For the supergalactic plane clustering, the deviation from isotropic background predication is most significant at energy greater than 32 EeV. However, this clustering is seen only in the strict data set. Figure 5.18 shows the distribution of the supergalactic latitude at $E \geq 32EeV$. At supergalactic latitude $-50° \sim +50°$, the data have 28 events but only 21.8 events are expected. The excess is only about 1.3σ. However, the deficit of event at $|sgl| > 50°$ is about 2.48σ. In order to produce such a pair of excess and deficit, the probability is only 0.5%, approximately 2.57σ.

Another interesting feature is that at low energy ($E < 3.2EeV$) most of the events come from low galactic latitude and high supergalactic latitude but this trend reverse at higher energy ($E > 10EeV$).

Table 5.15. The result of clustering analysis of monocular data.

	Energy (EeV)	Data	Mean	width	sigma	Probability
$\langle\|b\|\rangle$	0.2 – 0.4	31.91	32.43	0.18	-2.960	< 0.01
	0.4 – 1.0	31.58	32.21	0.18	-3.583	< 0.01
	1.0 – 3.2	31.82	32.48	0.30	-2.213	0.01
	3.2 – 10.0	32.21	32.06	0.56	0.260	0.64
	$\geq$ 10.0	33.93	32.21	1.11	1.545	0.95
RMS_b	0.2 – 0.4	38.50	38.92	0.153	-2.690	< 0.01
	0.4 – 1.0	38.00	38.56	0.17	-3.273	< 0.01
	1.0 – 3.2	38.16	38.75	0.29	-2.024	0.02
	3.2 – 10.0	38.31	38.19	0.55	0.225	0.58
	$\geq$ 10.0	39.93	38.54	1.10	1.266	0.89
$\langle\|sgl\|\rangle$	0.2 – 0.4	31.01	31.11	0.16	-0.628	0.26
	0.4 – 1.0	31.89	31.87	0.19	0.134	0.53
	1.0 – 3.2	32.24	31.92	0.31	1.048	0.85
	3.2 – 10.0	32.46	32.24	0.54	0.404	0.66
	$\geq$ 10.0	32.90	33.11	0.93	-0.223	0.43
RMS_{sgl}	0.2 – 0.4	37.35	37.52	0.17	-0.990	0.18
	0.4 – 1.0	38.41	38.33	0.18	0.404	0.61
	1.0 – 3.2	38.80	38.58	0.32	0.684	0.71
	3.2 – 10.0	38.63	38.88	0.57	-0.430	0.35
	$\geq$ 10.0	38.96	39.54	0.93	-0.624	0.28

Table 5.16. The result of clustering analysis of stereo data.

	Energy (EeV)	Data	Mean	width	sigma	Probability
$\langle\|b\|\rangle$	0.2 – 0.4	32.41	32.85	0.25	-1.761	0.02
	0.4 – 1.0	31.95	33.12	0.27	-4.348	< 0.01
	1.0 – 3.2	31.84	32.79	0.50	-1.913	0.02
	3.2 – 10.0	31.67	32.41	0.82	-0.901	0.18
	$\geq$ 10.0	33.77	30.39	2.23	1.518	0.93
RMS_b	0.2 – 0.4	38.84	39.21	0.24	-1.561	0.04
	0.4 – 1.0	38.21	39.44	0.29	-4.224	< 0.01
	1.0 – 3.2	37.92	38.95	0.45	-2.268	< 0.01
	3.2 – 10.0	38.13	38.60	0.84	-0.560	0.25
	$\geq$ 10.0	39.63	36.25	2.43	1.390	0.91
$\langle\|sgl\|\rangle$	0.2 – 0.4	32.34	32.00	0.21	1.618	0.94
	0.4 – 1.0	32.72	32.10	0.29	2.116	0.99
	1.0 – 3.2	33.56	32.69	0.51	1.712	0.96
	3.2 – 10.0	32.68	33.35	1.05	-0.647	0.27
	$\geq$ 10.0	31.65	34.61	2.56	-1.158	0.11
RMS_{sgl}	0.2 – 0.4	38.65	38.38	0.22	1.253	0.92
	0.4 – 1.0	39.24	38.50	0.30	2.160	0.98
	1.0 – 3.2	39.94	39.18	0.49	1.548	0.95
	3.2 – 10.0	38.72	39.89	1.05	-1.116	0.13
	$\geq$ 10.0	38.29	41.67	2.42	-1.400	0.10

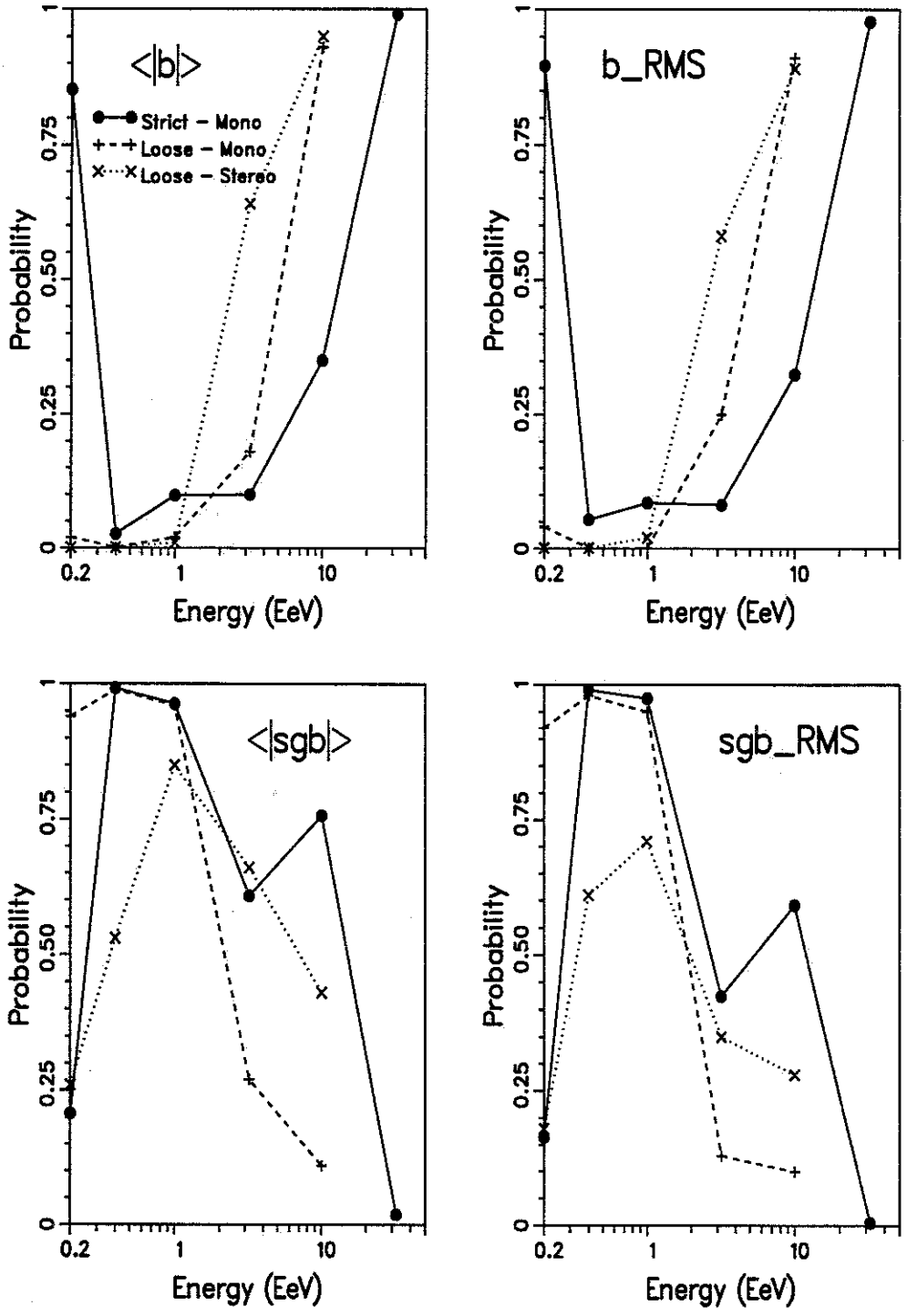

Figure 5.16. The probability of clustering along galactic plane or supergalactic plane that come from isotropic background.

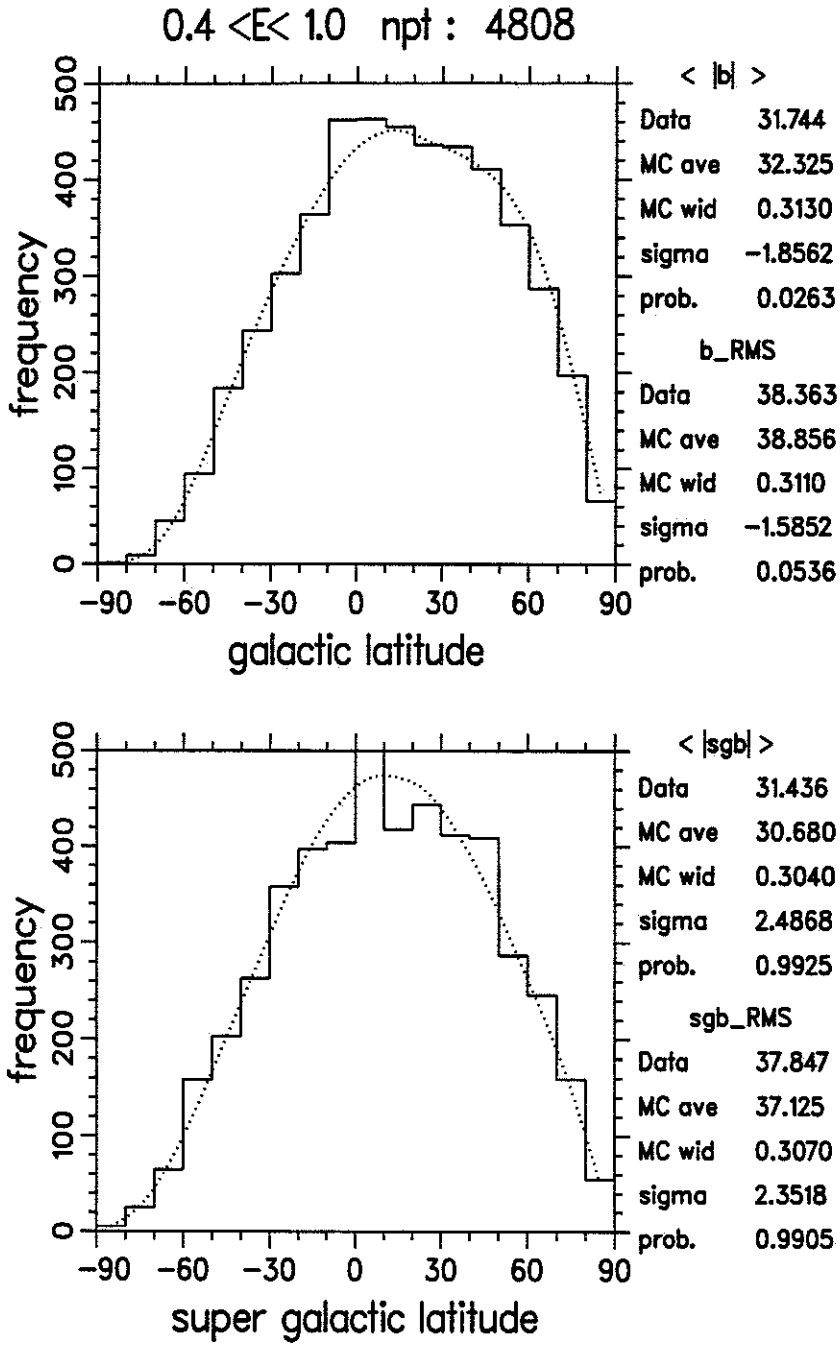

Figure 5.17. The galactic and supergalactic latitude distribution at energy $0.4 < E < 1.0 EeV$. The solid step line is data from strict data set. The dot line is the prediction from isotropic background.

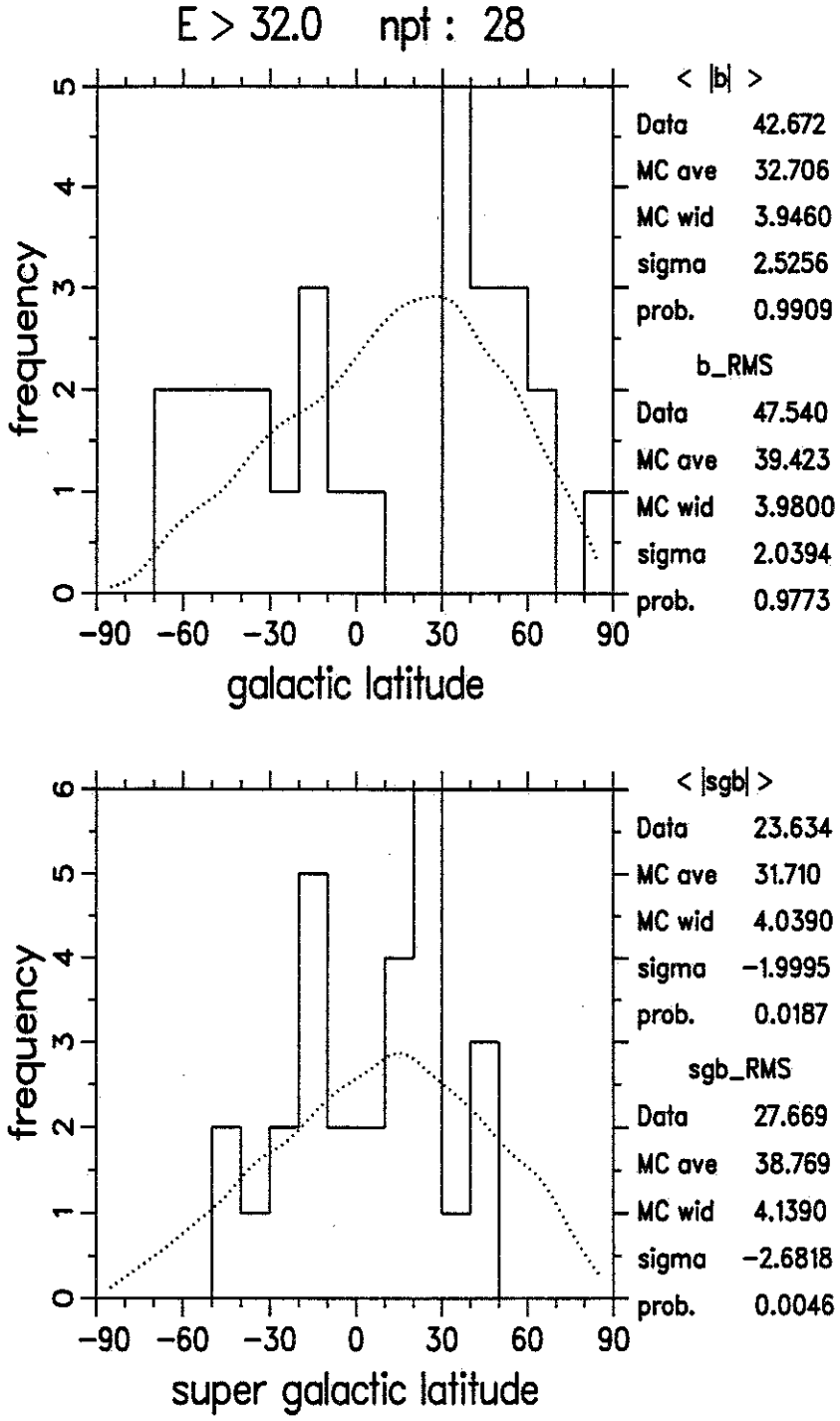

Figure 5.18. The galactic and supergalactic latitude distribution at energy $E > 32EeV$. The solid step line is data from strict data set. The dot line is the prediction from isotropic background.

CHAPTER 6

SUMMARY

The origin of extremely high energy cosmic rays is always an important topic. The Fly's Eye group has studied two of the most important topics of EHECR physics – the spectrum and composition. Results from those two studies show evidence of two components in EHECRs. One is a heavy source, mainly iron nuclei, which dominates at energy lower than $3EeV$. The other is a light source, mainly protons, which dominates at a higher energy. It is widely believed that the first (heavy) component originates in our galaxy and probably is a continuation of the *'knee'* region. Due to a lack of possible galactic acceleration mechanisms, the second (light) component is believed to be extragalactic in origin. The main task of the anisotropy analysis is then to determine where these EHECRs come from. This is the main concern of this dissertation.

It would be nice if we could trace back the trajectory of cosmic rays and see where they come from. Unfortunately, most of them are charged particles. Their trajectories are bent by magnetic fields. For iron nuclei at an energy of $15EeV$, the gyroradius in the galactic magnetic field is about $300pc$, equivalent to the thickness of the galactic disk. Below this energy, the smaller gyroradius will make detection of anisotropy more difficult. However at higher energy, protons appear to dominate the flux and should have good anisotropy. But the extremely low flux of these cosmic rays and the relatively small aperture of the current detector make detection of this anisotropy very difficult. Statistics are extremely low and result in high statistical fluctuation. Although many papers have reported on the study of anisotropy in the extrahigh energy region, the results are quite ambiguous.

This dissertation tries to dig out a small anisotropy buried in an isotropic background. Although some improvements were made from previous analyses, the result is still limited by low statistics and large fluctuation. I try to use several analyses and then draw a conclusion from the results of all analyses.

I start with a reexamination of system resolution and study the difference between the real detector and Monte-Carlo. Some systematic errors and differences are found. Section 6.1 reviews these errors and differences.

Section 6.2 reviews some major improvements presented in this dissertation. The results of anisotropy analyses are summarized in section 6.3. The final conclusion of this dissertation is in section 6.4.

6.1 Systematic Errors

In the sections 3.6 and 3.7, we observed some systematic errors in event reconstruction and in the detector Monte-Carlo. Here is a short summary.

- The relative error of R_p of mono data increases as the energy increases.
- The relative error of X_{max} and the energy have a linear relation with X_{max} or $\log_{10} Energy$. The relation may depend on composition and epoch.
- The mean track length of real data is shorter than that of the Monte-Carlo.
- The mean ψ of real data does not change much with energy. But the mean ψ of Monte-Carlo data decreases as the energy increases.
- The mean θ of real data is smaller than that of Monte-Carlo.

The effect of these systematic differences will change the aperture and make the resolution worse than predicted by Monte-Carlo. This dissertation makes no attempt to correct the spectrum and composition and does not use the zenith angle θ distribution of Monte-Carlo for acceptance. All the analyses use data from real events.

6.2 New Improvement

Several new improvements were made in this dissertation. Some of the major improvements are listed belowed.

- Reconstruct system on/off time from triggering pattern. This new system on/off time replaces the weather code and is a closer approximation to the real system on/off time.

- Study of the point spread function of zenith angle θ and azimuth angle ϕ. This function can predict the error distribution statistically. This improvement makes it possible to use events with large uncertainity and therefore increases statistics. This improvement also benefits to small scale anisotropy analysis.

- Using the point spread function, we are able to predict the shower zenith distribution more precisely and generate acceptance to produce a smooth isotropic background.

- A new term, the event rate, is introduced in the live time background prediction. This term helps to reflect the dynamic trigger condition caused by both detector and weather. It generates a more realistic background prediction. This background is quite consistent with the scrambled event background in large scale for both the mono and the stereo background. In small scale, there is approximately a 21% difference between two types of the stereo background. However, the mean difference in the mono background is only 4.3%.

- Based on my calculation, a new normalization constant, 1.437, was used in the galactic plane enhancement equation. The original value of 1.402 was used by Wolfendale and others.

- A new clustering analysis which studies the probability of events clustering along the galactic or the supergalactic equator was performed.

6.3 Summary of Anisotropy Analyses

There are three data sets. The first two, mono and stereo, are the event probability densities that use events that pass the standard data cuts and have a built-in point spread function. Thus the geometric information is correct but the energy factor may not be so precise. The third data set uses events that pass strict data cuts to insure good geometric and energy reconstruction but does not have a built-in point spread function.

In order to compare results from five analyses, I rewrote some results from significance σ to probability according to one sided Gaussian probability. It is the probability of an isotropic background generating an anisotropy as large as that of the observed data. The

smaller the probability, the larger the anisotropy. Some results of the analyses are listed in Table 6.1.

6.3.1 Anisotropy related to galactic structure

6.3.1.1 Isotropic background predication. In large scale, the live time and the scrambled events backgrounds are quite consistent. The systematic difference between the two types of background is less than 3±13% for mono data and less than 5±18% for stereo data. However, as the energy increases, the fluctuation increases due to the smaller number of events. All the subsequent analyses use the scrambled events backgrounds.

6.3.1.2 Six lobes analysis. We see some common trends between mono and stereo data. The north and south lobes have smaller event probability density than expected. The center lobe also has smaller event probability density than expected, whereas the anticenter lobe has more event probability density than expected. This effect cannot be completely explained by systematic error in the background prediction.

Table 6.1. Summary of analyses related to galactic structure.

		Probability					
Energy (EeV)		$0.2-0.4$	$0.4-1.0$	$1.0-3.2$	$3.2-10$	>10	>32
Six lobes analysis							
mono	north	0.4404	0.1515	0.1210	0.9441	0.4404	
	south	0.0013	0.0044	0.3264	0.1736	0.9767	
stereo	north	0.2090	0.0001	0.0031	0.5987	0.9788	
	south	0.1736	0.2420	0.5478	0.4168	0.3156	
Galactic plane enhancement factor							
	mono	0.0287	0.0125	0.0749	0.5517	0.8577	
	stereo	0.3783	0.0392	0.1038	0.3015	0.7454	
Galactic plane clustering (b_{RMS})							
	mono	0.01†	0.01†	0.01	0.64	0.95	
	stereo	0.02	0.01†	0.02	0.18	0.93	
	strict	0.852	0.026	0.098	0.100	0.350	0.991
supergalactic plane clustering (sgl_{RMS})							
	mono	0.18	0.61	0.71	0.35	0.28	
	stereo	0.92	0.98	0.95	0.13	0.10	
	strict	0.164	0.991	0.975	0.425	0.591	0.005

† : original probability < 0.01, use 0.01 as upper limit.

6.3.1.3 Galactic plane enhancement analysis. We see a positive galactic plane enhancement factor f_E at energy below $3.2EeV$. Although the significances are low, (highest significance 2.24σ), the trend is the same for mono, stereo, and 1993 stereo analysis. We do not find significant difference between the four general directions: center, forward, anticenter, and backward.

6.3.1.4 Galactic latitude gradient analysis. The galactic latitude gradient analysis does not show significant gradient in the whole sky or the four general directions, meaning that the arrival direction of cosmic rays is quite symmetric along the galactic plane.

6.3.1.5 Harmonic analysis. We search for harmonics in nine different declination bins. None of these bins have significant first and second harmonics. Although the harmonic analysis does not give us any information about galactic coordinates, it does give an independent view of the isotropic background.

6.3.1.6 Galactic plane clustering. Both the mono and stereo data sets support a clustering along the galactic plane at energy $< 3.2EeV$ with a probability <2% coming from random background fluctuation. But the strict data sets have an 85.2% probability at $0.2-0.4EeV$; then the probability drops to 2.6% at $0.4-1.0EeV$. All bins except one support anisotropy. The overall trends between mono, stereo, and strict data sets are the same: lowest probability (highest clustering effect) at $0.4-1.0EeV$ and probability rises as energy increases.

6.3.2 Anisotropy related to supergalactic structure

To look for anisotropy related to the supergalactic plane, we combined several energy intervals. These compound probabilities are listed in Table 6.2. For the higher energy bins, the clustering analysis shows a significant clustering effect along the supergalactic plane above $32EeV$. This effect is most significant in the strict data set. This effect is washed out in the same analysis when standard data cuts are used. The reason may be that the poor energy resolution in the mono/stereo data sets allows some lower energy events to penetrate into the higher energy bins and destroy the clustering effect.

Although both the strict data set and that of Stanev *et al.* support some effect of clustering along the supergalactic plane, the statistics are still low. The Akeno group also reports that about 30% of events that have energy $> 40EeV$ are concentrated in a band from $0°$ to $10°$ in the supergalactic latitude. They also have about 19% of events come from supergalactic latitude $|sgl| > 50°$. Contradictory to Akeno's result, our strict data sets have no events coming from $|sgl| > 50°$. This clustering effect is not yet solidly confirmed.

In another study, E. Waxman, *et al.* study the correlation of this clustering effect and the large scale structure of some nearby clusters of galaxies. They find the clustering effect but do not find a correlation of this effect with the known large scale structure [63]. Although this clustering effect is confirmed by Waxman *et al.* and by us, it may not be direct evidence of extragalactic origin of EHECRs.

6.4 Conclusion

Anything we see in anisotropy is a combination of background prediction and possible anisotropy. In this study, we generate two types of backgrounds (live time background and scrambled event background) and study the difference between them. Statistically, two backgrounds are quite consistent with each other in the larger scale comparison. However, the relative error between two backgrounds has a large fluctuation, typically $\pm 10\% \sim \pm 20\%$. The harmonics analysis shows no signs of significant deviation from the isotropic background. This result also supports the fact that the background is reasonably

Table 6.2. The compound probability of supergalactic plane clustering. These results combine several energy intervals, as shown on the first row.

		Compound Probability			
Energy (EeV)		≥ 3.2	≥ 10.0	≥ 32	$< 3.2EeV$
$< \|sgl\| >$	mono	0.3256	0.28		0.6376
	stereo	0.1341	0.10		0.9998
	strict	0.1484	0.0753	0.019	0.7798
sgl_{RMS}	mono	0.3256	0.28		0.5307
	stereo	0.0695	0.10		0.9994
	strict	0.0377	0.0202	0.005	0.7193

isotropic. However, the large fluctuation still plays an important role in interpreting our data.

If the scrambled events backgrounds are really isotropic, then the mean result of f_E and s should be 0. But instead of 0, we always have a certain number and certain fluctuation. The nonzero mean value tell us that there are some systematic errors in the background. How significant are these systematic errors? We can justify this question by the value of mean/fluctuation. If this number is within ± 1, it could be treated as statistical fluctuation and the background is reasonably isotropic (within 1 sigma). In our data, most of the analysis has the mean of background less than the fluctuation of background except at $E > 10EeV$. The highly fluctuated background at $E > 10EeV$ is a natural consequence of the scrambled events background when the number of events is low. We may readjust the background to let the mean of backgrounds equal 0, but this adjustment may introduce other unknown factors and may be valid for one analysis and invalid for other analyses. So no attempt has been made to adjust backgrounds.

Due to the small systematic error, our anisotropy result may not be as large as the observed number. However, we use statistical difference between data and background to examine the statistical significance of our data.

$$\sigma = \frac{\text{mean of data} - \text{mean of background}}{\sqrt{(\text{error of data})^2 + (\text{error of background})^2}}$$

This is the sigma I used in Chapter 5. In this way, our results are independent of systematic error of background and have the same statistical significance as results that use a perfect isotropic background.

We found some degree of anisotropy in the six lobes analysis, the galactic plane enhancement factor, and the galactic plane clustering. These effects are closely related to each other. The lower event probability density in north and south lobes will generate positive f_E and indeed positive f_E is observed at energy below $3.2EeV$. The clustering of events near the galactic plane will make north and south lobes have fewer events than expected and combined with no latitude gradient, a positive f_E must exist. These analyses form a consistent figure. They all show a possible excess of events near the galactic plane and a possible defict of events near the galactic poles at energy below $3.2EeV$.

However, these analyses use identical data and backgrounds. A consistant result in different analyses should be quite natural. Near the galactic plane, the systematic background fluctuation is only about 5%; our data have excess (925 out of 862.3 at $0.4 < E < 1.0EeV$) approximately 7.3%. Although this excess has a 2σ significance statistically, systematical error still dominates. Unless we can reduce the systematic error, we can not solidly conclude that there is an anisotropy.

From these anisotropy analyses, we see some evidence that there are certain degrees of anisotropy which relate to the galactic plane at energy $E < 10EeV$. We also see minor evidence to support supergalactic plane clustering. However, the results are limited by systematic error. A better isotropic background is necessary to reduce the systematic error and improve the statistical significance. More statistics at $E > 10EeV$ are still needed to prove the correlation between supergalactic structure and arrival direction of cosmic rays.

APPENDIX A

NORMALIZATION OF GALACTIC PLANE ENHANCEMENT FACTOR

Assume the normalization factor of the galactic plane enhancement factor is x,

$$\begin{aligned} I(b) &= I_0\left(1 - f_E + x \times f_E \mathrm{e}^{-b^2}\right) \\ r(b) &= \frac{I(b)}{I_0} = 1 - f_E + x \times f_E \mathrm{e}^{-b^2} \end{aligned}$$

the isotropic distribution would predict $I(b) = I_0$, so $r(b) = 1$. Two distribution should normalized to the same number in the range $-\pi/2 < b < +\pi/2$.

$$\begin{aligned} \int_{-\pi/2}^{+\pi/2} \cos b \ \mathrm{d}b &= \int_{-\pi/2}^{+\pi/2} r(b) \cos b \ \mathrm{d}b \\ &= \int_{-\pi/2}^{+\pi/2} \left(1 - f_E + x \times f_E \mathrm{e}^{-b^2}\right) \cos b \ \mathrm{d}b \end{aligned}$$

Rearrange the formula

$$f_E \int_{-\pi/2}^{+\pi/2} \cos b \ \mathrm{d}b = x f_E \int_{-\pi/2}^{+\pi/2} \mathrm{e}^{-b^2} \cos b \ \mathrm{d}b$$

The left hand side is

$$LHS = f_E \int_{-\pi/2}^{+\pi/2} \cos b \ \mathrm{d}b = f_E \ \sin b \ |_{-\pi/2}^{+\pi/2} = 2 f_E$$

The right hand side is

$$RHS = 2x f_E \int_0^{+\pi/2} \mathrm{e}^{-b^2} \cos b \ \mathrm{d}b$$

then x is

$$x = \frac{LHS}{RHS} = \frac{1}{\int_0^{+\pi/2} \mathrm{e}^{-b^2} \cos b \ \mathrm{d}b}$$

The denominator can be calculate by numerical integral,

$$\int_0^{+\pi/2} \mathrm{e}^{-b^2} \cos b \ \mathrm{d}b = 0.6957$$

So the normalization x is

$$x = \frac{1}{0.6957} = 1.4374$$

APPENDIX B

SHORT HISTORY OF FLY'S EYE OPERATION

1. **epoch 1 : 11/81 - 05/85**

   - 11/81 FE1 construction complete – 2π steradian coverage
   - 2/83 Individual tube threshold adjustment – increased sensitivity
   - 6/83 FE2 prototype (8 mirrors) – test of stereo methods

2. **epoch 2 : 11/85 - 06/87**

   - 11/85 UV filter installation – Improved Signal/Noise
   - 9/86 FE2 expansion (36 mirrors) – Increased stereo aperture
   - 11/86 FE2 construction complete – Stereo data taking began

3. **epoch 3 : 07/87 - 06/88**

   - 7/87 Mirror Anodization (FE1) – Improved Signal/Noise
   - 8/87 Mirror Anodization (FE2) – Improved Signal/Noise
   - 9/87 PeV "Blast" capability at FE2 – PeV γ ray astronomy
   - 12/87 New signal filtering at FE1 – Increased detector sensitivity
   - 4/88 Michigan muon array operating near FE2 – PeV γ ray astronomy

4. **epoch 4 : 07/88 - 04/90**

   - 8/88 Removal of channel 2 trigger at FE1 – attempted to increase detector sensitivity
   - 3/90 CASA on-line with 500 units – PeV γ ray astronomy

5. **epoch 5 : 05/90 - 09/91**

   - 2/91 2 mirror Hires1 prototype operational – New generation detector
   - 3/91 CASA/MIA completed

6. **epoch 6 : 10/91 - 07/92**

   - 10/91 Reinstall channel 2 at FE1 – Return to normal operation
   - 10/91 320 EeV event detected

7. **new generation : 08/92 - 10/95**

   - 7/92 Last FE2 data run
   - 1/93 Last FE1 data run
   - 2/93 14 mirror Hires prototype completed
   - 5/93 Restart FE2 to operate with Hires1 in stereo mode
   - 7/94 Start to decommission FE1
   - 10/95 FE1 decommission completed

APPENDIX C

THE LARGE SCALE BACKGROUND COMPARISON

We comapre two background in 10 degree bins of several coordinates, declination, right ascension, galactic longitude, and galactic latitudes. The *liv* is acceptance and event rate weighted live time. The *ave* is the mean value of 100 sets of scrambled event background.

$$\Delta(x,E) = \frac{\langle liv(x,E)\rangle - \langle ave(x,E)\rangle}{\langle liv(x,E)\rangle}$$

where x is a certain coordinate and E is energy. The relative differences are listed in tables C.1 to C.4.

Table C.1. The relative difference on large scale between *liv* and *ave* as function of declination. The unit is percentage %.

	Mono					Stereo				
DEC	1	2	3	4	5	1	2	3	4	5
-30	-13.34	-20.04	-31.85	9.32	-10.08	86.52	83.41	68.41	-8.89	94.53
-20	-11.73	-9.98	2.25	9.33	3.22	73.13	40.81	29.39	42.23	38.95
-10	10.51	11.35	9.61	7.66	22.81	15.37	17.36	13.41	-16.33	2.36
0	14.55	13.28	6.47	12.57	7.53	21.70	11.30	9.92	19.43	29.30
10	12.20	10.10	7.93	2.92	2.21	13.83	16.48	13.35	11.92	6.86
20	4.87	-1.00	1.31	0.41	3.80	5.00	7.56	1.86	8.53	-8.11
30	-4.90	-5.95	-9.86	-13.03	-30.47	-2.69	-13.91	-6.08	-27.22	-1.77
40	-19.07	-15.77	-13.88	-14.21	-0.88	-20.89	-21.55	-15.65	-10.88	-31.08
50	-14.76	-12.58	-9.48	-0.43	-22.61	-24.45	-16.61	-14.65	-10.05	6.10
60	-2.59	-0.66	0.59	8.33	-7.94	-6.36	-4.90	-4.88	7.72	-39.85
70	7.13	5.09	0.19	-2.83	4.09	5.37	3.29	-11.57	1.18	25.00
80	15.85	11.13	10.42	-7.57	18.86	7.26	0.04	11.72	20.49	29.39
90	25.27	18.07	19.58	-4.01	51.37	9.39	12.97	9.83	-16.25	-14.08

Table C.2. The relative difference on large scale between *liv* and *ave* as function of right ascension. The unit is percentage %.

	Mono					Stereo				
RA	1	2	3	4	5	1	2	3	4	5
10	-1.81	-1.85	-10.97	-8.05	1.06	1.30	-14.40	4.42	-5.99	8.84
20	-1.67	-1.60	-9.17	-4.03	-1.52	-6.01	2.51	5.40	-2.19	-3.46
30	-1.64	5.02	-4.97	-4.57	1.56	4.47	1.10	-5.36	1.55	-8.58
40	-0.89	1.19	-7.58	2.46	5.22	6.86	8.17	-13.65	4.81	10.13
50	-7.03	2.81	-2.91	2.53	12.44	-11.94	-4.51	-8.19	1.23	-0.26
60	-3.89	7.26	-2.60	-3.89	17.22	7.15	-0.74	-5.22	-0.12	-10.25
70	-1.56	7.23	-4.57	0.70	12.16	0.53	7.19	-6.72	-13.17	-23.52
80	3.25	4.47	5.78	-8.74	11.33	-7.15	4.19	-1.10	-7.24	-32.71
90	4.64	-0.16	8.49	-4.32	-2.35	-3.37	6.46	-5.07	0.63	-13.26
100	7.29	1.03	3.04	-3.03	1.43	-0.18	12.44	7.43	1.39	-48.04
110	8.09	5.40	5.13	2.83	0.17	11.65	-5.87	4.22	7.06	-70.19
120	3.51	4.28	6.14	1.20	2.78	7.82	1.88	11.26	8.87	-17.91
130	6.60	-2.40	13.04	4.72	6.65	8.18	-6.25	9.06	7.27	-24.15
140	4.97	-0.40	4.98	8.50	4.65	6.07	5.32	2.96	-1.22	-24.48
150	-0.53	0.78	2.82	2.37	3.89	-0.03	2.59	-4.18	13.03	37.35
160	-2.98	1.96	2.48	4.10	-6.76	-5.00	-0.16	1.91	10.47	-8.74
170	-2.86	-2.38	1.50	-7.69	-7.69	8.76	-4.02	-4.08	1.83	13.55
180	-3.28	-6.44	0.81	11.47	-10.44	-10.03	-3.22	-3.39	21.91	27.84
190	-1.53	2.08	-0.56	4.77	6.99	-2.56	1.12	7.16	17.02	21.54
200	2.09	4.31	-1.80	9.92	1.40	10.94	0.63	7.34	-3.00	25.11
210	-1.49	2.15	2.58	2.18	6.34	8.36	-3.87	8.45	-11.08	31.88
220	2.31	1.95	5.48	6.46	7.75	-16.98	2.86	4.37	-2.06	3.70
230	-0.13	1.22	3.07	-1.02	-6.01	0.77	7.25	4.66	-11.26	-6.72
240	-0.60	-0.05	0.16	3.33	-7.79	-8.53	-6.47	3.14	-19.44	9.82
250	-0.46	-3.88	2.81	8.51	-4.16	-6.29	4.07	2.01	-11.92	19.73
260	-2.77	-2.48	2.41	2.95	5.65	-2.81	1.39	6.39	-14.45	15.20
270	-2.24	2.22	1.52	-2.13	1.98	0.63	8.33	-3.13	-9.55	-9.27
280	3.24	1.92	-3.00	-0.51	-3.16	13.47	2.89	5.58	-22.15	-22.80
290	6.14	-0.07	-3.92	1.60	3.84	0.17	-4.94	-0.87	-1.84	-9.56
300	3.69	-1.06	-0.50	0.45	3.05	2.76	9.15	5.68	10.48	6.58
310	-3.26	-4.79	-2.93	-6.47	-11.90	0.85	2.87	-0.61	10.96	20.47
320	-5.99	-4.91	-4.67	0.26	-19.64	-4.34	-4.07	2.51	11.87	11.29
330	-5.10	-2.55	-0.92	-13.38	-16.68	-7.80	-9.69	2.50	4.32	28.38
340	-0.76	-6.16	-1.09	-6.30	-9.84	2.50	-4.18	-12.87	-1.44	12.70
350	2.51	-7.81	0.32	-1.11	-8.74	-5.85	-7.71	-12.72	-1.80	4.35
360	-2.49	-5.37	-4.39	-2.08	2.47	-0.49	-4.15	-6.83	1.08	21.65

Table C.3. The relative difference on large scale between *liv* and *ave* as function of galactic longitude. The unit is percentage %.

	Mono					Stereo				
l	1	2	3	4	5	1	2	3	4	5
10	5.68	3.69	-1.56	6.07	10.30	8.38	15.11	19.02	-7.15	3.49
20	3.96	11.35	1.94	18.25	20.60	8.76	11.27	12.01	5.91	14.74
30	5.28	7.90	2.43	8.95	9.86	5.66	10.03	17.23	-4.78	21.96
40	8.98	1.93	-3.38	-3.68	-4.65	8.25	-4.43	7.77	-2.79	-15.35
50	4.71	0.12	-1.24	3.68	2.53	-0.68	2.26	-12.44	-14.70	-7.40
60	-0.56	-4.70	-9.11	4.49	-4.99	1.16	-5.84	-5.17	-7.72	-9.38
70	-6.82	-8.23	-7.96	-7.28	-16.18	-5.37	0.20	-0.34	-9.44	3.66
80	-11.21	-9.24	-1.50	-15.00	-24.60	-8.89	-0.95	0.93	-12.61	23.55
90	-5.73	-6.44	3.98	-10.07	-24.42	-9.74	0.58	-1.94	5.67	7.97
100	-3.00	-9.68	0.02	-1.79	-7.79	-1.24	-9.94	-7.64	0.48	25.43
110	-1.48	-2.00	-2.23	-1.77	-5.60	-3.38	-7.69	-10.63	5.87	15.42
120	3.86	4.46	-3.68	-1.04	10.19	-2.01	-11.29	0.14	-4.91	4.80
130	3.63	5.57	1.16	-3.23	14.73	-6.01	2.64	2.47	-1.67	3.58
140	1.11	4.17	-1.28	-4.26	10.47	-4.17	-0.28	-0.21	3.31	-1.54
150	1.35	0.51	-4.18	-7.86	-4.02	-3.51	-0.18	-11.50	1.92	-20.23
160	-2.50	3.70	-4.41	3.38	10.28	7.45	-3.42	-17.25	-10.60	-51.92
170	-2.65	3.27	-0.46	2.78	7.71	-13.19	-7.44	-10.38	2.75	-27.09
180	-6.93	-1.28	-2.23	-3.60	1.64	-14.37	-9.46	-8.14	4.47	-18.43
190	-5.52	-2.81	-1.00	-0.80	-5.78	-11.70	-0.71	4.99	4.36	-26.34
200	-2.66	-4.03	2.64	-1.54	-0.15	11.31	-6.80	7.55	-9.78	-12.37
210	2.14	-2.00	-2.28	-3.38	10.67	15.06	7.14	2.05	2.65	20.35
220	8.38	7.55	8.29	16.52	7.24	15.74	12.43	-1.02	21.07	9.75
230	8.59	9.23	10.50	11.24	1.57	11.57	14.01	12.33	24.33	-25.29
240	9.25	9.53	12.98	0.19	6.42	21.61	22.56	18.43	12.35	23.95
250	9.42	8.29	13.57	4.54	2.45	23.75	21.36	20.25	10.14	13.03
260	9.31	-5.12	9.12	4.21	-19.86	8.61	19.60	5.08	24.64	-3.02
270	10.07	-14.48	6.94	7.62	-11.29	-4.46	7.53	9.95	33.52	24.74
280	7.03	-12.17	1.14	9.57	-45.31	0.49	16.60	11.61	26.14	39.04
290	4.11	-3.21	13.06	19.06	-6.43	12.47	11.65	13.36	11.06	48.77
300	12.48	4.20	11.12	5.16	11.28	9.50	12.19	3.10	8.20	26.99
310	6.58	5.51	5.50	19.41	-12.47	36.72	12.88	10.95	-1.80	33.61
320	3.12	0.37	1.00	-1.24	1.18	15.47	5.47	18.64	-1.77	50.14
330	6.70	5.01	11.75	-7.18	21.66	15.15	-1.95	40.73	-27.21	56.04
340	11.20	2.09	8.41	-9.08	6.57	17.43	5.17	34.67	-33.87	39.75
350	9.85	4.78	6.71	6.90	-10.05	11.01	6.56	17.30	-5.10	29.63
360	0.70	5.70	14.48	21.55	4.34	15.56	18.95	15.68	14.81	29.72

Table C.4. The relative difference on large scale between mean live time background *liv* and mean scrambled events background *ave* as function of galactic latitude. The unit is percentage %.

	Mono					Stereo				
b	1	2	3	4	5	1	2	3	4	5
-80	10.57	-16.78	-3.09	12.73	51.51	84.70	63.53	33.62	62.10	-3.70
-70	9.91	5.88	3.34	5.91	7.00	17.60	9.74	18.94	3.02	-54.62
-60	17.23	10.21	5.96	1.28	12.46	32.25	4.66	6.31	23.69	29.74
-50	12.62	13.38	0.07	4.76	16.77	19.88	14.77	7.59	10.26	28.32
-40	6.07	8.22	-2.64	0.46	11.31	8.19	6.76	1.97	8.55	-0.18
-30	-3.69	-0.32	-3.22	2.97	-10.82	-2.66	-0.98	-4.22	-2.46	10.63
-20	-9.32	-5.19	-8.02	-6.61	1.62	-7.89	-1.88	-9.57	-0.28	-10.51
-10	-8.79	-9.92	-10.86	-7.17	-13.06	-7.37	-7.67	-8.55	-6.29	-4.60
0	-6.13	-6.17	-3.05	-1.18	-14.19	-4.37	-1.87	-4.55	-1.65	-10.28
10	1.44	1.38	-1.00	1.06	-1.90	-5.48	-4.10	-2.51	0.77	-11.92
20	5.73	2.96	2.96	-3.41	4.25	5.46	3.28	1.53	-3.44	-13.08
30	7.08	4.18	5.90	-3.17	7.07	7.81	4.03	7.61	-3.11	-10.26
40	3.94	-0.73	7.31	0.99	9.95	0.35	2.38	8.23	-6.17	3.52
50	1.52	2.23	3.14	3.65	-1.11	-0.36	2.84	-0.43	1.07	-0.64
60	-1.83	1.07	1.28	5.06	-9.24	-3.29	-2.38	-0.28	5.85	8.34
70	-5.48	-3.34	-0.83	6.39	-6.06	-2.23	-3.36	-0.92	6.47	13.23
80	-7.68	-7.73	-7.81	-1.36	-6.09	-12.71	-14.80	-5.38	-7.17	35.85
90	-0.58	1.24	-9.96	0.14	-17.46	15.47	-5.91	18.33	-14.71	38.37

APPENDIX D

RESULTS OF HARMONICS ANALYSIS

The Rayleigh vectors of first and second harmonics are calculated by

$$
\begin{aligned}
x_1 &= \frac{2}{N}\sum_{\delta_1}^{\delta_2}\rho(l,b)\cos(\alpha) & \qquad x_2 &= \frac{2}{N}\sum_{\delta_1}^{\delta_2}\rho(l,b)\cos(2\alpha) \\
y_1 &= \frac{2}{N}\sum_{\delta_1}^{\delta_2}\rho(l,b)\sin(\alpha) & \qquad y_2 &= \frac{2}{N}\sum_{\delta_1}^{\delta_2}\rho(l,b)\sin(2\alpha) \\
R_1 &= \sqrt{x_1^2+y_1^2} & \qquad R_2 &= \sqrt{x_2^2+y_2^2} \\
\phi_1 &= \mathrm{Tan}^{-1}(\frac{x_1}{y_1}) & \qquad \phi_2 &= \frac{1}{2}\mathrm{Tan}^{-1}(\frac{x_2}{y_2})
\end{aligned}
$$

where ρ could be the event probability density of data or scrambled events and N is the total event probability density in that declination band. α and δ are the right ascension and declination of each point (l,b) where l is galactic longitude and b is galactic latitude. The Rayleigh vector distribution of scrambled events gives the mean and width of the isotropic background. The significance is defined as

$$\mathrm{Z} = \frac{\mathrm{data} - \mathrm{mean}}{\mathrm{width}}$$

The results of first and second harmonics are listed in Tables D.1 to D.4.

Table D.1. First harmonics of mono data.

Energy	Declination	Rayleight Vector $\|R\|$ Data	mean	width	$Z(\sigma)$	Phase (degree) Data	mean	width
	$-26 \sim -15$	1.559	1.583	0.019	-1.295	133.41	130.92	3.15
	$-15 \sim -5$	1.410	1.413	0.018	-0.191	123.04	128.28	2.58
	$-5 \sim 5$	1.251	1.255	0.016	-0.257	126.82	129.31	2.04
0.2	$5 \sim 15$	1.119	1.111	0.020	0.372	129.49	126.18	1.80
|	$15 \sim 26$	0.933	0.912	0.018	1.224	124.59	126.10	1.75
0.4	$26 \sim 38$	0.662	0.638	0.014	1.730	122.91	126.76	2.40
	$38 \sim 53$	0.158	0.129	0.019	1.544	117.63	127.75	7.95
	$53 \sim 90$	0.084	0.057	0.021	1.301	96.80	107.25	71.77
	$-26 \sim 90$	0.475	0.466	0.011	0.779	123.41	127.11	1.52
	$-26 \sim -15$	1.632	1.609	0.020	1.135	130.56	126.37	3.09
	$-15 \sim -5$	1.424	1.446	0.023	-0.937	128.79	127.40	1.98
	$-5 \sim 5$	1.292	1.283	0.021	0.425	127.38	127.89	1.81
0.4	$5 \sim 15$	1.125	1.161	0.017	-2.193	127.28	131.55	1.96
|	$15 \sim 26$	0.986	0.970	0.018	0.908	125.76	130.46	2.31
1.0	$26 \sim 38$	0.703	0.670	0.022	1.490	128.04	132.78	2.61
	$38 \sim 53$	0.209	0.172	0.027	1.365	109.63	116.93	8.77
	$53 \sim 90$	0.091	0.088	0.023	0.166	108.89	121.07	15.47
	$-26 \sim 90$	0.530	0.529	0.015	0.096	124.78	128.95	1.64
	$-26 \sim -15$	1.602	1.592	0.027	0.397	124.40	132.89	3.65
	$-15 \sim -5$	1.448	1.450	0.028	-0.066	125.24	127.75	2.86
	$-5 \sim 5$	1.268	1.306	0.031	-1.215	125.05	128.12	2.27
1.0	$5 \sim 15$	1.158	1.150	0.027	0.330	126.66	126.78	3.19
|	$15 \sim 26$	0.946	0.905	0.037	1.085	127.37	131.21	2.65
3.2	$26 \sim 38$	0.685	0.629	0.033	1.709	123.14	132.30	3.86
	$38 \sim 53$	0.113	0.153	0.038	-1.058	109.07	117.87	16.35
	$53 \sim 90$	0.096	0.073	0.032	0.728	87.84	86.79	38.66
	$-26 \sim 90$	0.540	0.539	0.022	0.003	122.86	127.47	2.47
	$-26 \sim -15$	1.574	1.583	0.052	-0.174	129.34	131.20	5.93
	$-15 \sim -5$	1.473	1.438	0.060	0.580	118.02	126.53	4.70
	$-5 \sim 5$	1.368	1.305	0.059	1.060	129.93	131.35	5.80
3.2	$5 \sim 15$	1.149	1.159	0.070	-0.150	135.64	126.04	5.93
|	$15 \sim 26$	0.955	0.943	0.071	0.173	120.47	133.46	6.40
10.0	$26 \sim 38$	0.593	0.727	0.066	-2.048	119.73	125.61	8.81
	$38 \sim 53$	0.236	0.176	0.083	0.717	144.49	105.31	54.71
	$53 \sim 90$	0.121	0.115	0.052	0.130	-157.27	53.99	65.19
	$-26 \sim 90$	0.529	0.553	0.040	-0.602	131.30	125.96	4.05
	$-26 \sim -15$	1.752	1.673	0.099	0.808	118.97	129.42	9.47
	$-15 \sim -5$	1.532	1.414	0.103	1.156	109.82	124.69	10.35
	$-5 \sim 5$	1.423	1.318	0.109	0.972	113.48	131.67	9.89
	$5 \sim 15$	1.225	1.241	0.111	-0.145	106.51	131.69	8.12
$\geq 10.$	$15 \sim 26$	0.817	1.007	0.093	-2.039	132.27	134.18	9.50
	$26 \sim 38$	0.700	0.737	0.142	-0.265	128.16	140.25	14.62
	$38 \sim 53$	0.262	0.363	0.146	-0.685	117.65	114.89	72.16
	$53 \sim 90$	0.362	0.170	0.097	1.980	-144.46	29.38	98.09
	$-26 \sim 90$	0.559	0.610	0.077	-0.664	129.83	131.81	6.67

Table D.2. Second harmonics of mono data.

Energy	Declination			Rayleight Vector $\|R\|$				Phase (degree)		
				Data	mean	width	$Z(\sigma)$	Data	mean	width
	-26	$\sim$	-15	0.570	0.649	0.059	-1.356	88.67	42.23	73.88
	-15	$\sim$	-5	0.320	0.279	0.052	0.800	61.53	66.84	32.46
	-5	$\sim$	5	0.166	0.093	0.039	1.869	34.49	28.35	15.74
0.2	5	$\sim$	15	0.225	0.243	0.042	-0.419	12.39	11.84	4.21
|	15	$\sim$	26	0.365	0.374	0.031	-0.290	8.33	4.98	1.90
0.4	26	$\sim$	38	0.376	0.390	0.019	-0.740	1.03	2.68	1.85
	38	$\sim$	53	0.087	0.080	0.021	0.343	19.16	18.60	9.74
	53	$\sim$	90	0.019	0.050	0.021	-1.479	8.52	31.36	18.75
	-26	$\sim$	90	0.159	0.155	0.011	0.360	9.11	10.20	2.36
	-26	$\sim$	-15	0.802	0.733	0.061	1.136	85.39	76.01	17.25
	-15	$\sim$	-5	0.295	0.377	0.056	-1.477	75.36	72.92	5.44
	-5	$\sim$	5	0.118	0.137	0.044	-0.426	46.81	46.04	11.92
0.4	5	$\sim$	15	0.200	0.124	0.028	2.708	6.73	8.93	8.54
|	15	$\sim$	26	0.262	0.272	0.027	-0.371	3.29	4.03	3.14
1.0	26	$\sim$	38	0.289	0.334	0.028	-1.577	-4.03	0.08	2.07
	38	$\sim$	53	0.088	0.050	0.024	1.606	20.97	16.88	19.00
	53	$\sim$	90	0.021	0.030	0.015	-0.575	-10.51	-22.69	52.89
	-26	$\sim$	90	0.106	0.086	0.011	1.751	6.40	9.25	4.36
	-26	$\sim$	-15	0.710	0.667	0.080	0.532	74.70	14.61	84.42
	-15	$\sim$	-5	0.375	0.364	0.072	0.152	72.02	70.08	28.35
	-5	$\sim$	5	0.139	0.139	0.062	-0.008	36.96	58.02	15.21
1.0	5	$\sim$	15	0.173	0.197	0.053	-0.461	12.42	11.72	9.69
|	15	$\sim$	26	0.332	0.383	0.062	-0.830	-0.42	-1.25	3.93
3.2	26	$\sim$	38	0.308	0.428	0.050	-2.414	-4.76	-2.17	2.88
	38	$\sim$	53	0.138	0.063	0.033	2.094	-12.43	23.61	39.23
	53	$\sim$	90	0.031	0.052	0.028	-0.739	-39.12	20.67	35.94
	-26	$\sim$	90	0.100	0.102	0.022	-0.064	0.99	9.94	6.95
	-26	$\sim$	-15	0.615	0.646	0.160	-0.198	81.93	38.77	71.39
	-15	$\sim$	-5	0.517	0.359	0.140	1.125	57.42	59.01	36.94
	-5	$\sim$	5	0.244	0.179	0.089	0.733	83.74	14.54	56.73
3.2	5	$\sim$	15	0.173	0.256	0.118	-0.700	-24.27	15.01	23.91
|	15	$\sim$	26	0.425	0.353	0.113	0.641	12.64	-2.15	9.66
10.0	26	$\sim$	38	0.435	0.234	0.068	2.941	-5.19	-7.56	14.69
	38	$\sim$	53	0.119	0.120	0.057	-0.013	-3.83	-39.36	25.66
	53	$\sim$	90	0.033	0.111	0.061	-1.273	0.22	-29.23	47.31
	-26	$\sim$	90	0.113	0.068	0.033	1.358	6.64	-12.00	28.64
	-26	$\sim$	-15	1.172	0.924	0.298	0.830	72.05	34.05	70.68
	-15	$\sim$	-5	0.760	0.408	0.183	1.923	51.15	26.87	54.36
	-5	$\sim$	5	0.544	0.294	0.163	1.531	51.35	2.37	59.06
	5	$\sim$	15	0.444	0.262	0.147	1.242	26.51	-3.76	56.06
$\geq 10.$	15	$\sim$	26	0.635	0.249	0.129	2.994	-0.86	7.64	26.74
	26	$\sim$	38	0.298	0.357	0.164	-0.359	-12.27	-6.26	21.80
	38	$\sim$	53	0.115	0.176	0.090	-0.684	-28.45	-7.75	57.24
	53	$\sim$	90	0.115	0.157	0.082	-0.506	-25.85	-0.79	57.87
	-26	$\sim$	90	0.137	0.095	0.044	0.957	11.99	8.04	52.74

Table D.3. First harmonics of stereo data.

Energy	Declination	Rayleight Vector $\|R\|$ Data	mean	width	$Z(\sigma)$	Phase (degree) Data	mean	width
	$-26 \sim -15$	1.777	1.653	0.153	0.810	107.72	128.46	35.28
	$-15 \sim -5$	1.487	1.464	0.051	0.465	115.60	124.04	3.85
	$-5 \sim 5$	1.289	1.309	0.043	-0.482	121.67	120.78	3.07
0.2	$5 \sim 15$	1.157	1.130	0.028	0.963	120.85	120.25	3.01
|	$15 \sim 26$	0.978	0.943	0.029	1.233	119.49	121.52	3.33
0.4	$26 \sim 38$	0.743	0.718	0.030	0.866	114.29	118.42	3.14
	$38 \sim 53$	0.201	0.120	0.039	2.049	84.94	76.94	21.14
	$53 \sim 90$	0.165	0.163	0.043	0.047	111.83	85.17	14.64
	$-26 \sim 90$	0.614	0.590	0.016	1.572	115.73	116.81	1.90
	$-26 \sim -15$	1.629	1.644	0.060	-0.250	120.94	122.79	6.07
	$-15 \sim -5$	1.464	1.486	0.044	-0.515	127.36	118.80	3.62
	$-5 \sim 5$	1.325	1.319	0.031	0.188	122.31	119.84	2.95
0.4	$5 \sim 15$	1.208	1.122	0.027	3.184	118.54	121.26	2.86
|	$15 \sim 26$	0.946	0.955	0.036	-0.278	123.27	124.02	2.93
1.0	$26 \sim 38$	0.691	0.685	0.037	0.174	121.86	126.08	5.46
	$38 \sim 53$	0.328	0.193	0.035	3.809	83.31	83.68	13.82
	$53 \sim 90$	0.224	0.163	0.044	1.400	87.89	82.94	15.39
	$-26 \sim 90$	0.667	0.620	0.019	2.519	115.90	117.94	2.44
	$-26 \sim -15$	1.576	1.619	0.080	-0.536	121.56	132.78	7.93
	$-15 \sim -5$	1.513	1.482	0.057	0.540	120.59	117.41	5.63
	$-5 \sim 5$	1.274	1.359	0.039	-2.163	128.38	119.45	4.83
1.0	$5 \sim 15$	1.228	1.143	0.046	1.829	119.34	121.39	4.87
|	$15 \sim 26$	1.028	0.946	0.050	1.646	112.32	119.41	4.28
3.2	$26 \sim 38$	0.626	0.652	0.060	-0.439	121.03	116.19	7.52
	$38 \sim 53$	0.224	0.194	0.070	0.424	106.60	89.55	42.74
	$53 \sim 90$	0.105	0.142	0.060	-0.628	128.04	76.65	51.25
	$-26 \sim 90$	0.650	0.629	0.031	0.675	119.22	116.29	3.44
	$-26 \sim -15$	1.299	1.689	0.126	-3.099	141.72	128.63	15.67
	$-15 \sim -5$	1.255	1.517	0.141	-1.866	116.51	124.66	10.85
	$-5 \sim 5$	1.332	1.287	0.101	0.448	118.19	123.42	9.88
3.2	$5 \sim 15$	1.106	1.125	0.082	-0.227	134.45	128.10	9.66
|	$15 \sim 26$	0.831	0.924	0.104	-0.896	125.62	127.96	9.47
10.0	$26 \sim 38$	0.772	0.642	0.125	1.037	116.34	134.37	9.10
	$38 \sim 53$	0.426	0.255	0.117	1.465	92.78	73.14	97.12
	$53 \sim 90$	0.051	0.297	0.118	-2.089	-16.17	64.85	55.91
	$-26 \sim 90$	0.572	0.630	0.063	-0.910	117.66	123.11	7.60
	$-26 \sim -15$	1.687	1.886	0.112	-1.767	142.47	109.28	50.21
	$-15 \sim -5$	1.446	1.717	0.176	-1.533	128.66	113.39	55.88
	$-5 \sim 5$	1.776	1.303	0.203	2.330	131.95	133.96	38.95
	$5 \sim 15$	1.564	1.216	0.186	1.863	119.68	137.89	18.14
$\geq 10.$	$15 \sim 26$	1.070	1.175	0.227	-0.463	133.94	128.68	21.08
	$26 \sim 38$	1.164	0.889	0.297	0.923	133.40	93.01	39.49
	$38 \sim 53$	0.732	0.696	0.281	0.127	144.98	27.70	28.88
	$53 \sim 90$	0.456	0.485	0.226	-0.129	92.90	-27.62	56.92
	$-26 \sim 90$	0.986	0.554	0.131	3.305	126.10	110.88	19.30

Table D.4. Second harmonics of stereo data.

Energy	Declination			Rayleight Vector $\|R\|$				Phase (degree)		
				Data	mean	width	$Z(\sigma)$	Data	mean	width
	-26	$\sim$	-15	1.216	0.947	0.415	0.647	61.31	10.34	67.03
	-15	$\sim$	-5	0.490	0.468	0.115	0.188	59.27	65.03	8.32
	-5	$\sim$	5	0.270	0.275	0.079	-0.065	42.70	50.58	9.95
0.2	5	$\sim$	15	0.272	0.302	0.044	-0.676	26.92	22.17	4.59
|	15	$\sim$	26	0.370	0.399	0.039	-0.748	14.26	9.46	3.57
0.4	26	$\sim$	38	0.303	0.298	0.035	0.117	2.88	7.68	3.44
	38	$\sim$	53	0.105	0.106	0.033	-0.009	29.71	21.63	11.12
	53	$\sim$	90	0.066	0.117	0.041	-1.257	-27.82	29.41	10.60
	-26	$\sim$	90	0.171	0.197	0.020	-1.332	16.82	19.36	2.69
	-26	$\sim$	-15	0.751	0.852	0.185	-0.544	73.48	68.44	28.71
	-15	$\sim$	-5	0.454	0.553	0.110	-0.902	70.68	62.18	5.92
	-5	$\sim$	5	0.271	0.288	0.060	-0.285	52.63	46.23	7.01
0.4	5	$\sim$	15	0.229	0.279	0.065	-0.780	32.93	16.04	4.99
|	15	$\sim$	26	0.355	0.361	0.044	-0.157	6.74	13.23	4.31
1.0	26	$\sim$	38	0.376	0.365	0.054	0.214	2.43	4.62	4.49
	38	$\sim$	53	0.132	0.095	0.047	0.802	26.89	44.58	39.57
	53	$\sim$	90	0.031	0.108	0.039	-1.973	-81.79	42.55	58.54
	-26	$\sim$	90	0.146	0.151	0.020	-0.213	20.18	27.32	4.69
	-26	$\sim$	-15	0.845	0.784	0.230	0.267	62.59	17.01	79.06
	-15	$\sim$	-5	0.535	0.534	0.147	0.009	68.85	60.40	7.56
	-5	$\sim$	5	0.179	0.300	0.090	-1.345	45.93	56.76	12.03
1.0	5	$\sim$	15	0.234	0.231	0.098	0.031	37.46	14.51	16.32
|	15	$\sim$	26	0.359	0.405	0.072	-0.631	12.20	5.98	5.23
3.2	26	$\sim$	38	0.345	0.454	0.074	-1.471	-8.52	-1.40	4.78
	38	$\sim$	53	0.052	0.126	0.053	-1.412	-3.04	11.06	17.81
	53	$\sim$	90	0.020	0.107	0.045	-1.902	86.01	14.30	62.51
	-26	$\sim$	90	0.115	0.155	0.041	-0.991	18.04	16.13	9.10
	-26	$\sim$	-15	0.141	1.015	0.329	-2.662	-25.54	26.20	67.91
	-15	$\sim$	-5	0.435	0.662	0.285	-0.798	23.61	37.72	55.79
	-5	$\sim$	5	0.360	0.413	0.165	-0.318	50.51	36.31	21.94
3.2	5	$\sim$	15	0.379	0.347	0.160	0.199	20.71	4.50	23.21
|	15	$\sim$	26	0.500	0.406	0.151	0.625	16.28	2.04	14.29
10.0	26	$\sim$	38	0.106	0.431	0.146	-2.223	23.37	-10.23	12.12
	38	$\sim$	53	0.162	0.231	0.108	-0.638	83.55	12.22	35.92
	53	$\sim$	90	0.148	0.207	0.106	-0.557	86.59	-23.81	33.49
	-26	$\sim$	90	0.129	0.191	0.079	-0.793	36.92	0.68	13.84
	-26	$\sim$	-15	0.951	1.632	0.324	-2.104	-80.52	17.37	55.25
	-15	$\sim$	-5	0.253	1.151	0.469	-1.915	88.46	22.62	59.96
	-5	$\sim$	5	1.274	0.590	0.303	2.260	86.75	-14.10	42.33
	5	$\sim$	15	0.780	0.515	0.233	1.137	67.16	-10.86	39.33
$\geq 10.$	15	$\sim$	26	0.238	0.531	0.262	-1.119	-13.70	-2.69	44.34
	26	$\sim$	38	0.390	0.615	0.319	-0.703	38.98	-5.88	27.41
	38	$\sim$	53	0.335	0.484	0.226	-0.659	9.63	-30.90	26.83
	53	$\sim$	90	0.854	0.340	0.187	2.756	-10.19	-18.95	52.04
	-26	$\sim$	90	0.123	0.250	0.136	-0.927	11.39	-12.22	38.69

REFERENCES

[1] D.J. Bird *et al.*, Proc. 23rd ICRC (Calgary), **2**:30, (1993)

[2] D.J. Bird *et al.*, Proc. 23rd ICRC (Calgary), **2**:34, (1993)

[3] D.J. Bird *et al.*, Proc. 23rd ICRC (Calgary), **2**:38, (1993)

[4] D.J. Bird *et al.*, Proc. 23rd ICRC (Calgary), **2**:51, (1993)

[5] D.J. Bird *et al.*, Proc. 23rd ICRC (Calgary), **2**:55, (1993)

[6] D.J. Bird *et al.*, Phys. Rev. Lett., **71**:3401, (1993)

[7] D.J. Bird *et al.*, Ap. J., **424**:491, (1994)

[8] M.A. Huang *et al.*, *Currents in High Energy Astrophysics*, Proc. of The 9th International School of Cosmic-Ray Astrophysics, ed. by M. Shapiro , R. Silberg, and J.P. Wefel (Kulwer Academic, Derdrecht, Netherlands, 1995), 123

[9] M.S. Longair, it High Energy Astrophysics, 2nd ed. (Cambridge University, Cambridge, 1992) **1**:10

[10] A.M. Hillas, *Cosmic Rays*, 1st ed (Pergamon, Hungary, 1972), 51

[11] A.M. Hillas, *Ann. Rev. Astron. Astrophys,* **22**:425, (1984)

[12] M.S. Longair, it High Energy Astrophysics, 2nd ed. (Cambridge University, Cambridge, 1992) **2**:313

[13] R.J. Protheroe, J. Phys. G **10**:L99, (1984)

[14] R.S. White, *Origin of Cosmic Rays, IAU Symposium No. 94*, ed. by M. Shapiro , R. Silberg, and J.P. Wefel (Kulwer Academic, Derdrecht, Netherlands, 1991), 249

[15] R.D. Blandford & J.P. Ostriker, Astrophy. J. **221**:L29 (1978)

[16] R.D. Blandford & J.P. Ostriker, Astrophy. J. **237**:793 (1980)

[17] J.R. Jokipii & G.E. Morfill, Astrophy. J. **290**:L1 (1985)

[18] J.R. Jokipii & G.E. Morfill, Astrophy. J. **312**:170 (1987)

[19] A.M. Hillas, J. Physics **G 8**:1461-1473, (1982)

[20] K. Greisen, Annu. Rev. Nuc. Sci., **10**:63, (1960)

[21] T.K. Gaisser, *Cosmic Rays And Particle Physics* (Cambridge Univ. Press. 1980), 27

[22] A.M. Hillas *et al.*, Proc 12th ICRC (Hobart) **3**:1001 (1971)

[23] E.N. Efimov *et al., Catalogue of Highest Energy Cosmic Rays*, ed. WDC-C2 for cosmic rays N.3 (1988)

[24] J.W. Elebert *et al.*, Proc. 18th ICRC (Bangalore), **6**:227, (1983)

[25] D.J. Bird *et al.* Ap. J. **441**:144, (1995)

[26] P. Sommers, Proc. Tokyo workshop on techniques for the study of extremely high energy cosmic rays, Tokyo, 23, (1993)

[27] K. Greisen, Phys. Rev. Lett. **16**:748, (1966)

[28] G.T. Zatsepin and V.A. Kuzmin, Zh. Eksp. Teor. Fiz. **4**:114, (1966)

[29] C.T. Hill & D.N. Schramm, Phys. Rev. **D31**:564, (1985)

[30] M. Teshima, 23rd ICRC (Calgary),Rapporteur talk 257 (1993)

[31] N. Hayashida *et al.*, Phys. Rev. Lett. **73**:3491 (1994)

[32] P. Sokolsky, 23rd ICRC (Calgary), Highlight talk 447, (1993)

[33] C.E. Fitchel and J. linsey, Astrophys.,J., **300**:483, (1986)

[34] R.W. Clay and A.G.K. Smith, *Astrophysical Aspects of the Most Energetic Cosmic Rays*, ed. M. Nagano and F. Takahara (World Sci., Singapore, 1991) 125

[35] Cassiday *et al.* Proc. 21st ICRC (Adelaide), **3**:196

[36] Cassiday *et al.* Astrophys. J. **351**:454

[37] J. Wdowcjyk and A.W. Wolfendale, J. Phys G, **10**:1453 (1984)

[38] X. Chi *et al.*, J. Phys G, **19**:780,788 (1993)

[39] S.M. Astley *et al.* Proc. 17th ICRC (Paris), **2**:156(1981)

[40] A.A. Watson *Advances in Space Research* (Elmsford, N.Y., Pergamon, 1984) **4**:35

[41] G.L. Cassiday *et al.*, Phys. Rev. Lett. **62**:383 (1989)

[42] G.L. Cassiday *et al.*, Phys. Rev. Lett. **63**:2329 (1989)

[43] M. Teshima *et al.*, Phys. Rev. Lett. **64**:1628 (1990)

[44] R. Ong, Talks at University of Utah, June 1996

[45] R.M. Baltrusaitis *et al.*, Astrophys. J., **293(3)**:L69, (1985)

[46] B.L. Dingus *et al.*, Phys. Rev. Lett., **61:**1906, (1988)

[47] Ya.B. Zeldovich, A.A. Ruzmaikin, and D.D. Sokoloff, *Magnetic Fileds In Astrophysics* (Gordon and Brech Sci. Pub., New York, 1983) 34

[48] R.M. Baltrusaitis *et al.*, Nucl. Instr. Meth., **A240**:410-428, (1985)

[49] G.L. Cassiday, Ann. Rev. Nucl. Part. Sci., **33**:321-349, (1985)

[50] K.D. Green, *The Cosmic Ray Spectrum Above 0.3EeV* PhD thesis (Univ. of Utah, Salt Lake City, Utah, 1992)

[51] Bunner, A.N., *The Atmosphere as a Cosmic Ray Scintillator*, PhD thesis (Cornell Univ., Ithaca, N.Y. 1964)

[52] R.M. Baltrusaitis *et al.*, Proc. 19th ICRC (La Jolla), **7**:155 (1985a)

[53] R.M. Baltrusaitis *et al.*, Proc. 19th ICRC (La Jolla), **7**:159 (1985b)

[54] J. Linsley, Proc. 18th ICRC (Bangalore), **12**:135 (1983)

[55] P. Sokolsky, P. Sommer, B.R. Dawson, Phys. Reports. (Elsevier Sci. Pub., North-Holland, 1992)**217(5):**247

[56] G. de Vaucouleures, *Vistas in Astronomy* **2**:77,(1956)

[57] G. de Vaucouleures, *Second Reference of Catalogue of Bright Galaxies* (Univ. of Texas Press, Austin, 1976)

[58] P.A. Shaver, and M. Pierre, *Astron. Astroph* **220**:35,(1989)

[59] A.A. Watson, Proc. Snowmass in print (World Scientific, 1994)

[60] T. Stanev and P.L. Biermann, Talks at the Fermilab Astrophysics Workshop, March (1995)

[61] T. Stanev *et al.*, Phys. Rev. Lett. **75:**3056, (1995)

[62] H.Y. Dai, private communication

[63] E. Waxman, K.B. Fisher, T. Piran, Astrophy. J. Apr (1996)

[64] A.A. Lee and R.W. Clay, Proc. 23th ICRC (Calgary), **2:**77, (1993)

[65] R.A. Fisher, *Statistical Methods For Research Workers*, 13th ed. (Hafner Pub., New York, 1958), 99

[66] W.T. Eadie, D. Drijard, F.E. James, M. Roos, and B. Sadoulet, *Statistical Methods in Experimental Physics* (North-Holland Pub., Amsterdam, 1971) 283

[67] W.A. Wallis., Econometrica, 10, (1942)